SPACE ENVIRONMENT TECHNOLOGIES

SET TR 2006-003

Comparative Aeronomy of the Upper Atmospheres of the Giant Planets

Henrik Melin

May 2006

Comparative Aeronomy of the Upper Atmospheres of the Giant Planets

A thesis by Henrik Melin
Submitted for the degree of Doctor of Philosophy

May 20, 2006, London

Atmospheric Physics Laboratory
Department of Physics and Astronomy
University College London

Abstract

This thesis presents a study of H_3^+ emission from Jupiter, Saturn and Uranus. This emission is associated with both auroral and solar processes, and can be used to trace energy inputs in the upper atmosphere.

For Jupiter, a detailed analysis of the H_3^+ emission is performed using a 1D self-consistent atmospheric numerical model and the detailed balance formulation for H_3^+ contained within a volume of H_2. It is shown that the effects due to departures from local thermodynamic equilibrium (LTE) are significant, reducing the intensity of the observed H_3^+. Evidence of this is shown to be present in published observations of the jovian aurora.

Using the non-LTE results, the auroral heating event observed by Stallard et al. [2002] on Jupiter is analysed in terms of energy inputs and outputs. It is shown that the dominant heating source is Joule heating and ion-drag, produced by the increase in ion velocity in the auroral electrojet. However, in the absence of the heating there are not enough heat sinks as to cool down the atmosphere quickly, indicative that the energy is re-distributed mechanically via thermally driven winds.

Using data from the United Kingdom Infrared Telescope (UKIRT), the first reliable auroral H_3^+ temperature of Saturn is determined: $T = 400 \pm 50$ Kelvin with a column-integrated H_3^+ density of $N = 4.6 \times 10^{16}$ m^{-2}. The variations in column density within the dataset are large, indicating large variations in the precipitation flux, while the temperature remains fairly constant.

On Uranus, infrared H_3^+ spectra covering a decade is analysed in an attempt to explain the observed variability. This forms the most comprehensive long-term study of H_3^+ emission to date. The variability is found to be complicated, with an auroral component of the total H_3^+ emission being of similar magnitude as the EUV-produced component. The auroral component appears to be controlled by geometry.

Acknowledgements

The making of a PhD is not an entirely individual effort. To the following, I extend my heartfelt gratitude:

- My supervisor, **Steve Miller**, for the stupendous guidance and coaxing he has provided over the past three years. He also understood the importance of me spending time in Hawaii, getting to grips with the finer points of infrared spectroscopy.
- **Jonathan Tennyson**, without whom this PhD would never have happened, or, have been funded (thanks **EPSRC**, **Perrin Fund** and **APL** for that too).
- **Tom Stallard**, who has been both a friend and a mentor, and with whom I spent considerable time observing up Mauna Kea.
- **Larry Trafton**, **Denis Grodent**, **Tom Geballe** and **Thérèse Encrenaz** who kindly shared their data and observations.
- The staff of the **NASA IRTF**, **UKIRT** and **Mauna Kea Support Services**.
- The truly amazing people that make up the **Atmospheric Physics Laboratory** (APL). Without them, my work would not have been such a joy.
- My mother and father (**Ingrid** and **Lars**), for their rock-steady support.
- **Louis**, **Domino** and **Lola** for offering a place to call home during the writing of this thesis, despite me not never really being around, and if I was, I was probably working.

Finally, I would like to recognise the unconditional friendship and encouragement offered by **Mary Hansen**, who so tragically died during the course of this PhD.

Go on a starlit night,
stand on your head,
leave your feet dangling
 outwards into space,
and let the starry
 firmament you tread
be, for the moment,
 your elected base.

Feel Earth's colossal weight
 of ice and granite,
of molten magma,
 water, iron, and lead;
and briefly hold
 this strangely solid planet
balanced upon
your strangely solid head.

Piet Hein

Contents

List of Figures

List of Tables

Chapter 1

Introduction

The four giant planets in our solar system are Jupiter, Saturn, Uranus and Neptune, in order of distance from the Sun. They are huge volumes of gravitationally bound gas, most of which is hydrogen ($\sim$ 75% by weight) and helium ($\sim$ 25%). Very little was known about these planets before they were visited by spacecraft – Pioneer 10 was the first probe to make a direct measurement of a giant planet (Jupiter in 1972). The many images and datasets beamed back to Earth ever since, from various probes, have provided the scientific community with many surprises and have captured the imagination of the general public.

It was not until the 1990s that instruments and telescopes positioned on Earth developed into tools that could be used to study the processes governing the upper atmospheres of the giant planets. In particular, it was the discovery of the molecular ion H_3^+, in combination with ever increasing spatial and spectral resolution of the available spectrographs, that enabled the detailed study of giant planet upper atmospheres. This thesis presents the study of H_3^+ emission from Jupiter, Saturn and Uranus.

Figure 1.1 shows the relative sizes of the Earth and the giant planets, highlighting why these planets are described as 'giant'. They are remarkably different from each other, not only in the way they appear through a telescope, but also in the way they are configured: Uranus and Neptune both have a very large offset between their rotational and magnetic pole, Saturn has a magnetic pole which is nearly perfectly aligned with its rotational pole, and Jupiter has an Earth-like configuration, where the magnetic axis is slightly offset from the rotational axis. Any theory describing the

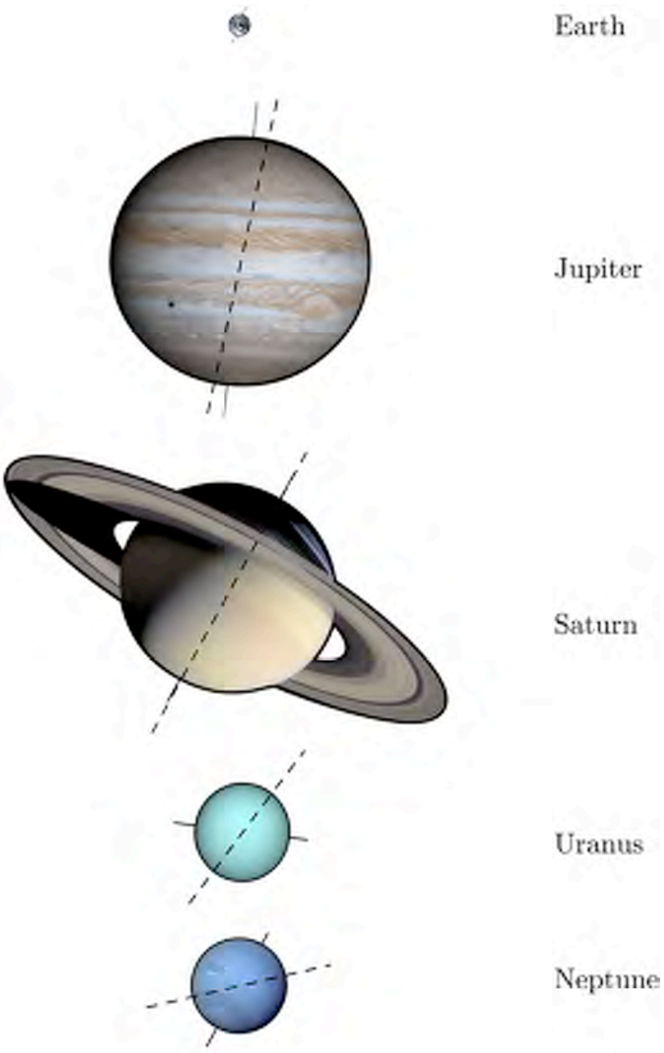

Figure 1.1: The Earth and the giant planets. The dashed line is the magnetic dipole axis and the solid line is the rotational axis. The planets are shown at an accurate relative size.

formation and evolution of the solar system must be able to account for all of these.

At the time of writing, 157 planets (`http://planetquest.jpl.nasa.gov`) have been detected orbiting stars other than the Sun. The smallest known extrasolar planet is estimated to be similar in size to Neptune (Butler et al. [2004]), and it is thought that the exoplanets found so far are similar to the giant planets in our own solar system (e.g. Williams [2004]). A comparative study recognising the differences, similarities and common processes within the solar system can be extended to these worlds we know very little about.

	Earth	Jupiter	Saturn	Uranus	Neptune
Mean Sun distance (AU)	1	5.2	9.5	19	30
Mean radius (km)	6,373	71,398	60,330	25,559	24,764
Spin period (h)	24	9.9	10.7	17.2	16.1
Magnetosphere radius	11 $R_\oplus$	50-100 R_J	14 R_S	18 R_U	23-26 R_N
Sunlight received (% of Earth)	100	3.7	1.1	0.3	0.1
Solar heating temperature (K)	255	110	82	60	50
Actual temperature at 1 bar (K)	300	165	134	76	72
Exospheric temperature (K)	700	1200	400	800	750
Solar wind density ($10^6 \mathrm{m}^{-3}$)	10	0.4	0.1	0.03	0.005
Energy balance[a]	1.0	1.67	1.78	1.14	1.9 - 2.9

Table 1.1: Table showing a selection of basic planetary and atmospheric parameters for Earth, Jupiter, Saturn, Uranus and Neptune. [a]The energy balance is the fraction between the energy emitted from a planet and the energy it absorbs from the Sun.

1.1 The upper atmosphere of the giant planets

The upper atmosphere is the outermost part of the atmosphere of a planet. It can be thought of as having two components: a neutral component and an ion component, and they are intrinsically linked through chemistry and the transfer of energy.

The neutral upper atmosphere is normally divided into the mesosphere, thermosphere and exosphere, in order of increasing altitude. In the mesosphere, the temperature decreases with increasing altitude until the mesopause is reached; from this point the temperature starts to increase with altitude (Hunten [1976]). This increasing temperature is seen in the thermosphere until the outermost layer of the atmosphere is reached – the exosphere, where the temperature remains constant with altitude. Another important boundary in the atmosphere is the homopause, at which the molecular diffusion is equal to the eddy diffusion. Below the homopause, each species in the atmosphere has the same scale height, such that the atmosphere can be characterised as 'well mixed'. Above the homopause, the scale height for the different species in the atmosphere is different and molecular diffusion controls the vertical mixing of the gas mix. The homopause and mesopause can be found at roughly the same altitude for each of the giant planets. The scale height of a particular species, i.e. the height over which the pressure is reduced by $1/e$ assuming hydrostatic equilibrium, is defined as:

$$h = \frac{kT}{mg} \tag{1.1}$$

where k is Boltzmann's constant, T is the temperature, m is the mass of the species and g is the gravitational constant.

The ionosphere of an atmosphere is defined by Schunk and Nagy [2000] as:

> *'The ionoshphere is considered to be that region of an atmosphere where significant numbers of free thermal ($< 1eV$) electrons and ions are present.'*

Depending on the definition of that *significant number*, ionospheres have been detected around seven of the nine planets in the solar system (Mendillo et al. [2002]). An ionosphere is the ionised component of an atmosphere and it is created by the ionisation of neutral gases by extreme ultraviolet (EUV) radiation from the Sun or other energy sources, such as particle precipitation. The only measurements of the altitude structure of the ionosphere of the gas giants are electron density profiles obtained from spacecraft flybys, e.g. by the Pioneers and the Voyagers.

The main constituent of the upper atmosphere of the giant planets is molecular hydrogen (Atreya [1986]). Therefore, ionised molecular hydrogen, H_2^+, plays a very important role in the formation of the ionosphere. This ion, once formed, reacts very rapidly with neutral H_2 to form H_3^+.

The energy balance of the upper atmosphere of the giant planets is a puzzle. There are seemingly not enough energy inputs to explain the very high observed temperatures seen in Table 1.1. In other words, the upper atmosphere is inexplicably hot (e.g. Strobel and Smith [1973] and Gladstone et al. [2002]). The EUV radiation that the giant planets receive from the Sun cannot inject enough energy to create the observed thermospheric temperatures. Consequently, there must be additional heat sources such as heating by particle precipitation or Joule heating and ion-drag (i.e. energy transferred from the magnetosphere). A detailed analysis of the different energy sources that might be available to the jovian system is presented in Chapter 3.

1.1.1 Jupiter

Jupiter is the fifth planet from the Sun and orbits at a distance of 5.2 Astronomical Units (AU). It is the largest planet in the solar system and the fourth brightest object in the sky (after the Sun, Moon and Venus). It rotates around its axis once every 9h55′, which is faster than any other planet. The fast rotation has important implications for

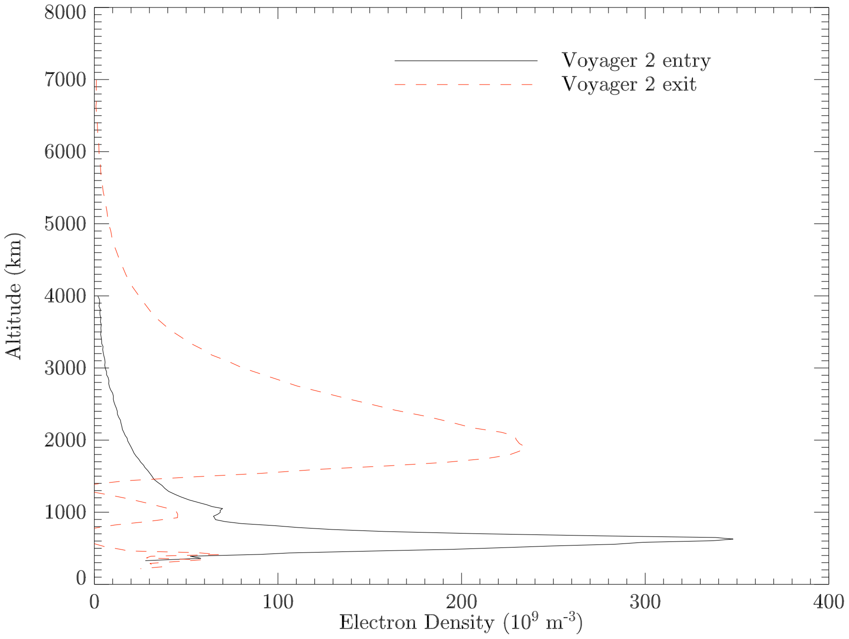

Figure 1.2: Jovian ionospheric electron density profiles derived from Voyager 2 radio occultation data. The data was taken during the 10^{th} and the 11^{th} of July 1979 UT at a latitude of 66°S (entry) and 51°S (exit).

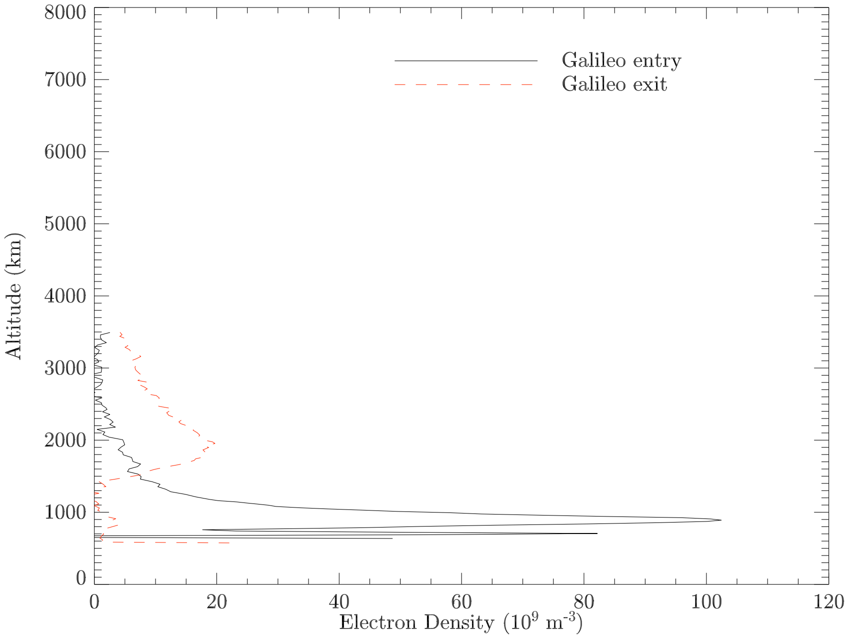

Figure 1.3: Jovian ionospheric electron density profiles derived from Galileo radio occultation data. The data was taken during the 8^{th} of December 1995 UT at a latitude of 24°S (entry) and 43°S (exit). This plot has the same units as Figure 1.2 above.

the dynamics of the atmosphere since it produces very strong Coriolis forces, which tend to prevent meridional wind systems from being established in favour of zonal winds. Jupiter also has the hottest upper atmosphere of the giant planets, indicative of the very powerful processes at work on this planet.

The ion part of an atmosphere can be investigated using electron density profiles derived from observations of solar or stellar occultations by a nearby spacecraft. The electron density profiles of Jupiter obtained by Voyager 2 (Hinson et al. [1998]) and Galileo (Hinson et al. [1997]) can be seen in Figures 1.2 and 1.3 respectively. The Voyager 2 data was taken at latitudes 66° and 51° South (entry and exit) and the Galileo data was taken at latitudes 24° and 43° South (entry and exit). There appears to be two types of profiles: one that peaks around 1,000 km (above the 1 bar level) taken at the occultation entry, and one that peaks around 2,000 km, obtained at occultation exit. It is not known why the two profiles are so very different, having a peak density at very different altitudes. In addition, the entry profiles have a lower density than the exit profiles and both Voyager 2 profiles show a much larger electron density than the Galileo profiles. These features are not reproducible with purely photochemical atmospheric models, which suggests that dynamical effects are playing a very important part in the jovian ionosphere. The Voyager 2 profiles were obtained at higher latitudes than the Galileo profiles, which might explain why the Voyager 2 electron densities are so much higher – these are closer to the auroral region, where large volumes of ions are produced via auroral processes.

Since Jupiter is the gas giant closest to us, and the biggest, it is consequently the most studied. Many of the phenomena subject to comparative aeronomy manifest themselves the strongest on Jupiter, and the planet has a long history of discovery 'firsts' associated with it, e.g. the first detection of H_3^+ outside the laboratory (Drossart et al. [1989]). Because of this, Jupiter is the giant planet that we know the most about, so the atmospheric structure and composition of Jupiter is a good starting point when studying the upper atmosphere of other gas giants. Jupiter has provided the precedence in trying to understand other gas giants, and a generic extrasolar planet is for this reason often assumed to be Jupiter like (Williams [2004]).

1.1.2 Saturn

Saturn, famous for its prominent ring system, is the sixth planet from the Sun and orbits at a distance of 9.5 AU. It is the only planet to have a density less than water. It has similar tropospheric cloud features as observed on Jupiter, although they display lower contrast. It is also a fast rotator, with a period as determined by Cassini SKR (Saturn Kilometric Radiation) observations of $P = 10h45'$, which is seven minutes faster than what was measured by Voyager 2 in 1981 ($P = 10h39'$) confirming the results of Galopeau and Lecacheux [2000]. The cause of this discrepancy is not known.

The electron density profiles of Saturn were obtained from radio occultation experiments performed by Pioneer 11 and Voyager 1 and 2. They observed a fast diurnal variation in the peak electron density, probably related to the fast rotation of the planet (Kliore et al. [1980] and Smith et al. [1983]).

The neutral component of Saturn's atmosphere is very similar to that of Jupiter, and so we expect the ionosphere of Saturn to be similar in chemistry and behavior. However, there are two major differences. Firstly, the ionospheric density calculated assuming a similar neutral component is about an order of magnitude larger than the observed density. Secondly, the diurnal variations in ionospheric density, inferred from Voyager 2 Saturn electrostatic discharges (SED) observations (Kaiser et al. [1984]), cannot be reproduced when modelling Saturn with a modified Jupiter model (e.g. Moses and Bass [2000], Waite and Cravens [1987] and Majeed and McConnell [1986]). This suggests that Saturn is in part governed by a different set of processes than observed at Jupiter.

One solution that reduces the large electron densities produced by the numerical models is to assume that water is transported from the rings, along the magnetic field lines, onto the upper atmosphere (Waite and Cravens [1987]). It is suggested that a water flux of 10^{11} molecules $\mathrm{m}^{-2}\mathrm{s}^{-1}$ and a small ($\sim 0.5 \times 10^{-3}$ Wm^{-2}) influx of low energy electrons could produce the observed electron densities at low latitudes. It is important to remember, however, that there are generally large variations for all the planets in the electron densities derived from occultation measurements.

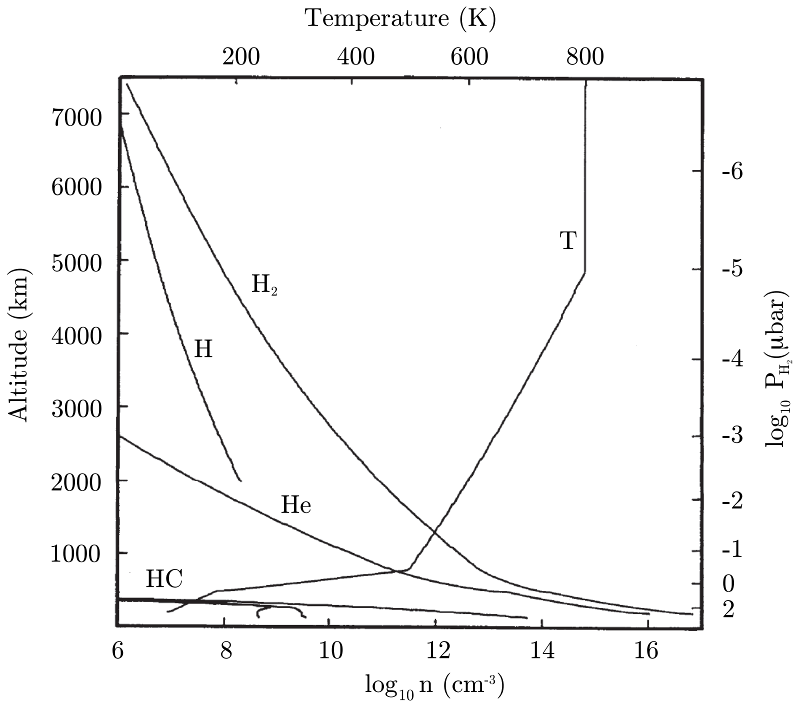

Figure 1.4: The atmospheric profile of Uranus as derived from the Voyager 2 encounter in 1986. After figure by Atreya [1986].

1.1.3 Uranus

Uranus orbits around the Sun at a distance of 19 AU and is about four times larger than the Earth. The only source for the structure of the upper atmosphere are the occultation experiments made by Voyager 2 in 1986. As on Saturn, there are low electron densities, which cannot be easily explained (Lindal et al. [1987]). The profiles display sharp and dense ionisation layers below 2,000 km. Above 2,000 km the electron number density is $\leq 10^9$ m^{-3} but the density remains above 10^8 m^{-3} up to an altitude of 10,000 km. This is indicative of an extended hydrogen corona around the planet (Tyler et al. [1986]).

The density and temperature structure of the upper atmosphere of Uranus, inferred from a number of Voyager 2 observations, can be seen in Figure 1.4. The dominant species is H_2 and the exospheric temperature is 800 K, with a temperature at the homopause of $\sim$ 100 K (Broadfoot et al. [1986]). The high thermospheric temperature is confirmed by H_3^+ observations by Trafton et al. [1993] and others.

1.1.4 Neptune

Neptune orbits around the Sun at a distance of 30 AU and it is the giant planet in the solar system we know the least about. It was visited by Voyager 2 in 1989 and almost everything we know about this planet is derived from this single encounter.

Lockwood and Thompson [2002] performed a long-term study of the near infrared magnitude of Neptune and found that it varies mainly according to solar cycle. Neptune is believed to have a strong internal heat source in order to remain hot at such a large heliocentric distance – the exospheric temperature of Neptune was calculated to be $T = 750$ K using Voyager 2 solar occultation data (Broadfoot et al. [1989]).

The important ionospheric probe H_3^+ has never been detected from the planet, despite numerous attempts (e.g. Feuchtgruber and Encrenaz [2003]). Consequently, Neptune is not included in this study.

1.2 Magnetosphere/ionosphere coupling

The Sun emits both radiation, of which EUV is particularly important, and energetic plasma, known as the solar wind. Each of these sources of energy is a mechanism for forming an ionosphere, via photoionisation and collisional ionisation respectively. The solar wind interacts with the upper atmosphere directly if the planet is un-magnetised, or is mediated by the magnetic field if one exists. The most luminous event that takes place in the upper atmosphere is the generation of aurora and the basic principle of how the aurora is generated is the same on all planets: charged particles are accelerated down the magnetic field lines (if the planet is magnetised) and when these particles impact on the upper atmosphere, they ionise and excite the gas and, thus, emission is produced.

In discussing the processes that control and feed the auroral phenomena on the giant planets, it is logical to start with an overview of what is known about the magnetosphere/ionosphere interaction on Earth.

1.2.1 Earth

The aurora as viewed from outside the Earth's atmosphere can be seen in Figure 1.5. It is clearly seen that it is indeed created at the very top layers of the atmosphere.

Both the red and the green aurora are caused by the excitation of oxygen, whereas the blue aurora is caused by the excitation of nitrogen. The aurora is known to vary over timescales of seconds over small spatial scales (e.g. Lummerzheim et al. [1997]).

The magnetic pressure, exerted by the magnetosphere, is balanced by the solar wind dynamic pressure on a surface known as the magnetopause. The solar wind is a hydrogen/helium plasma, an overall neutral mix of alpha particles, protons and electrons (Cowley [1996]), and is ejected from the surface of the Sun at speeds of 300-800 kms^{-1}.

The solar wind is entrenched in the magnetic field of the Sun, called the interplanetary magnetic field (IMF). Since the solar wind plasma is made up of an overall neutral mix of free-moving charged particles, the plasma acts as a perfect conductor to the magnetic field. Such a situation gives rise to the concept of the magnetic flux of the IMF being *frozen in* (Kivelson and Russell [1995]), which means that the magnetic field is locked into the plasma such that

$$\int \mathbf{B} dS = \text{constant} \tag{1.2}$$

for any surface $d\mathbf{S}$ that cuts through the flux tube. This means that a particle which is on the flux tube at the point at which the field becomes frozen will continue to be connected to this flux tube as the system moves through space.

The combination of the outward radial flow of the solar wind plasma, and the frozen in magnetic field of the Sun, gives rise to a spiral motion of the solar wind plasma. The angle from the Sun-planet line at which the plasma 'strikes' a planet, Φ, is given by

$$\tan\Phi = \frac{r\omega\cos\lambda}{v} \tag{1.3}$$

where r is the heliospheric distance, ω is the angular velocity of the rotation of the Sun, λ is the heliographic latitude and v is the solar wind flow speed.

A schematic illustration of the Earth's magnetosphere and its interaction with the solar wind can be seen in Figure 1.6. It shows how particles ejected from the Sun are caught in the magnetic field of the Earth. The particles then spiral down the field lines, because of the $\mathbf{v} \times \mathbf{B}$ Lorentz force, and eventually they impact the upper atmosphere, in the auroral zone (i.e. high latitudes), exciting the molecules in it. This

Figure 1.5: Aurora on Earth seen from Space Shuttle Discovery in May 1991 (Image credit: NASA Marshall Space Flight Center (NASA-MSFC)).

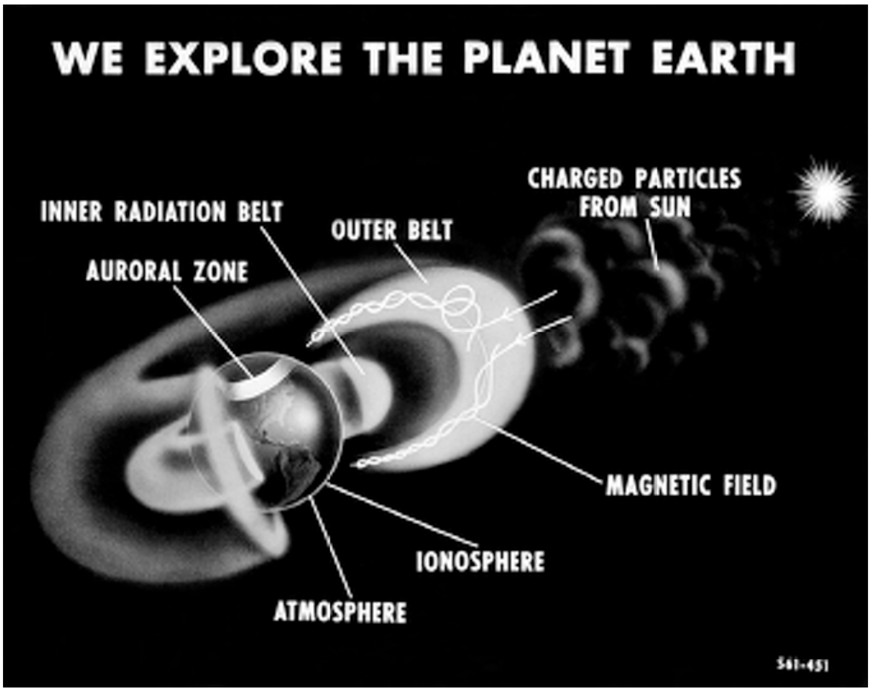

Figure 1.6: A schematic of the interaction between the solar wind and the Earth's magnetic field (Image credit: NASA Langley Research Center (NASA-LaRC)).

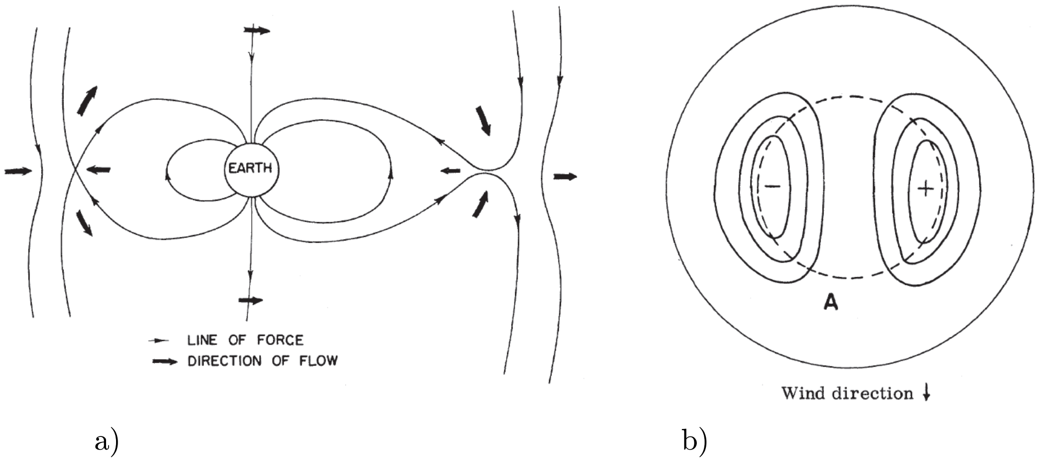

Figure 1.7: The illustrations of Dungey [1961] showing how magnetic reconnection sets up a plasma flow cycle. a) shows the creation of plasma flows away from the points of reconnection within the Earth's magnetosphere with the Sun to the left and b) shows the equipotentials of the plasma flows on the northern hemisphere of the Earth with the Sun being towards the top.

emission is observed as aurora, better known as northern or southern lights, depending at which pole it is observed. The illustration grossly oversimplifies this process and it is discussed in more detail below.

Dungey [1961] proposed that energy is transfered to the magnetosphere from the IMF through the process of reconnection. The figures contained within this article are shown in Figure 1.7. It shows how the magnetic field of the Earth interacts with the IMF in such a way that open magnetic field lines are created at the point of reconnection. This exerts a force (magnetic tension) that accelerates plasma away from the point of reconnection. Thus, the night-side reconnection creates a sunward flow of plasma, as illustrated in Figure 1.7a. The equipotentials on the northern hemisphere of this plasma flow can be seen in Figure 1.7b. Open field lines are created when the terrestrial and interplanetary magnetic field connect at the sub-solar point on the magnetopause. These open lines are then carried downstream by the magneto-sheath flow, due to the rotation of the planet, and eventually stretched into a long cylindrical tail. When the open field-lines reach the centre of the tail they reconnect with the IMF again, moving towards the dayside, where the process can repeat itself. This cycle is called the Dungey cycle (after Dungey [1961]).

At the point of reconnection there are open field lines that enable solar wind plasma to enter the magnetosphere of the Earth. The reconnection process occurs predominantly when the IMF is anti-aligned with the magnetic field of the Earth – the IMF is then said to be *pointing south.* Once plasma has entered the magnetosphere it forms boundary layers which connect to the dayside ionosphere, producing a relatively low energy precipitation ($\sim$ few hundred eV,). Plasma moves tail-ward via the Dungey cycle and enters the tail of the magnetosphere. Here, the plasma is heated by reconnection processes and forms a plasma sheet. Plasma can also be found closer to the planet in what is called the *plasmasphere* – cold plasma in a corotating orbit.

The movement of plasma in the magnetosphere sets up different current systems. The current system responsible for the creation of the night-side aurora is the Birkeland currents – defined as a current that is aligned with the magnetic field lines.

A charged particle that is traveling along a field line moves in a spiral motion around the field line due to the $\mathbf{v} \times \mathbf{B}$ force. As the particle moves, the magnetic moment and energy of the particle is conserved. Consequently, as it approaches increasing magnetic field strength, it will slow down until it it stops and travels the opposite direction. The points of zero velocity are called *mirror points.* A particle needs to overcome this trapping in order to travel down the magnetic field lines onto the upper atmosphere. This is done mainly by two processes: pitch-angle scattering and charge exchange. The *pitch angle* is the angle between the direction of the magnetic field and the spiral trajectory of a particle. If this angle is within a cone called the *loss cone* then the particle will not halt at the mirror point and will continue to travel down the field line – pitch-angle scattering is the interaction of the particle with a plasma wave that changes the pitch angle so that it is contained within the loss cone. A pitch angle, α, is within the cone if the following condition is met (Kivelson and Russell [1995]):

$$\sin\alpha < \sqrt{\frac{B_e}{B_i}} \tag{1.4}$$

where B_e is the minimum magnitude of the magnetic field on the flux tube and B_i is the field magnitude at the ionospheric end of the flux tube. The second way in which particles are lost to the earth's atmosphere, charge exchange, only affects charged particles. In this loss mechanism an energetic magnetospheric ion exchanges charged with a low energy neutral in the thermosphere. This produces a energetic neutral that can either escape to space or will be lost into the atmosphere.

The auroral activity observed on Earth is dependent on what the solar wind is doing and thus is said to be ‘externally’ driven. For example, when the Sun undergoes a coronal mass ejection (CME) in the direction of the Earth, there is a density shock-wave created in the solar wind. This causes a compression of the Earth’s magnetosphere which changes how the IMF and the magnetosphere interact. The result is increased auroral activity and geomagnetic sub-storms capable of causing major disruptions to radio communication networks.

The behavior of the ionosphere/magnetosphere system can be directly monitored by studying the aurora. This has lead to the notion of the upper atmosphere behaving like a TV screen, projecting events in the magnetosphere. If auroral emission is observed at a particular magnetic L-shell, then plasma must have been able to enter onto that field line, e.g. through reconnection or, if the field lines are open or if there is a plasma source, along a particular field line. In a similar fashion, studying the auroral processes on other planets can give us an insight to how those magnetospheres interact with the ionosphere, the solar wind and the IMF.

1.2.2 Jupiter

Jupiter has the largest magnetosphere and strongest magnetic field out of all the planets in the solar system. Therefore, any processes that are linked to the magnetosphere tend to be displayed with greater intensity here than on other planets. The aurora, as seen in the ultraviolet from the Hubble Space Telescope, can be seen in Figure 1.8. It shows discrete auroral arcs together with more diffuse polar regions, painting a complex picture of the auroral morphology, indicating that there are several processes at work.

With increasing latitude, the major features are: the footprints of the Galilean moons, then the bright main auroral oval, which is centred around the magnetic poles, and then the diffuse emission lying within this oval (Cowley et al. [2003b]).

Within the jovian magnetosphere there is a very powerful plasma source, namely the volcanic moon Io. The volcanic eruptions are triggered by Jupiter’s strong gravitational influence on the moon. It continually spews out volcanic material, which is quickly ionised by solar EUV radiation at a rate of at least 1,000 kg s^{-1} (Hill [1980]). This compares to the mass injected into the Earth’s magnetosphere by the solar wind

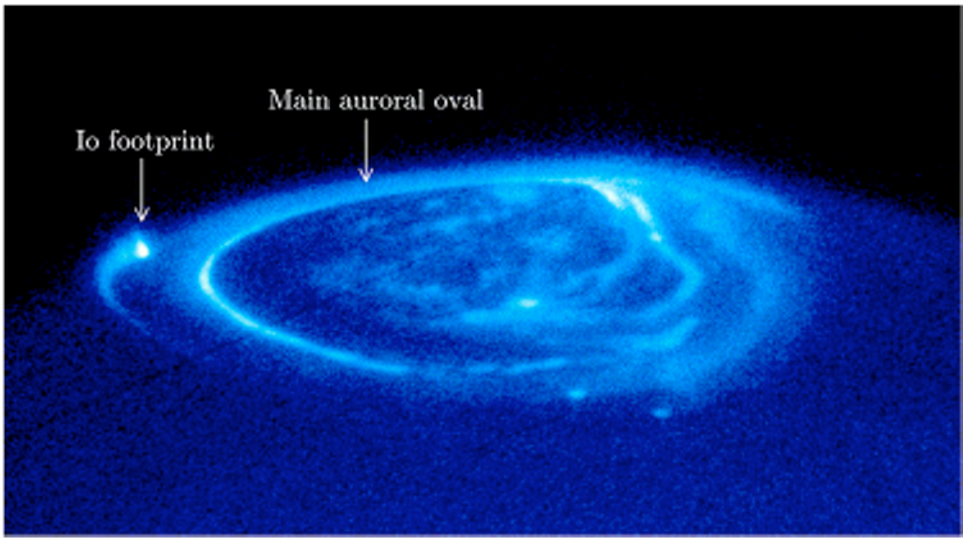

Figure 1.8: The jovian aurora as viewed by the Hubble Space Telescope (Image credit: NASA Jet Propulsion Laboratory). Note the Io footprint on the left hand side.

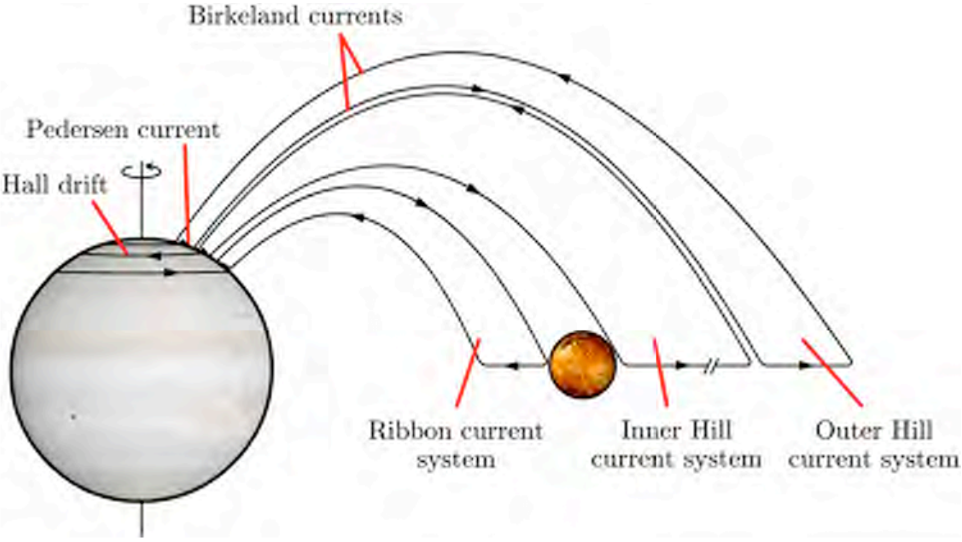

Figure 1.9: A schematic of the currents present in the jovian system. The currents connect the magnetosphere and ionosphere. Jupiter is on the left and Io is on the right. Note that the illustration is not to scale.

of ~ 20 kg s^{-1} . As Io rotates around Jupiter, completing a round trip in 42 hours, it continually ejects neutrals, that quickly become ionised, building up a plasma torus around the planet. The inward and outward migration of plasma out of the torus, caused by the current system illustrated in Figure 1.9, forms a plasma-sheet. The current system was conceptualised by Hill [1979]. The 'ribbon' system continually feeds plasma inward from Io, connecting to low latitudes in the auroral region. It is this plasma stream that creates the Io footprint emission, which can be seen in Figure 1.8. The Hill current system is created by the outward flow of plasma from Io, forming a plasma-sheet surrounding the entire planet. This plasma-sheet corotates with the magnetic field at relatively small distances from it; however, at larger distances (~17 R_J, Cowley et al. [2003a]), the corotation breaks down which in turn sets up field-aligned currents (Birkeland currents) whose plasma flows are responsible for the jovian main auroral oval. The breakdown of corotation is a result of the weakening magnetic flux at large distances from the planet, so it is unable to counter the inertial drag of the plasma-sheet.

The above explains the presence of the Io footprint and the main auroral oval (seen in Figure 1.8), but fails to explain the patchy emission inside the oval and, in particular, the well defined velocity structures within this region observed by Stallard et al. [2001]. Cowley et al. [2003b] used a simple three-component model to describe the plasma flow within the magnetosphere. Firstly, there is the Hill current system, illustrated in Figure 1.9, which feeds the main auroral oval. Secondly, plasma extending beyond the Hill current system is accelerated outward by centrifugal forces and is lost down the tail – this is known as the Vasyliūnas cycle. Thirdly, there is, as is observed on Earth, a Dungey cycle (see Section 1.2.1) transporting plasma from the solar wind into the magnetosphere. The last two plasma flows have high L-shells associated with them (i.e. high magnetic latitudes), providing a mechanism for producing auroral features at high latitudes. The velocity differences within the auroral region appear to be connected with different rates of corotation associated with the different plasma flows.

Since the aurora on Jupiter is fueled mainly by an internal plasma source, the system is said to be 'internally' driven, in contrast to the Earth, which has an externally driven aurora. The generation of the jovian auroral oval is also, to some extent, driven

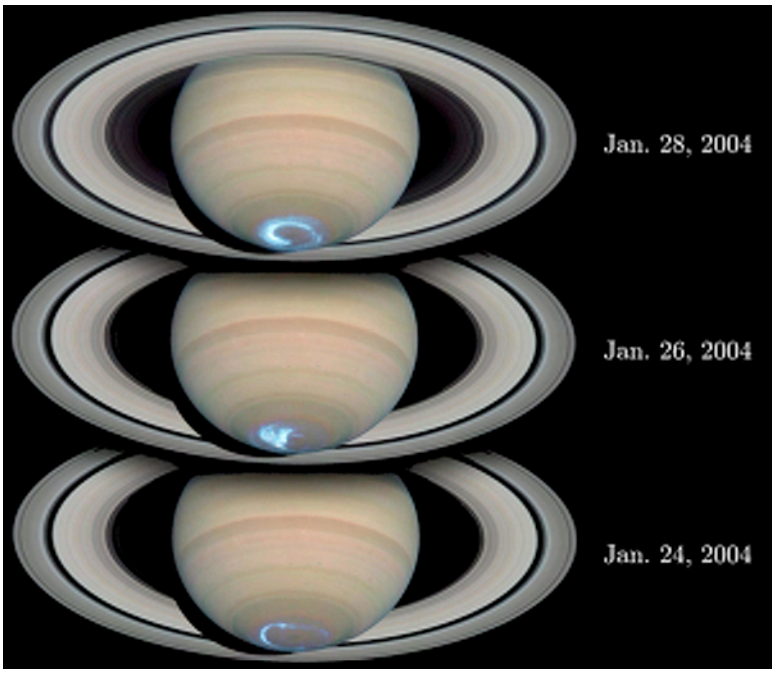

Figure 1.10: The kronian aurora as viewed by the Hubble Space Telescope overlayed on a visual image of Saturn taken by the Cassini imaging system (Image credit: NASA, ESA, J. Clarke (Boston University), and Z. Levay (STScI)).

by the fast rotation of the planet, causing the corotation of the plasma-sheet to break down.

1.2.3 Saturn

Ultraviolet images of Saturn's aurora, taken by the Hubble Space Telescope, can be seen in Figure 1.10. They clearly show a defined auroral oval, centred around the magnetic pole (which is almost perfectly aligned with the rotational pole), with dramatic morphological changes over the period of a few days.

Not much was known about the magnetosphere/ionosphere coupling on Saturn until very recently. Theoretical work by Cowley et al. [2004] indicated that Saturn's aurora is controlled by the Dungey cycle, in a similar fashion to the Earth, and that the very fast rotational period of Saturn plays an important role in controlling the way that the ionosphere interacts with the magnetosphere. This cycle on Earth lasts only one-eighth of the rotational period, but on Saturn, it lasts about five times the rotational period (Cowley et al. [2004]) due to the sheer size of the magnetosphere. This has the effect of restraining the ionosphere (in the Sun-Saturn frame of reference), causing it to sub-corotate. This is supported by velocity measurements of H_3^+ observed by Stallard et al. [2004]. These developments have led to the kronian aurora being described as Earth-like and solar wind driven (Cowley et al. [2004]). However, more recently, Clarke et al. [2005] used ultraviolet HST images to show that it displays significant morphological differences from the aurora we observe on Earth (see Figure 1.10). The UV aurora on Saturn varies on timescales of at least 10 minutes, with some features sub-corotating with the planet whilst others seem fixed with respect to local time. Their observations showed that the oval itself could quickly move in latitude and was often not centred about the magnetic pole. The UV images were compared to the solar wind pressure measurements by the CAPS instrument (Linder et al. [1998], Crary et al. [2005]) aboard the Cassini spacecraft. It was found that when the pressure increases, the brightest emission features moves to higher latitudes and the dawn-side polar cap is filled with strong emission. This event is explained by the gradual build-up of plasma in the magnetotail being released when the magnetosphere was ‘punched’ by the very sharp increase in solar wind pressure. In this case, the kronian magnetosphere is likely to be externally driven, as the auroral emission is closely linked to the activity of the solar wind.

1.2.4 Uranus

Uranus’ rotational axis is offset 97° from the normal to the ecliptic plane, and the magnetic field is offset about 59° from that. This indicates that the system is very different to those of Jupiter and Saturn, since the magnetic field is aligned with the Parker spiral angle at noon and anti-aligned at midnight. The effects this has on the magnetospheric plasma environment are as of yet unclear, and the analysis of auroral emission is expected to have added complications compared to that of Jupiter and Saturn.

Voyager 2 is the only spacecraft to have visited Uranus. Belcher et al. [1991] concluded that the moons do not contribute significantly as a plasma source and thus we would expect the system to be more or less controlled by the solar wind, i.e. externally driven. However, Uranus is incredibly hard to observe, partly because of its orientation and partly because of its distance from us (e.g. Trafton et al. [1999], and Chapter 5).

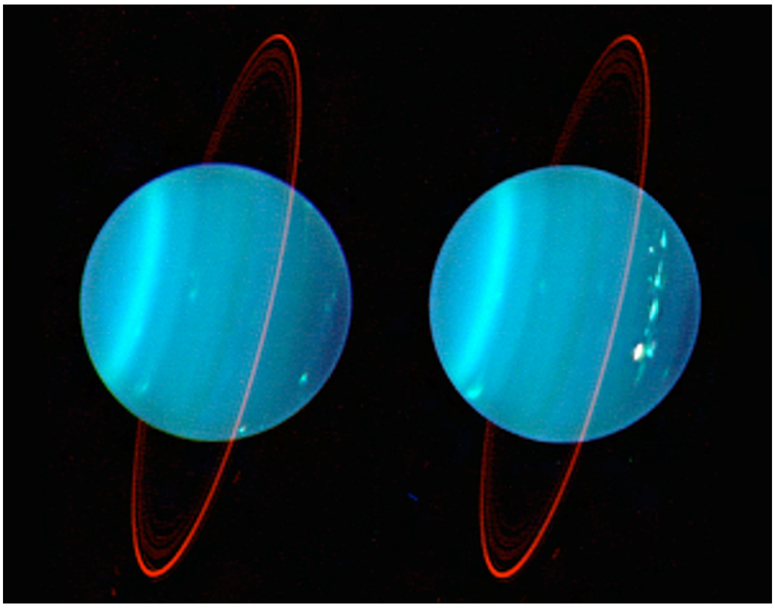

Figure 1.11: The two hemispheres of Uranus taken with the Keck Telescope on Mauna Kea, Hawaii. It shows distinct tropospheric features (Image credit: W.M. Keck Foundation and L. Sromovsky (UWM)).

Since there has only been one observation of Uranus' ultraviolet aurora, at poor spatial resolution (Herbert and Sandel [1994]), it is not known how the aurora varies over time and how it interacts with the spinning magnetosphere.

1.3 The H_3^+ molecular ion

Ever since H_3^+ was discovered on Jupiter (Drossart et al. [1989]) it has become one of the major sources of study used by scientists to directly observe ionospheric events. This section will give an overview of the history, structure and properties of H_3^+.

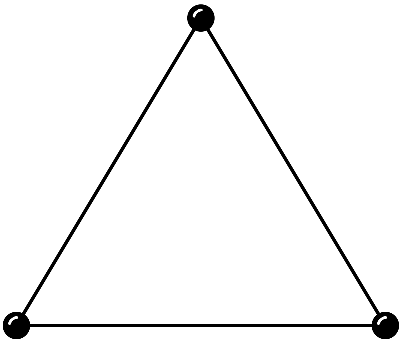

Figure 1.12: Schematic H_3^+ molecule.

H_3^+ is the very simplest of polyatomic molecules. At equilibrium, it has three hydrogen atoms arranged to form a triangle, as illustrated in Figure 1.12. In a similar way that H was the starting point for the study of monoatomic systems and H_2 for biatomic systems, H_3^+ has been the foundation for the development of solutions of the Schrödinger equation for polyatomic systems (McCall [2001]).

1.3.1 Definition of terms

- **Fundamental transition** – The series of lines (referred to as a band of lines) that is emission that originates from the first excited vibrational level of a molecule, i.e. $\nu_2 \rightarrow 0$. Since this is the first level to be populated once excitation occurs, the band consequently produces the strongest emission lines.

- **Hotband transition** – This is the band of lines that originates from the second excited vibrational level in a molecule, which is generally only populated once the the first vibrational level is completely filled. The hotband transitions are, as a rule, much weaker than the fundamental transitions. The term hotband comes from the fact that hot temperatures (i.e. greater than room temperature) are required to populate these levels.

- **Overtone transition** – These transitions originate from vibrational levels greater or equal to two (i.e. $\nu_2 \geq 2$), and are generally weaker than both fundamental transitions and hotband transitions.

- **Electronic transition** – A transition of an electron from energy level to another.

- **Rotational transition** – A change in rotational angular momentum. Since angular momentum is quantised, the rotational energy levels are discrete.

- **Vibrational transition** – A change in vibrational energy, whose levels are also quantised.

- **Forbidden transition** – A transition that does not follow the selection rules of quantum mechanics. These occur since the selection rules assume an ideal symmetry, which is not always the case. In general, these reactions are slow.

1.3.2 Discovery and historical background

H_3^+ was discovered by Thomson [1912, *Further Experiment on Positive Rays*] when he detected an ion with a mass-to-charge ratio of 3. In those days the chemical theory could not account for such a configuration and Thomson suggested, a few years later with the discovery of deuterium, that the molecule could be HD^+. It was not until the development of more detailed electronic structure calculations that H_3^+ was shown to be a stable species and, thus, a suitable candidate for explaining the findings of Thomson's 1912 experiment.

Many years later, H_3^+ spectral lines were observed in the laboratory for the first time by Oka [1980]. This discovery was made possible through the theoretical modelling of Carney and Porter [1980].

Initially, efforts to detect H_3^+ outside the laboratory focused on the largest known body of H_2 – the interstellar medium – but it was not there that the detection was made. Drossart et al. [1989] observed 2 μm emission from Jupiter's north pole when they found two unidentified lines, which were attributed to overtone bands of H_3^+, thanks to the theoretical work performed by Miller and Tennyson [1988]. This showed that on Jupiter, H_3^+ is produced in large quantities in the upper atmosphere, where precipitating particles ionise the neutral atmosphere, which is mostly H_2. Subsequently, attention turned to the other gas giants in search for the same phenomenon. Uranus was next in line for H_3^+ detection (Trafton et al. [1993]), followed by Saturn only a few months later (Geballe et al. [1993]). H_3^+ emission still has not been detected from Neptune (e.g. Feuchtgruber and Encrenaz [2003]).

1.3.3 Properties of H_3^+

The early H_3^+ calculations could not predict the correct equilibrium structure, but they did show that the reaction:

$$H_2 + H_2^+ \longrightarrow H_3^+ + H \tag{1.5}$$

is the most favoured for the formation of H_3^+. It is an exothermic reaction producing 1.7 eV of heat, and it is very rapid, occurring with a Langevin rate coefficient of 2×10^{-15} m^{-3} s^{-1} (Leu et al. [1973]). Since the reaction is exothermic, nearly all H_2

and H_2^+ that come into contact undergo this reaction and, thus, H_3^+ becomes a very important species in any molecular hydrogen environment where ionisation occurs. There are three main mechanisms for creating H_2^+. Firstly, collisional ionisation of H_2:

$$\mathrm{H_2} + e^* \longrightarrow \mathrm{H_2^+} + e + e \tag{1.6}$$

where e^* is an energetic electron, something which auroral processes are capable of providing large quantities of. Note that the secondary electrons can also have energies large enough to ionize molecular hydrogen, so that this process is repeated until the energy of the secondary electrons are small. Secondly, there is photoionisation by solar EUV radiation (here written as $h\nu$):

$$\mathrm{H_2} + h\nu \longrightarrow \mathrm{H_2^+} + e \tag{1.7}$$

Additionally, charge exchange with H^+ may occur:

$$\mathrm{H^+} + \mathrm{H_2} \longrightarrow \mathrm{H_2^+} + \mathrm{H} \tag{1.8}$$

This reaction often follows from the photoionisation or disassociation by precipitation particles, similar to Reactions 1.6 and 1.7 but for atomic hydrogen.

Once very rapidly formed, H_3^+ is destroyed mainly by collisions with other species, provided that the density is sufficiently large. The most important destruction mechanism is dissociative recombination with electrons.

$$\mathrm{H_3^+} + \mathrm{e^-} \longrightarrow \mathrm{H_2} + \mathrm{H} \tag{1.9}$$

and,

$$\mathrm{H_3^+} + \mathrm{e^-} \longrightarrow \mathrm{H} + \mathrm{H} + \mathrm{H} \tag{1.10}$$

but also,

$$\mathrm{H_3^+} + \mathrm{X} \longrightarrow \mathrm{HX^+} + \mathrm{H_2} \tag{1.11}$$

Flower [1990] showed that Reaction 1.11 is extremely efficient for any X species with proton affinities greater than those of H_2, but since the upper atmosphere of giant planets contains mostly hydrogen, this reaction is only important at the very lowest parts of the upper atmosphere, where hydrocarbons are very abundant (e.g. Grodent et al. [2001]). Since Reactions 1.9 and 1.10 describe the destruction of H_3^+ via electrons, the lifetime of H_3^+ is governed by the electron density. So, the lifetime of H_3^+ becomes:

$$\tau_r(\mathrm{H}_3^+) = \frac{1}{\delta[e^-]\kappa_r(H_3^+)} \tag{1.12}$$

where $\delta[e^-]$ is the electron density and $\kappa_r(\mathrm{H}_3^+)$ is the recombination rate constant. On Jupiter, at the altitude of the H_3^+ peak at around 500 km (Grodent et al. [2001]), the electron density is $\sim 10^{11}$ m^{-3} (see Figure 1.2 and Figure 1.3) and the recombination constant $\kappa_r(H_3^+) \sim 10^{-12}$ m^3 s^{-1} (Leu et al. [1973]), giving a lifetime of around 10 seconds. This is much smaller than the rotation period of the planet, so any H_3^+ produced by solar EUV is unlikely to be found on the night-side of the planet.

Emission from H_3^+

There are many atoms and molecules for which electronic transitions are very important, such as atomic hydrogen with its Lyman-α emission. However, H_3^+ lacks any stable excited electronic states, so there are no electronic transitions.

Since its equilibrium geometry is that of an equilateral triangle, D_{3h}, the H_3^+ molecule also lacks a permanent dipole. Thus there are no allowed pure rotational transitions. However, since centrifugal forces distort the triangle, producing very small temporary dipole moments, H_3^+ emits a forbidden rotational spectrum (Watson [1971]). Since the molecule is capable of such distortions, it is sometimes referred to as a 'floppy' molecule. Pan and Oka [1986] found that the forbidden vibrational spectrum of H_3^+ is several orders weaker than for other molecules with an allowed vibrational spectrum. Since H_3^+ is the lightest of polyatomic molecules, it is also worth noting that its forbidden rotational spectrum is a few orders of magnitude stronger than the forbidden rotational spectrum of other polyatomic molecules such as CH_4 and NH_3 (McCall [2000]).

Each and every rotation-vibration (ro-vibrational) energy level can be described by three quantum numbers: the rotational angular momentum J, its projection onto the molecular axis k, and the vibrational angular momentum l.

The forbidden vibrational transitions are governed by the following selection rules

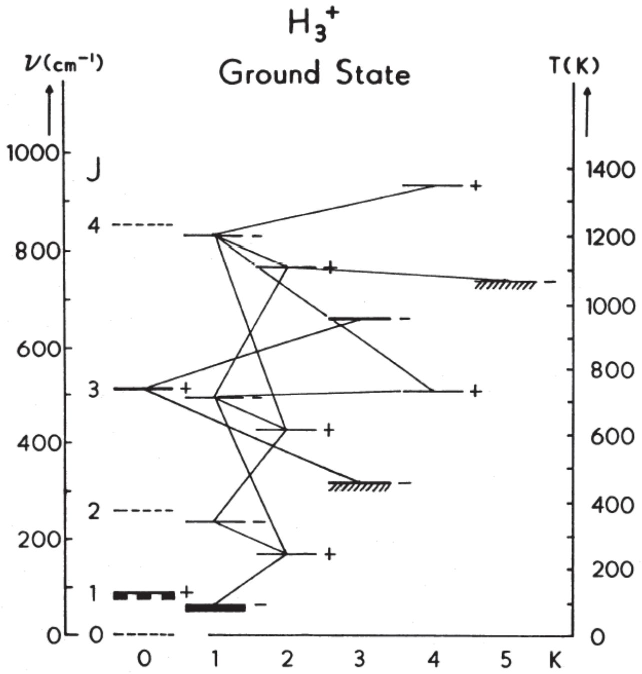

Figure 1.13: H_3^+ rotational levels in the ground vibrational state. Forbidden transitions are shown as connecting lines. The illustration is taken from Pan and Oka [1986].

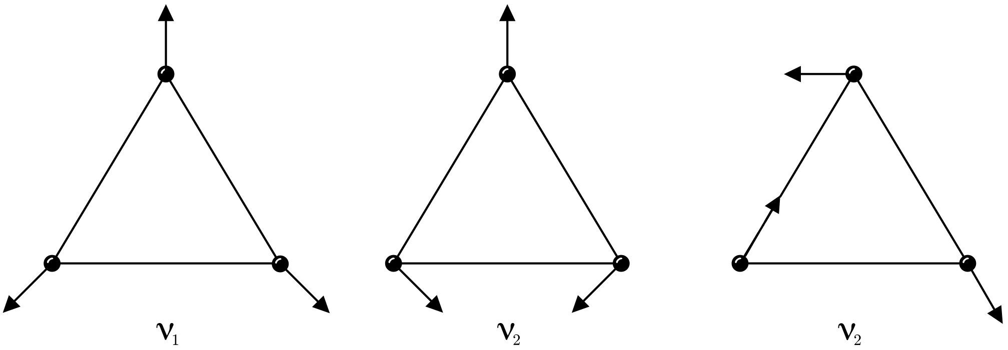

Figure 1.14: The vibrational modes of the atoms for the H_3^+ vibrational modes.

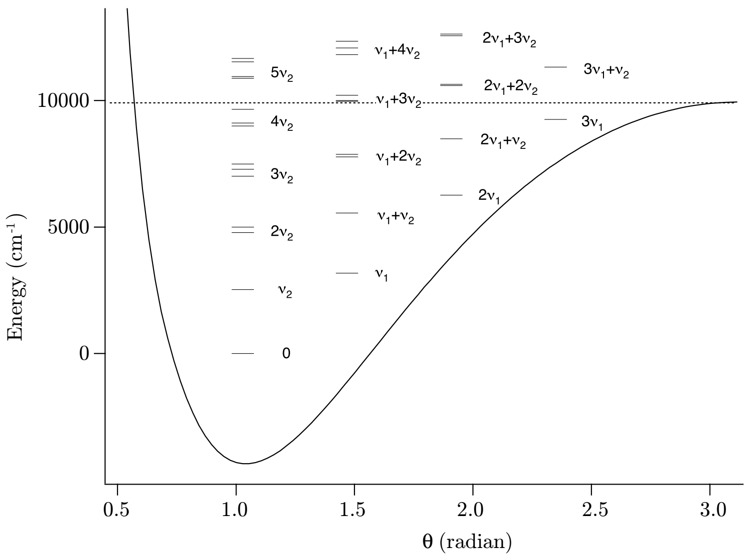

Figure 1.15: The potential energy of the vibrational levels of H_3^+. Figure after McCall [2001].

(Pan and Oka [1986]):

$$\Delta J = 0, \pm 1 \tag{1.13}$$

and

$$\Delta k = \pm 3 \tag{1.14}$$

The rotational levels within the first vibrational level, showing the forbidden transitions, can be seen in Figure 1.13.

Each vibrational level can be completely described by two vibrational mode quantum numbers, ν_1 and ν_2 and the vibrational angular momentum quantum number l. The vibrational states are schematically shown in Figure 1.14. The ν_1 state is the symmetric stretch vibration which retains D_{3h} symmetry, and is therefore not infrared active. The ν_2 state is the anti-symmetric stretch vibration, which is infrared active. The potential energy diagram for the vibrational levels can be seen in Figure 1.15.

The ro-vibrational transitions between the ν_2 state and the ground state are usually the most intense and, thus, the most suitable to look for when observing distant astronomical objects. The spectral lines produced by these transitions are observed in the L and L$'$ atmospheric windows between 3.0 and 4.1 μm.

1.4 Comparative aeronomy

Any comparative science seeks to observe the same process in different contexts, and seeks to find a theory that can explain every manifestation of that process (Vasyliūnas [2004]). Comparative science can also provide a very powerful test for an already established theory.

In terms of the giant planets, we observe auroral (and non-auroral) H_3^+ emission and the associated magnetosphere/ionosphere interaction, which might depend on a range of known and unknown parameters. If we are truly to understand the processes that govern the upper atmosphere of any giant planet, we should seek to explain the ones observed in our solar system in a unifying manner.

Obviously, we have different levels of knowledge for the four giant planets. Jupiter, which is the largest and brightest in the night sky, has been the subject of many studies, such that the processes that govern the jovian system are believed to be understood in great detail. Saturn and Uranus, however, we know less about. They are both very difficult to observe, for different reasons – Saturn has very weak H_3^+ emission, whereas the emission from Uranus is incredibly difficult to interpret due to the planet's peculiar configuration.

The planet which we know the most about in the solar system is the Earth. A lesson that can be learned from years of telluric atmospheric research is that the more we learn, the more detail we can discern, and the more questions are raised.

When the Voyagers finished their grand tour of the giant planets in our solar system, having studied all of them with the same set of instruments and techniques, a remarkable opportunity presented itself to perform a comprehensive comparative study covering a plethora of topics. One particular parameter that is closely related to auroral activity, is the plasma density as a function of L-shell. L-shell is defined as follows: for example, L = 2 refers to the field line that crosses the point at a distance of two planetary radii in the equatorial plane of the planet. Consequently, L-shell scales as the distance from the centre of the planet (Richardson et al. [1995]). The plasma density was observed by the Plasma Science Experiment (Bridge et al. [1977]) onboard the Voyager 2 spacecraft, capable of obtaining plasma velocity, density, temperature and pressure. Figure 1.16 shows the plasma density as a function of L-shell for the giant planets visited by Voyager 2. Jupiter clearly has the largest plasma

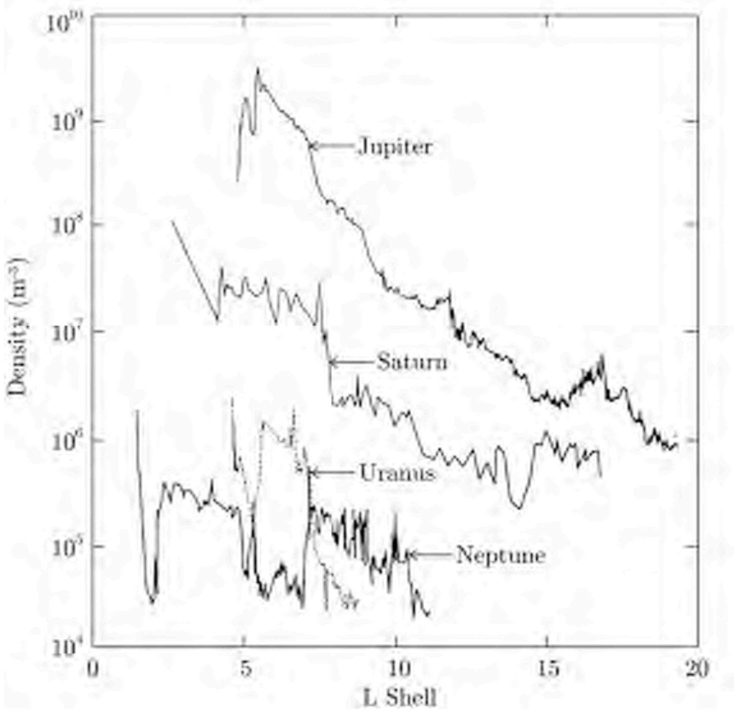

Figure 1.16: The plasma density as a function of L-shell for each of the giant planets visited by Voyager 2. After an illustration by Richardson et al. [1995].

density followed by Saturn, then Uranus and Neptune with very similar densities. The major difference between Uranus and Neptune is that Neptune has a significantly higher plasma number density beyond $L = 7$. The plasma density of Jupiter peaks at $L = 5.9$ which is where Io orbits, confirming that the moon is indeed the major source of plasma in the jovian system. In a similar fashion the plasma density on Neptune is dominated by the expulsions from the moon Triton at $L \sim 4$. Saturn has a plasma density of about 1% of that of Jupiter, and Uranus and Neptune have a plasma density of 1% of Saturn.

1.5 The Aim of this study

This study aims to investigate several outstanding issues in the understanding of the H_3^+ emission observed from the giant planets.

On Jupiter two theoretical studies have become available which has enabled the detailed analysis of the auroral H_3^+ emission. The self-consistent 1D numerical model due to Grodent et al. [2001] for the auroral region has provided density and temperature profiles that are matched to a range of multispectral observations. The altitude at which the H_3^+ emission is created will be analysed, as will the effects of departures from Local Thermodynamic Equilibrium (LTE) conditions using the detailed balance formulation of H_3^+ in a mixture of H_2 by Oka and Epp [2004]. It is possible that departures from LTE conditions in the upper atmosphere of Jupiter can explain differences in observed emission originating from different ro-vibrational H_3^+ transitions.

Using the profiles obtained from the non-LTE analysis, and considering theoretical arguments alone, the energy sources and sinks will be investigated for the auroral heating event observed by Stallard et al. [2002]. Analysing the energy sources for the observed increase in temperature, ion density and ion velocity gives us a valuable insight to the detailed energetics the the jovian system, and enables us to determine the process that injects the most energy into the auroral region during the event.

No reliable H_3^+ temperature exists for Saturn. Using three sets of data: 1999, 2004 and 2005 taken using the CGS4 spectrograph on United Kingdom Infrared Telescope (UKIRT), the temperature and ion density will be determined. These parameters are fed into atmospheric models that detail the energetics and dynamics. Establishing the variations in temperature and density over time will enable the estimation of the levels of particle precipitation into the thermosphere, and how the ionosphere reacts to those change.

On Uranus, it is not clear if the observed H_3^+ emission is a product of auroral or solar EUV ionisation. Making use of a unique dataset – spectra covering almost an entire solar cycle – held at the Atmospheric Physics Laboratory (APL), University College London (UCL), both a long-term and short-term analysis will be performed as to determine the dependency of the variations in the H_3^+ emission. For example, if there are cyclic variations with the solar cycle, then at least part of the emission must be produced by solar radiation processes. An emission model will be created with both a solar and an auroral H_3^+ component. The modelled auroral component is taken from the only unambiguous observation of Uranus aurora observed by Voyager 2 (Herbert and Sandel [1994]) in the UV. In addition NFSCam images taken in 1998 and 1999 will be compared to the emission model, in an attempt at identifying distinct auroral features.

Finally, the characteristics of the H_3^+ emission for the three planets can be compared, which enables the investigation of common processes.

Chapter 2

Observations and data analysis

This thesis makes use of mostly existing data, on which additional analysis is performed. However, new data to determine the ionospheric temperature and density of Saturn was taken in February 2004 and February 2005 using the United Kingdom Infrared Telescope (UKIRT). Stallard [2000] details of how data taken with the CSHELL spectrograph on the Infrared Telescope Facility (IRTF) was reduced and calibrated, and Trafton et al. [1999] details the reduction of spectra taken with the spectrograph SpeX on the same telescope.

The observations of Saturn made for this thesis were obtained using the CGS4 spectrograph on UKIRT between the 1st and the 3rd of February 2004 and between the 25th and the 28th of February 2005. The telescope and instrument will be discussed in Section 2.1 below.

Section 2.2 outlines the basic technique that will produce a usable spectrum from raw telescope data.

Section 2.3 derives an expression needed to correct for limb-brightening for a tilted oblate planet and analyse the accuracy to which line-of-sight corrections must be made. These calculations are important when determining true emission intensities and, thus, ion densities.

For this thesis a new H_3^+ spectrum analysis tool was developed. It fits a theoretical spectrum to an observed spectrum and derives temperature and ion density. The details of this routine are given in Section 2.4.

2.1 United Kingdom Infrared Telescope

UKIRT is located on the summit of Mauna Kea, Hawaii, USA. This exotic spot is one of the world's prime locations for ground-based observations due to its high altitude and favourable climate. The telescope has a primary mirror with a diameter of 3.8 meters and instruments are placed in the Cassegrain focus. It is the largest dedicated infrared telescope in the world. It currently operates at $f/36.4$, compared to $f/9$ in 1979. It is operated by the Joint Astronomy Centre in Hilo and is funded by the Particle Physics and Astronomy Research Council (PPARC).

Figure 2.1: United Kingdom Infrared Telescope (UKIRT) on the summit of Mauna Kea, Hawaii. It lies at an altitude of 4,194 meters above sea level.

UKIRT currently hosts the following instruments:

- **CGS4**: Cooled Grating Spectrometer 4. A spectrograph sensitive to infrared, capable of resolutions of 1,000 to 37,000 depending on the grating used. See Section 2.1.1 for more detail.
- **UIST**: UKIRT Imaging SpecTrometer. Capable of resolutions of up to $R = 2,300$ in the L$'$ atmospheric window. It has an image slicer which produces 14 spectra, each parallel with respect to each other. Using this, both an image and spectra for an entire spatial region can be acquired. However, Trafton et al. [2005] points out that UIST has serious throughput problems and suggested

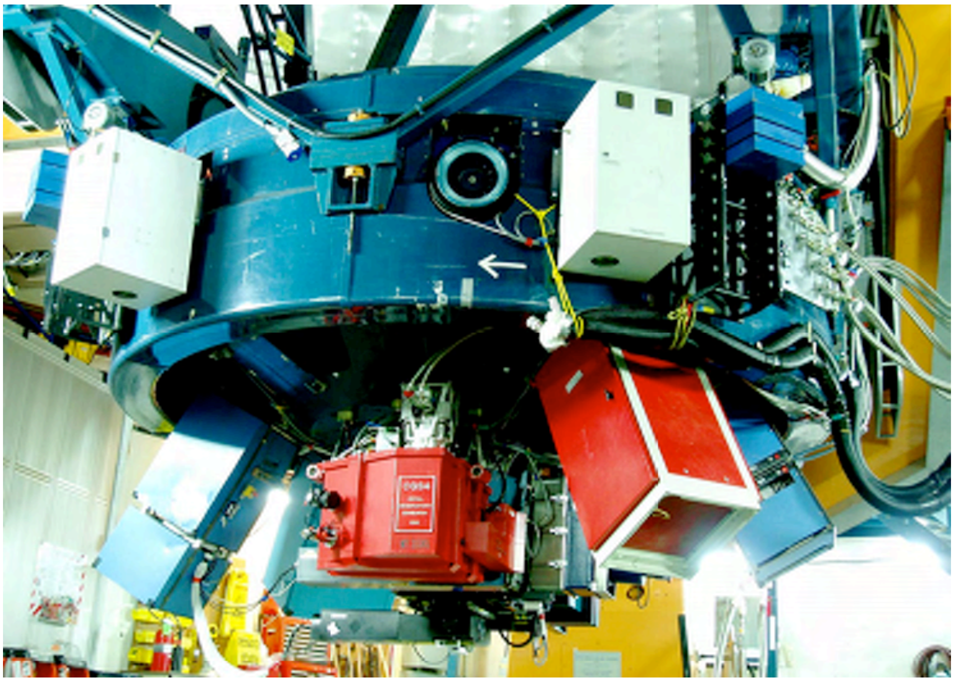

Figure 2.2: CGS4 (centre) mounted on the back of UKIRT.

that CGS4 would be more effective by a factor of 1.5, even taking into account that UIST can take 14 spectra in one exposure. Both the sets of observations performed for this thesis were originally planned for UIST, but the instrument was not functioning on both these occasions (failure of the cooling system and a jammed filter wheel in 2004 and 2005 respectively).

- **UFTI**: UKIRT Fast Track Imager. An 1 - 2.5 μm imager equipped with a 1024×1024 HgCdTe imaging array. More sensitive than UIST and has a larger field of view (but obviously without any spectrograph capabilities).
- **WFCAM**: The UKIRT Wide Field CAMera. Sensitive in the range 0.8 - 2.5 μm, each pixel with a field of view of $0.75'' \times 0.75''$. Designed for the UKIRT Infrared Deep Sky Survey (UKIDSS, Warren [2002]). It is mounted in the prime focus so it requires that all other instruments are removed.

2.1.1 CGS4

CGS4 is a 1 - 5 μm multi-purpose grating spectrometer with a 256 × 256 InSb CCD array. The camera is cooled by liquid nitrogen and closed cycle coolers in a cryostat.

CGS4 has a built-in black body emission source for obtaining flat-fields and an argon and a krypton arc-lamp for creating the wavelength calibration spectrum. All of the filter, slit and grating settings are motorised and are set in the *Observing Tool* software program which is used to create observing sequences (see Section 2.1.2). A picture of CGS4 mounted on the back of the telescope can be seen in Figure 2.2. A schematic layout can be seen in Figure 2.3.

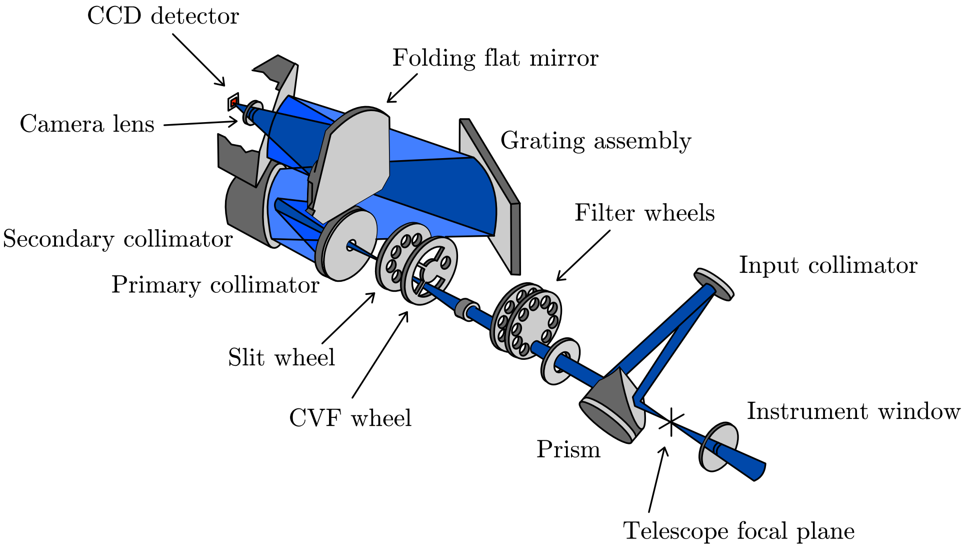

Figure 2.3: Schematic of CGS4. After a drawing of the optical layout of CGS4 on the Joint Astronomy Centre (JAC) website.

The length of the slit of CGS4 is about 90″. This is enough space to have Saturn's aurora in both the A-beam and B-beam, nodding the telescope between East and West parallel to the equator on Saturn. This has the effect of doubling the time spent on the planet and thus doubling the signal.

The 40 lines mm^{-1} grating

The 40 lines mm^{-1} grating gives a pixel size of $0.61'' \times 0.61''$ and the smallest available slit width is 1 pixel. It offers resolutions between $400 - 800 \times \lambda$ where λ is the central wavelength. This gives a resolution of $R = 1,520$ at $\lambda = 3.8\mu$m with coverage from 3.5 to 4.1 μm resulting in a grating dispersion of 0.0024 μm pixel^{-1}.

The 150 lines mm^{-1} grating

The 150 lines mm^{-1} grating provides resolving powers of $R = 3,000$ to 8,500, depending on the wavelength used. The pixel scale is 0.595″ perpendicular to the slit and 0.625″ along the slit.

The echelle grating

The echelle grating has 31 lines mm^{-1} and is capable of resolving powers of up to $R = 37,000$ or 8 kms^{-1}. The pixel scale along the slit depends on the wavelength used, but ranges from 0.78$''$ to 0.93$''$. The pixel scale perpendicular to the slit is always 0.41$''$.

2.1.2 The observing tool

Observations are planned and layed out in the *Observing Tool* and are structured into a `Minimum Schedulable Block` (MSB). In an MSB all the targets are specified, including standard stars and guide stars. Also, the offset coordinates from a given target are given for both the A beam (on target) and the B beam (on sky). When the telescope is instructed to slew to a planet, it points the telescope at the centre of the planetary disc and the spectrograph slit is aligned North-South on the sky. The slit angle, or position angle, is given in degrees East of North, but must be given as a negative number when using CGS4. The offset directions are defined as p – along the slit – and q – perpendicular to the slit – where the positive is leftward of the top of the slit. This means that, once the correct position angle is entered, only a q offset is required to move the telescope in such a way that the pole appears at at different positions along the slit. Saturn, as seen from Earth in February 2004, is shown in Figure 2.4. In this figure the slit was rotated -97° East of North. The offset, q, is determined using the plot showing how Saturn would look to an observer at any particular time (see Figure 2.4). The grid is generated by Saturn Viewer (`http://pds-rings.seti.org/tools/viewer2_sat.html`) and the diameter of Saturn is obtained from the Astronomical Almanac. The distance between the centre of the planet and the aurora is measured by hand using these aids.

2.1.3 UKIRT observing procedure

Since observations at UKIRT are almost completely automated there is a very well-defined observing procedure. This procedure is outlined below.

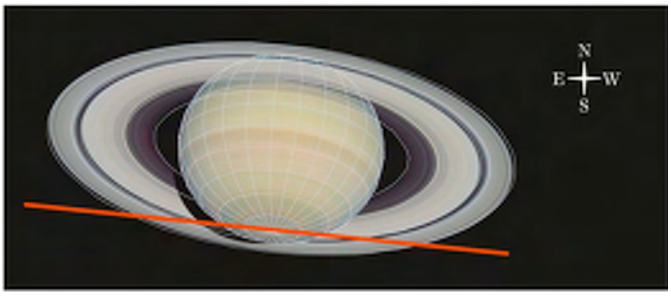

Figure 2.4: Setup of observing the southern aurora of Saturn. The line is the desired position of the slit, across the southern pole. Image credit: NASA, ESA and Erich Karkoschka (University of Arizona). The grid is taken from the Saturn Viewer website.

Definition of UKIRT software terms

- *Observing Tool* – A software utility in which observers plan and lay out their observations. It includes everything from standard stars to telescope offsets and tracking rates.
- *Query Tool* – The window in which observations are selected based on a range of criteria. All observations that are to be executed must be selected here.
- *Queue Monitor* – The window that holds the telescope commands that have been chosen to run and that are 'queueing' to enter the *Sequence Console*.
- *Sequence Console* – The individual telescope commands that make up an MSB in a list which can be paused and stopped.

Startup

All of the startup procedures involving the technical aspects of the telescope are done by the TSS (Telescope Support Staff). There are, however, a few procedures an observer needs to go through to get the system up and running. Firstly, the ORAC-DR (described in Section 2.2.1) can be set up before the telescope system is up and running, since it is data-driven and thus fully detached from the telescope control systems. Logging on to the computer `kauwa` as `observer` and running `oracdr_cgs4` in a terminal will initiate the pipeline. There are many options as how to run ORAC-DR but, in general, `oracdr -loop flag` will start a pipeline adequate for most science programs. To start the *Query Tool*, *Queue Monitor* and the *Sequence Console*, `ocs_up` is entered in a terminal on the computer `ohi` – here also logged in as `observer`.

At the beginning of each night, a series of CCD array tests are run on each instrument to get a handle on the read noise on the CCD on the different instruments. The tests are:

- CGS4 Array Test
- UFTI Array Test
- UIST Calculate Read Noise
- UIST Determine Bad Pixel Mask

These can be found in the *Calibrations* menu in the *Query Tool.* Once the telescope and the instruments are ready to go, an additional UFTI Aperture Test is performed to check that the pointing has not drifted during the day.

Observing with UKIRT

MSBs are selected from the *Query Tool* based on time of day (i.e. availability of target), τ (the column of water vapor in the air), seeing (a measure of atmospheric turbulence), cloud-cover, and brightness, or phase, of the Moon. The MSB is loaded within the *Query Tool* and can be sent to the *Queue Monitor*, which holds a list of sequences that are to be sent to the *Sequence Console.* An MSB is translated into commands that the telescope and the instrument – in this case CGS4 – can understand (but which the observer could likely not). The observing process is largely automated, with some intervention of the TSS, such as focusing and establishing the appropriate tracking method and setting the tracking rates. Tracking rates can be set in the MSB, but better results are usually achieved when this is done by the TSS.

2.2 Data reduction

Astronomical data taken at UKIRT is most easily reduced using the fully automated ORAC-DR software (see Section 2.2.1). Since UKIRT saves all instrument observations to a proprietary version of the NDF format (Native Dipso File format), *any* data must be piped through ORAC-DR if the files are to be processed by any other software. However, ORAC-DR has proven to be very reliable, and the program was used for the basic reduction of all of the Saturn data taken at UKIRT used in this thesis. Nevertheless, it is still important to understand the steps that are required to produce a usable spectrum from raw CCD images. This is discussed in detail below.

2.2.1 ORAC-DR

ORAC-DR is a data reduction (DR) pipeline made by Observatory Reduction and Acquisition Control (ORAC) systems. It was commissioned in 1999 to complement the existing *Observing Tool* to provide near publication quality data at the telescope.

ORAC-DR is data driven, i.e. it scans the directory in which raw images are saved, and runs when there is a new file. Each file is given a set of 'flags' depending on what kind of observation it is. In the *Observing Tool* a data-reduction recipe is selected for each type of observation, e.g. for a standard star the `STANDARD_STAR` recipe is used, and for Saturn the `EXTENDED_SOURCE` recipe is used. These are instructions on how to process the data – in case of the standard star, its flux is found in a star catalogue (SIMBAD) so that it can be used for flux calibration, and a calibration spectrum is automatically created (see Section 2.2.5).

An outline of use of ORAC-DR is:

- The pipeline is initialised by typing `oracdr_cgs4`. It is started by typing `oracdr -loop flag`. This is sufficient for processing most observations whilst on the summit. Offline reduction (i.e. away from the summit) may require other parameters such as the `-from x:y` command, where `x` and `y` are file numbers. This selects the range of files to reduce. There are many options to choose from.

- As long as the same object is observed, all the spectra are co-added into a group with the number of the first file of that group. Each individual spectrum is dark-framed, flat-fielded and sky-subtracted, then added to the group spectrum.

- There are two main display windows: the GAIA window that displays the incoming reduced spectrum in the form of the current group file, and the KAPPA window which shows histograms, extracted spectrum, and various other image functions.

- If something seems to have gone wrong, or if the pipeline failed to exit cleanly, or crashes, typing `oracdr_nuke` resets the environment and cleans up any crash debris.

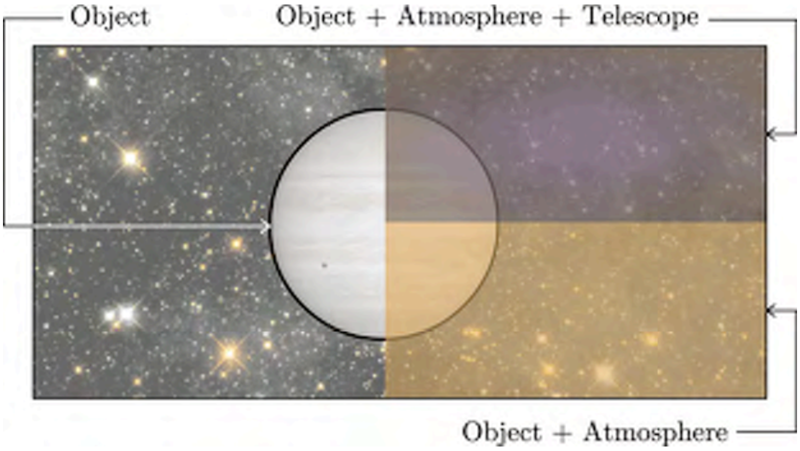

Figure 2.5: Schematic diagram showing how the addition of flux sources degrades the quality of an image.

2.2.2 Sky subtraction

Observing technique does, to a large extent, determine the way a set of data is processed. In normal infrared observing, the telescope takes an image of an object (A-beam – in this case Saturn) and then ‘nods’ to take an image of the sky (B-beam). These two frames can be described as the sum of flux sources according to (Cushing et al. [2004]):

$$A = dark + telescope + sky_a + object \tag{2.1}$$

$$B = dark + telescope + sky_b \tag{2.2}$$

Equation 2.1 is schematically shown in Figure 2.5. The process of sky subtraction becomes:

$$A - B = object + sky_a - sky_b \tag{2.3}$$

$$= object + R_{sky} \tag{2.4}$$

where *sky* is the emissions originating from the Earth’s atmosphere, *dark* is the thermal CCD current noise and *telescope* is the thermal signal from the telescope. R_{sky} is the difference in *sky* signal as per Equation 2.3. Under stable sky conditions, e.g. sky with no clouds and little turbulence, R_{sky} is very close to zero. In other words, the method of sky subtraction efficiently eliminates all unwanted *sources* of infrared radiation and leaves us with the signal of the object.

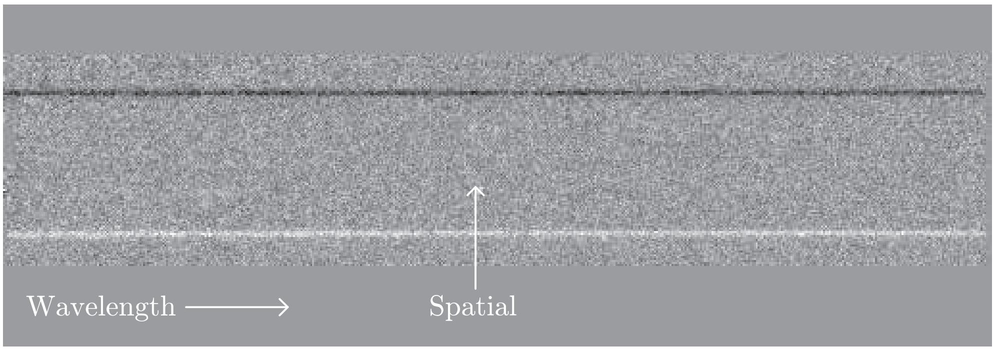

Figure 2.6: Image containing the spectrum of a star. The wavelength direction is in the horizontal plane and the spatial direction is in the vertical plane.

It is harder to correct for processes that *remove* light from the object signal, such as absorption by H_2O in the atmosphere, or attenuation and deformations introduced when the light passes through the optics and electronics of the telescope. Atmospheric absorption effects are removed by the process of flux calibration (discussed in Section 2.2.5) whereas internal effects are combatted by the process of flat-fielding discussed in Section 2.2.3.

When taking spectra of a star for the purpose of flux calibration (see Section 2.2.5), one can double the exposure time spent on the star by nodding the telescope such that the star is still on the slit in the B-beam. After the $object - sky$ subtraction this procedure produces a negative image of the object along with the positive. This is seen in Figure 2.6. The total signal is the sum of the positive and the negative.

2.2.3 Flat-fielding

One phenomenon that the process of sky subtraction cannot remove is non-uniformity of response of the CCD. This phenomenon is caused by either dust deposits on the CCD, optical imperfections, or by non-uniformity introduced by the manufacturing process. The non-uniformity of response can be quantified by taking a flat-field, an exposure of an evenly illuminated field of view, such as a lit dome. This is then normalised and every frame (e.g. every A-beam and B-beam) is divided by the flat-field. This has the effect of boosting the signal where it is being weakened. The method assumes that these effects are constant over timescales of a few hours. A flat-field taken with CGS4 can be seen in Figure 2.8.

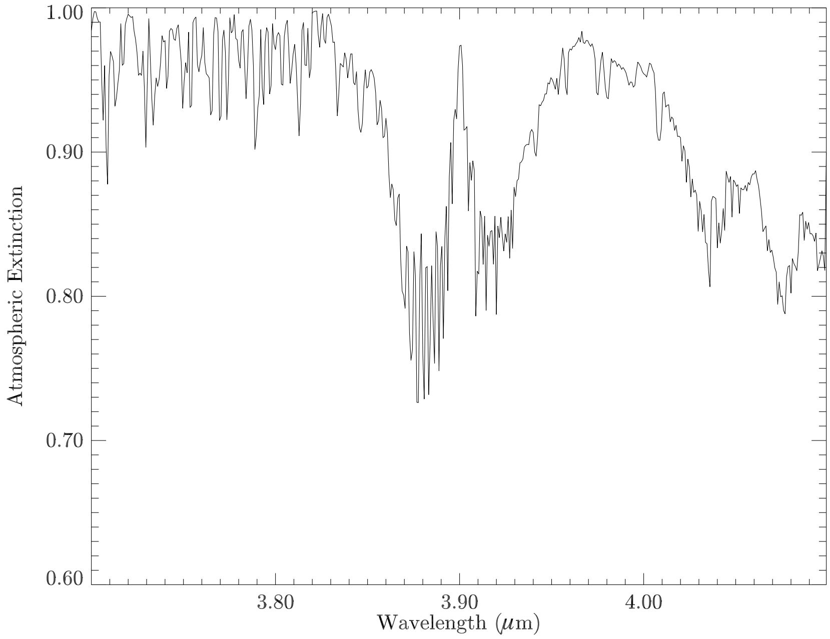

Figure 2.7: Atmospheric extinction as observed by Livingston and Wallace [1991] in the L″ spectral window.

2.2.4 Wavelength calibration

On the image produced on the the array of a spectrograph one direction is spatial, and the other is wavelength. In order to interpret the features seen on the array, it is necessary to determine what the wavelength scale is. This will tell us which spectral lines we are looking at, which in turn will enable us to investigate the physical conditions under which the lines were formed.

When fitting an H_3^+ spectrum, the best results are achieved when the fitting routine is fed a spectrum with a wavelength scale that is as close as possible to the zero velocity theoretical H_3^+ spectrum. This means that Doppler effects due to the motion of the planet around the Sun, winds or rotational motion must be compensated for. Consequently, an appropriate method of wavelength calibration is to match observed H_3^+ lines with lines from the line list of Neale et al. [1996]. This does, however, require that the H_3^+ lines are easily distinguishable, something that is not true for a very noisy spectrum. We must also have the confidence that the theoretical calculations of Neale et al. [1996] are indeed physical. Fortunately, they are known to be very accurate from many studies of H_3^+ since the laboratory discovery by Oka [1980].

The true wavelength scale of a spectrum, including any Doppler shift of spectral

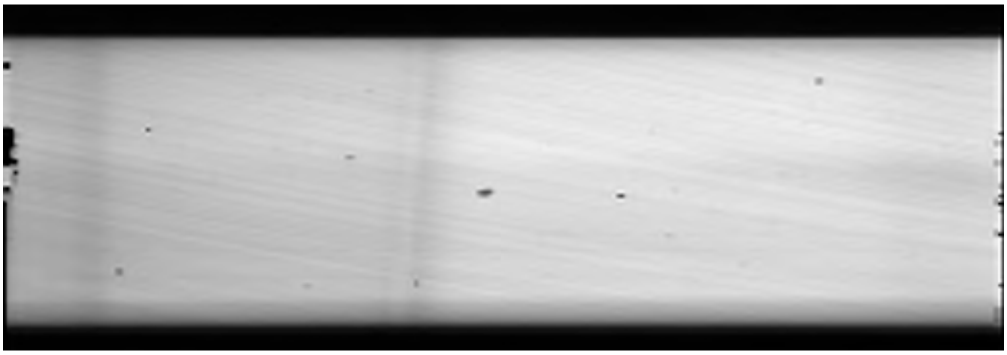

Figure 2.8: A flat-field taken with CGS4 on the United Kingdom Infrared Telescope (UKIRT).

lines due to motion, can be found by taking spectrum of argon or krypton lamps, mounted in the instrument (at zero velocity relative to the detector). These lamps have emission lines at known wavelengths in the infrared and are known as arc-lamps. This kind of wavelength calibration is important when one is extracting velocities from Doppler shifts or when trying to identify new spectral lines in astronomical objects. At medium resolution the H_3^+ spectrum emitted by giant planets (apart from Neptune, e.g. Feuchtgruber and Encrenaz [2003]) has been studied a great many times. All spectral lines that were hypothesised to be relevant by Neale et al. [1996] have subsequently been detected (e.g. Drossart et al. [1989], Lam et al. [1997a] and Stallard et al. [2001]).

An example of an Argon arc spectrum in the L′ atmospheric window centred around the 3.8 μm region can be seen in Figure 2.9.

2.2.5 Flux calibration

Flux calibration is the process of converting the number of counts received on a CCD to units of flux ($Wm^{-2}\mu m^{-1}$). This is done by taking the spectrum of a star whose flux is known, then deducing how many counts on the CCD that known flux produces. This can then be turned into a spectrum with units of [$Wm^{-2}\mu m^{-1}count^{-1}$]. The ideal star for flux calibration is a star of spectral type A0, since it has very few emission lines, emitting what is essentially a black body spectrum. An example of a spectrum of an A0 star can be seen in Figure 2.10. When the black body spectrum of the star passes through the Earth's atmosphere it is attenuated by absorption by H_2O and other species, e.g. CH_4 and CO_2. The fractional attenuation of the pre-atmospheric

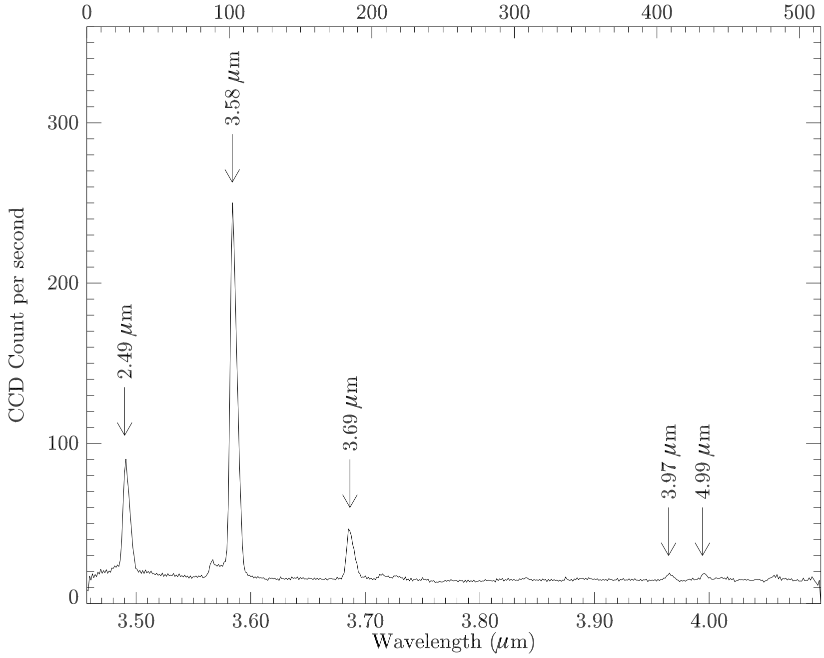

Figure 2.9: Arc spectrum used for wavelength calibration in the 3.5 to 4.1 μm region. The top scale is pixel position and the bottom scale is the resulting wavelength scale produced when fitting line position to the known wavelength of the arc lines.

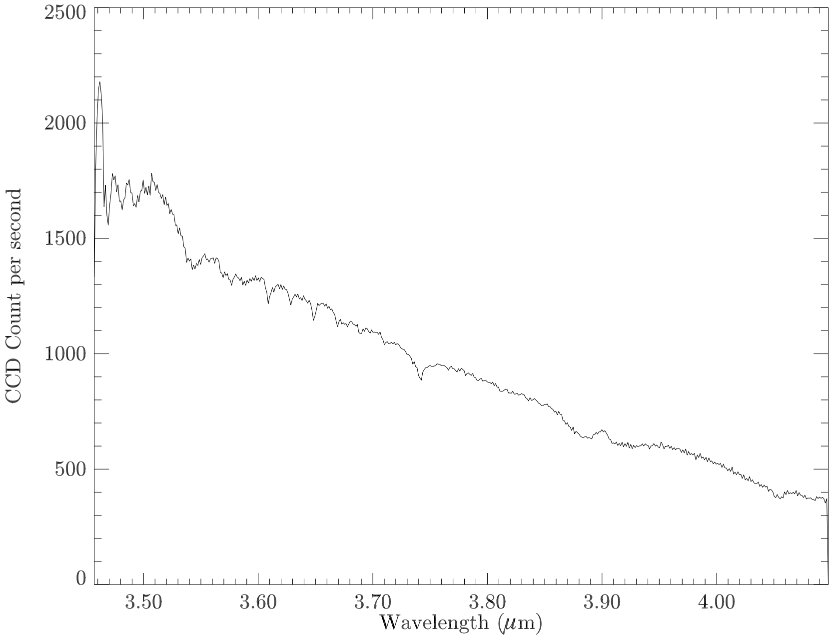

Figure 2.10: Spectrum of star HD 64648 used for flux calibration during the February 2005 UKIRT observations. Its magnitude in the L$'$ atmospheric window, at $\lambda = 3.8$ μm, is $m_{3.8} = 5.3$.

Sky Window	Wavelength (μm)	Flux (Wm$^{-2}\mu$m^{-1})
V	0.5556	3.44×10^{-8}
J	1.2500	3.07×10^{-9}
H	1.6500	1.12×10^{-9}
K	2.2000	4.07×10^{-10}
L	3.4500	7.30×10^{-11}
L'	3.8000	5.24×10^{-11}
M_1	4.8000	2.12×10^{-11}
M_2	7.8000	3.22×10^{-12}
M_3	8.7000	2.10×10^{-12}
M_4	9.8000	1.32×10^{-12}

Table 2.1: α Lyrae intensities in the atmospheric windows in the 0.5 to 10 μm region (Blackwell et al. [1983]). Note the multiple wavelengths in the M window.

solar spectrum, as observed by Livingston and Wallace [1991] at Mount Palomar, can be seen in Figure 2.7. Dividing the modelled star spectrum by the observed star spectrum produces a sensitivity spectrum whose purpose is twofold. Firstly, it flux calibrates the object spectrum and, secondly, corrects it for atmospheric extinction.

Atmospheric extinction is a function of atmospheric conditions and can vary over rather short timescales (< 1 hour). For this reason, some observers choose to bracket their observations of their target with observations of the standard star. However, since UKIRT does allocations by the hour rather than by night, and since Saturn's H_3^+ emission is very faint (e.g. Geballe et al. [1993]), the standard star was only observed in the beginning of the MSB to maximise time spent integrating on the planet.

The black body spectrum

Stars are classified into different spectral types and each such spectral type corresponds to a black body temperature. If a star has a spectrum that can be characterised as a black body spectrum, i.e. the star has few or no emission lines in the infrared, then it is possible to create a model spectrum based on the infrared magnitude and spectral type of the star. The magnitude of a star is a measure of its flux at a particular wavelength, and the spectral type describes the intensity distribution of the spectrum.

Magnitude is measured relative to α Lyrae (Vega) which is defined to have zero magnitude at all wavelengths. The intensities of α Lyrae for the different atmospheric windows can be seen in Table 2.1.

The flux, $F_\lambda(m_\lambda)$, at wavelength λ for a star with magnitude m_λ is given by:

$$F_\lambda(m_\lambda) = F_\lambda(\alpha \text{ Lyrae}) \times 10^{-0.4 m_\lambda} \tag{2.5}$$

where $F_\lambda(\alpha$ Lyrae) is the flux of α Lyrae at wavelength λ as tabulated in Table 2.1. For example, the flux of a star at 3.8 μm in the L$'$ atmospheric window ($\lambda = 3.8$ μm) is given by:

$$I_{3.8} = 5.24 \times 10^{-11} \times 10^{-0.4 m_{3.8}} \tag{2.6}$$

where $m_{3.8}$ is the magnitude of the star at 3.8 μm. This gives the intensity at a particular wavelength (in units of Wm$^{-2}\mu$m^{-1}). Now the modelled black body spectrum with a temperature corresponding to the star's spectral type can be scaled to match this value such that the intensity at any wavelength is

$$I_{bb}(\lambda) = I_{3.8} \left(\frac{3.8}{\lambda}\right)^5 \frac{\exp \frac{14388}{3.8T} - 1}{\exp \frac{14388}{\lambda T} - 1} \tag{2.7}$$

where $I_{bb}(\lambda)$ is the black body intensity, λ is the wavelength in μm and T is the temperature. An example of a black body spectrum in the L and L$'$ atmospheric windows can be seen in Figure 2.11.

The calibration spectrum

If a star emits a spectrum in the form of a perfect black body, any attenuation introduced when the light passes through the Earth's atmosphere would show up in the observed spectrum as departures from a black body curve. The atmospheric extinction as observed on Mount Palomar by Livingston and Wallace [1991] can be seen in Figure 2.7. This was at very high resolution and we expect that the spectral resolutions available at UKIRT will blur out the very sharp features seen in this spectrum. The calibration spectrum $F(\lambda)$ is given by:

$$F(\lambda) = \frac{F_{bb}(\lambda)}{F_{star}(\lambda)} \tag{2.8}$$

where $F_{star}(\lambda)$ is the flux of the star spectrum in units of CCD counts per second. The calibration spectrum is in units of flux in [Wm$^{-2}\mu$m^{-1}count^{-1}] and is used to convert the observed CCD counts per second to a physical flux. It also corrects for

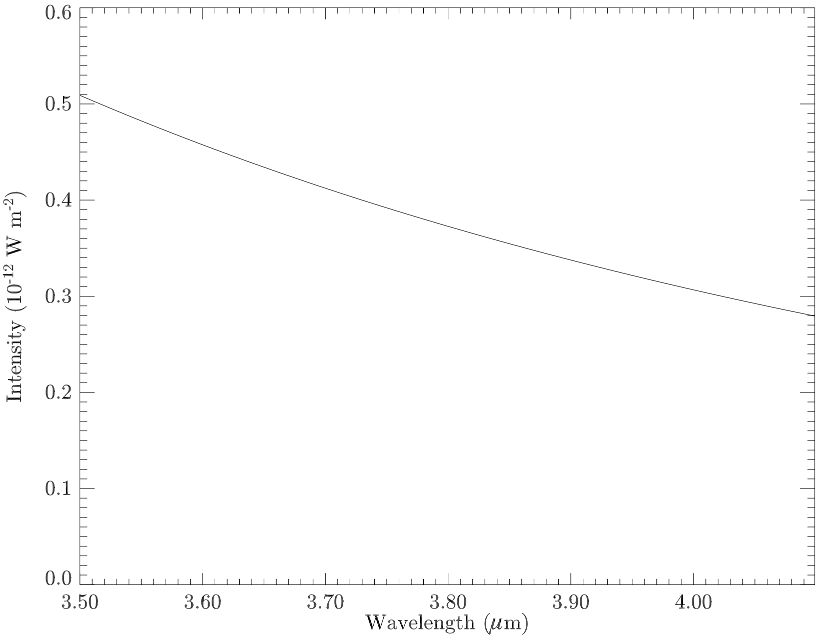

Figure 2.11: Black body spectrum for a star with L magnitude $m_{3.8} = 3.4$ and a spectral type A0 ($T = 10,000$ K).

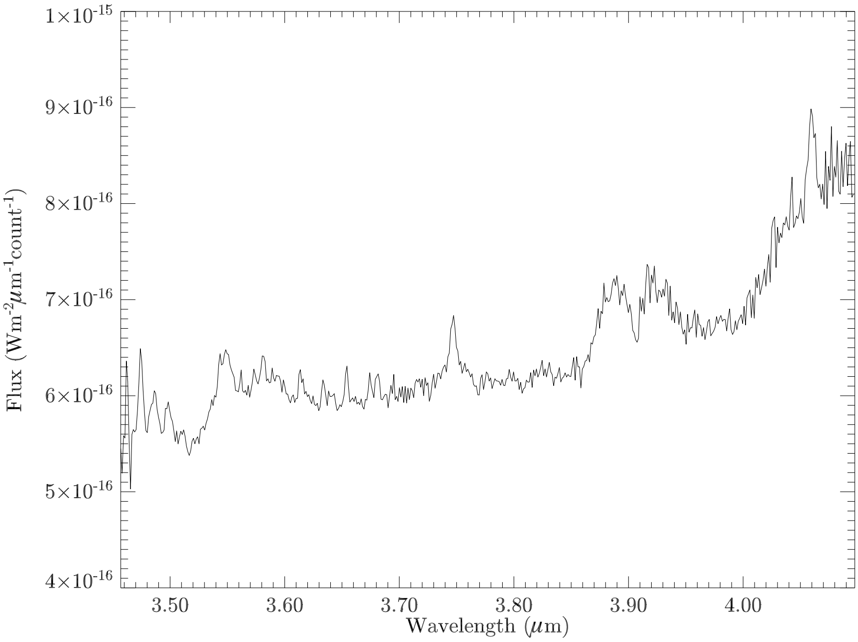

Figure 2.12: Calibration spectrum generated with HD 64648. It has a temperature of $T = 9,900$ K.

atmospheric attenuation.

2.3 Line-of-sight corrections

H_3^+ emission is emitted over a range of altitudes in the upper atmosphere of the giant planets (e.g. Achilleos et al. [1998b]) which gives rise to the effect of increased brightness when observing close to the limb of a planet. This is because a longer column of gas is observed due to the curvature of the planet. This section will explain how to correct for this and will contrast the difference between treating a planet as a sphere and as an oblate spheroid.

A planet can be described as an oblate spheroid – a flattened sphere where the polar radius, R_p, is smaller than the equatorial radius R_e. Any point on this planet, such as a pixel in the slit of a spectrograph, can be described by two distances: x and z, as illustrated in Figure 2.13. x is the distance from the centre on the planet in the East to West direction and z is the distance from the centre of the planet in the North to South direction. Note that the slit is aligned in the North-South direction in this figure. In the following treatment, the line-of-sight correction will be evaluated for a point and thus the orientation of the slit becomes unimportant.

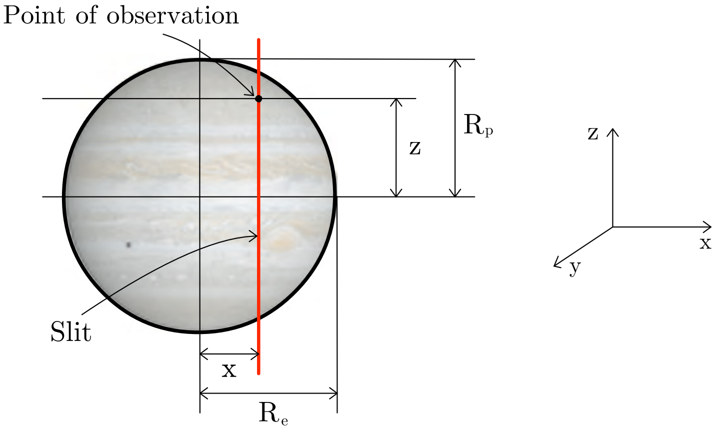

Figure 2.13: Observational configuration of a planet (here Jupiter) as seen from the Earth. The slit is a distance x from the centre of the planet and the observation is made at the point (x, z). The coordinate system is defined with z running South to North, x running from West to East. y is in the direction of line-of-sight of the observer.

The H_3^+ emission is produced in a shell of thickness h that is assumed to be constant at all latitudes and longitudes. The shell can therefore be thought of as being contained between two oblate spheroids, an inner one with an equatorial radius of R_e (i.e. the 'surface' of the planet) and an outer one with equatorial radius $R_e + h$. Both these spheroids are rotated by an angle θ – the sub-observer latitude on the planet. If the coordinate system is defined as in Figure 2.13 then the pathlength, L, is given by:

$$L = \Delta y = y_{R_e+h}(x, z) - y_{R_e}(x, z) \tag{2.9}$$

where $y_{R_e+h}(x, z)$ is the position on the y-axis of the outer spheroid, $y_{R_e}(x, z)$ is the y position of the inner spheroid.

Here, a detailed mathematical analysis is performed to ascertain how the added complexities of treating a planet as an oblate spheroid affects the correction factor, compared to approximating a planet to a sphere.

The following treatment assumes that the emitting layer of gas is optically thin in the infrared, i.e. that the light emitted at the bottom of the ionosphere is not attenuated by particles or processes as it travels upwards towards the observer. Another assumption is that the H_3^+ shell is uniform in composition and relatively thin – in the case of Jupiter the layer is estimated to be 500 km – based on the H_3^+ height density profile of the jovian auroral region produced by Grodent et al. [2001].

The observed pathlength can be thought of as having two components – one due to longitudinal curvature and the other due to latitudinal curvature.

2.3.1 Longitudinal correction

We define an oblate spheroid, representing a planet, tilted by an angle θ – the sub-observer latitude. The coordinate system is defined as in Figure 2.13, with the y axis running in the line-of-sight of the observer, the x axis running East to West, and the z axis running South to North.

A cut through the equator of an oblate planet becomes two concentric circles – one defining the inner and the other the outer limits of the H_3^+ emitting layer. The inner circle has a radius of R_e and the radius of the outer circle is R_{e+h}. This is shown in figure 2.14. In this Figure, a is the radius of the major axis of the ellipse produced by a cut in the $z - y$ plane at the equator at distance x, and b is the pathlength of H_3^+ at position x.

In Figure 2.14, there are two right angle triangles which can described by Pythago-

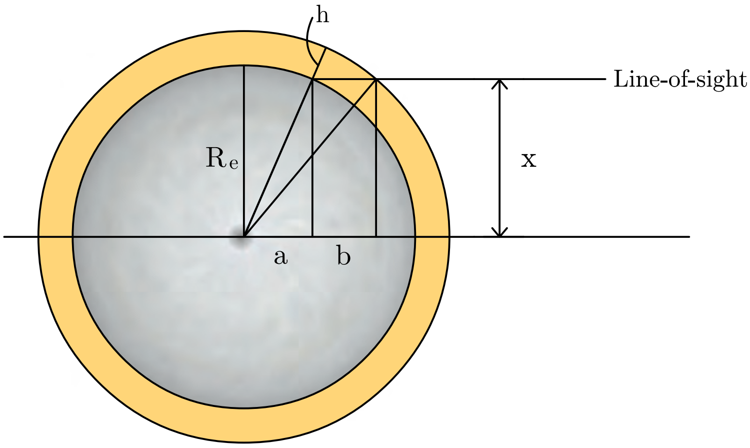

Figure 2.14: View of the cut through the equatorial plane of an oblate planet.

ras' theorem:

$$x^2 + a^2 = R_e^2 \tag{2.10}$$

and

$$x^2 + (a + b)^2 = (R_e + h)^2 \tag{2.11}$$

where b is the H_3^+ pathlength at the equator at distance x, and h is the thickness of the H_3^+ shell. Combining Equations 2.10 and 2.11 gives the following expression for the pathlength b:

$$b = \sqrt{(R_e + h)^2 - x^2} - \sqrt{R_e^2 - x^2} \tag{2.12}$$

In the next section b will be used to calculate the observed pathlength at (x, z). If the planet was being treated as a perfect sphere, Equation 2.12 describes the line-of-sight pathlength of H_3^+ where x is the radial distance between the centre of, and any point on, the planet. The pathlength is then independent of sub-observer latitude.

2.3.2 Latitudinal correction

The latitudinal correction factor is slightly more complicated since a cut in the $z - y$ plane at distance x would reveal a tilted ellipse rather than a circle. This is shown in Figure 2.15. From Equation 2.10 we find that the radius of the ellipse produced by cutting in the $z - y$ equatorial radius, a, is given by:

$$a = \sqrt{R_e^2 - x^2} \tag{2.13}$$

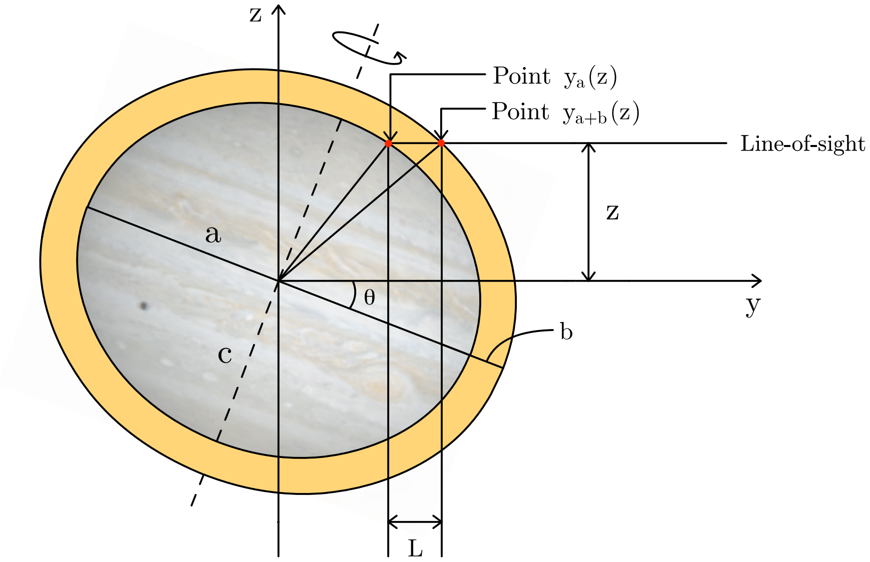

Figure 2.15: A planet cut in the $z-y$ plane a distance x from the planet.

Assuming that the concentric ellipses at all possible values of x have the same eccentricity, the distance c as defined in Figure 2.15 is given by:

$$c = R_P \frac{a}{R_e} = Rp \frac{\sqrt{R_e^2 - x^2}}{R_e} \tag{2.14}$$

The equation for an ellipse in the $z-y$ direction at a position x is given by:

$$\left(\frac{y}{a}\right)^2 + \left(\frac{z}{c}\right)^2 = 1 \tag{2.15}$$

where (y, z) is a point on the ellipse.

A 2D cartesian coordinate transformation of the point (y, z) rotated by an angle θ to coordinates (y_θ, z_θ) is given by:

$$y_\theta = y\cos\theta - z\sin\theta \tag{2.16}$$

$$z_\theta = y\sin\theta + z\cos\theta \tag{2.17}$$

An ellipse defined by (x_θ, y_θ) is given by, substituting Equation 2.16 and 2.17 into Equation 2.15:

$$\left(\frac{y\cos\theta - z\sin\theta}{a}\right)^2 + \left(\frac{y\sin\theta + z\cos\theta}{c}\right)^2 = 1 \tag{2.18}$$

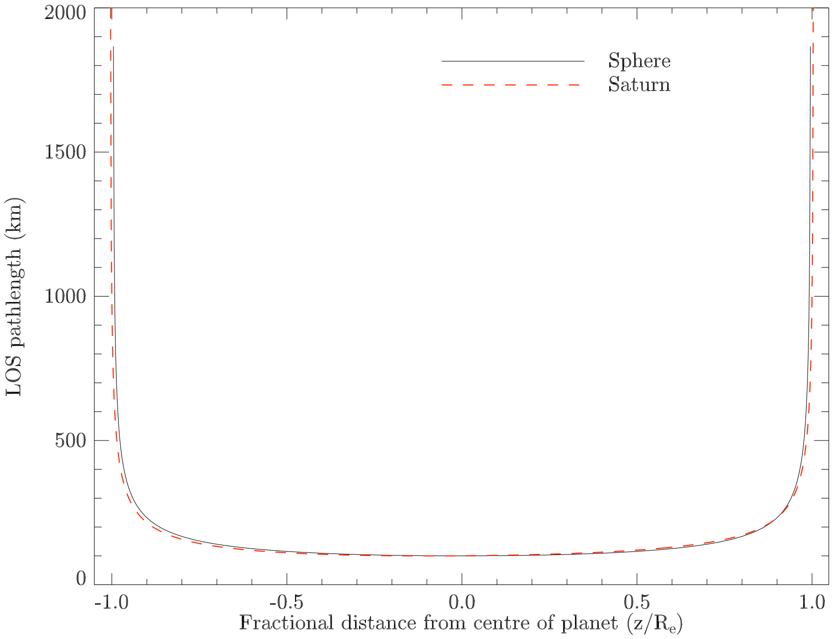

Figure 2.16: Pathlength of the emitting H_3^+ layer of a sphere with a radius equal to the equatorial radius of Saturn (solid line) and Saturn represented by a spheroid (dashed line) with a sub-observer latitude of 45° North and $x = 0$. The pathlength is assumed to be 100 km.

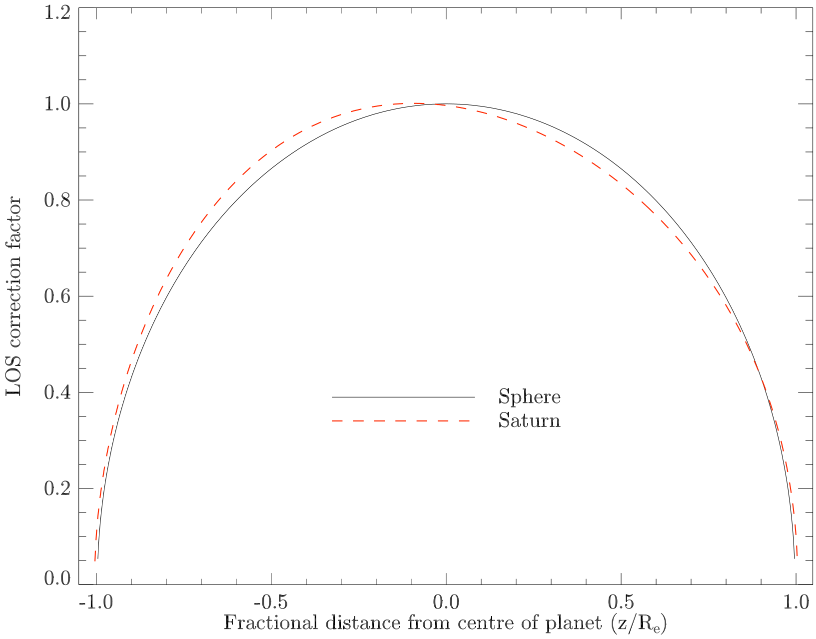

Figure 2.17: Line-of-sight correction factor for an emitting H_3^+ shell with a height of 100 km for a sphere and an oblate representation of Saturn. The sub-observer latitude is 45° North and $x = 0$.

which, when expanded, can be written as:

$$
\begin{gathered}
y^2(c^2\cos^2\theta + a^2\sin^2\theta) + y^2 z\cos\theta\sin\theta(a^2 - c^2) + \\
z^2(c^2\sin^2\theta + a^2\cos^2\theta) - a^2c^2 = 0
\end{gathered} \tag{2.19}
$$

which is of the form of a quadratic equation:

$$y^2 k_1 + y k_2 + k_3 = 0 \tag{2.20}$$

which has the well-known solution:

$$y = \frac{-k_2 \pm \sqrt{k_2^2 - 4k_1k_3}}{2k_1} \tag{2.21}$$

Comparing Equation 2.20 with Equation 2.19 gives the coefficients:

$$k_1 = c^2\cos^2\theta + a^2\sin^2\theta \tag{2.22}$$

$$k_2 = 2z\cos\theta\sin\theta(a^2 - c^2) \tag{2.23}$$

$$k_3 = z^2(c^2\sin^2\theta + a^2\cos^2\theta) - a^2c^2 \tag{2.24}$$

Inserting these coefficients into Equation 2.21 gives $y_a(x, z)$. The coefficients for $y_{a+b}(x, z)$ are as above, but replacing a with $a + b$ and c with $c + b$:

$$k_1 = (c + b)^2\cos^2\theta + (a + b)^2\sin^2\theta \tag{2.25}$$

$$k_2 = 2z\cos\theta\sin\theta((a + b)^2 - (c + b)^2) \tag{2.26}$$

$$k_3 = z^2((c + b)^2\sin^2\theta + (a + b)^2\cos^2\theta) - (a + b)^2(c + b)^2 \tag{2.27}$$

This enables us to find L as defined in Equation 2.9, since we know b from Equation 2.12, a from Equation 2.13 and c from Equation 2.14. The factor then needed to correct for the line-of-sight effect is given by:

$$D = \frac{h}{\Delta y} = \frac{h}{L} \tag{2.28}$$

In the case of Saturn, R_e = 60,268 km, R_p = 54,890 km (The Astronomical Almanac), assuming a shell thickness of h = 500 km and a sub-observer latitude of, say, 45°. Note that the H_3^+ emission does not emanate from the surface of the planet, which is defined as 1 bar, but some 1000km above that. The resulting pathlength at $x = 0$ is shown in Figure 2.16, and is compared to that of a perfect sphere. In Figure 2.17, the line-of-sight correction factor, D, is plotted. Figure 2.18 shows the difference, ΔL, between the pathlength of the sphere and the oblate spheroid.

Figure 2.18 shows that for scenarios where the data has an error on the intensity of more than ~10% or is of poor spatial resolution, a spherical line-of-sight correction, rather than the oblate spheroid, is sufficient.

2.3.3 The importance of the absolute pathlength

Since the correction factor is the fraction between the observed pathlength and the pathlength at the equator, how important is the absolute thickness of the emitting H_3^+ layer? To investigate this, the spherical line-of-sight correction given in Equation 2.12 is calculated for a planet where the emitting layer is 0.1% and 10% of the planetary radius. The resulting line-of-sight correction factor can be seen in Figure 2.19. The difference between the two curves starts to become apparent at about a fractional distance from the centre of the planet of 0.8 R_e and a major divergence is seen beyond 0.95 R_e. This means that the knowledge of the absolute thickness of the emitting layer is only relevant when observing close to the limb on a planet on which a spatial resolution of $\sim$ 5% of R_e can be achieved, including the effects of seeing. Whilst such detail can be achieved on Jupiter (e.g. Stallard et al. [2002]), it cannot be achieved on Saturn or Uranus with the instruments available for the data analysed in this thesis.

2.4 Fitting H_3^+ spectra

In order to extract information about the physical characteristics of an observed region, the H_3^+ spectrum needs to be matched to a theoretical one, giving temperatures and column-integrated densities. First, we need an algebraic formulation of an H_3^+ emission spectrum which gives us the equation for use with minimising techniques to fit to an observed spectrum.

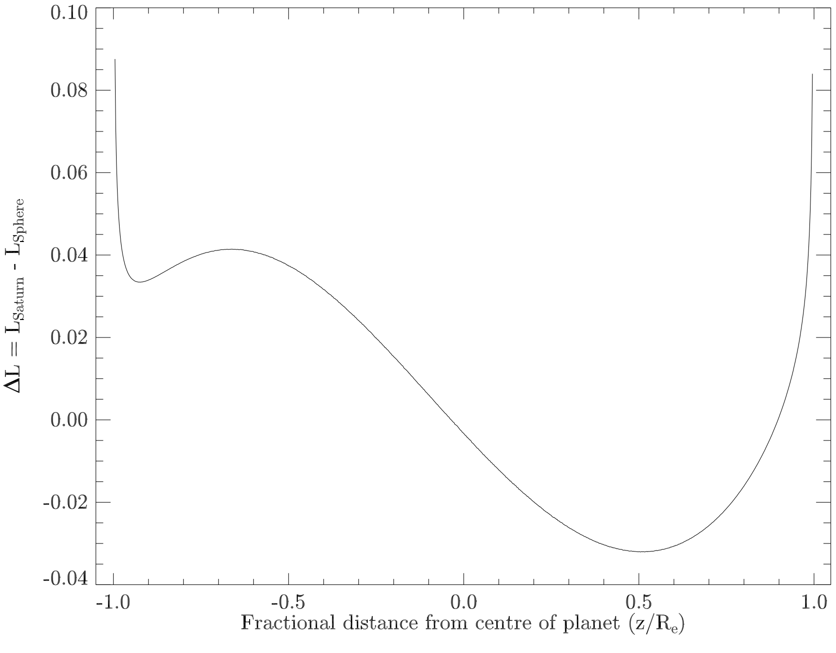

Figure 2.18: The difference between the pathlength of a sphere and the pathlength on Saturn given a sub-observer latitude is 45° North and $x = 0$.

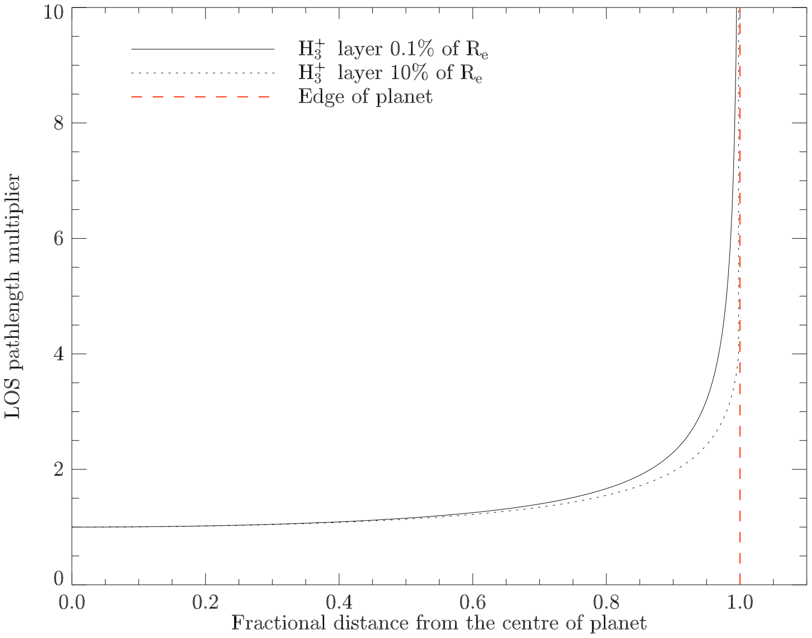

Figure 2.19: The line-of-sight pathlength multiplier for a H_3^+ emitting layer of 0.1% and 10% of the planetary radius.

2.4.1 H_3^+ transition intensities, I_i

For a gas in Local Thermodynamic Equilibrium (LTE), the fraction of molecules, N_i, in energy level i is given by:

$$N_i = \frac{N}{Q(T)}(2J+1)g_{ns}\exp\left[\frac{-E_i}{kT}\right] \tag{2.29}$$

where N is the total number of molecules, $Q(T)$ is the temperature dependent partition function, E_i is energy of level i, J is the rotational angular momentum of level i and g_{ns} is the spin weighting associated with ortho ($g_{ns} = 4$) and para ($g_{ns} = 2$) symmetry states.

If a transition is between an upper level i and lower level f, the intensity emitted by a molecule is given by:

$$I(\omega_{if}) = 100 \times hc\omega_{if}A_{if} \tag{2.30}$$

where ω_{if} is the wavenumber of the emission (cm^{-1}), A_{if} is the Einstein-A transition probability of spontaneous emission (in units of s^{-1}) and the factor of 100 converts the units of the wavenumber of cm^{-1} to m^{-1} (units in this thesis are SI wherever possible).

Putting Equation 2.29 together with Equation 2.30 and normalising to units of per steradian (str^{-1}) we have:

$$I(T) = \frac{N \times g_{ns}(2J+1)100hcw_{if}A_{if}}{4\pi Q(T)}\exp\left[-\frac{100 \times hcw_{upper}}{kT}\right] \tag{2.31}$$

where h is Planck's constant, k is Boltzmann's constant and c is the speed of light. This enables us to relate the observed intensity to a temperature and column-integrated density, assuming conditions of LTE. Obviously, at least two intensities, given as a ratio, are needed to constrain *both* temperature and density. To complete Equation 2.31 we need the transition parameters (A_{if}, g_{ns}, ω_{if}, J and ω_{upper}) and the partition function $Q(T)$. The references of these are discussed below.

2.4.2 H_3^+ line list

The transition parameters are given in a spectral line list. The H_3^+ spectral line list was compiled from Neale et al. [1996] which lists some 3 million transitions. Many of these lines are not relevant for fitting planetary spectra since ionospheric temperatures are moderate (a few hundred to a few thousand K) and at such temperatures many transitions in this list are very weak. A C++ program was constructed that sifted through the line list, picking out transitions with large Einstein A coefficients and hand-assigned nuclear spin weighting (i.e. a value of g_{ns} of either 2 or 4). This yielded 3,027 lines between 1.3 μm and 6.7 μm.

2.4.3 H_3^+ partition function

The partition function is a parameter that describes the statistical properties of a system in Local Thermodynamic Equilibrium (LTE). Neale and Tennyson [1995] expressed the partition function, Z, as:

$$\log_{10}(Z) = \sum_{n=0}^{6} a_n \left(\log_{10} T\right)^n \tag{2.32}$$

where T is the temperature and a_n are the constants defined as:

$$\begin{aligned}
a_0 &= \, 78.6233962485680706 \qquad &(2.33)\\
a_1 &= -\, 134.822002886523251 \qquad &(2.34)\\
a_2 &= \, 88.4482694968956480 \qquad &(2.35)\\
a_3 &= -\, 25.9274134010262429 \qquad &(2.36)\\
a_4 &= \, 2.60233376654769222 \qquad &(2.37)\\
a_5 &= \, 0.224167420795110400 \qquad &(2.38)\\
a_6 &= -\, 0.0452550693680233290 \qquad &(2.39)\\
& &(2.40)
\end{aligned}$$

The partition function can be seen in Figure 2.20.

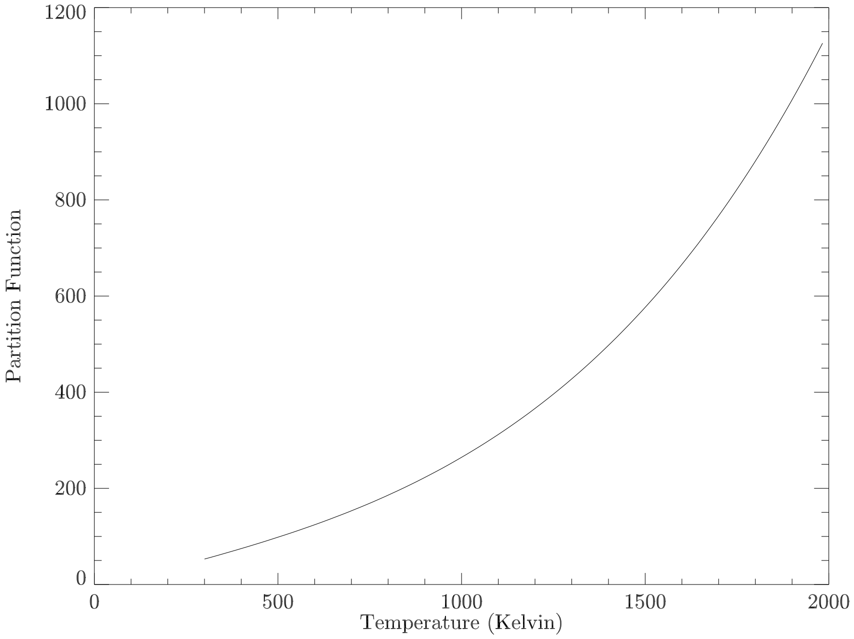

Figure 2.20: The H_3^+ partition function as given by Neale and Tennyson [1995] for $0 \leq T \leq 2{,}000$ K.

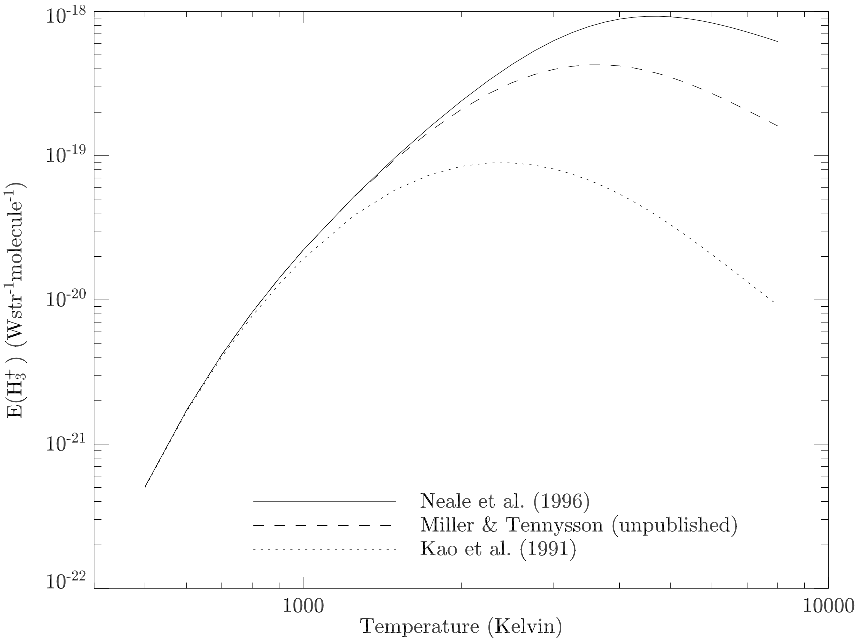

Figure 2.21: Total emission of an H_3^+ molecule, $E(H_3^+)$, versus temperature. In this work the line list of Neale et al. [1996] is used.

2.4.4 Total H_3^+ emission

The total emission, E(H_3^+), is the sum of intensities emitted at all wavelengths by all levels in a H_3^+ molecule at a certain temperature when the condition of Local Thermodynamic Equilibrium (LTE) holds. The total H_3^+ emission is a measure of how much thermal energy the molecule radiates at a certain temperature. When observing H_3^+ in giant planet ionospheres, this energy is lost since it is radiated into space.

The parameter was introduced to the context of planetary atmospheres by Lam et al. [1997a] due to the anti-correlation between fitted temperature and column density. The total emission per molecule as a function of temperature can be seen in Figure 2.21. There are three different profiles, based on the line lists of Neale et al. [1996], Miller & Tennyson (unpublished) and Kao et al. [1991] respectively. The more lines that are included in the calculations, the higher the intensity at a certain temperature. However, even though Neale et al. [1996] lists far more lines than any other line list, the vast majority are extremely weak at ionospheric temperatures of giant planets.

The total emission per steradian of all the molecules in a column of H_3^+ is given by:

$$E(H_3^+) = N(H_3^+)E_{H_3^+}^{mol}(T) \tag{2.41}$$

where $N(H_3^+)$ is the column density, T is temperature and $E_{H_3^+}^{mol}(T)$ is the temperature-dependent total emission per molecule, plotted in Figure 2.21.

The Neale et al. [1996] total emission curve was fitted using the `poly_fit.pro` procedure in IDL. Only temperatures relevant to giant planet atmospheres were included such that the temperature range is $0 \leq T \leq 2000$ K. The total emission per molecule is given by the following equation:

$$E_{H_3^+}^{mol}(T) = a + bT + cT^2 + dT^3 + eT^4 \tag{2.42}$$

where for $500 \leq T \leq 900$ K:

$$a = -6.11904 \times 10^{-21} \tag{2.43}$$

$$b = 4.96694 \times 10^{-23} \tag{2.44}$$

$$c = -1.43608 \times 10^{-25} \tag{2.45}$$

$$d = 1.60926 \times 10^{-28} \tag{2.46}$$

$$e = -3.87932 \times 10^{-32} \tag{2.47}$$

and for $900 \leq T \leq 2000$ K:

$$a = -8.24045 \times 10^{-21} \tag{2.48}$$

$$b = 3.54583 \times 10^{-23} \tag{2.49}$$

$$c = -8.66269 \times 10^{-26} \tag{2.50}$$

$$d = 9.76608 \times 10^{-29} \tag{2.51}$$

$$e = -1.61317 \times 10^{-32} \tag{2.52}$$

In order to determine the accuracy of this fit, the Neale et al. [1996] curve was divided by Equation 2.42 for both temperature ranges. As can be seen in Figure 2.22 the two curves do not diverge more than a fraction of a percent and thus the fit is considered to be good – well within the errors on the temperatures and column density from ground-based infrared observations (e.g. Stallard [2000]). The fit derived by Stallard [2000] can be seen compared to the fit obtained here in Figure 2.23. It clear that the new low temperature is a great improvement.

2.4.5 The H_3^+ fitting routine

A fitting routine is a program that matches an observed spectrum to a theoretical H_3^+ spectrum, usually utilising iterative minimising techniques. This enables observers to attribute a temperature and column density to the region that the H_3^+ was produced in (assuming conditions of LTE). Here, an algebraic formulation of a spectrum in conjunction with the use of a minimising technique invoking Cramer's Rule (Bevington and Robinson [2003]) is used.

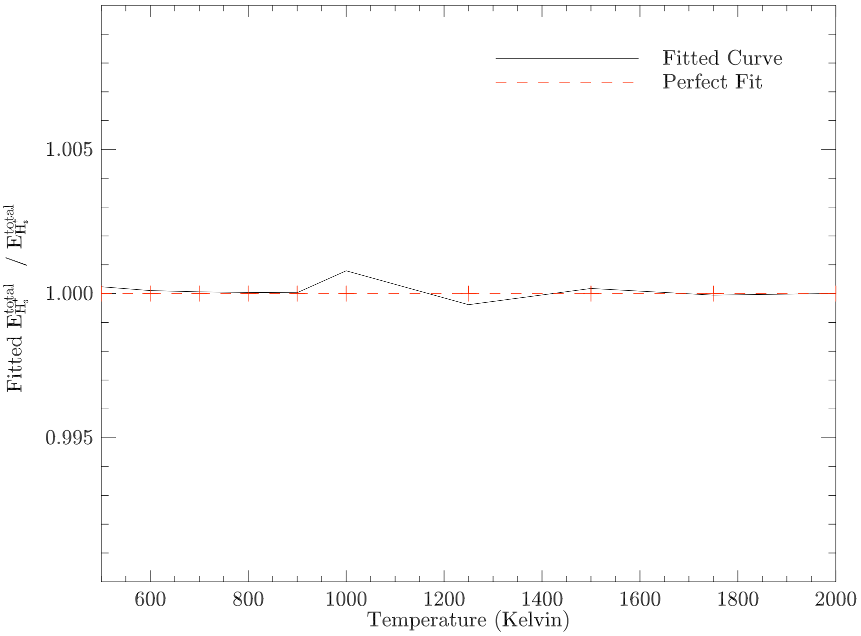

Figure 2.22: Ratio between the total emission curve as calculated by Neale et al. [1996] and the function fitted to it in this thesis. The crosses are the temperatures for which Neale et al. [1996] calculated the total emission.

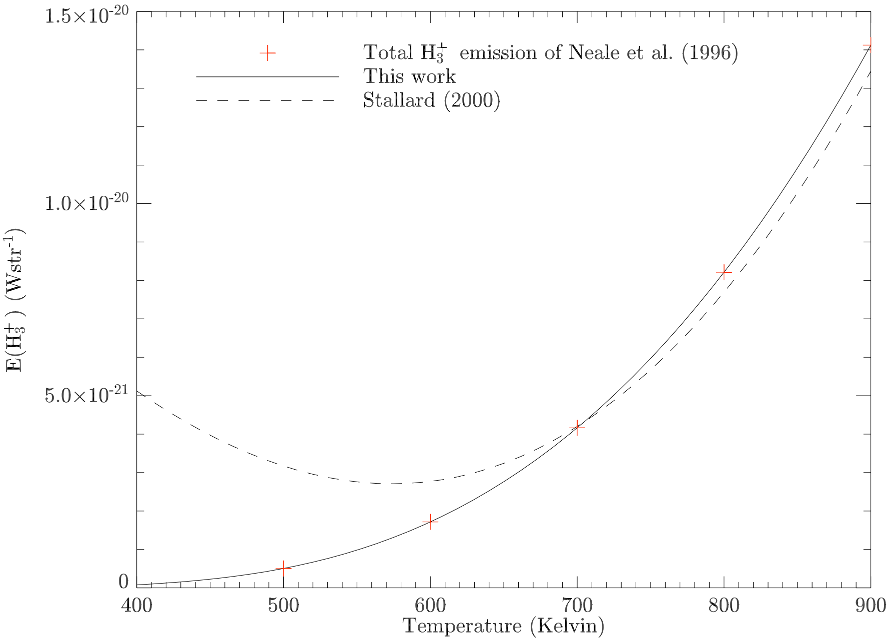

Figure 2.23: The total H_3^+ emission curve and the fit derived in this thesis and that of Stallard [2000].

Motivation

Lam et al. [1997a] showed that there is an anti-correlation between the fitted temperature and column density, especially when looking at a spectrum with low signal-to-noise ratio. There are two major factors attributed to the fitting routine that might have an adverse effect on the quality of the fit. First, the width of the spectral lines needs to be as accurate as possible to get an accurate integrated flux of any given H_3^+ transition. For example, if one assumes too large a full-width at half maximum (FWHM), the column density has to be larger to account for the intensity held in the widened line. Conversely, if the FWHM is too small, the derived column density would be too low. Second, the wavelength scale needs to be as close to the theoretical H_3^+ spectrum of Neale et al. [1996] as possible so that the peak of any given transition can be located with accuracy.

A number of requirements were drawn up for a new and improved fitting routine. The routine needed:

1. To fit temperature, column density, and a constant background level.
2. To fit a wavelength shift parameter, which could be a function of wavelength, correcting for errors in the wavelength calibration. This would be a separate stage to 1.
3. To fit a FWHM, also possibly a function of wavelength, to ensure that the correct integrated line intensity is fitted, since total line flux is a function of the line width for a given height. This, too, would be a separate stage to both 1 and 2.
4. To improve the runtime speed, compared to the existing fitting routine, by means of code optimisation and data shielding – e.g. limiting the line list data only to cover the relevant region defined by the wavelength scale of a spectrum.
5. To have the program suggest first estimates of everything but temperature, in order to make it more straightforward to use.
6. An easy-to-use IDL interface, which in turn would call the external C++ routine.

With this in mind it was decided that the existing FORTRAN 77 code utilising existing NAG routines was redeveloped using C++ and a hard-coded fitting routine using standard function derivatives and a least square fitting method invoking Cramer's Rule (Bevington and Robinson [2003]).

Equation of a spectrum

The spectral function is described by a sum of gaussians (see Lam et al. [1997a] for the comparison of different line functions), each describing the intensity of a particular transition (Lam et al. [1997a]). For a given line width, σ or $\sigma(\lambda)$, and an ion density, ρ, the intensity, $I(\lambda)$, is given by:

$$I(\lambda) = \rho \sum_{i=0}^{n_{lines}} \frac{I_i(T)}{\sigma_i(\lambda)\sqrt{2\pi}} \exp\left(-\frac{(\lambda - (\lambda_i + s(\lambda)))^2}{2\sigma_i(\lambda)^2}\right) + k \tag{2.53}$$

where

$$\text{FWHM} = \sqrt{2\pi}\sigma \tag{2.54}$$

where λ is the wavelength, n_{lines} is the number of transitions that are being added, $I_i(T)$ is the intensity of transition i at a temperature T, k is the background level of the spectrum, and $s(\lambda)$ is the shift between the observed and listed transition wavelength. It is needed to introduce this parameter because a spectral line can be red- or blue-shifted and there can be errors in the wavelength calibration. Let $s(\lambda)$ be governed by a general power law:

$$s(\lambda) = \sum_{i=0}^{i} b_i \lambda^i \tag{2.55}$$

where b_i is the series constant. Similarly, we can expand the line width σ to be a function of wavelength with constants a_j such that:

$$\sigma(\lambda) = \sum_{j=0}^{j} a_j \lambda^j \tag{2.56}$$

This enables the parameterisation of variations of σ as a function of wavelength.

Fitting technique

The flowchart outlining the different steps involved in fitting a spectrum is shown in Figure 2.25.

The steps in sequential order are:

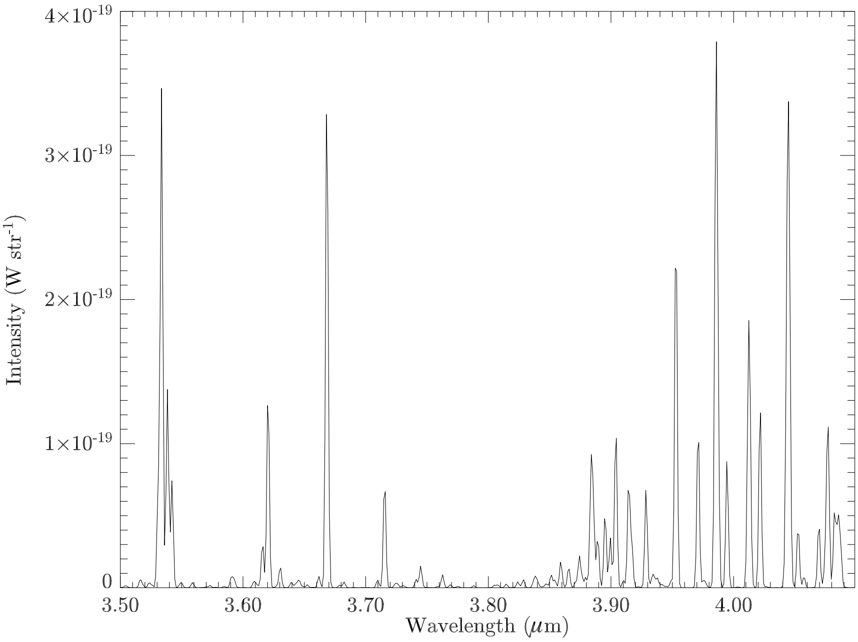

Figure 2.24: Modelled H_3^+ spectrum of a single molecule emitting at 1,000 K with a FWHM of 0.05 μm.

1. Load a reduced spectrum in units of $[\mathrm{Wm^{-2}\mu m^{-1}str^{-1}}]$ into the program. This usually consists of an array of wavelength values with corresponding intensity values.
2. Guess initial values for the variables to be fitted. The user must always provide a guess for the temperature T. The column density is estimated by dividing the peak intensity in the spectrum with the intensity emitted by one molecule at temperature T. The wavelength shift is estimated by finding the difference in λ between the peak intensity in the observed and the theoretical spectrum. The line width is estimated by making a rough measurement of the width of the line with the maximum intensity in the observed spectrum.
3. The shift is fitted to any order according to Equation 2.55.
4. The line width is fitted to any order according to Equation 2.56.
5. Fit temperature, column density, and background level of the spectrum.
6. Check if the change in temperature and column density is very small, or else go back to 3 and reiterate.

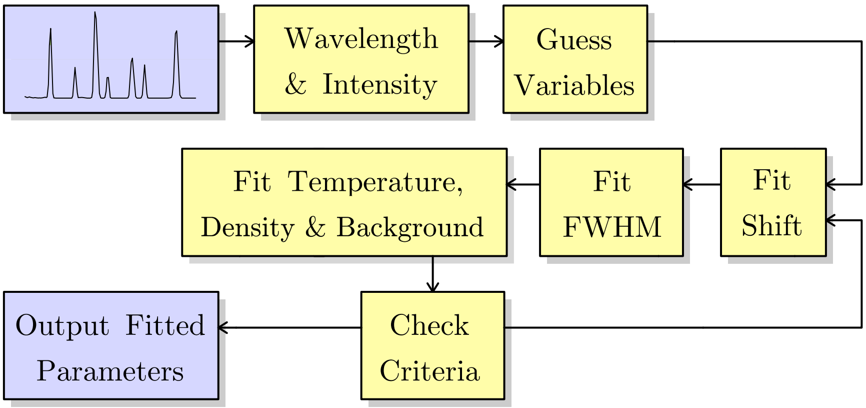

Figure 2.25: The flowchart of the H_3^+ spectrum fitting routine.

Mathematical approach

Let $F(a, b, c)$ be a function with three free parameters a, b and c. We want to fit these three parameters to a dataset f_i where i is the i^{th} measurement. We define the partial derivatives of our function:

$$A \equiv \frac{\partial F(a, b, c)}{\partial a} \tag{2.57}$$

and

$$B \equiv \frac{\partial F(a, b, c)}{\partial b} \tag{2.58}$$

and

$$C \equiv \frac{\partial F(a, b, c)}{\partial c} \tag{2.59}$$

Now, we define the difference between the measurment f_i and the calculated value as:

$$\eta_i = f_i - F_i(a_0, b_0, c_0) \tag{2.60}$$

where $F_i(a_0, b_0, c_0)$ is function F evaluated at point i using estimates a_0, b_0 and c_0. We invoke Cramer's Rule (Bevington and Robinson [2003]) and define the following matrices each describing three simultaneous linear equations.

$$\mathbf{Z} = \begin{pmatrix} \sum A_i^2 & \sum A_i B_i & \sum A_i C_i \\ \sum A_i B_i & \sum B_i^2 & \sum B_i C_i \\ \sum A_i C_i & \sum B_i C_i & \sum C_i^2 \end{pmatrix} \tag{2.61}$$

$$\mathbf{A} = \begin{pmatrix} \sum A_i\eta_i & \sum A_iB_i & \sum A_iC_i \\ \sum A_i\eta_i & \sum B_i^2 & \sum B_iC_i \\ \sum A_i\eta_i & \sum B_iC_i & \sum C_i^2 \end{pmatrix} \tag{2.62}$$

$$\mathbf{B} = \begin{pmatrix} \sum A_i^2 & \sum A_i\eta_i & \sum A_iC_i \\ \sum A_iB_i & \sum B_i\eta_i & \sum B_iC_i \\ \sum A_iC_i & \sum B_i\eta_i & \sum C_i^2 \end{pmatrix} \tag{2.63}$$

$$\mathbf{C} = \begin{pmatrix} \sum A_i^2 & \sum A_iB_i & \sum A_i\eta_i \\ \sum A_iB_i & \sum B_i^2 & \sum B_i\eta_i \\ \sum A_iC_i & \sum B_iC_i & \sum C_i\eta_i \end{pmatrix} \tag{2.64}$$

Now the shift from the initial guesses is given by the following expressions:

$$\Delta a = \frac{|A|}{|Z|} \tag{2.65}$$

$$\Delta b = \frac{|B|}{|Z|} \tag{2.66}$$

$$\Delta c = \frac{|C|}{|Z|} \tag{2.67}$$

$$\tag{2.68}$$

The matrices above are re-calculated until Δa, Δb and Δc are sufficiently small as to change the values a, b and c insignificantly. The partial derivatives for all the relevant functions are detailed in Appendix A.

Error on fitted parameters

We define $S' = \sum \eta_i^2$ so that $S' \rightarrow S$ as we iterate towards convergence. If a spectrum has N pairs of wavelength and intensity values then the standard deviation, μ, of a single dependent datum is given by:

$$\mu = \pm\sqrt{S'/(N-\nu)} \tag{2.69}$$

where ν is the degrees of freedom in the fit. Then the formal uncertainty, i.e. the standard error, for a parameter number p, Δ_p is:

$$\Delta_p = \pm \frac{\mu}{\sqrt{\frac{|Z|}{|\mathrm{cofac} Z_{p,p}|}}} \tag{2.70}$$

where $|\mathrm{cofac}\ Z_{p,p}|$ is the determinant of the ν-1 dimensional matrix formed by removing row p and column p from matrix Z. Note that these errors do not include any error introduced in the flux-calibration of the spectrum, such that the error is purely based on the spread of the data.

The total emission is given in Equation 2.41 and is a function of temperature and column density of H_3^+. Since the fitting routine gives the standard errors of both these parameters, we can use the rules of propagation of errors to find the standard error on E(H_3^+). In general, for $z = f(w, x, y, ...)$, the error, Δz is given by

$$\Delta z = \left(\frac{\partial f}{\partial w}\right) \Delta w + \left(\frac{\partial f}{\partial x}\right) \Delta x + \left(\frac{\partial f}{\partial y}\right) \Delta y + ... \tag{2.71}$$

E(H_3^+) is described by equation 2.41. The error, $\Delta E(H_3^+)$, becomes:

$$\Delta E(H_3^+) = \left(\frac{\partial E(H_3^+)}{\partial N}\right) \Delta N + \left(\frac{\partial E(H_3^+)}{\partial T}\right) \Delta T \tag{2.72}$$

where

$$\frac{\partial E(H_3^+)}{\partial N} = E_{H_3^+}^{mol} \tag{2.73}$$

and

$$\frac{\partial E_{H_3^+}}{\partial T} = N(b + 2cT + 3dT^2 + 4eT^3) \tag{2.74}$$

which uses the expression for $E_{H_3^+}^{mol}$. The value for the constants b, c, d and e depend on what temperature range is being fitted, as discussed in Section 2.4.4.

2.4.6 IDL interface

Whilst the fitting routine can be used as a standalone C++ program, it makes more sense to develop an IDL application program interface (API) for the routine, especially when the vast majority of the data handling is done in IDL. The IDL routine `h3p_fit_auto.pro` communicates with the C++ routine via binary data files and

Observation	Fitted T (K)	Publ. T (K)	Fitted N ($10^{15}m^{-2}$)	Publ. N ($10^{15}m^{-2}$)
1992 Apr 1	758 ± 37	757 ± 25	1.95 ± 0.41	2.14
1993 May 3	734 ± 28	751 ± 65	2.09 ± 0.36	1.74
1993 May 4	727 ± 25	735 ± 65	1.90 ± 0.30	1.74
1993 May 5	650 ± 16	660 ± 65	3.16 ± 0.40	2.74
1994 Jul 20	616 ± 12	635 ± 65	4.50 ± 0.50	3.79
1994 Jul 23	620 ± 17	648 ± 75	5.07 ± 0.75	4.28
1995 Jun 11	738 ± 37	717 ± 70	1.05 ± 0.23	1.56
1995 Jun 12	638 ± 24	662 ± 70	2.33 ± 0.46	1.94
1995 Jun 13	641 ± 29	668 ± 70	2.26 ± 0.53	1.91
1995 Jun 14	679 ± 33	717 ± 70	2.25 ± 0.54	1.43

Table 2.2: A comparison between the values of temperature T and column density N published in Trafton et al. [1999], and the values obtained using the fitting routine described in this chapter. Note that the errors on the fitted temperature do not include any uncertainty introduced in the process of flux calibration. Trafton et al. [1999] does not give errors for the column density.

the IDL command `spawn`, which enables the execution of any `unix` command. This procedure is discussed in more detail in Appendix B.3.

2.4.7 Integrity of fitting routine

Since the fitting routine was written from scratch it needed to be tested against established fitting software such as the existing `Fortran 77` routine. Some of the data presented in Chapter 5 was originally published by Trafton et al. [1999] with fitted temperatures and column densities. The same data was fitted with the new routine and a parameter comparison can be seen in Table 2.2. The majority of the fits are equivalent, falling within the errors of each other, for any particular spectrum. Therefore, the two routines are assumed to be equivalent.

Chapter 3

Jupiter

3.1 Introduction

Since the discovery of H_3^+ on Jupiter (Drossart et al. [1989]) this molecular ion has been used as a probe in a large number of studies of giant planet ionospheres (e.g. Trafton et al. [1999], Stallard et al. [2002], Rego et al. [2000], Stallard et al. [1999]). In determining temperatures and column densities, all of these studies have assumed conditions of Local Thermodynamic Equilibrium (LTE) or Quasi-LTE (Miller et al. [1997]). As will be discussed in Section 3.1.1, it is likely that non-LTE effects may play an important role in determining the energetics of the jovian thermosphere/ionosphere system.

This chapter aims to investigate whether or not the jovian upper atmosphere is in a state of LTE or non-LTE, at what altitude non-LTE effects become significant, and how these effects change the properties of the H_3^+ emission that is observed from Earth. In the second part of the chapter, using the non-LTE analysis, the auroral heating event reported by Stallard et al. [2002] will be examined in terms of energy balance: what are the energy sources and what loss mechanisms for the energy are there?

Three previous studies have investigated the extent to which H_3^+ is in LTE in the jovian upper atmosphere: Miller et al. [1990], Kim et al. [1992] and Stallard et al. [2002]. Miller et al. [1990] measured lines from both the the first and second vibrationally excited levels and concluded that the ratio was approximately in LTE proportions. Kim et al. [1992] did a modelling study that showed that while two vibrational levels might be behaving as in LTE in relation to each other, the high rate of radiative de-excitation of vibrationally excited levels meant that they were underpopulated compared with the ground state above an altitude of about 650 km, which corresponds to the ionisation peak of their model.

Two models have recently become available: the self-consistent jovian ionospheric model of Grodent et al. [2001] and the principle of detailed balance formulation of a mixture of H_3^+ in H_2 by Oka and Epp [2004]. Applying the latter to the jovian ionospheric density and temperature profiles enables us to calculate what fraction of the LTE population in the H_3^+ vibrational manifolds are present when the LTE requirement is relaxed. The effects of non-LTE are found to be very significant at altitudes above 2,000 km above the 1 bar level. These depopulation effects can explain the discrepancy between the column densities observed by Stallard et al. [2002] and Raynaud et al. [2004].

3.1.1 Local thermodynamic equilibrium on Jupiter

A volume of gas can be considered to have two types of energies: firstly an internal energy, determined by the relative populations of energy levels of the atoms and molecules, and secondly, an external energy, or kinetic energy, determined by the distribution of particle velocities within the volume. When these two are in equilibrium, the system is said to be in a state of local thermodynamic equilibrium (LTE) – the associated internal and external temperatures are equal. Such conditions would also mean that the distribution of the populated atomic or molecular states are easily determined using Boltzmann statistics.

One can imagine several situations in which LTE would break down. Since the main mechanism for the internal and external energy to ‘communicate’ in the upper atmosphere of planets is intermolecular collisions, one could envisage that LTE would break down in low density environments where collisions are few and far between. A departure from LTE would also be likely in a high temperature environment where levels with high energy are populated, with few collisions being able to depopulate from that state. Both of these conditions are met in the upper atmosphere of the giant planets (e.g. for Jupiter see Figures 3.1 and 3.2). This motivates us to study the effects of departure from LTE of H_3^+ in the jovian upper atmosphere, for which we have a self-consistent atmospheric model available – that of Grodent et al. [2001].

3.1.2 Previous treatments of non-LTE effects on Jupiter

LTE cannot hold if the lifetimes of the H_3^+ excited states are greater than the lifetime of the ion itself. If this was true, all non-zero levels would be underpopulated with respect to an LTE distribution since any excitation would lead to a prompt depopulation. The ion lifetime is given by Equation 1.12 and is governed primarily by the electron density. The lifetime is calculated in Section 1.3.3 to be $\sim$ 10 seconds at the altitude of the H_3^+ peak at around 400 km (Grodent et al. [2001]). The radiation lifetime of the $\nu_2 \rightarrow 0$ fundamental transition is equal to the inverse of the Einstein A coefficient: $A_{if}^{-1} = 127^{-1} = 8$ milliseconds (Neale et al. [1996]). Clearly, the lifetime of the molecular ion is much longer than the radiation lifetime, and so the most basic criteria for LTE is satisfied at the H_3^+ density peak in the upper atmosphere of Jupiter.

LTE also breaks down if the H_3^+ excitation rate is much smaller than the lifetime of the excited levels. H_3^+ is thought to be excited through proton hopping (Miller et al. [1997]):

$$H_3^+ + H_2^* \rightarrow H_2 + H_3^{+*} \tag{3.1}$$

where * denotes an excited molecular state. The fraction of H_2 particles with sufficient kinetic energy to excite H_3^+ to $\nu_2 = 1$ are governed by the familiar thermal Boltzmann distribution (assuming LTE). At 1000 K the fraction is:

$$\frac{N_{H_2}(E > E_{\nu_2=1})}{N_{H_2}} = \exp\left(-\frac{E_{\nu_2=1}}{kT}\right) = \exp\left(-\frac{100 \times 2616.6hc}{k \times 1000}\right) = 0.02 \tag{3.2}$$

where $N_{H_2}(E > E_{\nu_2=1})$ is the number of H_2 molecules capable of exciting H_3^+ to the $\nu_2 = 1$ level, N_{H_2} is the total number of excited molecules, $E_{\nu_2=1}$ is the energy of the $\nu_2 = 1$ level (given in Table 3.4) and T is the temperature. The factor of 100 converts the units of the upper energy level from cm^{-1} to m^{-1}. Assuming a proton hopping rate of 2×10^{-15} $\mathrm{m^3s^{-1}}$ (Theard and Huntress [1974]) and an H_2 density of $\sim 10^{19}$ m^{-3} at the H_3^+ peak (Grodent et al. [2001], see Figure 3.2 in this thesis) – the collisional population time, τ_c, for the ν_2 level becomes:

$$\tau_c = \frac{1}{0.02 \times 2 \times 10^{-15} \times 10^{19}} = \frac{1}{400} = 2.5 \times 10^{-3} \text{ seconds} \tag{3.3}$$

This is only about a third of the radiation lifetime of 8 ms, which indicates that the ν_2 level may be depopulated faster than it is being populated, which results in the level being underpopulated. This was noted by Kim et al. [1992], who analysed the statistical equilibrium of the vibrationally excited levels of H_3^+ in the auroral region on Jupiter. They concluded that this would lead to an overpopulation of the ground state of about 10, although the relative population of vibrational manifolds might still be in LTE proportion. They included the effect of near-resonance of the $H_3^+(\nu_2 = 2)$ and H ($\nu = 1$) which would produce an overpopulation of the $H_3^+(\nu_2 = 2)$ compared to a simple collisional/radiative detailed balance calculation. However, Stallard et al. [2002] found no observational evidence for this effect.

3.1.3 Quasi local thermodynamic equilibrium

As discussed in the above section, one can not safely assume that the jovian upper atmosphere is in Local Thermodynamic Equilibrium. To combat this uncertainty, Miller et al. [1990] suggested that a gas could be in a state of quasi-LTE in which vibrational levels might have a 'sub-thermal' population with respect to the ground state but are populated at an LTE ratio *with respect to each other.* If this indeed was the case then physical parameters such as temperature and H_3^+ density could be determined using the LTE assumption.

The majority of the spectroscopic studies observing H_3^+ in the upper atmospheres of the giant planets have made use of ratios of lines in the ν_2 fundamental manifold to determine column-averaged temperatures and densities. These lines are observed in the L$'$ infrared window at around 4 μm. The concept of quasi-LTE works fairly well for the calculation of *total* H_3^+ emission (E(H_3^+) – see Section 2.4.4) since:

1. Whilst vibrational levels might not be fully thermalised, we do expect to find almost full thermalisation within any given vibrational manifold. This is because H_3^+ lacks a permanent dipole making radiative transitions with only a change in rotational state extremely slow ($\sim 10^4$ seconds), leaving plenty of time for collisional thermalisation (McCall [2000]).

2. The lack of a permanent dipole moment also has the effect that the ground state does not radiate via pure rotational transitions. Hence, only transitions

involving vibrationally excited levels are important when calculating the total emission of H_3^+.

3. Typical thermospheric temperatures on Jupiter tend to be ~1,000 K. At these temperatures the ν_2 manifold is responsible for $\sim 90\%$ of the infrared emission from H_3^+, if the excited states are populated according to, or close to, LTE (Miller et al. [1990]). As it turns out, this percentage is likely to increase in conditions of non-LTE, since the ν_2 level is effected less by these effects than, say, the $2\nu_2$ level (see the following sections).

3.2 The Grodent et al. [2001] model

Grodent et al. [2001] developed a one-dimensional self-consistent model of the auroral region of Jupiter. They investigated the coupling between the energy deposited by auroral electron precipitation, thermospheric temperature and composition structure. The model combines a two stream (up and down) electron transport model detailing the balance between heating by particle precipitation (electrons in this case) and cooling by CH_4, C_2H_2 and H_3^+ (as detailed in Waite et al. [1997]).

The model of Grodent et al. [2001] takes account of non-LTE effects by quenching the intensity of H_3^+, and thus the cooling properties of the ion. It assumes that all levels of H_3^+ are effected to the same extent. In this chapter the non-LTE effect on each vibrational level will be analysed in order to explain observational properties of the H_3^+ emission.

Grodent et al. [2001] consider two 'flavours' of aurora, firstly that of a 'discrete' aurora, corresponding to the bright discrete arc observed in the morning sectors at high latitudes on the northern jovian hemisphere. Secondly, the 'diffuse' aurora - corresponding to the diffuse, unstructured aurora observed in the polar cap and in the afternoon sectors, as illustrated in Figure 3.3. Throughout this thesis only the profiles associated with the discrete aurora are considered since this region is easy to distinguish with high resolution spectrographs available on modern telescopes. It is also the region which exhibits the brightest H_3^+ intensity, thus providing observations with large signal-to-noise ratios (SNR). This is important when determining the temperature from a ratio between weak lines.

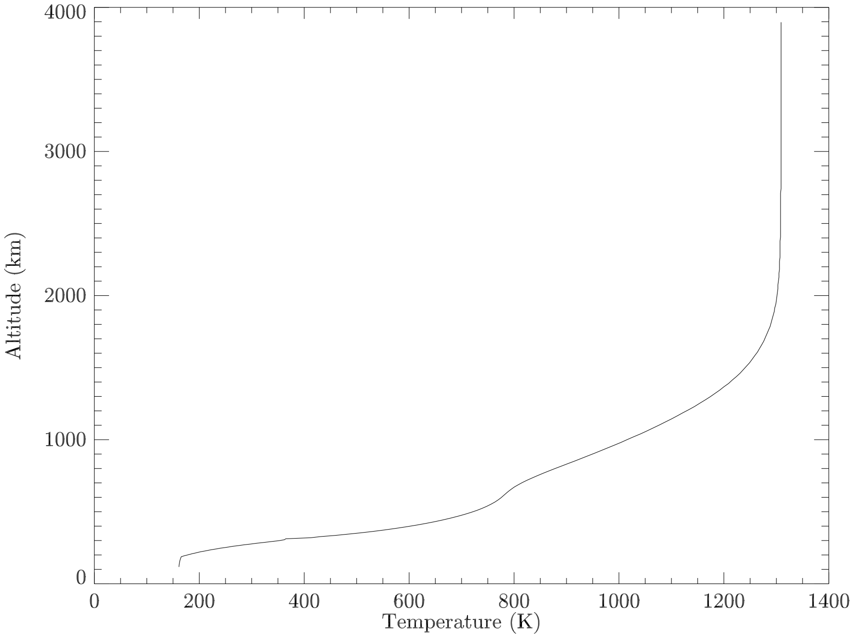

Figure 3.1: Temperature, T_i, versus altitude, h_i, from Grodent et al. [2001]. The zero altitude is defined as the 1 bar level in the jovian atmosphere.

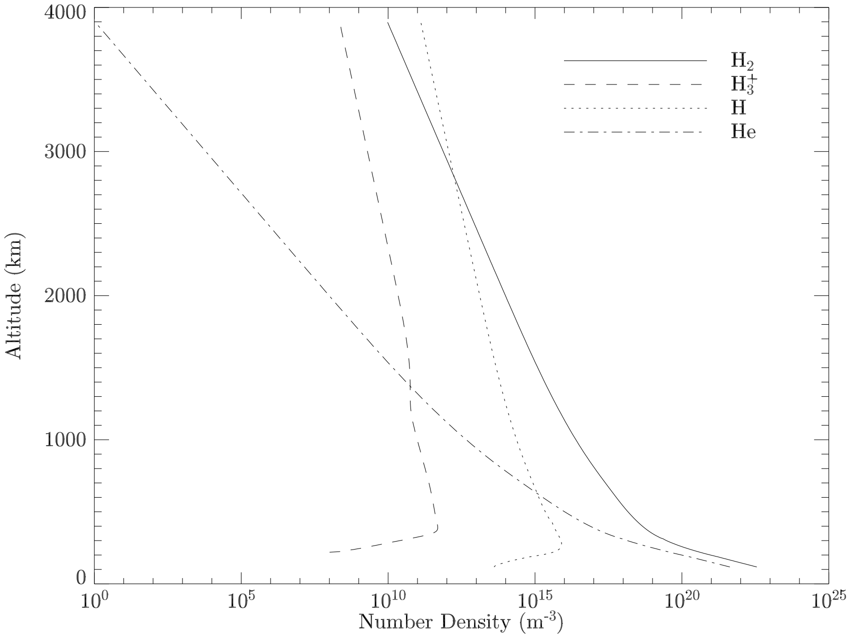

Figure 3.2: Number density versus altitude plots for H, H_2, H_3^+ and He. The zero altitude is defined as the 1 bar level in the atmosphere.

It is of note that the differences between the temperature and density profiles for the discrete and the diffuse aurora are small and swapping discrete for diffuse would not make much of a difference in the analysis in this chapter.

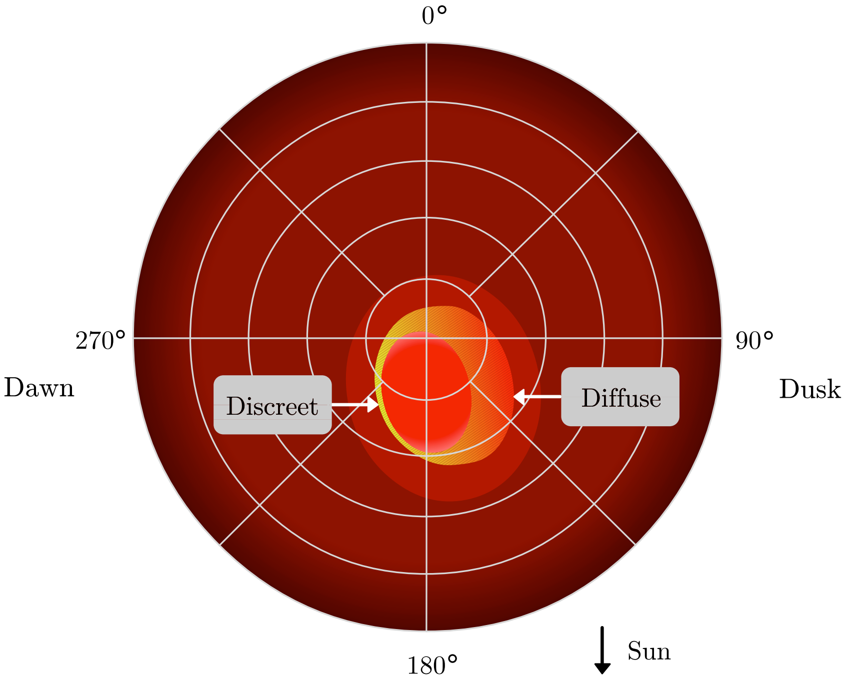

Figure 3.3: Schematic diagram showing the morphology of the jovian H_3^+ aurora as seen from above the north pole (after illustration by Satoh et al. [1996]). Lighter colours indicate higher auroral H_3^+ intensities.

In the Grodent et al. [2001] model, the energy of the precipitating electrons are constrained to reproduce the results of a number of temperature and density observations, covering multiple spectral regions. Since emission from Jupiter is known to be time-variable over short timescales (Stallard [2000]), and since the aurora also displays significant spatial variability (e.g. Stallard [2000] and Morioka et al. [2004]), care must be taken to distinguish the differences between conditions in which measurements were made. The fact that the energetics governing the thermosphere/ionosphere system on Jupiter are poorly understood can make this distinction a difficult one to make. The initial temperature profile of Grodent et al. [2001] is the descent measurements of the Galileo probe taken at a latitude of 6.5° N (Seiff et al. [1997]).

The discrete aurora has an incoming electron flux represented by a triple Maxwellian distribution described by:

$$\phi(E) = k_1\phi_1 \frac{E}{E_1} e^{-E/E_1} + k_2\phi_2 \frac{E}{E_2} e^{-E/E_2} + k_3\phi_3 \frac{E}{E_3} e^{-E/E_3} \tag{3.4}$$

where E_i (where i=1, 2 and 3) is the peak energy of the distribution, ϕ_i is the energy flux and k$_i$ is a normalisation constant. For the discrete aurora: $\phi_1 = 100$ erg cm^{-2} s^{-1}, $E_1 = 22$ keV, $\phi_2 = 10$ erg cm^{-2} s^{-1}, $E_2 = 3$ keV, $\phi_3 = 0.5$ erg cm^{-2} s^{-1}, $E_3 = 0.1$ keV (using the units given in Grodent et al. [2001]). The resulting neutral temperature profile can be seen in Figure 3.1. It shows a steadily increasing temperature up to an altitude of about 1,800 km, which then remains at a constant temperature up through the atmosphere of about 1,300 K. The density versus altitude plots for H, H_2, H_3^+ and He can be seen in Figure 3.2. The H_3^+ density peak occurs at about ∼400 km, where the temperature is ∼600 K. However, H_3^+ falls off relatively slowly in the atmosphere, having about 20% of its peak density at an altitude of 1,000 km. Up to 3,000 km the dominant species is H_2.

The model of Grodent et al. [2001] is a 1D electron precipitation degradation model that aims to match the thermally equilibrated profiles to fit a number of temperature and density measurements derived from both infrared and ultraviolet observations. This means that there are energy inputs missing, such as Joule heating, ion-drag and horizontal winds. This lack of energy sources is compensated for by a larger flux of precipitating particles, enabling the model to equilibrate at observed temperatures.

There are several other models of the jovian upper atmosphere including three dimensional global circulation models such as JIM (Achilleos et al. [1998a]) and JTGCM (Bougher et al. [2005]). These have the benefit of including the effects of Joule heating, ion-drag and meridional winds and horizontal diffusion. JIM (which is available at APL) is *fed* an assumed thermal profile since it does not have sufficient mechanisms to produce the large observed temperatures. This means that the model is not fully thermally equilibrated. In addition, the model is numerically unstable; see Williams [2004] for a detailed discussion of stability issues in JIM. What JIM can be used for is the analysis of auroral dynamics and the transport of energy, which doesn't require long timescales, but do require a fully coupled 3D ionosphere/thermosphere model.

Using the discrete temperature and density profiles of Grodent et al. [2001] the intensities of the two lines observed by Stallard et al. [2002] were modelled as a function of altitude. The ratio between the height-integrated intensities of these two lines gives a temperature of 930 K, which is in good agreement with observations.

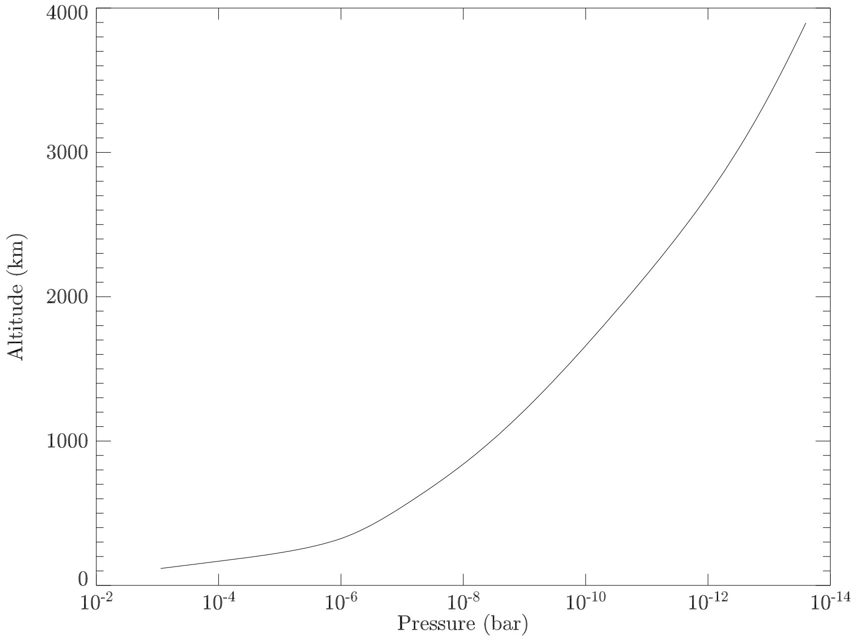

Figure 3.4: Pressure as a function of altitude for the *discrete* aurora of Grodent et al. [2001].

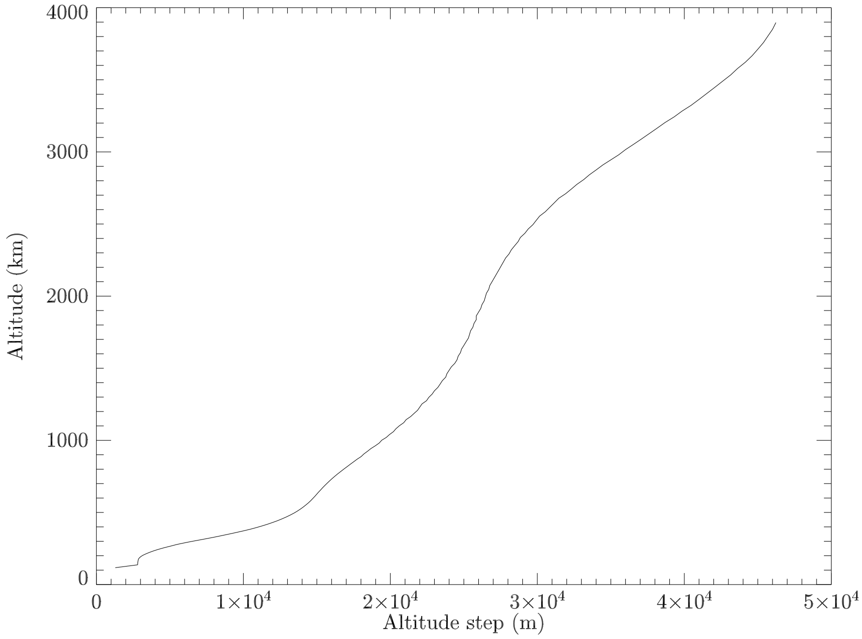

Figure 3.5: The height of each model step throughout the jovian atmosphere in the Grodent et al. [2001] model.

3.2.1 Results from Grodent et al. [2001]

The model of Grodent et al. [2001] shows that H_3^+ plays a crucial role in the thermosphere as a coolant, regulating the net heating. This result is confirmed by the exo-planet model of Williams [2004], whereby a Jupiter-like planet at distance of 0.1 AU does not loose its upper atmosphere thanks to the cooling properties of H_3^+ which is created in vast quantities at such distances.

The precipitating electron energy distribution is detailed in Section 3.2. Grodent et al. [2001] shows that the 22 keV component heats the atmosphere between 10^{-4} and 10^{-6} bar and the 3 keV component heats the region directly above the homopause at 10^{-6} to 10^{-9} bar. This means that most of the 22 keV heating is absorbed and re-radiated to space by hydrocarbons below the homopause. It is the 3keV energy component that has the largest effect on H_2 and H_3^+ temperatures. The very lowest energy component of the electron flux (0.1 keV) controls the exospheric temperature. As a consequence of this, the H_3^+ thermal emission is more responsive to changes in the softer part of the electron energy distribution than the highly energetic one. Grodent et al. [2001] suggested that the study of H_3^+ emission might not be suitable for tracking *total* energy inputs into the upper atmosphere. However, work done by Millward et al. [2002] using JIM suggested, on contrary, that H_3^+ is indeed a good 'tracer' of the energy inputs. This difference arises from the differences between a one-dimensional electron degradation model and JIM, which results in higher energy electrons ($\sim$ 60 keV) depositing the bulk of their energy *above* the homopause.

The inability of the high energy component to heat the region surrounding the homopause does, according to Grodent et al. [2001], indicate that there is an additional significant stratospheric heat source. The hydrocarbons are very efficient heat sinks since they have a temperature-dependent thermal emission and have high densities at, and around, the homopause (Drossart et al. [1993]). In Section 3.5, the energy inputs and outputs available to the upper atmosphere of Jupiter will be discussed in more detail.

3.2.2 The Grodent et al. [2001] data

The output model run of Grodent et al. [2001] was obtained for the discrete aurora. The supplied parameters can be seen in Table 3.1. For instance, the H_3^+ density per

Parameter	Symbol	Units
Temperature	T_i	K
Altitude	h_i	m
Pressure	P_i	bar
H density	$\delta_i[\mathrm{H}]$	m^{-3}
H_2 density	$\delta_i[\mathrm{H}_2]$	m^{-3}
H_3^+ density	$\delta_i[\mathrm{H}_3^+]$	m^{-3}
He density	$\delta_i[\mathrm{He}]$	m^{-3}
CH_4 density	$\delta_i[\mathrm{CH}_4]$	m^{-3}
C_2H_2 density	$\delta_i[\mathrm{C}_2\mathrm{H}_2]$	m^{-3}

Table 3.1: The parameters supplied from the Grodent et al. [2001] model.

unit volume (m^{-3}) at model level i is given by $\delta_i[\mathrm{H}_3^+]$ such that the height-integrated column density is given by:

$$N[\mathrm{H}_3^+] = \sum_i \delta_i[\mathrm{H}_3^+] H_i \tag{3.5}$$

where H_i is the height, in meters, of each model level i. H_i is given by:

$$H_i = h_{i+1} - h_i \tag{3.6}$$

such that the height of level i is given by the difference between the height of level $i+1$ and i. The very top altitude step is assumed to have the height of the step below it. The height of each altitude step, H_i, as a function of altitude can be seen in Figure 3.5. There are 200 altitude levels in the model.

3.3 The Oka and Epp [2004] non-LTE H_3^+ model

The recent model of Oka and Epp [2004] devised a new formulation for the detailed balance calculation for a mixture of H_3^+ in H_2. The H_3^+ energy levels are populated by collisions and are depopulated both by spontaneous emission and collisions. The paper deals with rotational levels, which are observed in the interstellar medium (e.g. Goto et al. [2002]) but the approach is readily adaptable for modelling the populations of the vibrational states observed on Jupiter (e.g. Stallard et al. [2002] and Raynaud et al. [2004]). Here, we shall apply the formulation of Oka and Epp [2004] to H_3^+ vibrational-only states.

Assuming an initial vibrational distribution in LTE, the principle of detailed balance is the explicit calculation of the rates of individual population and de-population processes within a parcel of gas. These calculations are performed for a large number of time-steps until there is a balance between the assumed population and de-population mechanisms.

Radiative process

Oka and Epp [2004] argue that since the background radiative temperature is much less than the vast majority of emission frequencies (in terms of energy), absorption and induced emission can be ignored. This assumption is also true in the upper atmosphere of Jupiter where H_3^+ is believed to be excited mainly through collisions, and the effects of self-absorption are believed to be negligible. Thus, the only radiative process being considered is spontaneous emission. The rate of spontaneous emission of H_3^+ comes from the ab-inito calculations of Dinelli et al. [1992] and follows very rigorous selection rules.

Collisional process

Since H_3^+ has a charge we expect it to behave radically differently from neutral molecules such as H_2. This is because charged particles have cross sections governed by the r^{-4} Langevin potential instead of the weaker r^{-6} van der Waals potential (r is the distance from the barycentre of the molecule). Strong collisions such as:

$$H_3^+ + H_2 \rightarrow (H_5^+)^* \rightarrow H_3^+ + H_2 \tag{3.7}$$

tend to have *very* loose selection rules (Oka [1973]). This prompted Oka and Epp [2004] to adopt the assumption of ‘complete randomness’, which is to treat collisional transition as not having any selection rules whatsoever. In reality, these transitions still have to adhere to some nuclear spin rules, but these are ignored in this formulation. We are left with one single guiding principle – the principle of detailed balancing, which can be formulated as:

$$\frac{k_{a\rightarrow b}}{k_{b\rightarrow a}} = \frac{g_b}{g_a} \exp\left(-\frac{E_b - E_a}{kT}\right) \tag{3.8}$$

where $k_{a\rightarrow b}$ is the rate constant for the collisional transition from level a to b, T is the temperature and g_a and E_a are the statistical weight and energy level a respectively. Adapting the assumption of complete randomness, Equation 3.8 becomes:

$$k_{a\rightarrow b} = C_{a\rightarrow b}\sqrt{\frac{g_b}{g_a}}\exp\left(-\frac{E_b - E_a}{2kT}\right) \tag{3.9}$$

where

$$C_{a\rightarrow b} = C_{b\rightarrow a} = C\left[1 + \sum_c \left(\frac{g_c}{\sqrt{g_b g_a}}\right)^{\frac{1}{2}} \exp\left(-\frac{E_c - 0.5(E_b + E_a)}{2kT}\right)\right]^{-1} \tag{3.10}$$

where C is the Langevin rate constant, which is independent for all the transitions a, b and c. The value of this constant is taken to be $C = 2 \times 10^{-15}$ m^{3}s^{-1} (Theard and Huntress [1974]). The expression within the square bracket is a normalisation factor that keeps Equation 3.8 consistent.

Deriving non-LTE populations

In a steady state scenario, the change in population over time dt is given by:

$$\frac{dn_b}{dt} = \sum_a \left[A_{a\rightarrow b}N_a - A_{b\rightarrow a}N_b\right] + \sum_a \left[k_{a\rightarrow b}N_a - k_{b\rightarrow a}N_b\right] N_{H_2} = 0 \tag{3.11}$$

where $A_{a\rightarrow b}$ is the Einstein A coefficient for spontaneous emission between level a and b and N_a is the number density of level a. The first term on the right hand side requires that $E_b > E_a$ while the second term requires that $E_a > E_b$. Equation 3.11 has two variables: the H_2 number density, N_{H_2}, and the temperature, T, which is used in finding the k terms (Equation 3.8 and 3.9). The fraction of an original LTE population that is still present in conditions of non-LTE is calculated by solving Equation 3.11 for a large number of time-steps until dn_b/dt is very small.

Accuracy of Oka and Epp [2004] model

The validity of the non-LTE model of Oka and Epp [2004] relies on three assumptions:

1. The validity of the steady state assumption.

2. The correctness of the Einstein A coefficients. The coefficients used in this thesis

are listed in Table 3.2 – taken from Dinelli et al. [1992].

3. The collisional rate constants are given in Equation 3.9. This is the same as relying on the assumption of complete randomness in determining which levels are populated through collisional excitation.

The first point was justified by the molecular lifetime being orders of magnitude longer than the radiation lifetime. It was seen in Section 3.1.2 that this is also true for the upper atmosphere of Jupiter. Oka and Epp [2004] estimate the error introduced by this assumption to be of the order of a few percent of the population calculated for each level. The lines listed in Dinelli et al. [1992] are known to be accurate through both astronomical and laboratory observations of H_3^+. Consequently, the major source of inaccuracy of this model is the assumption of complete randomness. However, until more detailed quantum mechanical calculations of individual collision rates become available, this is, at present, a valid approximation.

3.3.1 Modelling non-LTE effects on H_3^+ on Jupiter

The effects of lifting the requirement of LTE on the H_3^+ emission will be investigated by combining the principle of detailed balance formulation due to Oka and Epp [2004] and the jovian atmospheric model of Grodent et al. [2001]. Each level in the Grodent et al. [2001] model has an associated thermospheric neutral temperature and an H_2 density. Using these two parameters, the fraction of the H_3^+ LTE population present in conditions of non-LTE is calculated through an iterative process, as set out in Section 3.3.

The initial H_3^+ population of the model is the LTE distribution of Grodent et al. [2001]. Then, iterating through small time-steps ($\sim 10^{-9}$ seconds), the population is calculated as described in Section 3.3. The size of time-steps are scaled as the number density at each altitude level such that:

$$\Delta t_i = \Delta t_0 \left(\frac{\delta_0[\mathrm{H}_2]}{\delta_i[\mathrm{H}_2]} \right)^{\frac{1}{2}} \tag{3.12}$$

where Δt_n is the time-step at altitude level i and $\delta_0[\mathrm{H}_2]$ is the H_2 density at reference level 0 with a pre-defined timescale of Δt_0. The density at level i is $\delta_i[\mathrm{H}_2]$. When applied to Grodent et al. [2001] these values are $\Delta t_0 = 10^{-10}$ seconds and $\delta_0[\mathrm{H}_2] =$

Nbr	E (cm^{-1})	1	2	3	4	5	6	7	8	9	10	11	12	13	14	15
1	0.0	-	-	-	-	-	-	-	-	-	-	-	-	-	-	-
2	2521.3	128.8	-	-	-	-	-	-	-	-	-	-	-	-	-	-
3	3178.4	-	0.9	-	-	-	-	-	-	-	-	-	-	-	-	-
4	4777.0	-	139.2	-	-	-	-	-	-	-	-	-	-	-	-	-
5	4997.4	144.6	256.0	0.2	< 0.1	-	-	-	-	-	-	-	-	-	-	-
6	5553.7	0.4	16.5	127.4	0.6	0.5	-	-	-	-	-	-	-	-	-	-
7	6262.0	-	0.2	-	-	0.1	2.3	-	-	-	-	-	-	-	-	-
8	7003.5	15.7	133.1	0.5	85.5	35.1	35.1	-	-	-	-	-	-	-	-	-
9	7282.5	-	242.2	-	-	232.6	0.5	-	0.1	-	-	-	-	-	-	-
10	7492.6	-	476.5	-	-	468.2	0.9	-	< 0.1	-	-	-	-	-	-	-
11	7769.1	-	74.1	-	-	108.5	179.3	-	1.3	-	-	-	-	-	-	-
12	7868.7	14.4	0.1	119.5	20.1	2.8	2.8	0.6	0.7	0.4	0.1	-	-	-	-	-
13	8487.0	1.5	3.0	< 0.1	0.5	1.0	1.0	123.5	0.1	0.2	-	1.1	1.5	-	-	-
14	8996.6	-	65.9	-	-	273.2	1.8	-	136.9	-	-	-	0.5	0.5	-	-
15	9107.6	6.8	35.5	2.1	252.1	12.4	12.4	< 0.1	135.8	21.5	0.3	0.9	< 0.1	< 0.1	-	-
16	9251.5	-	0.5	-	-	0.8	1.4	-	< 0.1	-	-	-	< 0.1	< 0.1	-	-
17	9650.6	0.3	0.8	6.4	122.6	340.0	340.0	0.3	96.7	138.2	106.6	16.3	2.8	0.3	0.1	0.3

Table 3.2: The Einstein A coefficients of the vibrational H_3^+ transitions used to calculate the non-LTE population of the model atmosphere of Grodent et al. [2001]. The Einstein A coefficients come from Dinelli et al. [1992]. The numbers labelling the rows and columns are the vibrational levels listed in Table 3.3.

Nbr	(ν_1, ν_2^l)	E (cm^{-1})
1	(0, 0^0)	0.0
2	(0, 1^1)	2521.3
3	(1, 0^0)	3178.4
4	(0, 2^0)	4777.0
5	(0, 2^2)	4997.4
6	(1, 1^1)	5553.7
7	(2, 0^0)	6262.0
8	(0, 3^1)	7003.5
9	(0, 3^3)	7282.5
10	(0, 3^3)	7492.6
11	(1, 2^0)	7769.1
12	(1, 2^2)	7868.7
13	(2, 1^1)	8487.0
14	(0, 4^0)	8996.6
15	(0, 4^2)	9107.6
16	(3, 0^0)	9251.5
17	(0, 4^4)	9650.6

Table 3.3: The H_3^+ pure vibrational levels included in the non-LTE analysis of Jupiter's upper atmosphere.

10^{20} m^{-3}. For each altitude level, 500,000 time-steps were used.

The collisional excitation and de-excitation rates are equal according to the principle of detailed balancing and are taken to be equal to the Langevin rate for proton hopping: 2×10^{-15} m^{3}s^{-1} (Theard and Huntress [1974]).

Included in the calculations were the 17 lowest vibrational levels of H_3^+, up to $4\nu_2$ originating at 9650.6 cm^{-1}, as given in Dinelli et al. [1992]. The transitions included in the model are listed in Table 3.2 with their associated Einstein A coefficients. The vibrational levels are defined in Table 3.3.

The output of this model is the fraction of the LTE population of H_3^+ that would be present in non-LTE conditions for each of the altitude levels in the model of Grodent et al. [2001]. Let F_i be the fraction at model level i for a particular vibrational level. This parameter can be seen in Figure 3.6. Note that this plot only shows the ν_2 vibrational levels; the ν_1 transitions are, however, included in the detailed balance calculation.

The fraction of the LTE population present in conditions of non-LTE can be seen in Figure 3.6. Any non-LTE effects start being noticed at an altitude of about 800 km, and at 2,500 km all of the pure ν_2 vibrational levels are completely depopulated.

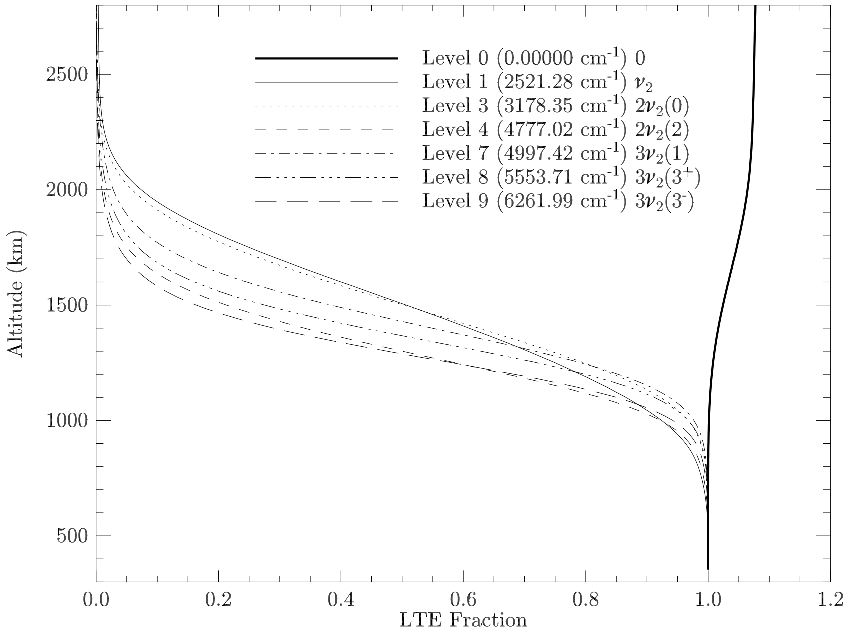

Figure 3.6: Plot showing the fraction the LTE population of pure ν_2 vibrational manifolds present under non-LTE conditions.

The ground (0) state becomes slightly over-populated because of the depopulation of the excited states. Note that different ν_2 levels depopulate at different rates and reach a complete depopulation at different altitudes.

It is apparent from Figure 3.6 that any non-LTE effects are important at high altitudes in the jovian atmosphere (h_i > 2,500 km above the 10 mbar level). If H_3^+ is not being excited it looses its very important role as a coolant and, as the ν_2 levels depopulate, we would expect the atmosphere to heat up. This, in turn, would feed back into both the results of Grodent et al. [2001] and the detailed balance calculations. It is important to understand that this treatment is a first iteration and as such a first approximation to the behavior of the jovian upper atmosphere in conditions of non-LTE.

3.4 H_3^+ volume emission profiles

Understanding from what altitudes in the jovian upper atmosphere the H_3^+ emission is produced is instrumental in putting the fitted parameters of a spectrum into a global context. If the emission is from high up in the atmosphere, near the exosphere, then a low density, high temperature environment is sampled. On the other hand, if

Parameter	$\nu_2 \rightarrow 0$	$2\nu_2 \rightarrow \nu_2$
Upper energy level (E')	2616.6 cm^{-1}	5250.2 cm^{-1}
Einstein A coefficient (A_{if})	129 s^{-1}	66 s^{-1}
Nuclear spin weighting (g_{ns})	4	2
Angular momentum quantum nbr (J)	1	4
Transition frequency (ω_{if})	2529.6 cm^{-1}	2532.3 cm^{-1}

Table 3.4: Transition parameters for the H_3^+ lines observed by Stallard et al. [2002]: the fundamental Q(1, 0^-) $\nu_2 \rightarrow 0$ and the hotband R(3, 4^+) $2\nu_2 \rightarrow \nu_2$.

Parameter	$2\nu_2(2) \rightarrow 0$	$3\nu_2(3) \rightarrow \nu_2$
Upper energy level (E')	4777.2 cm^{-1}	4750.0 cm^{-1}
Einstein A coefficient (A_{if})	151 s^{-1}	347 s^{-1}
Nuclear spin weighting (g_{ns})	2	4
Angular momentum quantum nbr (J)	2	6
Transition frequency (ω_{if})	5266.3 cm^{-1}	7790.0 cm^{-1}

Table 3.5: Transition parameters for the H_3^+ lines observed by Raynaud et al. [2004]: the overtone R(6, 6^+) $2\nu_2(2) \rightarrow 0$ and the hot overtone R(5,6^+) $3\nu_2(3) \rightarrow \nu_2$.

the emission originates from close to the homopause, a high density, low temperature environment is observed (e.g. Drossart et al. [1993]).

Using the profiles of Grodent et al. [2001], the volume H_3^+ emission of a given transition can be modelled as a function of altitude for both LTE and non-LTE conditions.

3.4.1 Calculating the intensity profiles

Under conditions of Local Thermal Equilibrium, the intensity, $I_i(T_i)$, at each Grodent et al. [2001] model level i, at temperature T_i, is given by (in units of Wm^{-3}str^{-1}):

$$I_i(T_i) = \delta_i[H_3^+] \times \frac{g_{ns}(2J+1)100hc\omega A_{if}}{4\pi Q(T_i)} \exp\left(\frac{-100hcE}{kT_i}\right) \tag{3.13}$$

where

$$\frac{100hc}{k} = 1.439 \tag{3.14}$$

when E is in units of cm^{-1} and the factor of 100 converts cm^{-1} to m^{-1}. Using the results from Section 3.3.1 it is now possible to determine how the volume-intensity profile would alter if the LTE assumption broke down. We know the fraction of the LTE population present in conditions of non-LTE, F_i, for any particular vibrational level at model level i. The intensity at each model level then becomes:

$$I_i(T_i) = F_i \times \delta_i[\mathrm{H}_3^+] \times \frac{g_{ns}(2J+1)100hc\omega A_{if}}{4\pi Q(T_i)} \exp\left(\frac{-1.439E}{T_i}\right) \tag{3.15}$$

Specific for every transition is F_i, g_ns, J, A_if, ω and E. The transition data for the H_3^+ spectral lines observed by Stallard et al. [2002] and Raynaud et al. [2004] are given in Table 3.4 and Table 3.5. The non-LTE population attenuation parameter, F_i, for each of these lines are defined by the upper level, as given in these tables. E.g. for the Stallard et al. [2002] the levels are $2\nu_2(2)$ and $3\nu_2(3)$ are written in Table 3.3 as $(0, 2^2)$ and $(0, 3^3)$ respectively.

The volume intensity profiles for the four lines can be seen in Figures 3.7, 3.8, 3.9 and 3.10.

3.4.2 Discussion

The first feature of note in the volume intensity plots in Figures 3.7, 3.8, 3.9 and 3.10 is that H_3^+ emission is produced over a wide range of altitudes, from the density peak at around 500 km, to about 3,000 km for the LTE, and up to about 2,000 km for the non-LTE case. This would indicate, as might have been expected, that the single temperature thin shell approximation for the upper atmosphere is not valid. The transitions are formed at a wide range of altitudes sampling a wide range of temperatures and densities. This calls for a new way of analysing the auroral emission, preferably with a ionosphere/thermosphere atmospheric model, such as Grodent et al. [2001].

The intensity profiles in Figures 3.7 to 3.10 in more detail:

1. **Figure 3.7:** In LTE conditions, the fundamental $\nu_2 \rightarrow 0$ produces large intensities at low temperatures at around 500 km, with a second peak at around 1,700 km. This secondary peak is caused by a slight density fluctuation in conjunction with sharply increasing temperature (see Figures 3.1 and 3.2). Under non-LTE conditions, the intensity at lower altitudes is, for most parts, preserved but the secondary intensity peak is removed as ν_2 moves to depopulate completely at around 2,000 km.

2. **Figure 3.8:** In LTE conditions, this transition has an intensity peak at 1,700 km

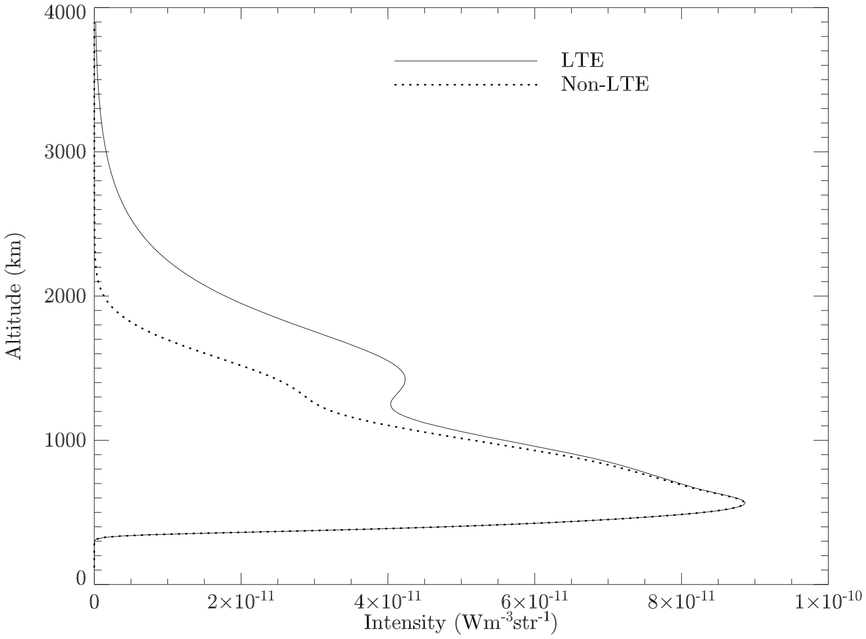

Figure 3.7: Intensity versus altitude profile for the H_3^+ fundamental $Q(1,0^-)$ $\nu_2 \rightarrow 0$ transition.

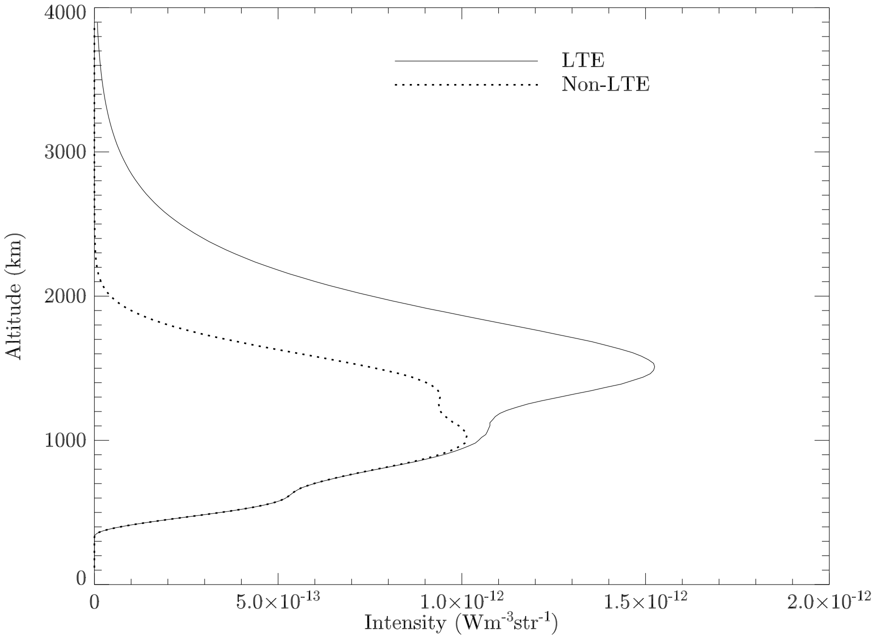

Figure 3.8: Intensity versus altitude profile for the H_3^+ hotband $R(3, 4^+)$ $2\nu_2(0) \rightarrow \nu_2$ transition.

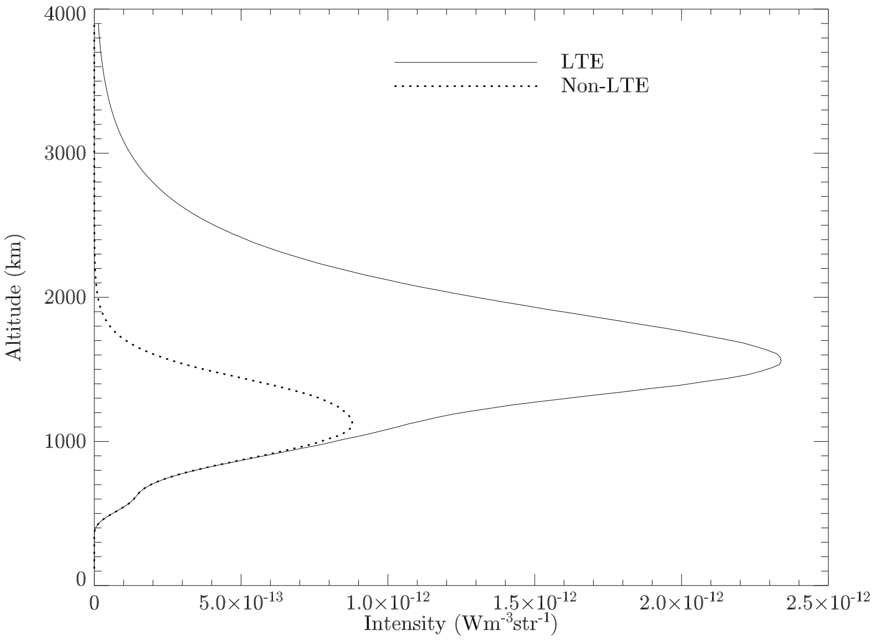

Figure 3.9: Intensity versus altitude profile for the H_3^+ overtone R(6, 6^+) $2\nu_2(2) \rightarrow 0$ transition.

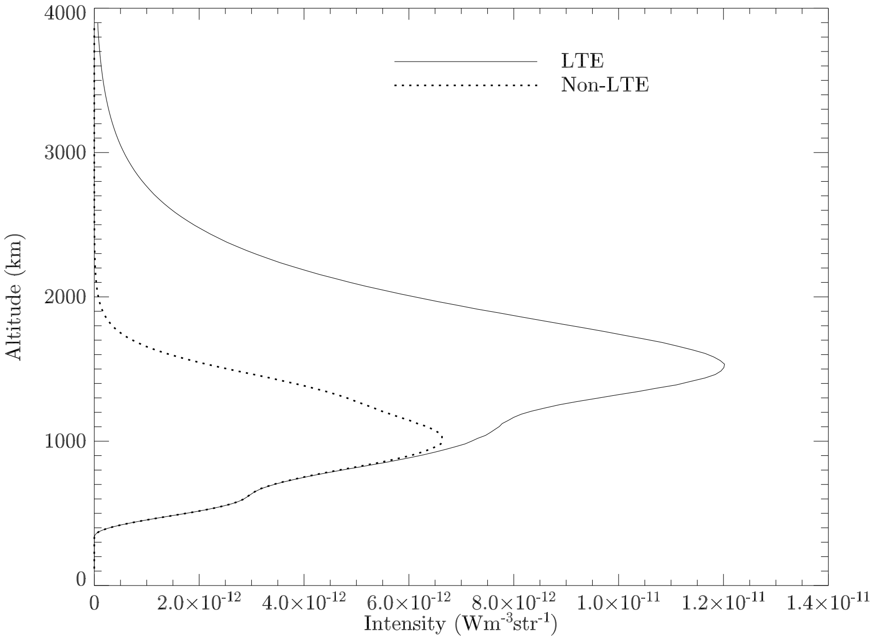

Figure 3.10: Intensity versus altitude profile for the H_3^+ hot overtone R(5, 6^+) $3\nu_2(3) \rightarrow \nu_2$ transition.

where the temperature is high enough to populate the $2\nu_2(0)$ level significantly. However, the distribution is very broad, with intensity being produced across a distance of some 2,000 km. Under non-LTE conditions, the peak is lowered to $\sim$ 1,000 km and the integrated intensity (i.e. the area under the graph) is significantly more reduced for R(3, 4^+) than for Q(1, 0^-). This means that both the temperature and column density will be underestimated when derived using the ratio of these lines. More physically, however, these two lines clearly sample different parts of the ionosphere in conditions of LTE, but when the LTE condition is relaxed, they are formed at similar altitudes.

3. **Figure 3.9:** This overtone line was the first H_3^+ transition to be observed from Jupiter (Drossart et al. [1989]). Under conditions of LTE it is formed over a large range of altitudes, similar to the Q(1, 0^-) line, peaking at an altitude of about 1,600 km. The intensity in conditions of non-LTE is severely reduced and the intensity peak is shifted down to around 1,000 km.

4. **Figure 3.10:** This is a hot overtone and is effected by non-LTE effects in a similar fashion to R(6, 6^-).

3.4.3 Comparing profiles with observations

Two groups have recently used high resolution spectra to examine the jovian northern aurora. Stallard et al. [2002] measured the Q(1, 0^-) $\nu_2 \rightarrow 0$ transition at 3.953 μm. Raynaud et al. [2004] recorded the spectrum between 2 μm and 2.02 μm which included the transition R(6, 6^+) $2\nu_2 \rightarrow \nu_2$. At comparable temperatures, they found very different column densities – using non-LTE modelling we shall attempt to explain this effect. Two lines from each of these two studies were modelled in the previous section. Note that the published intensities of Stallard et al. [2002] are too small by a factor of $\sqrt{2\pi}$ (Stallard, personal communication).

Modelling the observed spectra

For each line within the observed regions (2 μm and 4 μm), its volume intensity profile was calculated as in Section 3.4.1. This profile was then integrated with altitude to give a total column intensity. This assumes that the H_3^+ emission is optically thin,

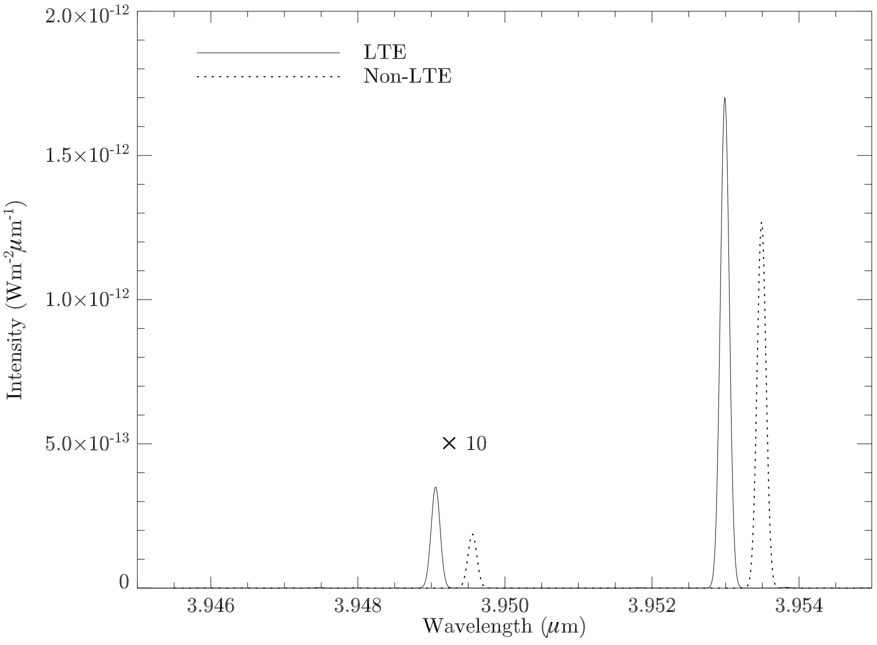

Figure 3.11: Modelled Stallard et al. [2002] spectrum. Note that the hotband, on the left, has been multiplied by a factor of 10 and that the non-LTE spectrum (dashed) has been shifted to higher wavelengths for ease of viewing.

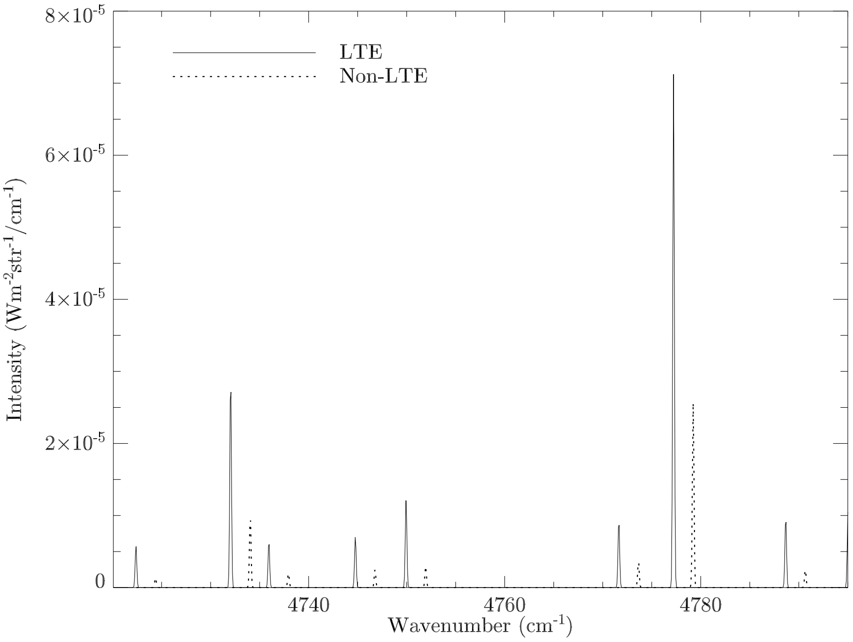

Figure 3.12: Modelled Raynaud et al. [2004] spectrum. Note that the non-LTE spectrum (dashed) has been shifted to higher wavenumbers for ease of viewing.

i.e. that light emitted from the bottom of the atmosphere is not absorbed, scattered or attenuated by the atmosphere above it (Lam et al. [1997a]; Miller et al. [1997]). This was done for both the LTE and the non-LTE scenario. The modelled spectrum covering the same region as observed by Stallard et al. [2002] can be seen in Figure 3.11. The modelled spectrum covering the region observed by Raynaud et al. [2004] can be seen in Figure 3.12. Note that, in both figures, the non-LTE spectrum is shifted to slightly higher wavelengths (or wavenumbers) for ease of viewing and that the hotband (at $\lambda = 3.949$ μm) line in Figure 3.11 has been multiplied by a factor of 10. The two modelled spectra are shown using the same intensity units as published by the respective authors.

In the modelled spectra shown in Figures 3.11 and 3.12, the under-population of the vibrationally excited states due to non-LTE effects led to a reduction in observed line intensities compared to the modelled LTE spectrum. In addition, different lines are affected more than others such that any temperature derived from line ratios will be different in the LTE treatment compared to the non-LTE treatment.

The effect on temperature derived from line ratios

Using the same technique it is possible to calculate what temperature the two emission models would produce.

The temperature, T, as a function of line ratio, is given by Stallard [2000] for the Q(1, 0^-) and R(3, 4^+) lines that they measured:

$$T = \frac{3783.3}{-0.2637 - \ln\left(\frac{I(R(3,4^+))}{I(Q(1,0^-))}\right)} \tag{3.16}$$

where $I(R(3,4^+))$ is the intensity of the hotband and $I(Q(1,0^-))$ is the intensity of the fundamental as observed by Stallard et al. [2002]. Note that this equation assumes conditions of LTE. Using the intensities of the modelled LTE and non-LTE spectrum seen in Figure 3.11, we can use this equation to calculate the temperature an observer would derive ratioing these lines. The temperature of the LTE spectrum is 1054 K whereas the temperature calculated for the non-LTE spectrum is 900 K. The temperature derived from the LTE spectrum is close to the maximum temperature derived by Stallard et al. [2002] of 1065 ± 15 K, whereas the non-LTE temperature is closer to the minimum temperature of 940 ± 15 K. Thus, the derivation of effective column temperatures using lines from different vibrational manifolds must be treated with caution: the under-population of vibrational levels tends to result in an underestimation of the column temperature. This has the additional effect of producing column densities that underestimate the true column of H_3^+.

Observational evidence for non-LTE effects on Jupiter

Raynaud et al. [2004] reported a line-of-sight corrected absolute flux of the R(6, 6^+) line of 1.4 μWm^{-2}str^{-1}. This is in agreement with the value of Drossart et al. [1989] of 1.6 μWm^{-2}str^{-1}. Stallard et al. [2002] found the Q(1, 0^-) line to have an absolute flux of 28.8 μWm^{-2}str^{-1}.

Table 3.6 shows the intensity ratio between the Q(1, 0^-) and the R(6, 6^+) lines for observed intensities, modelled LTE intensities, and modelled non-LTE intensities. The measured line intensity of Q(1, 0^-) is 26% of the calculated LTE strength and 35% of the non-LTE intensity. Similarly, the measured R(6, 6^+) intensity is 10% of the LTE intensity and 27% of the non-LTE intensity. For the LTE calculations these percentages are very different, well outside the uncertainty in the intensity. Assuming a 10% error on the intensity, the closest the non-LTE intensity would be is 23% and 11%. These values are seemingly incompatible.

However, the ratio between the observed intensity and the non-LTE modelled intensity are very similar, 27% and 35%. This close correspondence indicates that the two sets of measured line intensities are indeed compatible when taking non-LTE effects into account. This explains how two sets of intensities – one at 2 μm and at 4μm – which appear to be incompatible, when adopting the LTE single shell H_3^+ emission model, become compatible when analysed using non-LTE modelling. This is because high ν_2 levels are underpopulated, producing less intensity than they would at conditions of LTE.

The reason for the modelled non-LTE intensity being a factor of ∼3 stronger than both the observed intensities in the two wavelength reasons is discussed below.

	Q(1, 0^-) ($\mathrm{Wm^{-2}str^{-1}}$)	R(6, 6^+) ($\mathrm{Wm^{-2}str^{-1}}$)
I_o	2.9×10^{-5}	1.4×10^{-6}
I_{LTE}	1.1×10^{-4}	1.4×10^{-5}
I_{nLTE}	8.1×10^{-5}	5.1×10^{-6}
I_o/I_{LTE}	26 %	10 %
I_o/I_{nLTE}	35 %	27 %

Table 3.6: The observed intensity, I_o, the modelled LTE intensity, I_{LTE}, and the modelled non-LTE intensity, I_{nLTE}, for the Q(1, 0^-) and R(6, 6^+) H_3^+ transitions. Note that the observed intensities, I_o, are subject to an error of ± 10%.

The column density of H_3^+ in Grodent et al. [2001]

The precipitating energy of Grodent et al. [2001] is set as to reproduce a set of multi-spectral temperature measurements, originating from different altitudes in the atmosphere. The resulting H_3^+ density is large, 18×10^{16} $\mathrm{m^{-2}}$, and much higher than any empirical density determination of H_3^+ on Jupiter. This is explained by comparing the densities to those determined by Lam et al. [1997a], using CGS4 on UKIRT. Grodent et al. [2001] argue that the narrow auroral structure observed in the ultraviolet, is likely to be seen in the infrared. The observed Lam et al. [1997a] column density is averaged over a $3'' \times 3''$ slit, and Grodent et al. [2001] argued that a discrete auroral arc would only cover some 20% of that area. This would require the intensity, and therefore the column density, to be multiplied by a factor of 5 in order to get the response as if the entire pixel was filled with discrete auroral emission. This factor is known as the 'filling factor'.

The Grodent et al. [2001] model produces a column density of 18×10^{16} $\mathrm{m^{-2}}$. This gives an intensity of the Q(1, 0^-) line of $I_{nLTE} = 8.1 \times 10^{-5}$ $\mathrm{Wm^{-2}str^{-1}}$, which is about a factor of three larger than the intensity observed in the same line by Stallard et al. [2002] of $I_o = 2.9 \times 10^{-5}$ $\mathrm{Wm^{-2}str^{-1}}$ (including the factor of $\sqrt{2\pi}$ associated with the data). Similarly, for the R(6, 6^+) line, the observed intensity is $I_o = 1.4 \times 10^{-6}$ $\mathrm{Wm^{-2}str^{-1}}$, but the modelled non-LTE spectrum gives an intensity of $I_{nLTE} = 5.1 \times 10^{-5}$ $\mathrm{Wm^{-2}str^{-1}}$. Both these observations are ~ 30% of their modelled value, indicating that the H_3^+ density in the model is too large by about a factor of three.

Using the results from Section 3.4.3, it is possible to estimate the height integrated H_3^+ column density that may have been present when the two sets of observations were made. Taking into account that both observations have the same proportion – 1/3, of the intensity obtained through the non-LTE modelling – gives a column density of $\sim 6 \times 10^{16}$ m^{-2}. It is clear that the column density derived from the non-LTE model – based on the temperature and density profiles of Grodent et al. [2001] – is significantly greater than the one derived using the assumption that the H_3^+ originates from a thin shell in conditions of H_3^+.

Despite the large variability of H_3^+ known to occur in the auroral region of Jupiter the non-LTE analysis can explain why column densities deduced from a 2 μm spectra are consistently lower than those derived from 4 μm spectra. This is because levels such as the $2\nu_2$ vibrational level, observed at around 2μm, are depopulated to a greater extent than the ν_2 level at 4μm.

Obviously, the observations of Stallard et al. [2002] and Raynaud et al. [2004] are not simultaneous. Simultaneous high-resolution observations in both the K, L and L$'$ atmospheric window would be crucial in gaining further understanding of how non-LTE conditions effect the H_3^+ emissions, and the implications for the overall energy budget of the jovian ionosphere.

3.5 Analysing an auroral heating event

Using CHSELL (Greene et al. [1994]) on the NASA Infrared Telescope Facility (IRTF) Stallard et al. [2002] observed an auroral heating event between the 8th and 11th of September 1998. During this event the LTE temperature increased from 940 to 1065 K (both with an error of ±15 K), the column density rose from 6.2×10^{15} m^{-2} to 7.2×10^{15} m^{-2}, and the line-of-sight ion wind velocity in the direction opposite to planetary rotation due to the Hall conductivity rose from 0.5 kms^{-1} to 1.0 kms^{-1}. This wind is also known as the electro-jet (e.g. Achilleos et al. [2001]). Note that the published column density of Stallard et al. [2002] is too low by a factor of $\sqrt{2\pi}$ (Stallard, private communication), making the real values: 1.5×10^{16} m^{-2} to 1.8×10^{16} m^{-2}. Using the above non-LTE treatment of the jovian aurora, the energetics of this event will be examined in detail.

The main energy sources, energy loss mechanisms and the altitude at which these processes occur will be calculated using the profiles of Grodent et al. [2001] and the non-LTE treatment of the jovian upper atmosphere.

3.5.1 Overview of auroral region energetics

One of the most fundamental problems with giant planet ionospheres is that they are considerable hotter than what one would expect from just considering the energy of the solar radiation that the atmosphere absorbs. This is especially true at low-to-middle latitudes (Strobel and Smith [1973]; Yelle and Miller [2004]). The discovery of the aurora by Broadfoot et al. [1979] prompted a discussion of high rates of particle precipitation as a primary heating source (Waite et al. [1983]). The plasma flows measured by Voyager (Eviatar and Barbosa [1984]) hinted that the jovian ionosphere might be subject to currents, driven by the electric field, capable of producing large amounts of Joule heating. More recently, heating due to the breaking of gravity waves in the jovian upper atmosphere has been proposed (Young et al. [1997]). However, it is as of yet unclear if these waves actually heat (Young et al. [2005]); have little effect (Matcheva and Strobel [1999]); or even cool the upper atmosphere (Hickey et al. [2000]).

With reasonable suggestions for what could produce large amounts of energy, Waite et al. [1983] suggested that the heating itself would drive meridional (i.e. equator-ward) winds that would transport the energy down to lower latitudes. However, modern 3D general circulation models (GCMs) of Jupiter (e.g. Achilleos et al. [1998a] and Bougher et al. [2005]) have shown that the winds needs to be very strong – McGrath et al. [1989] required windspeeds of some 20 kms^{-1} to overcome the coriolis force. (This force tends to deflect winds traveling equator-ward, so that they remain fixed in latitude.) Yelle and Miller [2004] deemed such large windspeeds unfeasible.

Naturally, when considering the energy balance of the jovian upper atmosphere one must also take loss mechanism into account. Energy can be lost through downward conduction, losing energy to lower altitudes (e.g. Grodent et al. [2001]). Another important cooling mechanism is the thermal emission of the molecular ion H_3^+, denoted as $E(H_3^+)$ (e.g. Miller et al. [1994] and Section 2.4.4). At lower altitudes the radiative loss due to hydrocarbons become important (Drossart et al. [1993]). There is also the possibility of loosing energy to lower latitudes by mechanical means – meridional winds as modelled by global 3D circulation models (e.g. Achilleos et al. [1998a] and Bougher et al. [2005]).

The following treatment will analyse the energetics of the heating event observed by Stallard et al. [2002], assuming that some degree of scalability of the profiles of Grodent et al. [2001] is valid.

The processes that are going to be considered are:

1. The energy required to heat the upper atmosphere of Jupiter, based on the temperature increase using the modelled heat capacity.
2. The Joule heating and ion-drag, computed through the increase in ion velocities and modelled conductivities making use of the ion/neutral coupling coefficients.
3. The energy injected via particle precipitation required to produce the H_3^+ densities consistent with measured intensities. This process also gives rise to the Pedersen conductivity.
4. The energy lost to space through H_3^+ thermal emission (i.e. cooling).
5. The cooling due to the downward conduction of heat.
6. The cooling due to the thermal emission of hydrocarbons (CH_4 and C_2H_2).

Magnetosphere/ionosphere/thermosphere coupling

In considering the energy balance of Jupiter it is critical to consider how energy contained in the planet's giant magnetosphere is transferred into the upper atmosphere. Hill [1979] proposed that the upper atmosphere is coupled with the equatorial plasmasheet created by the ionisation of material ejected from Io during volcanic eruptions. The plasma co-rotates with the magnetosphere close to the planet, but further away corotation breaks down, since the corotation speed becomes very large at large distances from the planet. Since the magnetosphere is coupled to the ionosphere, a lag to corotation in the magnetosphere leads to a lag to corotation in the ionosphere, setting up currents (i.e. charged particles moving with respect to the neutrals). These currents, also known as the Hall currents, transfer energy to the neutrals via collisions, which is the process of Joule heating, or frictional heating (e.g. Waite et al. [1983]). There is also the transfer of bulk kinetic energy from the ions to the neutrals. This is known as ion-drag.

The magnetospheric current system also accelerates electrons from the plasmasheet, down the field lines, giving them very large kinetic energies (keV). When they strike the atmosphere they excite the gases within it. This gives rise to emission, which has been observed at wavelengths from the far ultraviolet to the far infrared, and is the brightest auroral emission seen in the solar system (Clarke et al. [1989]). This 'internal' mechanism is able to produce very large quantities of auroral particles, and by contrast, can produce many orders more emission than is observed on Earth, where auroral particles originate from the solar wind (i.e. an 'external' plasma source).

3.5.2 The Grodent number - N_G

Stallard et al. [2002] observed an increase in temperature from 940 to 1065 K (± 15 K) over three days. These temperatures were calculated using the intensity ratio of the H_3^+ R(3, 4^+) and Q(1, 0^-) lines, assuming a thin emitting shell of H_3^+ in conditions of LTE. The expression for the intensity ratio can be found in Stallard [2000] and is given by:

$$\frac{I_b}{I_a} = \gamma \exp\left(\frac{E_b - E_a}{kT}\right) \tag{3.17}$$

where

$$\gamma = \frac{g_a(2J_a+1)\omega_a A_a}{g_b(2J_b+1)\omega_b A_b} \tag{3.18}$$

where T is the temperature, k is Boltzmann's constant, and E is the upper energy level of the transition – the subscript a refers to parameters associated with the hotband R(3, 4^+) and b refers to the parameters associated with the fundamental Q(1, 0^-). The parameters in the expression for γ are defined in Table 3.4. Putting in the value for the temperatures published by Stallard et al. [2002], of 940 K and 1065 K gives an intensity ratio at the start of the event of 0.014 and at the end of the event of 0.022.

In order to associate these ratios with an atmospheric temperature profile, a scaling factor is defined: the Grodent number, N_G, such that $N_G = 1.0$ gives the discrete temperature profile of Grodent et al. [2001]. It is desirable to keep the temperature at the homopause constant at $T_0 = 161$ K since it is known to be fairly constant over time (e.g. Seiff et al. [1997] and Hubbard et al. [1995]). The reason for this was shown by Drossart et al. [1993] to be that T_0 is controlled by the thermal radiation of hydrocarbons lost to space at, or around, the homopause. The temperature at level i, $T_i(N_G)$, becomes:

$$T_i(N_G) = (T_i^G - T_0) \times N_G + T_0 \tag{3.19}$$

where T_i^G is the original temperature profile for the discrete aurora of Grodent et al. [2001]. The profiles for $N_G = 0.8$, 0.9, 1.0, 1.1 and 1.2 can be seen in Figure 3.13.

Equation 3.19 represents a linear first order approximation to model the response of the jovian ionosphere/thermosphere system to different energy sources and sinks. A more complete approach would be to reconfigure the numerical model of Grodent et al. [2001] to re-calculate the full range of Joule heating, ion-drag, particle precipitation, H_3^+ cooling and downward conduction parameters. That is, however, outside the scope of this thesis.

It is important to emphasise that the model of Grodent et al. [2001] is run to produce a temperature profile that is consistent with observed temperatures. This is achieved by varying the precipitation energy distribution. In theory, one can create any desired temperature profile, only by inputting the energies at the altitudes that such a profile would require. Such an argument also apply to how the atmosphere would react to a heating event. Because of this modelling ambiguity, the temperature profile scaling described in Equation 3.19 is considered to be a reasonable estimate of how the temperature behaves in response to varying energy inputs.

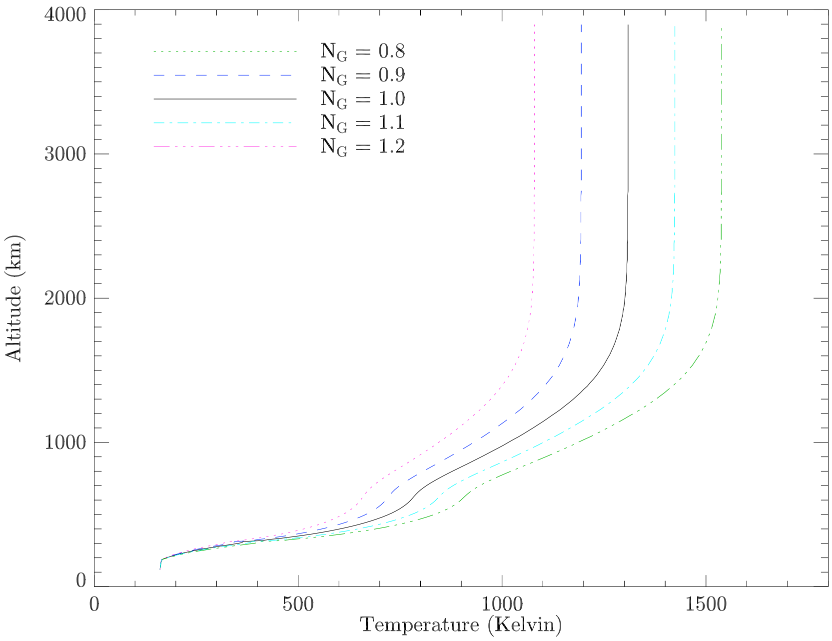

Figure 3.13: The temperature profile of Grodent et al. [2001] scaled by $N_G = 0.8$, 0.9, 1.0, 1.1 and 1.2 as defined in Equation 3.19.

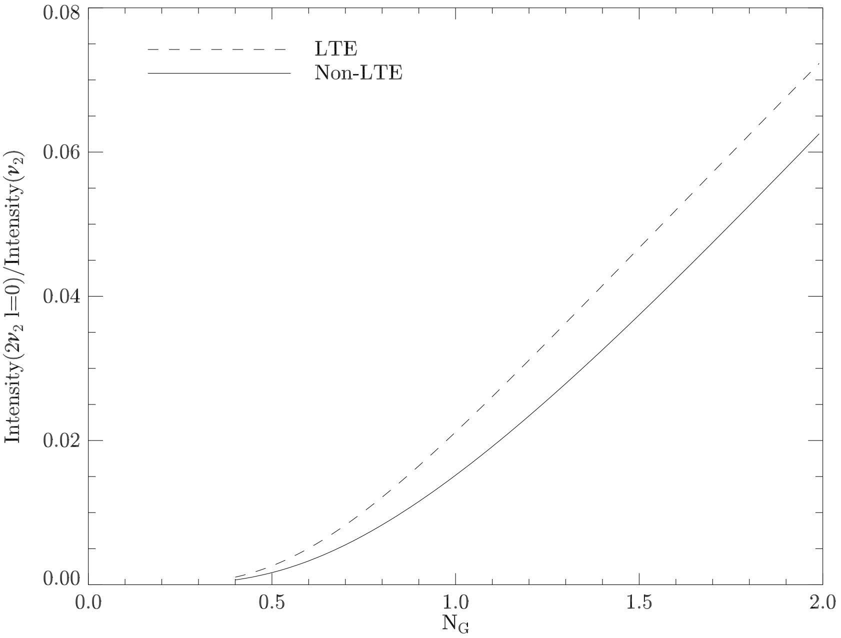

Figure 3.14: Intensity ratio of the two lines observed by Stallard et al. [2002], Q(1, 0^-) and R(3, 4^+), as a function of Grodent number, N$_G$, for both LTE and non-LTE scenarios.

3.5.3 Intensity ratio versus N$_G$

Now that we have a straightforward parameterisation of the temperature profile, we need a relationship between the observed line ratio and the temperature profile needed to create it.

Starting at N$_G$ = 0.4 and stepping up to N$_G$ = 2.0 in steps of 0.05, the intensity profile of both the H_3^+ Q(1, 0^-) $\nu_2 \rightarrow 0$ and R(3, 4^+) $2\nu_2 \rightarrow \nu_2$ lines were calculated as a function of altitude and then altitude-integrated to give total intensity for both LTE and non-LTE conditions, just as in Section 3.4.1. The height-integrated intensity of the R(3, 4^+) transition was divided with the height integrated intensity of the Q(1, 0^-) transition as to calculate the line ratio. Line ratio as a function of N$_G$ can be seen in Figure 3.14. The figure shows that a given line ratio would result in very different temperature profiles for the LTE and non-LTE cases. In other words, the thin shell in LTE treatment of the H_3^+ emission underestimates the ionospheric temperature.

The two curves in Figure 3.14 were fitted using `poly_fit.pro` in IDL, which fits a fifth order polynomial to the data. The fit was of the form:

$$N_G = a_0 + a_1 R + a_2 R^2 + a_3 R^3 + a_4 R^4 + a_5 R^5 \tag{3.20}$$

where R is the observed intensity ratio, $I(\mathrm{R}(3, 4^+)/I(\mathrm{Q}(1, 0^-)$. For the LTE scenario, the constants of Equation 3.20 are:

$$a_0 = \quad 3.73 \times 10^1 \tag{3.21}$$

$$a_1 = \quad 5.08 \times 10^1 \tag{3.22}$$

$$a_2 = - \quad 1.73 \times 10^3 \tag{3.23}$$

$$a_3 = \quad 4.53 \times 10^3 \tag{3.24}$$

$$a_4 = - \quad 5.65 \times 10^5 \tag{3.25}$$

$$a_5 = \quad 2.68 \times 10^6 \tag{3.26}$$

For the non-LTE case, the constants of Equation 3.20 are:

$$a_0 = \quad 3.88 \times 10^1 \tag{3.27}$$

$$a_1 = \quad 6.88 \times 10^1 \tag{3.28}$$

$$a_2 = - \quad 2.92 \times 10^3 \tag{3.29}$$

$$a_3 = \quad 8.86 \times 10^4 \tag{3.30}$$

$$a_4 = - \quad 1.30 \times 10^6 \tag{3.31}$$

$$a_5 = \quad 7.20 \times 10^6 \tag{3.32}$$

Using these equations, we can obtain the temperature profile at the beginning and at the end of the Stallard et al. [2002] heating event, for both LTE and non-LTE scenarios. These temperature profiles, as defined by the intensity ratio, can be seen in Figure 3.15. The change in temperature during the event, ΔT, can be seen in Figure 3.16 for both the LTE and non-LTE scenarios. The LTE increase in temperature is just over 200 K at the exosphere, whilst the non-LTE exospheric temperature is just under 230 K. This indicates that during such conditions more work would be required to heat the atmosphere.

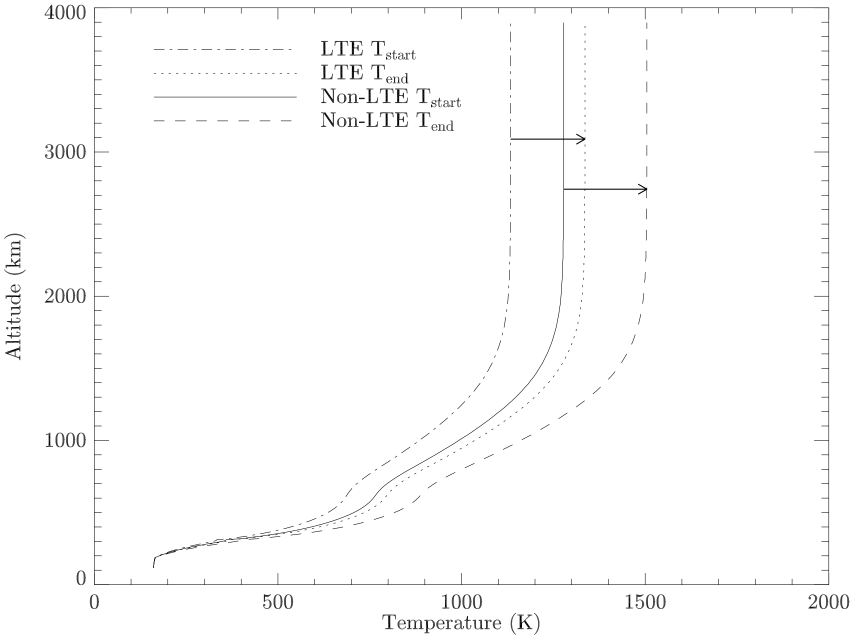

Figure 3.15: Temperature profiles at the start and at the end of the event observed by Stallard et al. [2002], for both LTE and non-LTE scenarios. The profiles are derived from the observed line ratio and scaled as the Grodent et al. [2001] temperature profile. The arrow shows the direction of the event.

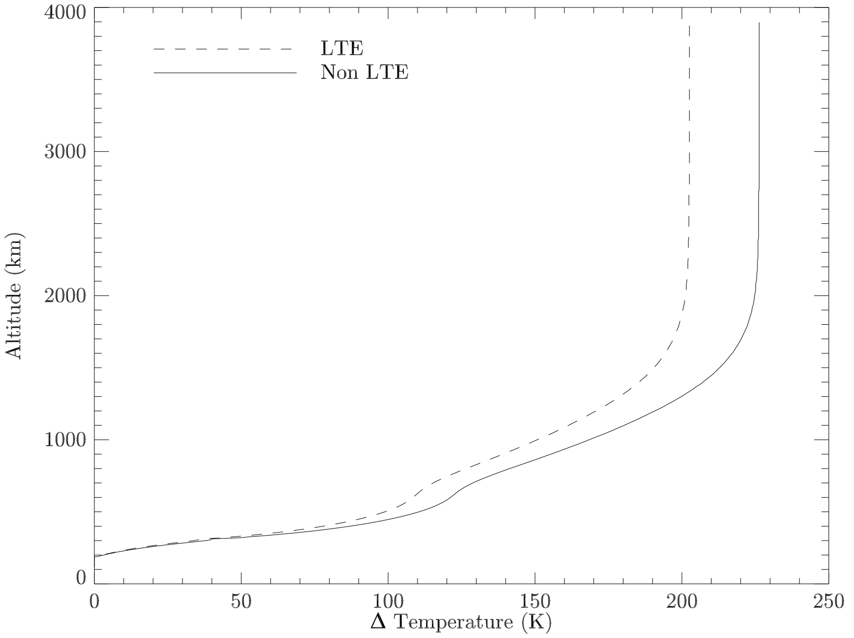

Figure 3.16: The difference between the start and end temperatures of the event shown in Figure 3.15.

3.5.4 Energy required to heat the auroral region

The power required to change the temperature, P, of a parcel of gas with specific heat capacity c_p, is given by:

$$P = \frac{c_p \Delta T}{\Delta t} \tag{3.33}$$

where Δt is the time in seconds during which the heating is applied. Stallard et al. [2002] reported 2.9 days between the two observations – that is, time of mid-observation on the 8th to the mid-point of observation on the 11th. Consequently, $\Delta t = 2.9 \times 24 \times 3600 = 250{,}560$ seconds. The temperature increase, ΔT, during the event can be seen in Figure 3.16. Now, the heat capacity is given by (in units of $\mathrm{JK^{-1}m^{-3}}$):

$$c_p = \delta[\mathrm{H}]\frac{5}{2}k + \delta[\mathrm{H_2}]\frac{7}{2}k + \delta[\mathrm{He}]\frac{5}{2}k \tag{3.34}$$

where δ is the number density of the species in the square bracket and k is Boltzmann's constant ($k = 1.38\times10^{-23}$ $\mathrm{JK^{-1}}$). Only the number densities of atomic hydrogen, $\delta[\mathrm{H}]$, molecular hydrogen, $\delta[\mathrm{H_2}]$, and helium, $\delta[\mathrm{He}]$, needs to be taken into account since they are by far the most abundant species in the jovian thermosphere (see Figure 3.2). The calculated heat capacity of the atmosphere of Grodent et al. [2001] can be seen in Figure 3.17. The heat input per unit volume can be seen in Figure 3.18. Integrating Figure 3.18 over altitude gives the total work required to heat the atmosphere. The energy required is 65 $\mathrm{mWm^{-2}}$ for the LTE case and 73 $\mathrm{mWm^{-2}}$ for the non-LTE case. Note that these values represent the heating rate which is additional to that on the 8th of September. It shall be assumed, for arguments of simplicity, that the jovian upper atmosphere was in a steady state on this date. It turns out that this approximately true for the non-LTE case (see Section 3.5.11).

3.5.5 The H_3^+ density scaling

In Section 3.4.3, it was shown that the column density of H_3^+ in the Grodent et al. [2001] model is overestimated by a factor of 3. Only the non-LTE analysis of the H_3^+ emission could explain the observed discrepancy in column density. As a consequence, only the non-LTE profiles will be considered in analysing the heating event of Stallard et al. [2002].

In order to establish what this H_3^+ density scaling factor was on the 8th and

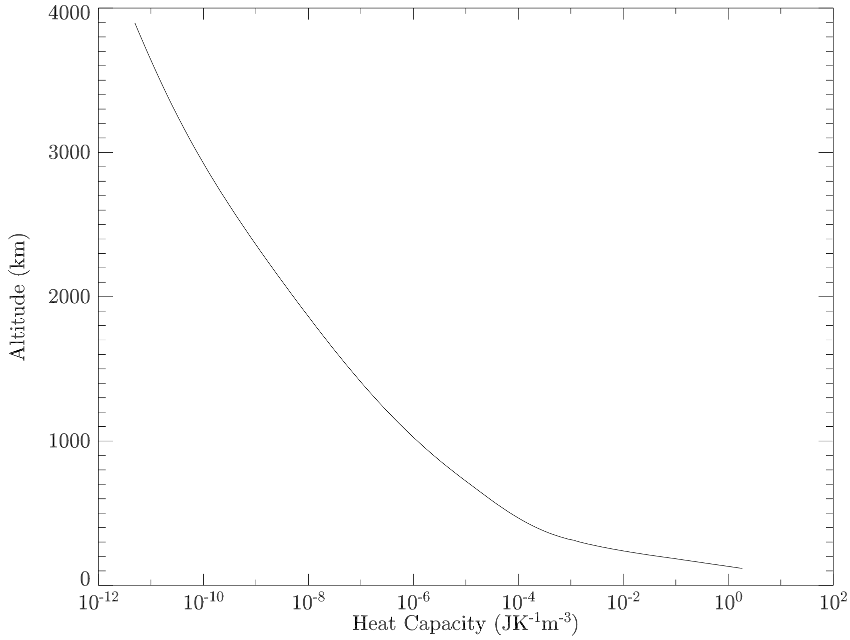

Figure 3.17: Modelled heat capacity of the jovian ionosphere using the density profiles of Grodent et al. [2001].

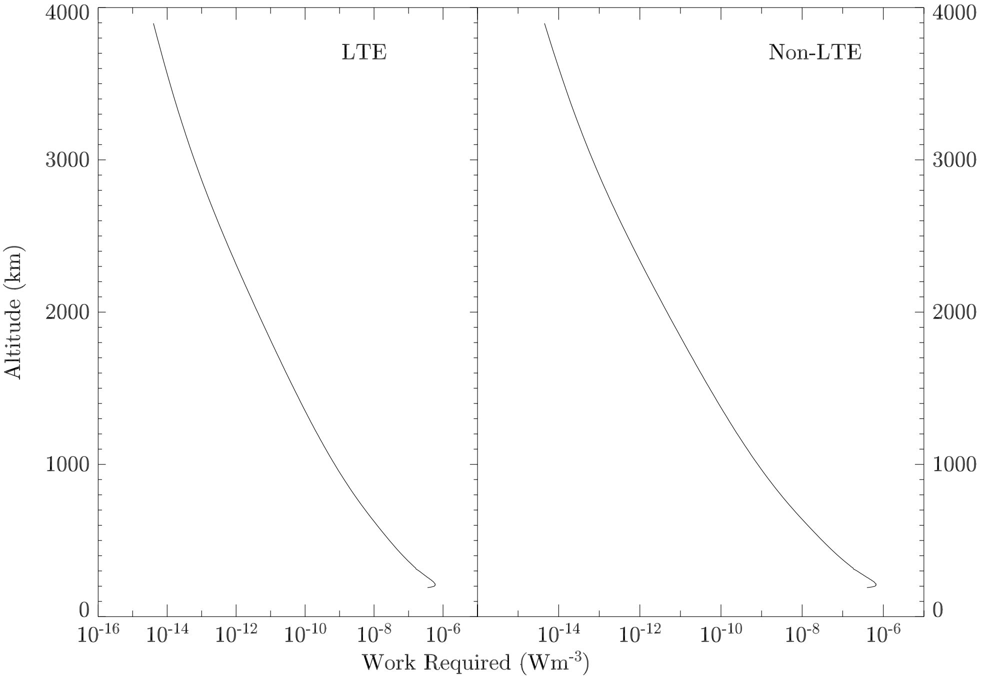

Figure 3.18: Energy required to heat the atmosphere for the LTE case (left) and non-LTE case (right).

Parameter	8th Sept.	11th Sept
N_G	0.97	1.17
Observed intensity ($Wm^{-2}str^{-1}$)	2.24×10^{-5}	3.36×10^{-5}
Modeled intensity ($Wm^{-2}str^{-1}$)	6.18×10^{-5}	8.85×10^{-5}
Intensity fraction	0.364	0.381

Table 3.7: The observed and modeled intensity of the H_3^+ Q(1, 0^-) fundamental line on September 8th and September 11th.

the 11th of September, the intensity of the Q(1, 0^-) line as observed by Stallard et al. [2002] is compared to the emission in the same line as modelled through the Grodent et al. [2001] atmosphere, using the temperature profile as defined by the non-LTE value of N_G (defined by Equation 3.19). Note that the intensities published by Stallard et al. [2002] need to be multiplied by a factor of $\sqrt{2\pi}$, since this factor was left out when calculating the total flux contained within a gaussian. The FWHM of their observations was 3.1×10^{-4} μm (Stallard [2000]).

The values for the integrated intensity of Q(1, 0^-) for the two dates can be seen in Table 3.7. As before, we use fraction between the observed and modelled intensity to determine the column density for a particular observations. The density scaling factor for the 8th of September is 36.4% and for the 11th it is 38.1%. The scaled density profiles can be seen in Figure 3.19. The column density on the 8th becomes N = 8.74 $\times$ 10^{16} m^{-2} and on the 11th N = 9.14 $\times$ 10^{16} m^{-2}, considerably greater than that derived from assuming that the H_3^+ emission originates from a thin in conditions of LTE.

3.5.6 Work done by Joule heating and ion-drag

Joule heating is the heating due to the passage of a current through a resistive medium. On Jupiter, this current is set up by the current system illustrated in Figure 1.9. As this current, which is comprised of charged particles in the form of both ions and electrons, moves through the co-rotating neutral atmosphere, and energy is transferred through ion-neutral collisions.

Miller et al. [2005] showed that the energy transferred from the magnetosphere by means of accelerating ions in the thermosphere via the equator-ward electric field, E_{eq}, is given by:

$$H = (1-k)^2 E_{eq}^2 \Sigma_p + k(1-k) E_{eq}^2 \Sigma_p \tag{3.35}$$

where the first term on the right-hand side represents Joule heating and the second is ion-drag heating. The k parameter is given by:

$$k = \frac{v_n}{v_i} \tag{3.36}$$

where v_n is the velocity of the neutrals and v_i is the velocity of the ions in the same region. k varies between 0 and 1 – its true value is not known, but JIM gives values of k = 0.5 to 0.7 at the H_3^+ ion peak (Millward et al. [2002]). Cowley and Bunce [2001] uses a value of $k = 0.5$ in their theoretical studies of the jovian magnetosphere/ionosphere interaction. In this study, in compliance with these studies, $k = 0.5$ is used, which gives equal contributions of Joule heating and ion-drag.

The magnitude of the equator-ward electric field, E_{eq}, is given by:

$$E_{eq} = v_i B_z \tag{3.37}$$

where B_z is the strength of the magnetic field, which is assumed to be perpendicular to the H_3^+ ion velocity in the frame of reference of the planet. The line-of-sight velocities were 0.5 kms^{-1} on the 8th, accelerating up to 1.0 kms^{-1} on the 11th. The velocity observations of Stallard et al. [2002] were made with a central meridian longitude $\lambda_{III} = 155°$ to $160°$ (IAU System III longitude). The co-latitude of the slit was $\sim 20°$ and the angle of the electrojet to the XZ plane was between 2° and 7°, and the sub-Earth latitude was 3° N, resulting in real electro-jet velocities of 0.55 kms^{-1} on the 8th and 1.1 kms^{-1} on the 11th (i.e. a correction of about 10% for the line-of-sight effect).

If $B_z = 1 \times 10^{-3}$ Tesla (Connerney et al. [1998]), then $E_{eq} = 0.55$ Vm^{-1} in the beginning, and $E_{eq} = 1.10$ Vm^{-1} at the end of the observed heating event. It is assumed that both the ion velocity and electric field are altitude independent such that Equation 3.35 can be used to calculate the increase in local heating rates at all Grodent et al. [2001] model levels. The column-integrated heating due to Joule heating and ion-drag is 67 mWm^{-2} on 8th September and 277 mWm^{-2} on 11th September. This gives an increase of 210 mWm^{-2}, resulting in an average increase of 105 mWm^{-2}, assuming a linear increase in heating rate.

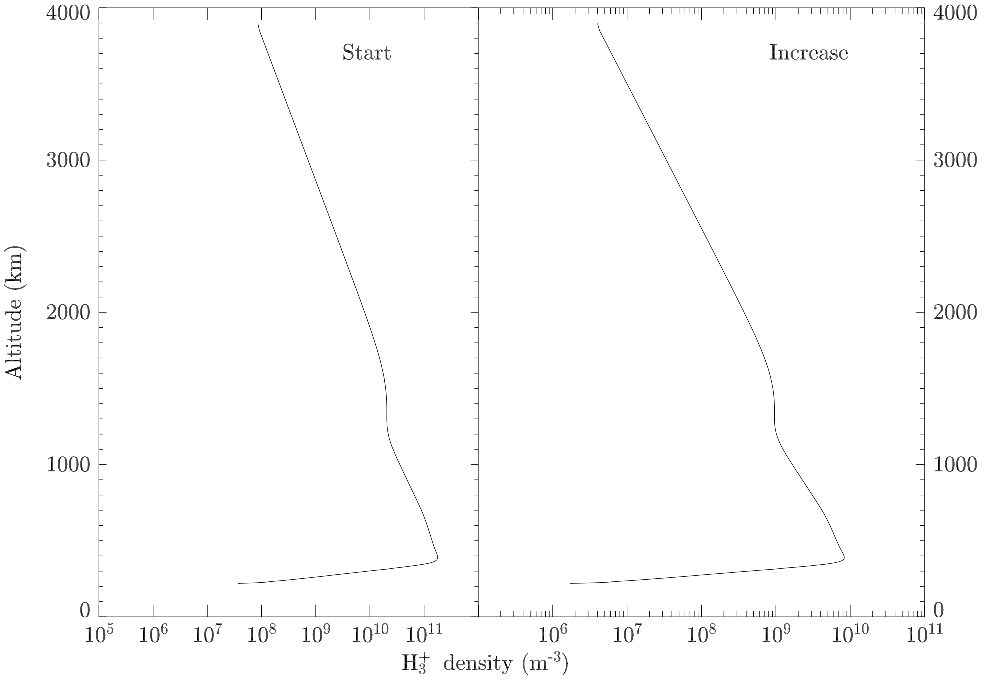

Figure 3.19: The scaled H_3^+ density profiles of Grodent et al. [2001] for the start of the event (left) and the increase in density during the event (right).

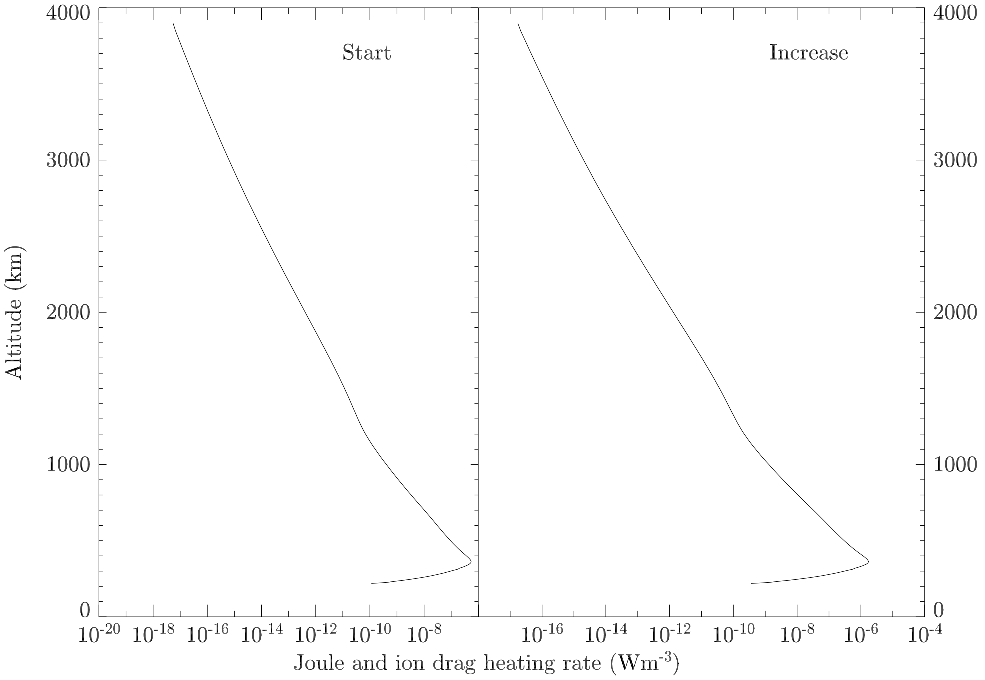

Figure 3.20: The Joule heating at the start of the event (left) and the increase in Joule heating during the event (right).

Pedersen conductivity

Conductivity is the measure of the ability of an atmosphere to carry currents, such as the large scale currents induced by the plasma motions in the magnetosphere. Generally, this parameter is split into two components – the magnetic field aligned Pedersen conductivity and the magnetic field perpendicular Hall conductivity. Since the Hall conductivity is perpendicular to the electric field, it does not contribute to the Joule heating or ion-drag. The Pedersen conductivity, Σ_p, is given by (Kivelson and Russell [1995]):

$$\Sigma_p = \frac{n_i q^2}{m_i} \frac{\nu_{in}}{(\nu_{in}^2 + \Omega_c^2)} \tag{3.38}$$

where ν_{in} is the collision frequency between the ion and the neutrals and Ω is the gyrofrequency of the charged particle with number density n_i and mass m_i. In our case, the charged particle is H_3^+, which has a charge $q = 1.60 \times 10^{-19}$ C and a mass $m_i = 3 \times 1.67 \times 10^{-27}$ kg.

Charged particles moving in a magnetic field are subjected to a Lorentz Force, **F**, according to

$$\mathbf{F} = q(\mathbf{E} + \mathbf{v} \times \mathbf{B}) \tag{3.39}$$

where q is the charge of the particle, **E** is the electric field, **v** is the velocity and **B** is the magnetic field. This force gives rise to a spiral motion of the charged particle. The frequency of this spiral motion, the frequency of gyration, Ω_c, is given by:

$$\Omega_c = \frac{q B_z}{m_i} \tag{3.40}$$

where m_i is the mass of the charged particle and B_z is the vertical magnetic field strength. The magnetic field in the aurora is $\sim$ 10 Gauss or 1 mTesla (see Millward et al. [2002] and Connerney et al. [1998]), then the gyrofrequency becomes:

$$\Omega_c = \frac{q B_z}{m_i} = \frac{1.60 \times 10^{-19} \times 10^{-3}}{3 \times 1.67 \times 10^{-27}} = 32000 \text{ Hz} \tag{3.41}$$

The collision frequency of H_3^+ with H_2, ν_{in}, is taken from Geiss and Buergi [1986] and is given by:

$$\nu_{in} = \frac{2.1 \times 10^{-15}}{3.46} (\delta[\mathrm{H_2}] + \delta[\mathrm{H}]) \tag{3.42}$$

where $\delta[\mathrm{H_2}]$ is the H_2 density and $\delta[\mathrm{H}]$ is the H density. This is the same collision frequency used in JIM, the model used to analyse conductivity in the upper atmosphere of Jupiter (Millward et al. [2002]).

The Pedersen conductivity as a function of altitude can be seen in Figure 3.21. Note that the peak of the conductivity coincides with the peak of the H_3^+ density, as expected.

3.5.7 Energy deposited through particle precipitation

The 1D model due to Grodent et al. [2001] varies the energy deposited by electrons into the upper atmosphere to match a range of observed temperatures and ion densities. This is likely to overestimate the total energy of the precipitating particles since they have to compensate for the energy sources for which the model cannot account for, such as Joule heating, ion-drag and the redistribution of energy due to winds. Therefore, whilst the energy deposition is consistent with measurements, the flux itself cannot be taken to be 'true' electron flux.

Millward et al. [2002] used the JIM to model the response in the production of H_3^+ to the injection of energetic electrons.

Grodent et al. [2001] had a two stream (i.e. up and down) electron precipitation model with a total energy input flux of 110 erg cm^{-2} s^{-1} and peaks at $\sim$ 20 keV. Millward et al. [2002] found the following expression for 10 keV electrons:

$$\log_{10} N = 0.435 \times \log_{10} F_e + 12.28 \tag{3.43}$$

where N is the column density of H_3^+ in cm^{-2} and F$_e$ is the flux of 10keV electrons in erg cm^{-2}s^{-1}. Note that a doubling of the electron flux does not lead to a doubling of the H_3^+ column density - this is because the overall density is controlled by the rate of dissociative recombination with electrons, as per Reactions 1.9, 1.10 and 1.11. Assuming that the Grodent et al. [2001] model produces a similar response of H_3^+ density to electron flux, we can write Equation 3.43 in the form:

$$\log_{10} N(\mathrm{H_3^+}) - \log_{10} N_0(\mathrm{H_3^+}) = 0.435(\log_{10} F_e - \log_{10} F_0) \tag{3.44}$$

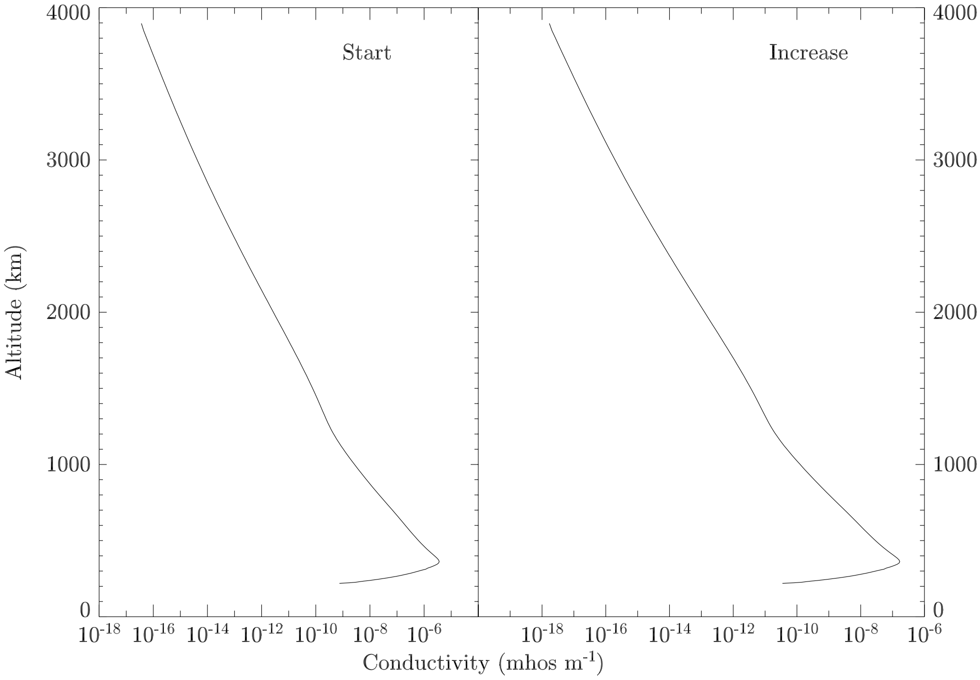

Figure 3.21: Pedersen conductivity at the start of the event (left) and the increase during the event (right).

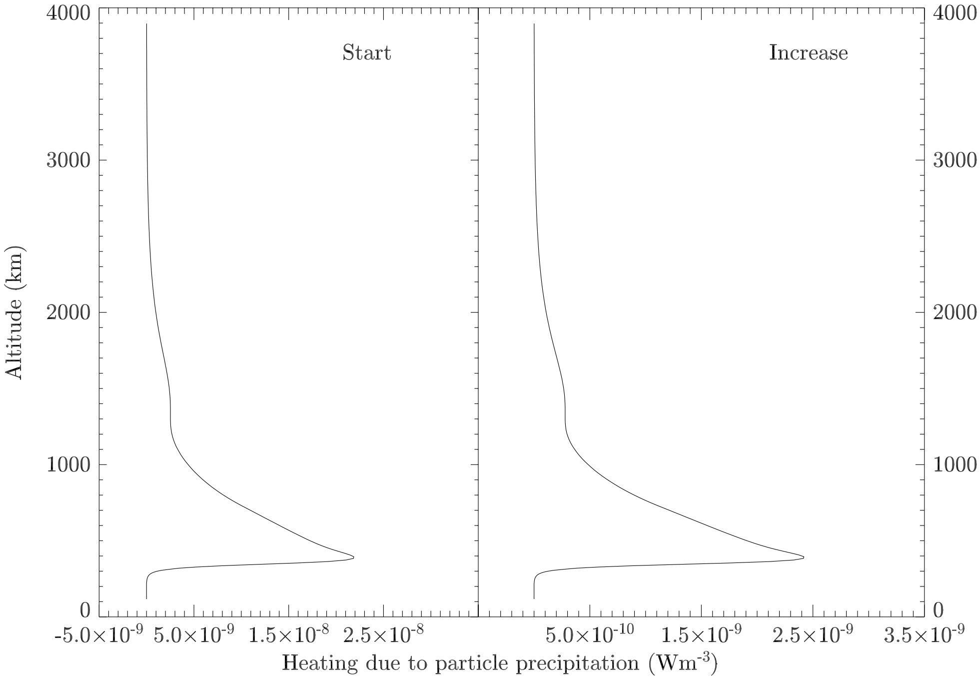

Figure 3.22: The heating due to particle precipitation at the beginning of the event (left) and during the event (right).

where $N_0(\mathrm{H}_3^+)$ and F_0 are the column density and precipitation flux values of Grodent et al. [2001]. For the discrete aurora $N_0(\mathrm{H}_3^+) = 18 \times 10^{12}$ cm^{-2} and $F_0 = 110$ ergs s^{-1} cm^{-2}.

This treatment gives an electron flux $F_e = 10.8$ mWm^{-2} on 8th of September and $F_e = 12.0$ mWm^{-2} on 11th September. The total increase in precipitation flux is 1.2 mWm^{-2}. If one assumes that the increase in H_3^+ density is linear during the event, then the average increase in particle precipitation heating is 0.6 mWm^{-2}.

The deposition of particle precipitation energy, assuming that it has the same altitude shape as H_3^+ density distribution, can be seen in Figure 3.22.

The Grodent et al. [2001] model requires an electron flux of 110 mWm^{-2} to produce the discrete aurora, which is a factor of ~ 10 higher than found here. This simple comparison seems to suggest that by no means is particle precipitation the main energy source in the auroral region on Jupiter.

3.5.8 Downward conduction of heat

This section will investigate whether or not conduction, i.e. vertical transport of heat, affects the energy balance of Jupiter's upper atmosphere.

The upward flux of heat at any point in the atmosphere is given by:

$$F_{dc} = -\lambda \frac{dT}{dz} \tag{3.45}$$

where T is the temperature, z is the altitude and λ is the thermal conductivity. The latter is given by Yelle and Miller [2004] in units of mWm^{-2} (K/m)$^{-1}$:

$$\lambda = AT^s \tag{3.46}$$

with $A = 2.5$ and $s = 0.75$. The upward flux of energy on September 8th and September 11th can be seen in Figure 3.23. However, a flux can have a zero net heating effect since heat can flow both up and down. Therefore, we consider the *net* heating per unit volume:

$$H_{dc} = -\frac{dF}{dz} = -\frac{d\left(-\lambda \frac{dT}{dz}\right)}{dz} = \frac{d\left(\lambda \frac{dT}{dz}\right)}{dz} \tag{3.47}$$

Parameter	CH_4	C_2H_2
Spin weighting – g	3	2
Upper energy level – E	1306	729
Transition frequency – ω	1306	729
Einstein A coefficient – A	2.5	5.0

Table 3.8: The parameters used to calculate the energy lost through radiation to space by hydrocarbons as outlined by Drossart et al. [1993].

The net heating due to conduction as a function of altitude can be seen in Figure 3.24. The integrated conduction is very small: $H_{dc} = 0.26$ mWm^{-2} on the September 8th and $H_{dc} = 0.35$ mWm^{-2} on the September 11th. This gives an average heating rate, assuming a linear increase, of 0.045 mWm^{-2}.

3.5.9 Energy lost through hydrocarbon cooling

Drossart et al. [1993] showed that cooling by hydrocarbon emission play an important role in controlling the energy budget below the homopause on Jupiter. The most important hydrocarbons are methane (CH_4) and acetylene (C_2H_2). The density profiles of these two species of Grodent et al. [2001] can be seen in Figure 3.25.

The total emission from a particular hydrocarbon is given by Drossart et al. [1993] as:

$$I = \frac{gNhc\omega A_{if} \exp\left(-E/kT\right)}{2(1 + \exp\left(-E/kT\right))} \tag{3.48}$$

where g is the nuclear spin weighting, N is the number density, ω is the transition frequency, A_{if} is the Einstein A coefficient, and E is the upper energy level. Table 3.8 lists the parameters used to calculated the radiation to space in this analysis. The density of CH_4 and C_2H_2 is taken from the same model run output of Grodent et al. [2001] used throughout this chapter (see Figure 3.25). Grodent et al. [2001] assume that only hydrocarbon emission from an altitude above ~ 200 km is able to escape the jovian upper atmosphere – any emission from below this altitude would be re-absorbed almost instantly. The same assumption is adopted here. The hydrocarbon cooling can be seen in Figure 3.26. The column-integrated heat lost due to hydrocarbon radiation is 65.5 mWm$^{-2}(2\pi\text{str})^{-1}$ and 103.3 mWm$^{-2}(2\pi\text{str})^{-1}$ on 8th and 11th of September respectively. Assuming a linear increase gives an average change in hydrocarbon cooling of 18.9 mWm$^{-2}(2\pi\text{str})^{-1}$. Note that $\sim$ 80% of the thermal hydrocarbon emission is due to CH_4.

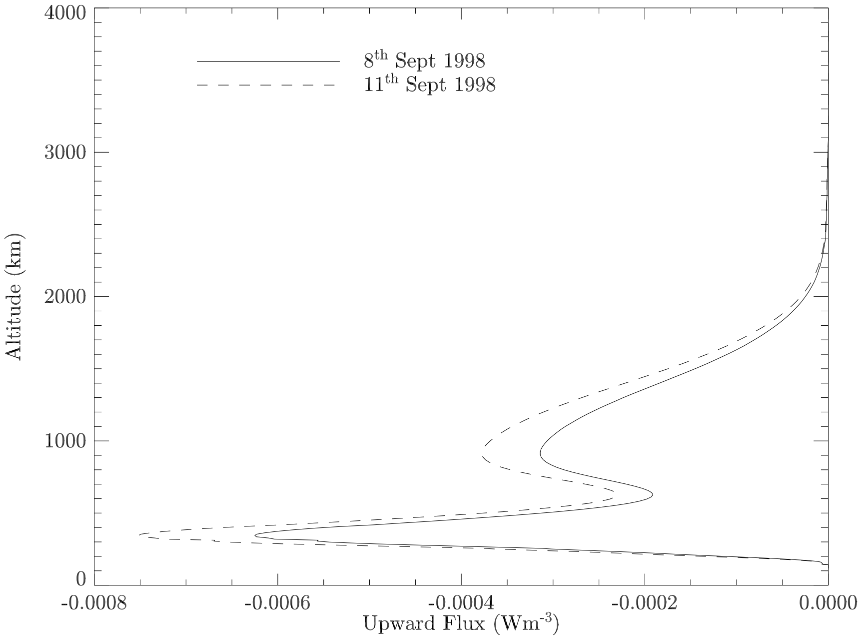

Figure 3.23: The upward flux on September 8th and September 11th.

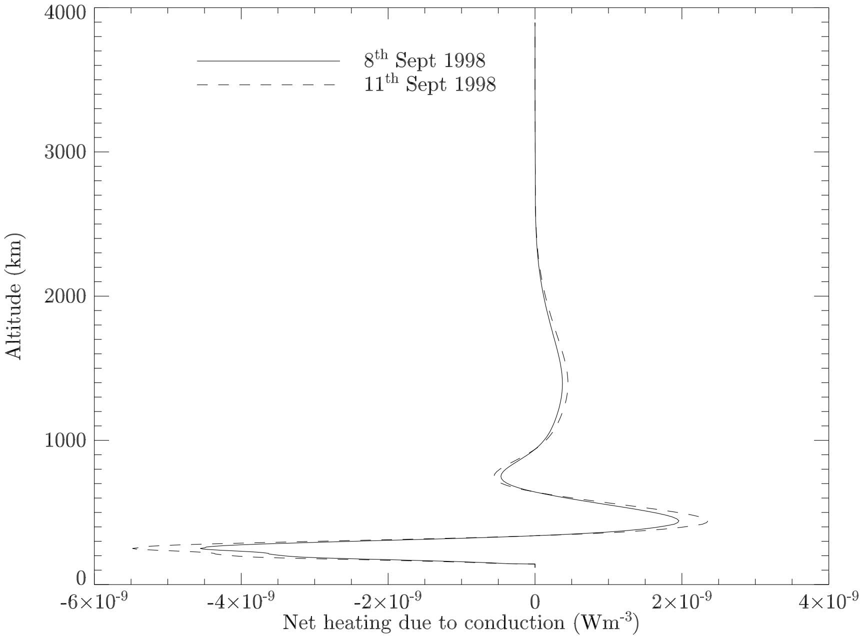

Figure 3.24: The net heating due to conduction.

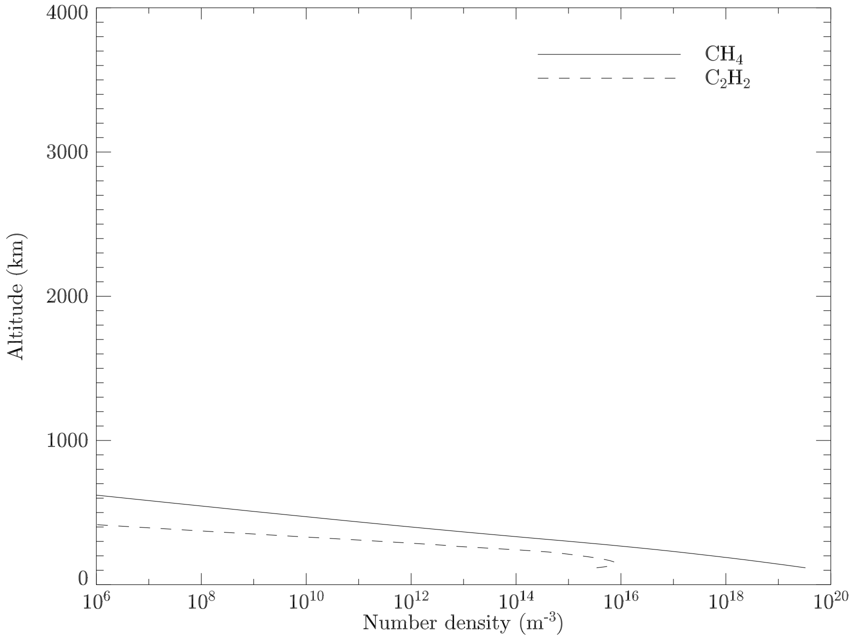

Figure 3.25: The volume density of methane (CH_4) and acetylene (C_2H_2) of Grodent et al. [2001].

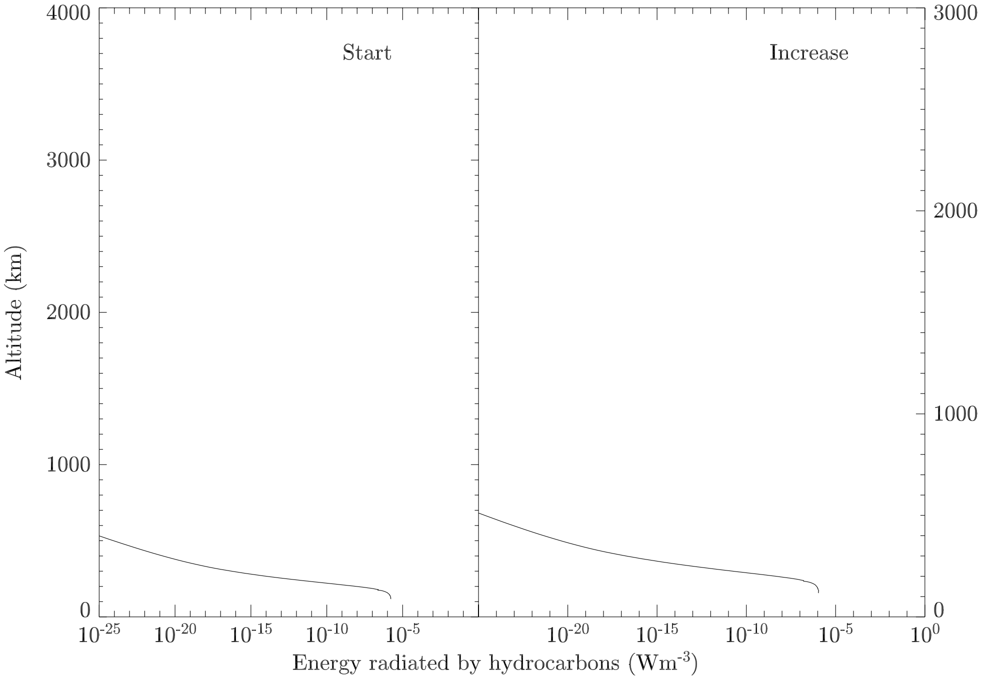

Figure 3.26: The energy radiated by hydrocarbons at the start of the event (left) and the increase during the event (right).

3.5.10 Energy lost through H_3^+ emission

Many studies have highlighted the cooling properties of the H_3^+ ion (e.g. Lam et al. [1997a], Williams [2004]), and authors have suggested that it is indeed the main coolant in the upper atmosphere of Jupiter (e.g. Waite et al. [1997]). Rego et al. [2000] suggested that, on Jupiter, the energy input due to particle precipitation was roughly balanced by the energy lost through thermal emission of H_3^+.

Since about 90% of the H_3^+ emission on Jupiter arises from the ν_2 vibrational level (Miller et al. [1990]) it shall be assumed that the total emission from H_3^+, $E(H_3^+)$, is attenuated in conditions of non-LTE in the same way as the ν_2 level. Previously, in Section 3.3.1, the non-LTE population density attenuation for the vibrational manifolds of H_3^+ was calculated. The attenuation curve for ν_2 can be seen as the solid thin line in Figure 3.6. Let this fraction be $F(z)$, where z is altitude, then the energy lost at any point in the atmosphere is:

$$H(\mathrm{H}_3^+) = 2\pi \times E_{tot}(T) \times T(z) \times \delta[\mathrm{H}_3^+] \times F(z) \tag{3.49}$$

where $E_{tot}(T)$ is the total emission per molecule (in units of Wstr^{-1}) at temperature T. $\delta[\mathrm{H}_3^+]$ is the number density of H_3^+ and the 2π is the emission emerging to one hemisphere. It is assumed that emission travelling towards lower altitudes is re-absorbed and thus does not have a net effect on the cooling of the atmosphere as a whole.

The column-integrated values for $H(\mathrm{H}_3^+) = 5.1\ \mathrm{mWm}^{-2}$ on 8th of September and $H(\mathrm{H}_3^+) = 10.0\ \mathrm{mWm}^{-2}$ on 11th of September. Again, assuming a linear increase in H_3^+ density, we get an average increase of $2.5\ \mathrm{mWm}^{-2}$ – this is about four times larger than the energy injected through particle precipitation and about 50 times the energy lost by downward conduction.

3.5.11 Discussion

Table 3.9 shows a summary of the calculated energy sources and sinks. There is only a net heating rate of $7.4\ \mathrm{mWm}^{-2}$ on September 8th when $N_G = 0.97$. This suggests that that the atmosphere is close to thermal balance, and since the Grodent et al. [2001] profile is based on a thermally equilibrated atmosphere, this might be expected for $N_G \approx 1$. Consequently, the assumption that the atmosphere was in a steady state

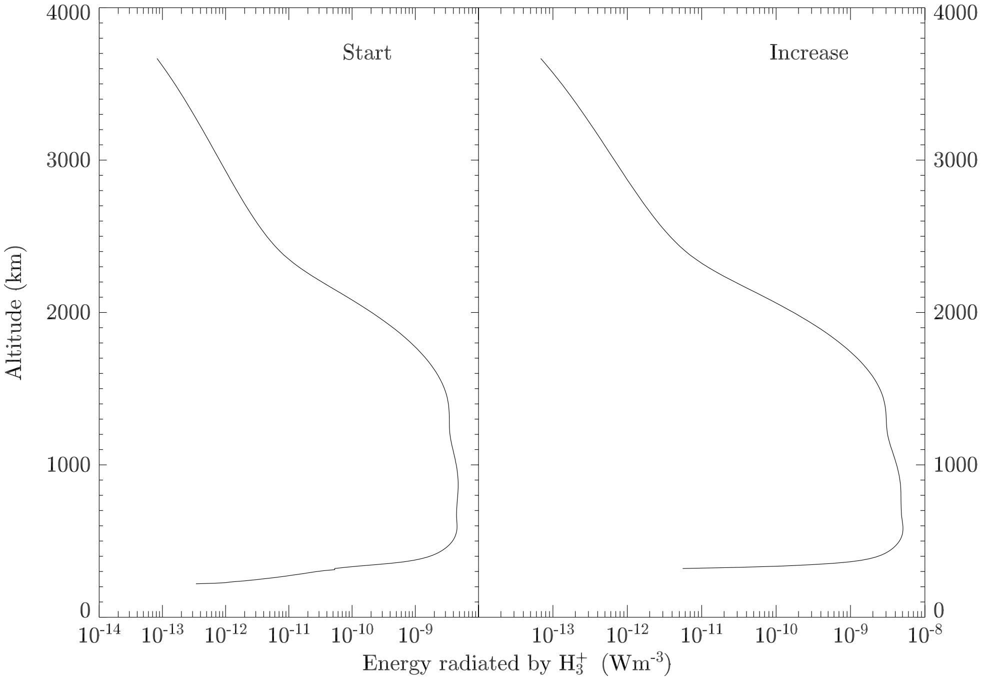

Figure 3.27: The energy radiated by H_3^+ at the start of the event (left) and the increase in radiated energy (right).

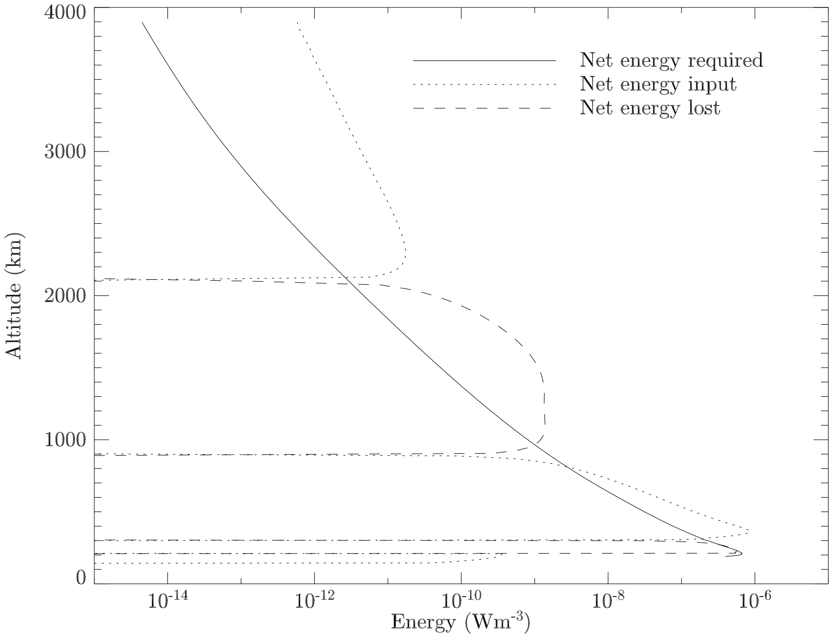

Figure 3.28: The energy required, the energy input, and the energy lost in the analysis of the event observed by Stallard et al. [2002].

Heating/cooling term	September 8th	September 11th
Joule heating and ion-drag	67.0	277.0
Particle precipitation	10.8	12.0
Downward conduction	-0.3	-0.4
$E(H_3^+)$ cooling	-5.1	-10.0
Hydrocarbon cooling	-65.5	-103.3
Net heating rate	7.4	175.3

Table 3.9: The heating and cooling rates in mWm^{-2} for the auroral heating event. Loss mechanisms are given as negative heating rates.

at the beginning of the event is justified.

The heating rate on September 11th is 175.3 mWm^{-2}. This confirms that we are observing an event of considerable heating, and the atmosphere at $N_G = 1.17$ is very much out of thermal balance.

Table 3.10 summarises the average change in heating rates assuming a linear increase in H_3^+ density and temperature. The analysis of the auroral event, both in terms of heating and ion velocities, observed by Stallard et al. [2002], gives an insight to the energy balance of Jupiter's upper atmosphere. A minimum heating rate of 73 mWm^{-2} was required to heat the auroral region just on the basis of the temperature change. The main source for energy in the jovian aurora is the Joule heating and ion-drag. This is mainly because of the large increase in the equator-ward electric field due to the increase in ion velocity. The energy injected through particle precipitation is smaller by a factor of 2 and is similar to the energy being lost through H_3^+ radiation. The largest energy sink is that of radiation to space by hydrocarbons at, or below, the homopause.

Figure 3.28 compares the increased heating rate due to particle precipitation, Joule heating and ion-drag, minus the increase in H_3^+ and hydrocarbon emission to the required increase in heating rate, as a function of altitude. It shows that energy is not necessarily deposited at an altitude where it is required to heat the atmosphere. Joule heating and ion-drag deposit energy at an altitude that corresponds to the peak in H_3^+ density, which also corresponds to the peak in the Pedersen conductivity. This is some 150 km higher than required, indicating that heat must be conducted downward and that part of this energy will be lost through or at the homopause by the radiation from hydrocarbons. Above 1,000 km there is a shortfall in the increase in heating rate to produce the required temperature profile as defined by the N_G. This shortfall could

Heating/Cooling term	Energy (mWm^{-2})
Required increased heating rate (non-LTE case)	73
Average increase in Joule heating and ion-drag	105
Average increase in particle precipitation	0.6
Average increase in downward conduction	-0.04
Average increase in H_3^+ cooling	-2.5
Average increase in hydrocarbon cooling	-18.9
Calculated net increased heating rate available	84.1

Table 3.10: Average changes in heating and cooling rates. Loss mechanisms are given as negative heating rates.

be explained by the redistribution of energy by horizontal winds, or by a slowing of the rate at which energy is conducted downward.

If there are winds that redistribute energy to lower latitudes, than they will act as a heat sink in the auroral region. Naturally, winds can also redistribute the auroral H_3^+ such that the introduction of one heat sink removes another. However, since the lifetime of H_3^+ is relatively short (of the order of seconds – see Equation 1.12), we do not expect vast quantities of H_3^+ of auroral origin at non-auroral latitudes. Therefore, the process of redistribution of energy by winds is a plausible additional heat sink.

The increase in Joule heating and ion-drag is primarily driven by the increase in the electric field due to the increased ion windspeeds. It is also, to a lesser extent, driven by the increase in H_3^+ ion density. The increase in equator-ward electric field indicates a increased lag in corotation. Cowley and Bunce [2001] and Southwood and Kivelson [2001] both suggest that this may occur as the ram pressure on the jovian magnetosphere falls off due to rarefaction in the solar wind. However, it should be noted that the emission from Jupiter's auroral region is intrinsically variable.

The auroral heating event of Stallard et al. [2002] must be followed by a period of cooling as to bring the upper atmosphere back to an equilibrium state (i.e. $N_G \approx 1.0$). It was shown in this chapter that the main mechanisms for local cooling is H_3^+ and hydrocarbon infrared emission, with a small amount of heat conducted downward. If, shortly after September 11th, the heating terms of Joule heating and ion-drag returned to their values on September 8th, then the cooling terms would dominate, as so to bring the temperature down again. The total average rate of cooling is 21.5 mWm^{-2}, which means it would take the atmosphere between 10 and 15 days to cool back down, if the heating terms were to return to their value on September 8th. The timescale of this is comparable with the expected solar wind cycle of $\sim$ 30 days, during which further heating events are likely.

The values obtained for the heating rates can be compared to those obtained by Bougher et al. [2005], who used the Jupiter Thermospheric General Circulation Model (JTGCM). They found a Joule heating rate of 70.0 mWm^{-2}, precipitation heating of 1.75 mWm^{-2}, and a total IR cooling of 17.5 mWm^{-2}. Their 3D model enabled the study of dynamical cooling, i.e. the removal of energy by winds, and found that to be 35 mWm^{-2}. These values are comparable to those found in this chapter, and so Bougher et al. [2005] is believed to be fairly representative of actual jovian conditions. Bougher et al. [2005] were, however, forced to scale down their Joule heating input by a factor of 30% to avoid very large exospheric temperatures of $T \approx 2800$ - 3000 K. The reason for this 30% factor is reported to be unclear. However, Bougher et al. [2005] uses the Grodent et al. [2001] H_3^+ profile to calculate the Pedersen conductivity, Σ_p, and the H_3^+ density is shown in this chapter to be overestimated by a factor of 3 in Grodent et al. [2001]. Consequently, we suggest that the factor of 30% introduced by Bougher et al. [2005] is needed, since their H_3^+ density profile is too large. (Note also that there appears to be a factor of 10^3 labelling error on their Figures 11 and 13, which makes their plot seem inconsistent with Grodent et al. [2001].)

Chapter 4

Saturn

4.1 Introduction

Only a handful of studies have investigated the properties of H_3^+ on Saturn. The ion was first detected on the planet by Geballe et al. [1993]. Even though they could not derive a temperature from their spectrum – they could only positively identify the H_3^+ fundamental R(3, 3^-) line – they concluded that the H_3^+ ion temperature is compatible with the 800 K derived from the Voyager 2 stellar occultations analysed by Festou and Atreya [1982]. Stallard et al. [1999] produced a latitudinal intensity profile of Saturn showing that, unlike Jupiter, there is no detectable H_3^+ at non-auroral latitudes, given the sensitivity of the instrument used. However, they detected an oval-like structure at the south pole, as was first imaged in the UV by Trauger et al. [1998b]. Stallard et al. [2004] used the H_3^+ fundamental Q(1, 0^-) line to derive auroral ion velocities, detecting a lag from corotation across the auroral polar region. Cowley et al. [2004] explains this by describing the aurora as solar wind driven (in contrast to Jupiter's aurora, which is fueled mostly by an internal plasma source). In effect, parts of the kronian ionosphere are locked to the movement of the solar wind.

The only study that ascribes a temperature to a H_3^+ spectrum of Saturn is Miller et al. [2000], but the re-analysis of their spectrum in this chapter shows that the published temperature is incorrect. In addition, a temperature will be derived from spectra taken in February 2004, establishing the first reliable ionospheric H_3^+ temperature determination of Saturn.

All observers of kronian H_3^+ note that the emission is extremely weak – only a few percent of that observed on Jupiter (Geballe et al. [1993]) – which would seem to indicate that the ion density is much lower than that of Jupiter. This may be due to less strong 'internal' plasma sources, like volcanically active moons. Another reason may be that Saturn has a high homopause, resulting in more hydrocarbons higher up in the atmosphere. The hydrocarbons destroy H_3^+ rapidly via the following reaction (Stallard et al. [1999]):

$$H_3^+ + XH \rightarrow XH_2^+ + H_2 \tag{4.1}$$

where X are hydrocarbons such as CH_3, C_2H, C_2H_3, etc. Another alternative source of H_3^+ depletion was proposed by Connerney and Waite [1984], whereby water molecules from the rings migrate onto the upper atmosphere, destroying H_3^+ via the following reaction:

$$H_3^+ + H_2O \rightarrow H_3O^+ + H_2 \tag{4.2}$$

Bergin et al. [2000] used the Infrared Space Telescope (ISO) to detect the 557 GHz H_2O emission from the upper atmospheres of both Jupiter and Saturn. Since water is much heavier than the main constituents of the upper atmosphere (H and He), it would sink through the upper atmosphere, if put there. Therefore, water must be continually replenished. Moses and Bass [2000] modelled the response of the ionosphere to the influx of water from the rings, showing that a constant flux would indeed reduce the H_3^+ density. However, this is likely to have little effect to the ion density in the polar region since the field lines connecting to the rings (which enable the transport of H_2O) connect at much lower latitudes ($\theta < 75$). The presence of water in the inner region of the magnetosphere, at L-shells connecting to low latitudes, was confirmed by Young et al. [2005].

Another plausible explanation for the very low H_3^+ intensity is that the thermosphere of Saturn is cold, such that, even though there are large amounts of H_3^+, the total emission from the region remains low.

On Jupiter, the temperature and column density determinations of H_3^+ have enabled the analysis of the energy balance of the auroral regions. The temperature is used to constrain ionosphere/thermosphere models, giving us a better understanding of the processes that govern this very dynamic region.

4.2 Properties of Saturn's aurora

Pioneer 11 arrived at Saturn in 1979 as the first spacecraft to visit the planet. Its onboard ultraviolet photometer detected emission from hydrogen that varied greatly in latitude and was stronger around the poles compared to at lower latitudes (Judge et al. [1980]). This was the first observation of the aurora on Saturn. Two years later the planet was visited by Voyager 2, whose onboard Ultraviolet Spectrometer (UVS) detected a narrow auroral oval at around 10° co-latitude which displayed a large variation in intensity (Sandel and Broadfoot [1981]). The intensity of the ultraviolet H_2 emissions vary in total radiated power between $< 10^8$ W to a few $\times\ 10^{10}$ W (Trauger et al. [1998b]).

Saturn's aurora is well studied in the ultraviolet (e.g. Trauger et al. [1998b] and Clarke et al. [2005]). However, from what we know on Jupiter, there can be significant morphological differences between what is observed in the UV (which are emissions from H_2) and what is observed in the infrared (which are emissions from H_3^+). Most notably, there are dark regions within the jovian aurora oval in the UV that display significant emission in the infrared (see Yelle and Miller [2004]). Consequently, there could be similar morphological differences between studies using different wavelengths on Saturn. Whilst the study of H_3^+ emission from Saturn is in its infancy compared to the work done on Jupiter, it is very important parameters in understanding the complete picture of auroral processes.

4.2.1 The ionospheric temperature of Saturn

The upper atmosphere of Saturn, at a latitude of 3.8°N, was probed by an occultation between Voyager 2 and the star δ Scorpii in August 1981. The subsequent analysis of this event by Festou and Atreya [1982] derived an exospheric temperature in the equatorial region of $T = 800^{+150}_{-120}$ K. This disagrees with the earlier analysis of the same event by Sandel et al. [1982], which yielded an exospheric temperature of 400 K (with no error given). In addition, the Voyager 2 solar occultation at latitude 25.5° North analysed by Smith et al. [1983] gave an exospheric temperature of 420 ± 30 K. The discrepancy of $\sim$ 400 K is large. If these variations are real they are, by contrast, a much larger variation than what was observed by Lam et al. [1997a] at low latitudes on Jupiter. Atreya et al. [1984] suggested that there might be a real physical difference between the exospheric temperatures at the two latitudes. However, it is extremely difficult, in terms of dynamics and energy inputs, to explain why the equatorial region should be twice as hot as the low- to mid-latitudes. If energy is continually being deposited in the auroral region then it is intuitive that the auroral region remains hotter than the equatorial region.

The NASA/ESA/ASI spacecraft Cassini is currently orbiting in the kronian system and continues to be a source of exciting new knowledge. It is collecting a huge dataset covering many wavelengths and measuring particles and fields in-situ that will give us enormous insight over the coming years into the processes that govern this fascinating system. To increase the science return of this mission, it is of great importance to back up Cassini's observations with ground-based campaigns, both in terms of confirmation and correlation.

4.3 Observations

In determining the ionospheric temperature of Saturn, three datasets covering a wide range of resolving powers will be analysed. All observations were taken with the near-infrared spectrograph CGS4 (Cool Grating Spectrometer 4) on the United Kingdom Infrared Telescope (UKIRT – described in more detail in Section 2.1). The three datasets that are being analysed in this chapter, together with the grating used, are:

- September 1999 – medium resolution (150 lines mm^{-1} grating)
- February 2004 – high resolution (echelle grating)
- February 2005 – low resolution (40 lines mm^{-1} grating)

The September 1999 spectrum was first published by Miller et al. [2000] and is said to fit to a temperature of 600 K. In this work the spectrum will be re-analysed. The other two sets of observations – February 2004 and February 2005 – were performed as support observations for the Cassini spacecraft. The observations were proposed so that a reliable temperature could be ascribed to the auroral ionosphere by observing emission from H_3^+ in the L and L′ atmospheric windows.

The derivation of temperatures from spectra in this chapter *assumes* that the H_3^+ emission from the upper atmosphere of Saturn can be approximated as originating

UT Date	Instrument	λ_c (μm)	$\lambda/\Delta\lambda$	Slit ($''$)	Integration (mins)
17/09/1999	CGS4	3.60	5570	0.6 × 2.8	210
02/02/2004	CGS4	3.535	35000	0.6 × 2.4	26
02/2005	CGS4	3.80	1520	0.6 × 2.4	165

Table 4.1: Breakdown of the observations of Saturn analysed in this chapter. λ_c is the central wavelength of the spectrum.

from a thin shell in a state of Quasi Local Thermodynamic Equilibrium (Quasi-LTE). It was seen in the previous chapter that non-LTE effects had significant implications for the emission of H_3^+, especially when deriving temperatures and densities using spectral lines from different vibrational manifolds. It is likely that non-LTE effects has a role to play on Saturn too, although we do not yet have the means to investigate the extent to which it quenches the emission observed from the planet. In the meantime, as was the case for Jupiter for a great many years, it is assumed that the conditions of the upper atmosphere of Saturn can be approximated by Quasi-LTE.

4.3.1 September 1999 data

This data was originally published by Miller et al. [2000]. They observed the southern auroral region of Saturn with CGS4 on UKIRT at medium resolution ($R = 5570$) at around 3.6 μm in the L atmospheric window on the 17th of September 1999.

The published spectrum can be seen in Figure 4.1. Miller et al. [2000] quoted a temperature of 600 K which lies between the two analyses of the Voyager 2 occultation experiment by Festou and Atreya [1982] and Sandel et al. [1982]. This spectrum will be re-calibrated and re-analysed with the fitting routine described in Section 2.4 yielding a much lower temperature, more in agreement with the 400 K of Sandel et al. [1982].

A comparison of the spectrum of Miller et al. [2000] (seen in Figure 4.1), with the three theoretical spectra in Figure 4.2, clearly shows the incompatibility with the higher temperature, as a high temperature would require the ratio between the R(3, 3^-) and the R(1, 1^+) + R(1, 0^+) (doublet) to be $\sim$ 1, whereas a much lower ratio is actually observed. This fact motivated us to re-analyse this spectrum in more detail.

The spectrum covered a wavelength range from 3.52 μm to 3.68 μm, and the 2D spectral image of Saturn can be seen in Figure 4.3 with wavelength in the horizontal direction and spatial direction in the vertical. The observational configuration of the 1999 data can be seen in Figure 4.4. The slit was aligned North-South on the planet and the spatial resolution was $0.595'' \times 0.695''$ per pixel, with a grating dispersion of 0.2 nm per pixel using the 150 lines mm^{-1} grating on CGS4. The resolving power was $R = 5570$. At the time of observation, the sub-observer latitude on Saturn was -19.6° and the polar diameter was $17.8''$.

The data was taken between 12:12 UT and 17:46 UT on the 17th of February 1999 and was reduced by the ORAC-DR pipeline (see Section 2.2.1). It comprises of 15 exposures of 14 minutes each, making a total integration of 210 minutes. Each exposure is comprised of 6 coadds of 240 seconds each. The star HD 15335 was used as a flux calibrator – a G0V star with an L′ magnitude of $m_{3.8} = 4.43$ and a temperature of $T = 5930$ K (Alonso et al. [1999]).

During the observations, the telescope was nodded from the object beam (or the A beam) in such a fashion that the auroral region of Saturn was still lying across the slit in the B beam. This created, after the process of sky subtraction, a negative image of Saturn, as seen in Figure 4.3.

All the detectable H_3^+ emission from Saturn in the spectral image shown in Figure 4.3 covers vertical pixels number 70 to 71 for the positive and number 121 to 122 for the negative, with pixel row numbers being measured from the top of the image. These co-added rows can be seen in Figure 4.1, the spectral lines as identified by Miller et al. [2000] are indicated. The other lines present in the spectrum are likely to be reflected sunlight as the hydrocarbons below the homopause do not absorb at certain wavelengths. This lack of absorption is also seen at lower latitudes on Saturn, where the features are more prominent. A mid-latitude spectrum can be seen in Figure 4.7. In order to produce a clearer auroral H_3^+ spectrum, the mid-latitude spectrum was scaled to the same amplitude as the auroral one. The scaled spectrum was then subtracted from the auroral spectrum, removing most of the hydrocarbon features. The result of this scaling and subtraction can be seen in Figure 4.8.

Due to slight variations in sky emissions, the background level of the sky-subtracted spectrum is not completely constant. Since the fitting routine described in Section 2.4 only fits a constant background level to each spectrum – higher order background variability needs to be removed. A background level was fitted to Figure 4.8 and is shown as a dashed line in that figure. This background level was subtracted from the spectrum, and the resulting spectra is shown in Figure 4.9.

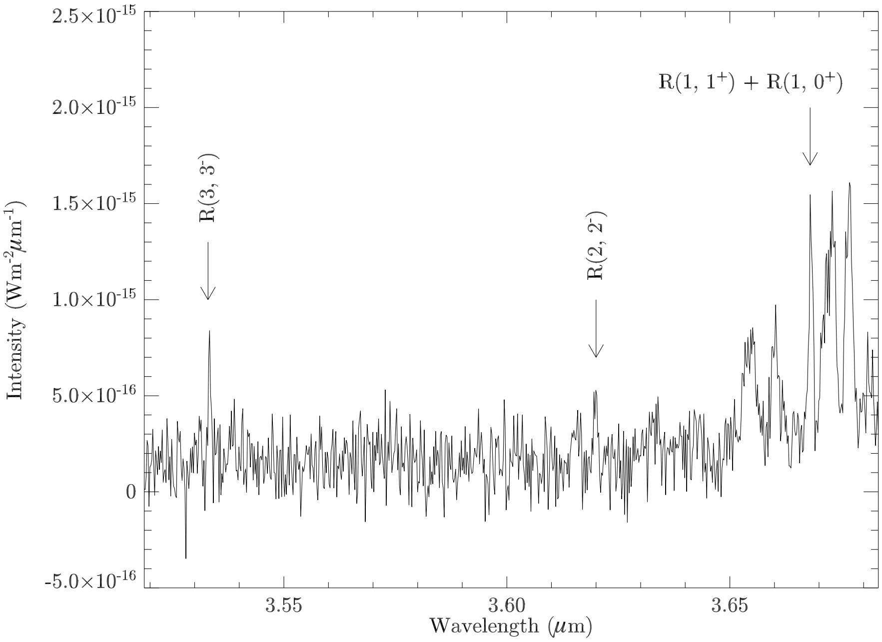

Figure 4.1: The H_3^+ spectrum of Saturn's south pole published by Miller et al. [1990]. It was reported to have a temperature of $T = 600$ K.

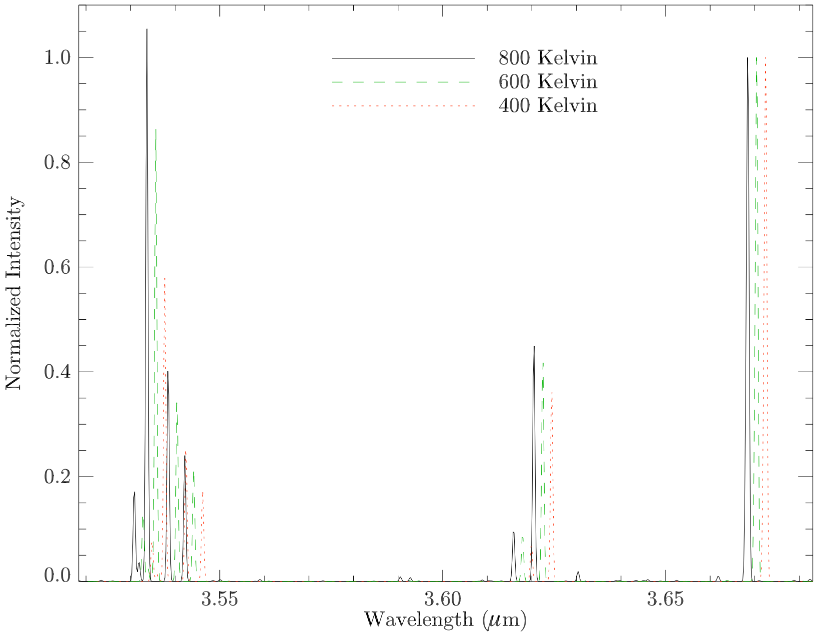

Figure 4.2: Theoretical H_3^+ spectra at temperatures of 800, 600 and 400 K. The spectra are normalised to the R(1, 1^+) + R(1, 0^+) line, and the 600 and 400 K spectra are shifted respectively by 0.002 and 0.004 μm to higher wavelengths for ease of viewing.

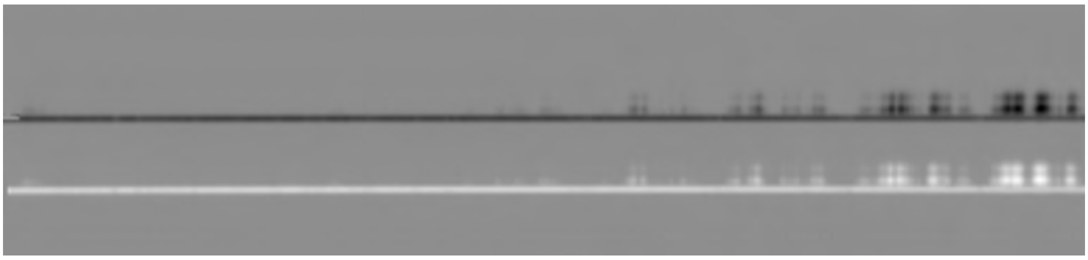

Figure 4.3: The 1999 Saturn data. Horizontal axis is wavelength and vertical axis is spatial. The continuum is the spectrum of the rings as per Figure 4.4. The bottom is the 'negative' image – the result of observing Saturn in the B beam. The top 'positive' image is the result of observing Saturn in the A beam. These two are combined to give the total signal.

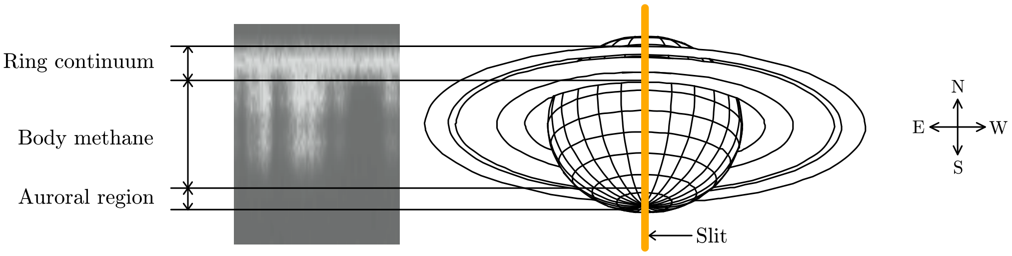

Figure 4.4: Observational configuration of the September 1999 data. The slit is aligned North-South on the planet. Part of the observed spectrum is seen on the left, with the ring continuum spectrum at the top.

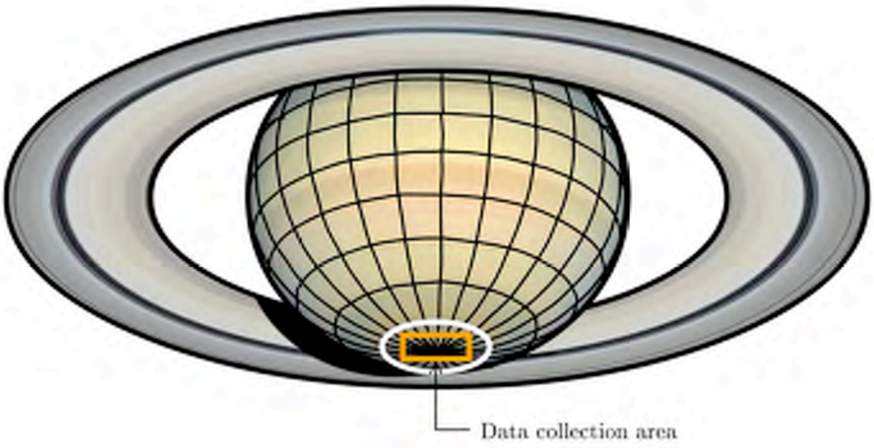

Figure 4.5: The CGS4 data collection area on Saturn in September 1999. The white circle indicate 15° co-latitude.

Figure 4.5 shows the area over which the spectrum was integrated (two rows were added to give the total auroral signal). The aurora is believed to be located at a co-latitude of ∼ 15° (e.g. Stallard et al. [1999]). Since the data collection area in Figure 4.5 falls entirely within the 15° co-latitude oval, there is no filling factor required, i.e. the spectrum in Figure 4.8 only samples the auroral region within which H_3^+ is believed to be formed by particle precipitation. It is of note that whilst the UV aurora forms a ring at co-latitude 15° (e.g. Trauger et al. [1998a]) the H_3^+ emission is contained entirely within that oval.

Analysis

To establish confidence that this spectral region is suitable for temperature determinations, an auroral spectrum of Jupiter taken on the same night was analysed with the H_3^+ spectrum fitting routine, discussed in Section 2.4.5. The spectrum can be seen in Figure 4.6 and it identifies for the first time the H_3^+ R(2, 0^-) hotband. The Jupiter spectrum fits to a temperature of $T = 1090 \pm 20$ K, which is within the range of previous observed temperatures for Jupiter (e.g. Lam et al. [1997a] and Raynaud et al. [2004]). Similarly, the derived column density for Jupiter is $N = 2.04 \pm 0.08 \times 10^{16}$ m^{-2}, which is also within the range of previously observed column densities. Maillard et al. [1990] observed what appeared to be a consistent under-population of the R(3, 3^-) line in their observations of Jupiter. Since we derived a 'normal' temperature and density, we find no evidence for this under-population. If the line was indeed under-populated, a much lower temperature would be derived, since cold H_3^+ in LTE is characterised by a low R(3, 3^-) to R(1, 1^+) + R(1, 0^+) ratio (< 1). In conclusion, this spectral region is suitable for temperature determinations on Saturn and we are confident that the flux calibration is reasonable.

Figure 4.2 shows three normalised theoretical H_3^+ spectra – one at 800 K, one at 600 K and one at 400 K. The R(3, 3^-) to R(1, 1^+) + R(1, 0^+) ratio of these modelled spectra is ∼ 1 at 800 K, ∼ 0.8 at 600 K, and ∼ 0.6 at 400 K. The ratio of these two lines in Figure 4.1 is ∼ 0.5, indicating that the spectrum is incompatible with a temperature of 600 K, and is more in line with $T \approx 400$ K. Figure 4.9 shows the spectrum of Miller et al. [2000] fitted with a fixed temperature of $T = 380$ K, giving a good fit to the spectrum. The error on this temperature can be estimated by finding

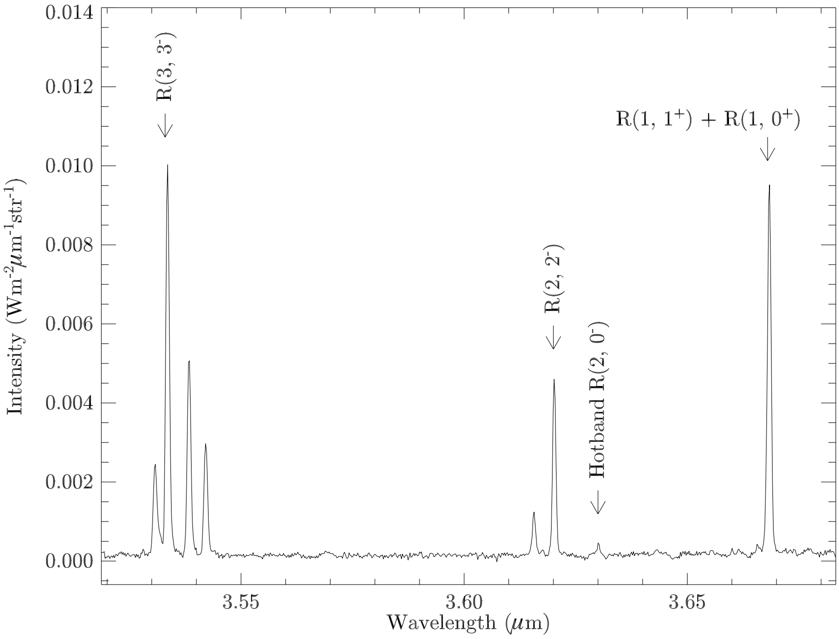

Figure 4.6: Spectrum of the northern aurora of Jupiter taken on the 17th of September 1999 (UT). It contains very distinct H_3^+ lines and has a fitted temperature of 1090 ± 20 K.

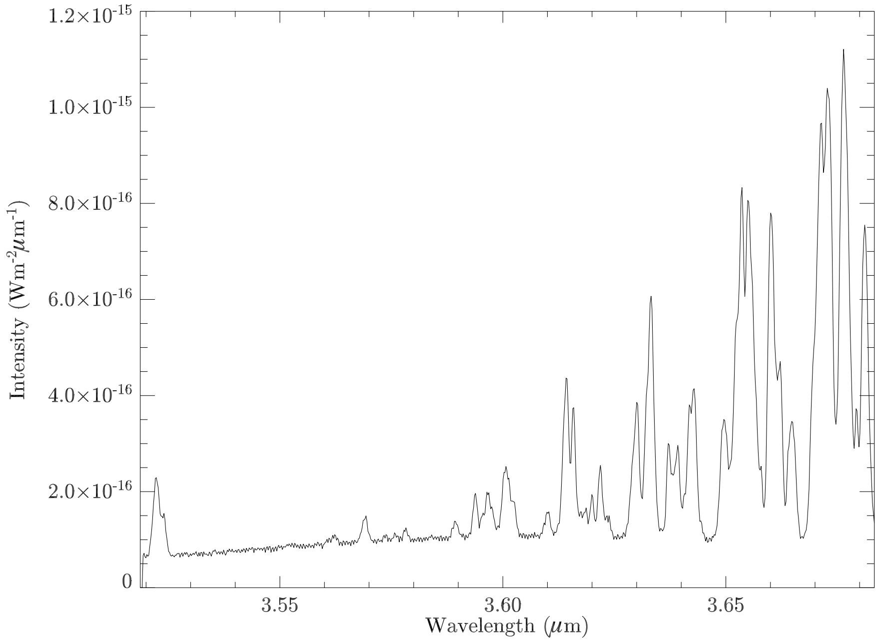

Figure 4.7: Mid-latitude spectrum of Saturn taken on the 2nd of February 2004. It shows reflected sunlight that the hydrocarbons in the troposphere were unable to absorb.

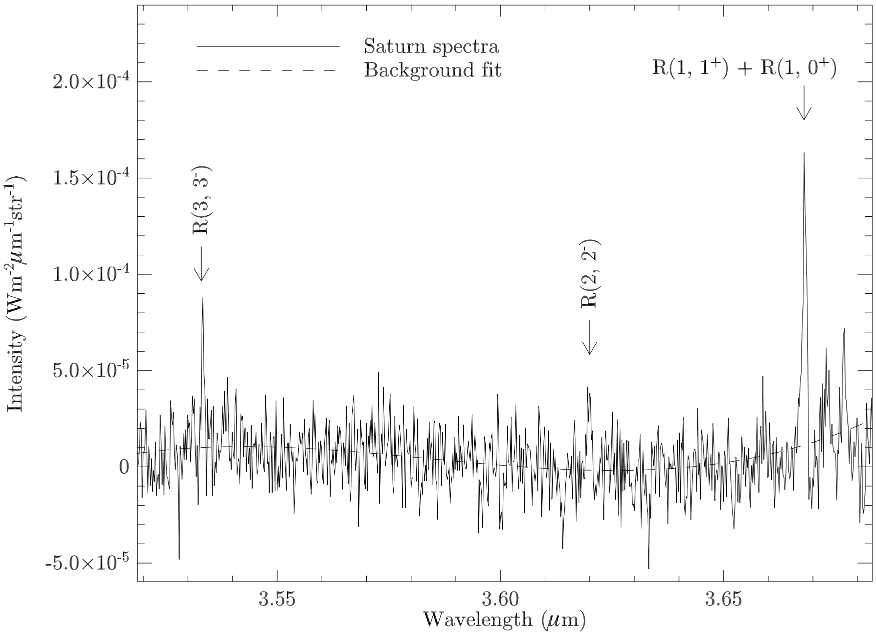

Figure 4.8: The September 1999 spectrum of Saturn with the scaled mid-latitude spectrum subtracted. Note that the intensity of the R(1, 1^+) + R(1, 0^+) is not affected by the process of methane subtraction.

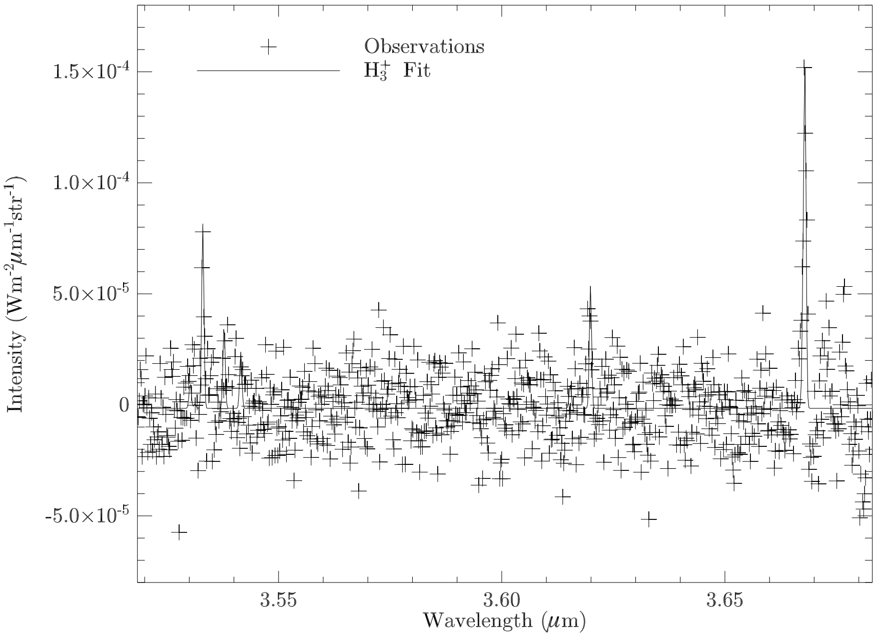

Figure 4.9: The 1999 Saturn spectrum fitted with a model H_3^+ spectrum with a temperature of $T = 380$ K, assuming LTE.

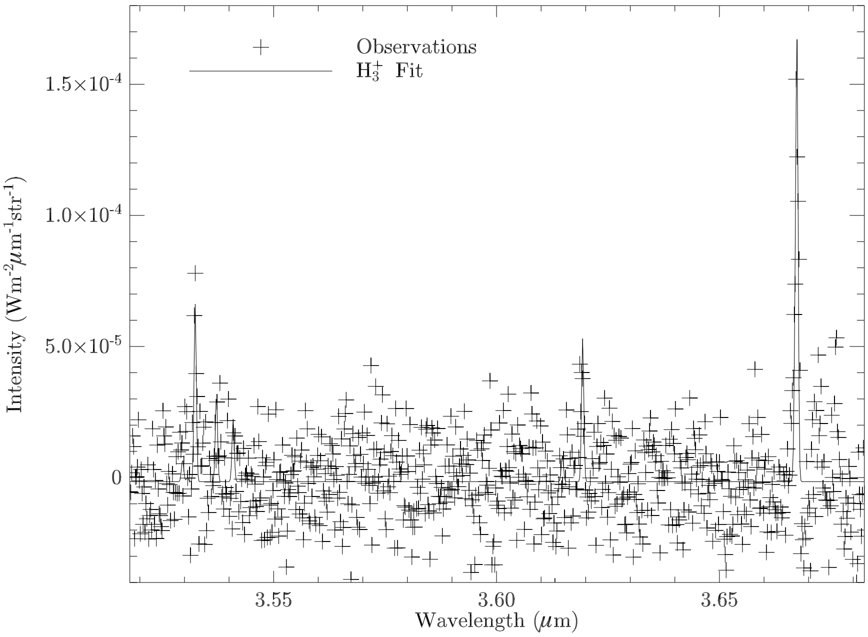

Figure 4.10: The September 1999 Saturn spectrum fitted with a model H_3^+ spectrum with a temperature of $T = 310$ K, assuming LTE.

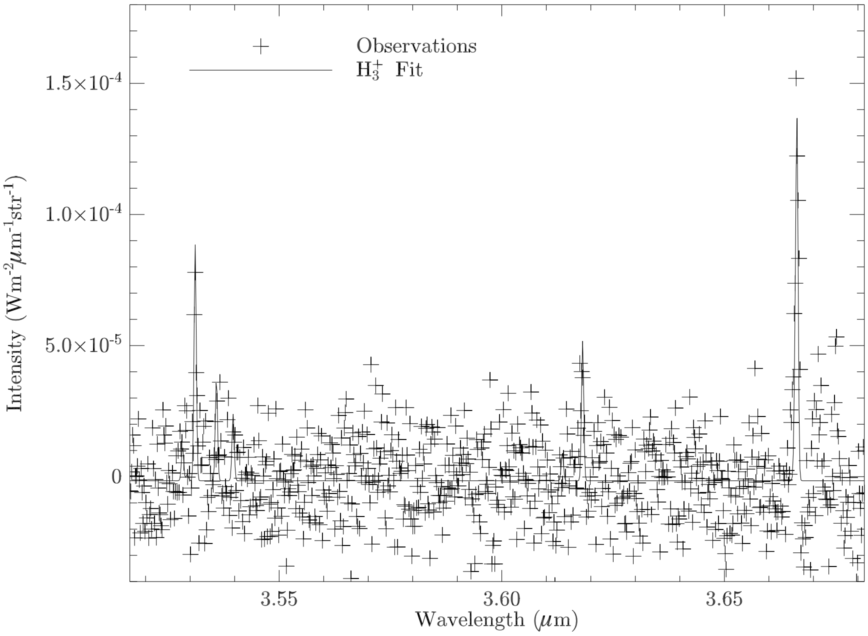

Figure 4.11: The September 1999 Saturn spectrum fitted with a model H_3^+ spectrum with a temperature of $T = 450$ K, assuming LTE.

the temperature lower and higher than the 380 K at which the fit becomes poor. Figures 4.10 and 4.11 shows the spectrum fitted with a temperature of 310 K and 450 K respectively. Since both of these fits are about 20% out, and considering the large noise on the data, an error of ± 70 K is likely to be a reasonable estimate of the error. Hence, the H_3^+ temperature on Saturn in September 1999 was $T = 380 \pm 70$ K.

The column density is very hard to constrain at these low temperatures, especially with large errors on the temperature. This is because small changes in temperature at low temperatures gives rise to a larger relative increase in intensity than at higher temperatures. This is highlighted in Figure 4.27, which shows the possible H_3^+ column densities for a range of temperatures given a fixed intensity in the R(3, 3^-) line. The September 1999 data is represented by the dashed line in this plot.

The column density in Figure 4.27 is calculated using:

$$N = \frac{I_{obs}}{I_{calc}(T)} \tag{4.3}$$

where I_{obs} is the observed integrated intensity of a particular H_3^+ transition in units of [$\mathrm{Wm^{-2}str^{-1}}$] and $I_{calc}(T)$ is the calculated intensity per molecule of the same transition, at a particular temperature T in units of [$\mathrm{Wstr^{-1}}$]. For all observations the R(3, 3^-) line was used. The calculated line-of-sight uncorrected column density at $T = 380$ K is $N = 4.6 \times 10^{16}$ $\mathrm{m^{-2}}$.

The line-of-sight correction close to the edge of the planet is shown in Section 2.3.3 to be a function of the thickness of the emitting layer of H_3^+. The observations were made at a fractional distance from the centre of the planet of 0.9. This gives a correction factor of 0.41 for a 100 km thick emitting layer, and 0.42 for a 1000 km thick layer. Since the difference is small we take the correction factor to be 0.41. This gives a line-of-sight corrected column density of $N = 1.9 \times 10^{16}$ $\mathrm{m^{-2}}$.

4.3.2 September 2004 data

A total of 15 hours of observing time was awarded on UKIRT between the 1st and 3rd of February 2004. This run was originally scheduled to use the UKIRT Imaging Spectrometer (UIST – described briefly in Section 2.1) but due to a failure in its cooling mechanism, CGS4 in echelle mode was used instead. The first night was lost due to poor weather so most of the observing was done on the 2nd of February. A

Group Nbr	UT Start	Nbr Coadds	ITIME (s)	Comment
75	06:40:19	32	960	Unusable
107	08:03:36	12	360	–
119	08:40:40	40	1200	–

Table 4.2: The group files of Saturn reduced by ORAC-DR on the 2nd February 2004. ITIME is the integration time per group. The exposure time per exposure is 30 seconds.

large fraction of the allocated hours were saved in the UKIRT queue system to be used at a later date, when UIST would be functional again. None of the allocated hours were used on the 3rd of February.

Table 4.2 lists the observations that were made of Saturn on the 2nd of February 2004. A total of 52 frames, each with an exposure time of 30 seconds were co-added to form an image with a total of 26 minutes exposed on Saturn. The 2D spectral image can be seen in Figure 4.14. The data was reduced, but not flux calibrated, using ORAC-DR. The data collection area on the southern aurora of Saturn for this dataset can be seen in Figure 4.12. It is apparent that there is no filling factor required for this set of observations. Again, all the detectable H_3^+ was summed to form the total signal.

The configuration of the observations can be seen in Figure 4.13. At the time of observation the sub-observer latitude on Saturn was -25.4° and the polar diameter was 18.6″. The slit was aligned East-West on Saturn across the polar cap and set to a width of one pixel (0.61″). In the sky (B) beam the telescope was nodded 60″ East, parallel to Saturn's equator in such a way that Saturn remained on the slit. In this fashion, both a positive and a negative image were produced when the first object frame was sky-subtracted, as shown in Figure 4.14. Order number 15 on the echelle grating was used to produce a high-resolution spectrum covering 3.521 μm to 3.549 μm with a grating dispersion of 0.1 nm per pixel. The resolution was $R \sim$ 35,000.

The auroral region (as indicated by Figure 4.13) of groups 107 and 119 were co-added and flux calibrated using the star spectrum of HD 46553 – spectral type A0V, L′ magnitude $m_{3.8} = 5.3$ and $T = 9900$ K (Leggett et al. [2003]). (Group 75 was unusable since the telescope drifted off the planet and a problem occured with the slit position angle. See Table 4.2.)

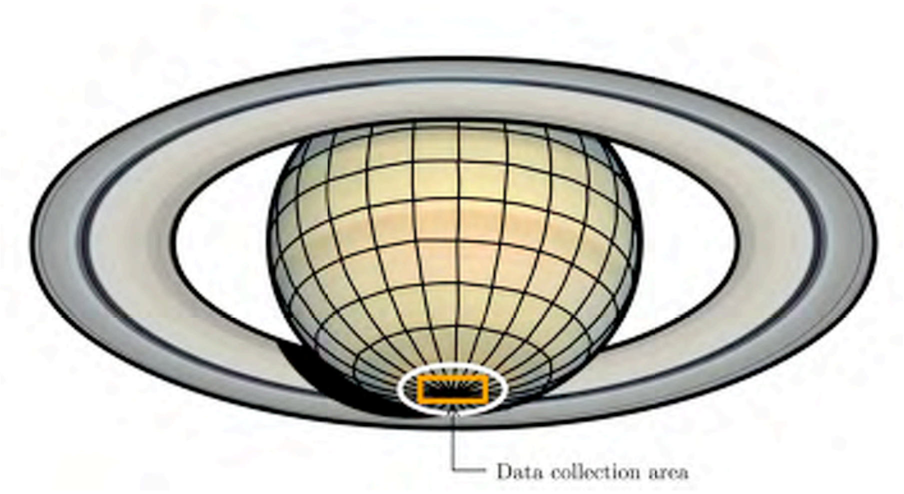

Figure 4.12: The CGS4 data collection area on Saturn in February 2004. The white circle indicate 15° co-latitude.

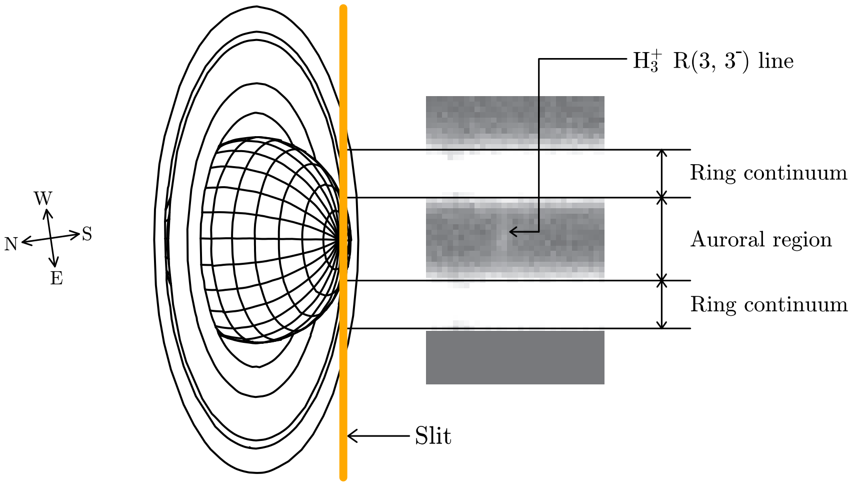

Figure 4.13: Observational configuration of the February 2004 data. The slit is aligned East-West on the planet. Part of the observed spectrum is seen on the right, with the ring continuum spectrum at the top and bottom and the auroral region sandwiched in-between.

Analysis

As before, a spectrum of Jupiter was taken as to determine if this spectral region is indeed useful in determining H_3^+ temperatures and densities. The Jupiter spectrum was taken on the 1st of February 2004 and was exposed for a total of 60 seconds. The spectrum, seen in Figure 4.15, is fairly noisy because of the short integration time. It fits to a temperature of $T = 1200 \pm 200$ K. As this is within the range of temperatures previously observed on Jupiter, it is concluded that this spectral region can indeed be

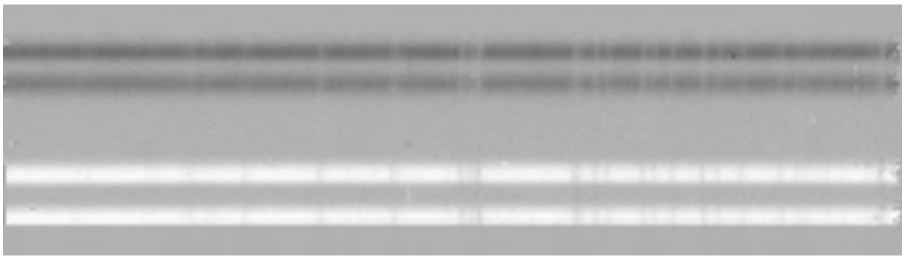

Figure 4.14: Group 107 of the Saturn 2004 data (see Table 4.2). Horizontal axis is wavelength and vertical axis is spatial. The continuum is the spectrum of the rings. The top dark signal is the negative of the lower, brighter, signal – these two are combined to give the total signal.

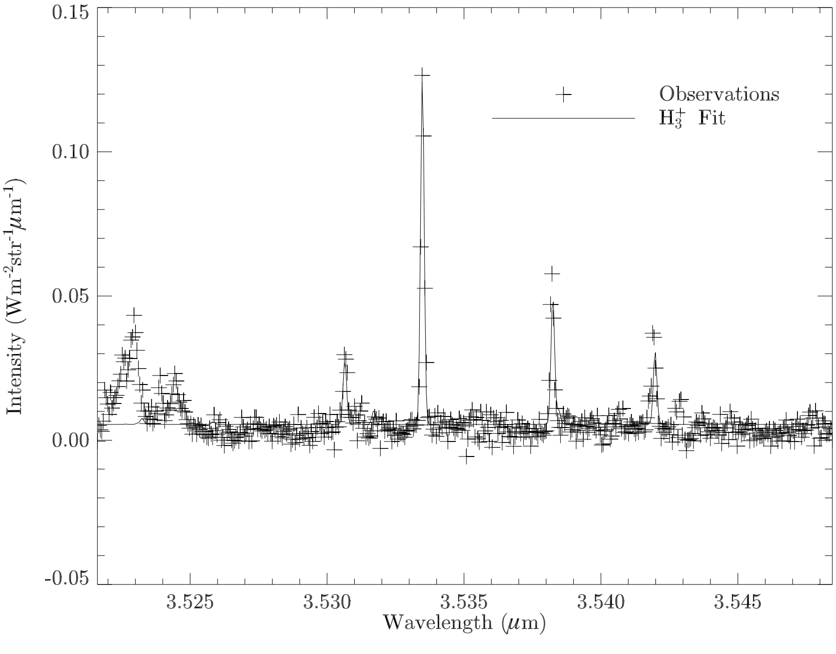

Figure 4.15: The Jupiter spectrum taken on the 1st of February 2004. It fits to a temperature of 1200 ± 200 K.

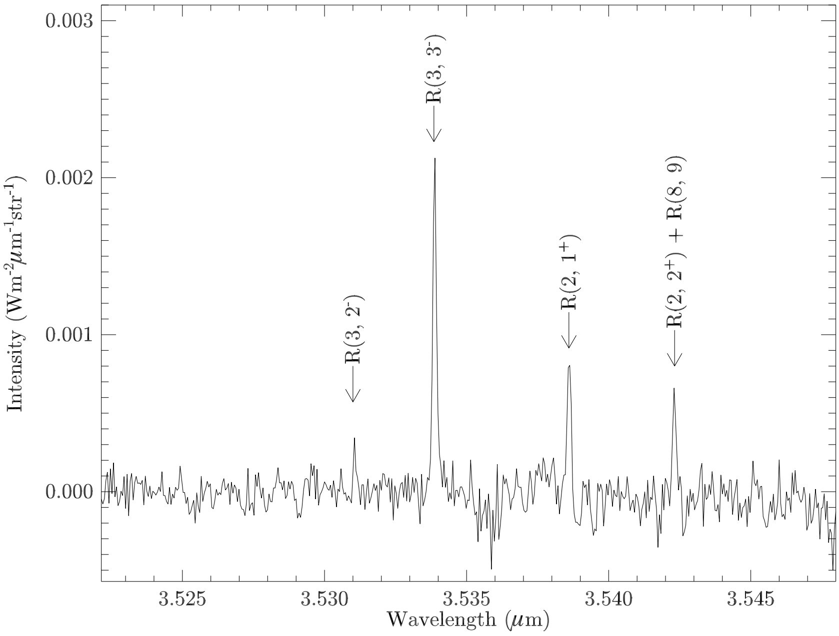

Figure 4.16: The flux calibrated spectrum of Saturn taken on the 2nd of February 2004.

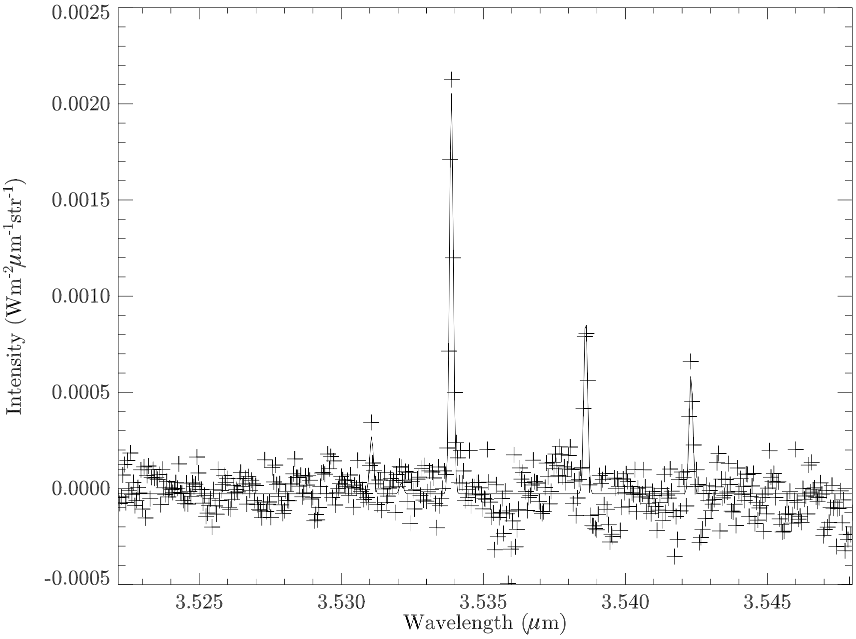

Figure 4.17: The 2004 Saturn spectrum fitted to a temperature of 420 ± 70 K, assuming conditions of LTE.

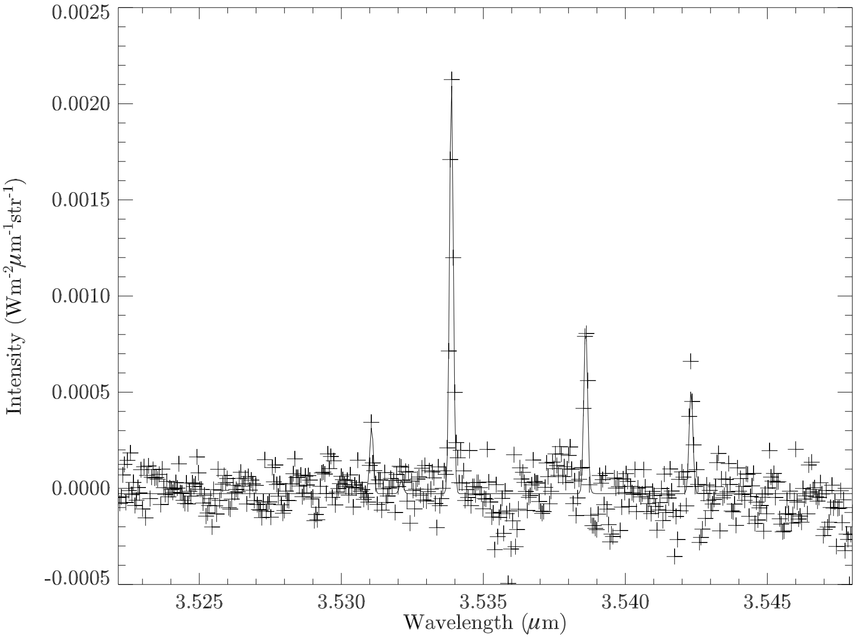

Figure 4.18: The 2004 Saturn datum plotted with a model H_3^+ spectrum of 600 K, assuming LTE.

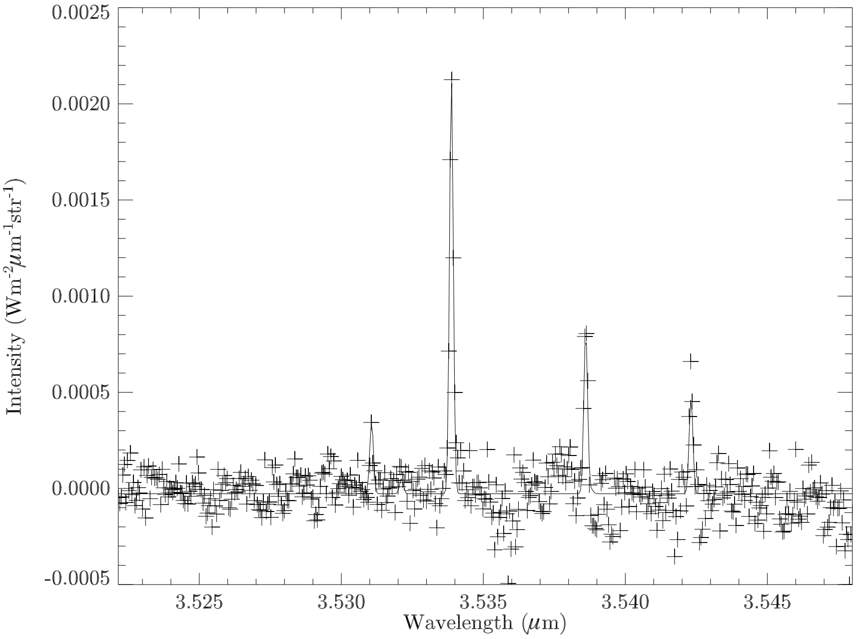

Figure 4.19: The 2004 Saturn datum plotted with a model H_3^+ spectrum of 800 K, assuming LTE.

used to determine ionospheric H_3^+ temperatures. The fitted column density of Jupiter is $N = 3 \pm 1 \times 10^{16}$ m^{-2}.

The Saturn spectrum was fitted using the routine described in Section 2.4 and was found to have a temperature of 420 ± 70 K. It is notable that this temperature has a lower error associated with it than the Jupiter spectrum. This is partly because of the short integration time on Jupiter and partly because of the steeper ratio evolution of the observed lines at lower temperatures compared to at higher temperatures.

The line-of-sight uncorrected column density derived from the R(3, 3^-) line at $T = 420$ K is $N = 1.3 \times 10^{17}$ m^{-2}. The fractional distance from the centre of the planet was ~0.8, which gives a line-of-sight correction factor of 0.56, producing a line-of-sight corrected column density of $N = 7.3 \times 10^{16}$ m^{-2}.

The column density is, as in 1999, very difficult to pin down and relies largely on the assumed temperature. The dotted line in Figure 4.27 shows the possible column densities over a range of temperatures for the total intensity observed in the R(3, 3^-) line. Note that the 2004 spectrum yields much larger column densities than all the other observations. This may suggest that:

1. There is a problem with using HD 46553 (a cold G0V) star as a flux standard.
2. There were variable sky conditions during observations (which passed unnoticed).
3. A process is at work which increases the column density by a factor of ~ 4 compared to 1999. One explanation could be an increased precipitation flux.

The fact that the Jupiter column density appears to be in accordance with other works (e.g. Lam et al. [1997a]) would suggest that the flux calibration is reasonable. Note, however, that the high end of the February 2004 temperature limit yields a similar column density to that of the low temperature limit of the September 1999 data.

4.3.3 February 2005 data

As in 2004, 15 hours of observing time was awarded to use UIST on UKIRT to observe the auroral region of Saturn between the 26th and the 28th of February 2005 and, once again, UIST was out of commission, this time due to a jammed filter wheel. It was decided to perform an equivalent medium resolution observation using the CGS4

40 lines mm^{-1} grating covering both the L and L$'$ atmospheric windows, producing a spectrum covering 3.5μm to 4.1μm. This gave a grating dispersion of 2.4 nm per pixel and a resolution of $R = 1520$. Spectra taken with such a configuration have produced very reliable H_3^+ temperatures on Jupiter (e.g. Lam et al. [1997a]).

The position-angle (or slit-angle) was set to -96.79°, which aligned the slit East-West across the polar cap. This configuration was identical to that of February 2004, shown in Figure 4.13.

During the observations of 2005, the telescope had major problems tracking on Saturn. Consequently, the group files were rendered useless since they were blurred by the gradual drift of the telescope away from Saturn. Instead, the ring gap of each individual image of acceptable contrast was recorded for the duration of the observing run. The ring gap is the distance, in pixels, between the rings, as indicated by a and b in Figure 4.20. A large ring gap means that the slit is positioned far down the planet, whereas a very narrow ring gap means a near pole-aligned slit. Our region of interest was the pole and surrounding co-latitudes down to $\sim 15°$. Therefore, if the ring-gap was smaller than 10 pixels, or $6''$, it was accepted, since one pixel is $0.61''$. A total of 165 minutes (2.75 hours) of usable time was spent on Saturn. Note that quite a few of the spectra were exposed on much lower latitudes and some were even close to equatorial. The co-add of all the acceptable Saturn spectra can be seen in Figure 4.21.

The data collection area was similar to that of 2004 seen in Figure 4.12, requiring no filling factor.

The star HD 64648 was used for flux calibration. It has a spectral type A0V, a temperature of T = 9,900 K and a magnitude in the L$'$ window of $m_{3.8} = 5.3$. The data reduction was performed as before within ORAC-DR using an `EXTENDED_SOURCE` recipe.

Analysis

The H_3^+ Q region (3.9 to 4.1 μm) has proven to contain a very reliable and accurate set of lines used to derive the ionospheric temperatures on both Jupiter and Uranus (e.g. Lam et al. [1997a] and Encrenaz et al. [2003]). The February 2005 Saturn spectrum can be seen in Figure 4.21. It shows that a low resolution spectrum covering this wide

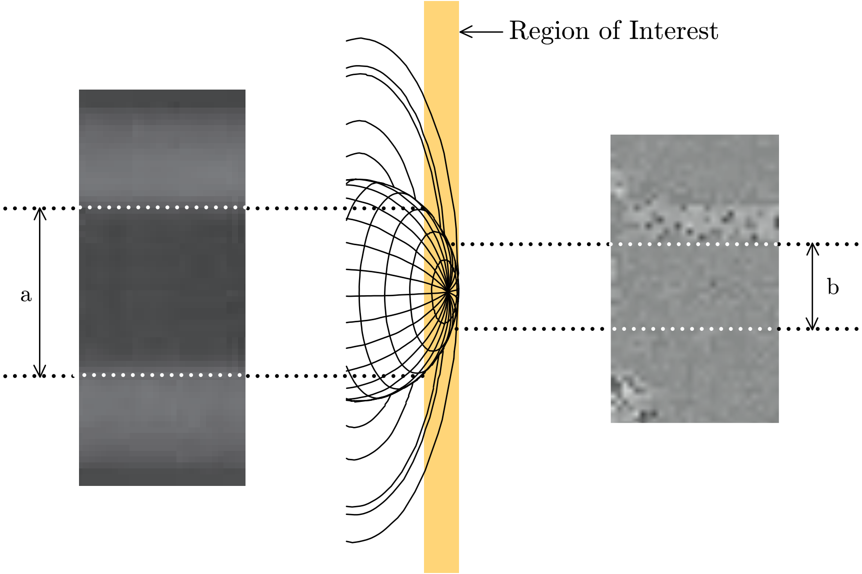

Figure 4.20: Schematic of how the ring gap facilitates the determination of location on Saturn. Note that only a very small part of both spectra is shown here.

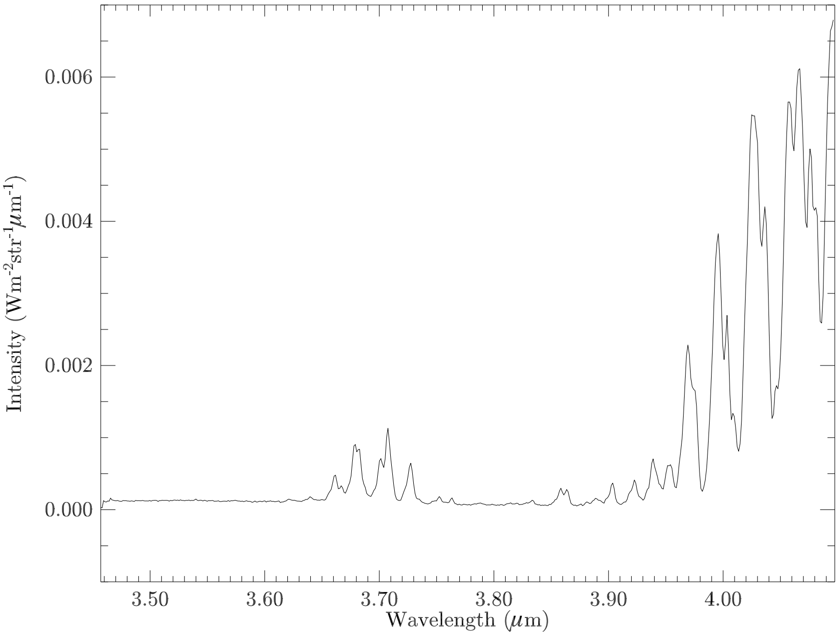

Figure 4.21: The flux calibrated spectrum of Saturn taken in February 2005. It exhibits the lack of absorption of sunlight due to low altitude hydrocarbons.

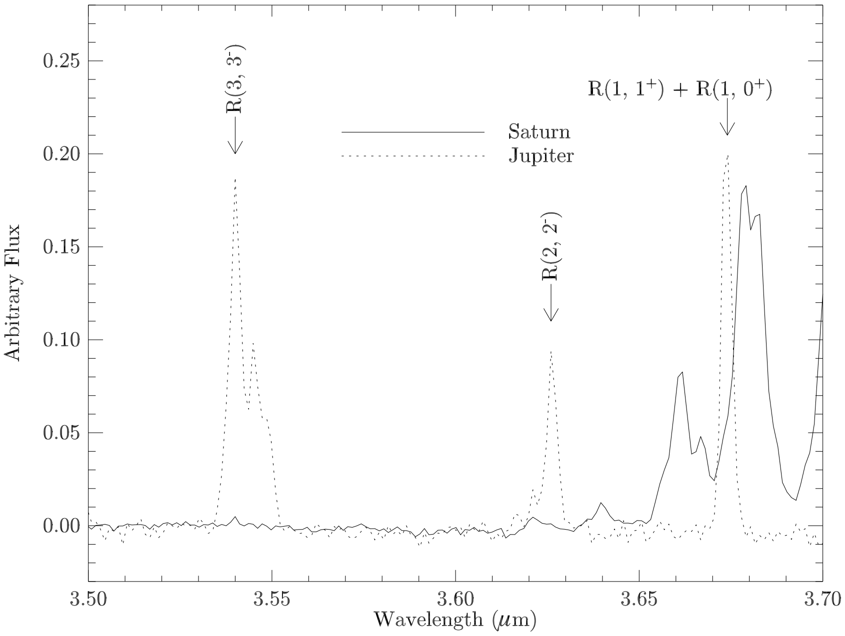

Figure 4.22: The spectrum of Saturn of February 2005 compared to the Jupiter spectrum from the same observing run. Note that this figure only plots between 3.5 μm and 3.7 μm.

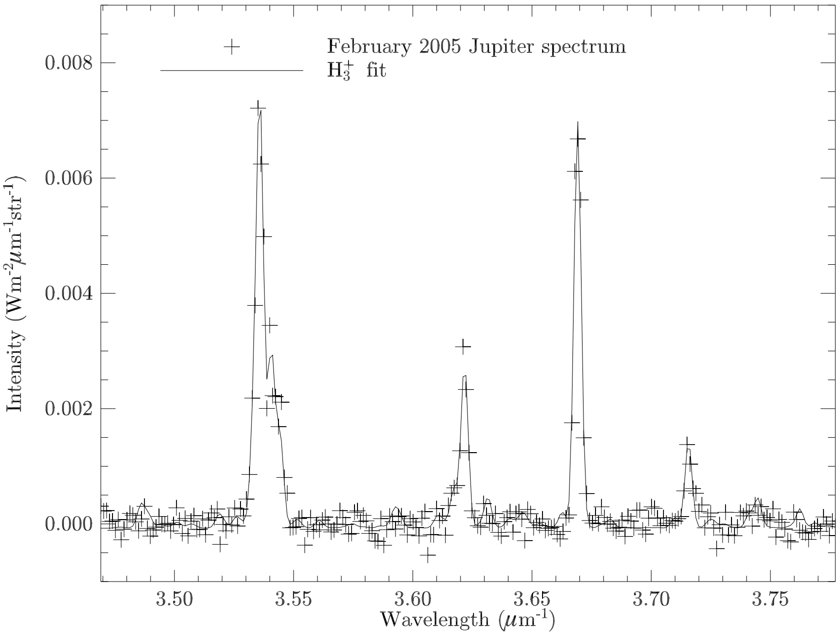

Figure 4.23: The Jupiter spectrum taken in February 2005 fitted with a temperature of $T = 1170 \pm 40$ K.

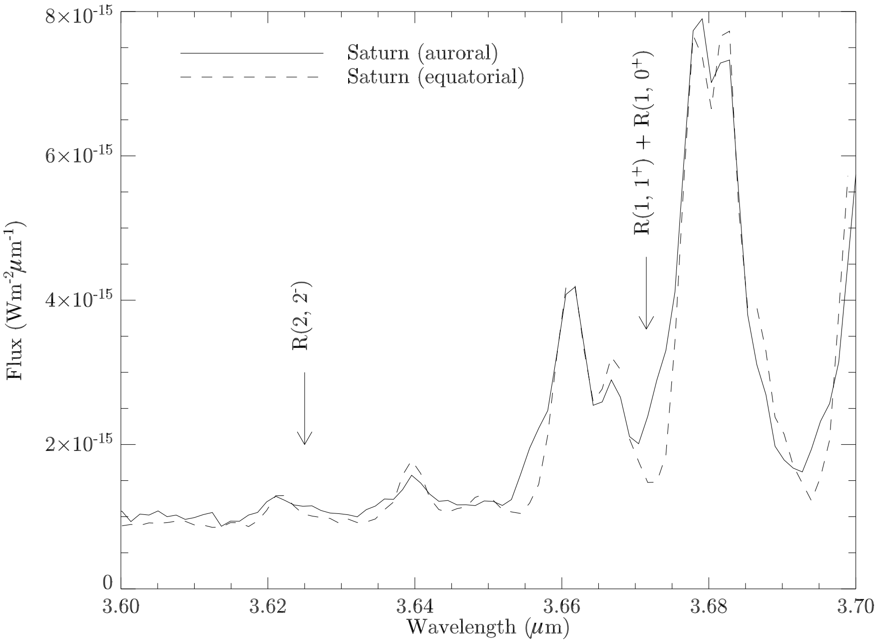

Figure 4.24: The auroral (solid) and equatorial (dashed) spectrum of Saturn of February 2005. The equatorial spectrum shows only hydrocarbon whilst the auroral spectrum shows the methane in combination with what could be the R(1, 1^+) + R(1, 0^+) H_3^+ line at 3.67 μm.

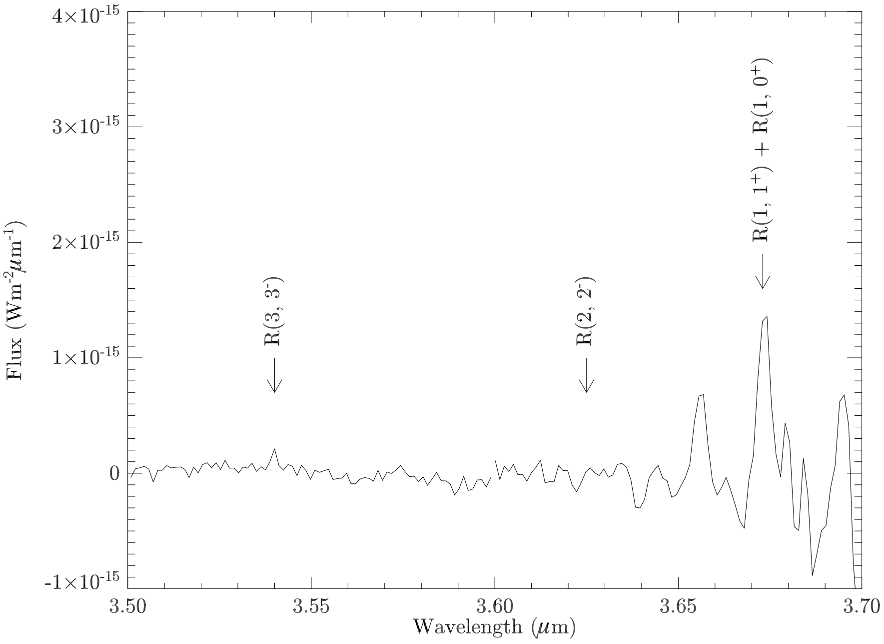

Figure 4.25: The difference between the two spectra shown in Figure 4.25. If the lack of hydrocarbon absorption is constant at all latitudes, this spectrum would show the pure auroral H_3^+ spectrum.

spectral region is useless in terms of identifying H_3^+ lines and deriving LTE temperatures from these. The prominent lines seen in Figure 4.21 are the reflected sunlight not absorbed by the hydrocarbons at and around the homopause, and completely swamp any H_3^+ emission. The only candidate H_3^+ line is the R(3, 3^-) at 3.53 μm. This part of the spectrum is shown in Figure 4.22 together with the Jupiter spectrum taken on the same run, indicating where we might find the other adjacent lines.

In trying to find the doublet R(1, 1^+) + R(1, 0^+) line, the low-latitude spectrum due to lack of hydrocarbon absorption from September 1999 was scaled and degraded to the same resolution used in 2005. This spectrum can be seen in Figure 4.24. The resultant subtracted spectrum is seen in Figure 4.25. It is very difficult, due to the low resolution and crudeness of method, to positively identify the R(1, 1^+) + R(1, 0^+) line from this subtraction. If the subtraction does indeed bring out the R(1, 1^+) + R(1, 0^+) line, then it gives a ratio with the R(3, 3^-) line of ~ 0.2, yielding a temperature of $T \approx 200$ K.

In order to constrain the range of possible column densities as a function of temperature, the R(3, 3^-) line was fitted with a gaussian. This fit can be seen in Figure 4.26. The FWHM of the fit is 0.0018 μm and the height of the line is 2.1×10^{-5} Wm$^{-2}\mu$m^{-1}str^{-1}. The column density derived from the emission per molecule, assuming LTE for a range of temperatures, can be seen in Figure 4.27. As can be seen, there is a wide range of column densities within any small temperature region. At $T = 400$ K, the line-of-sight uncorrected column density is $N = 5.2 \times 10^{16}$ m^{-2}.

The configuration was very similar to that of 2004. The fractional distance from the centre of the observations was ~ 0.8, giving a line-of-sight correction factor of 0.56. This gives a line-of-sight corrected column density of $N = 2.9 \times 10^{16}$ m^{-2} assuming a temperature of 400K.

4.4 Discussion

The temperature found in September 1999 is $T_{99} = 380 \pm 70$ and the temperature found in February 2004 is $T_{04} = 420 \pm 70$. It was not possible to derive a temperature from the 2005 data. Therefore, the average temperature is 400 K. The combined error

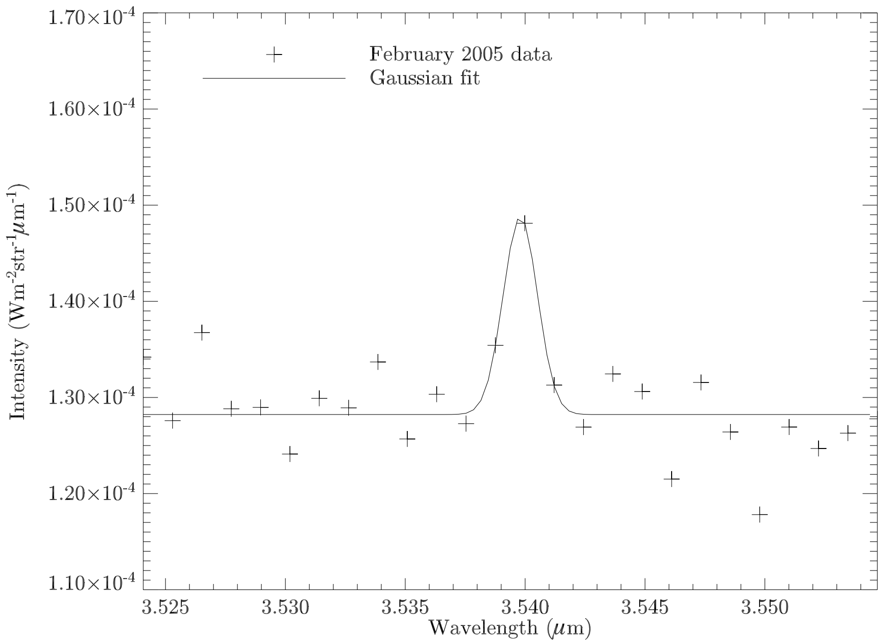

Figure 4.26: The R(3, 3^-) line in the February 2005 data fitted with a gaussian. The FWHM is 0.0018 μm.

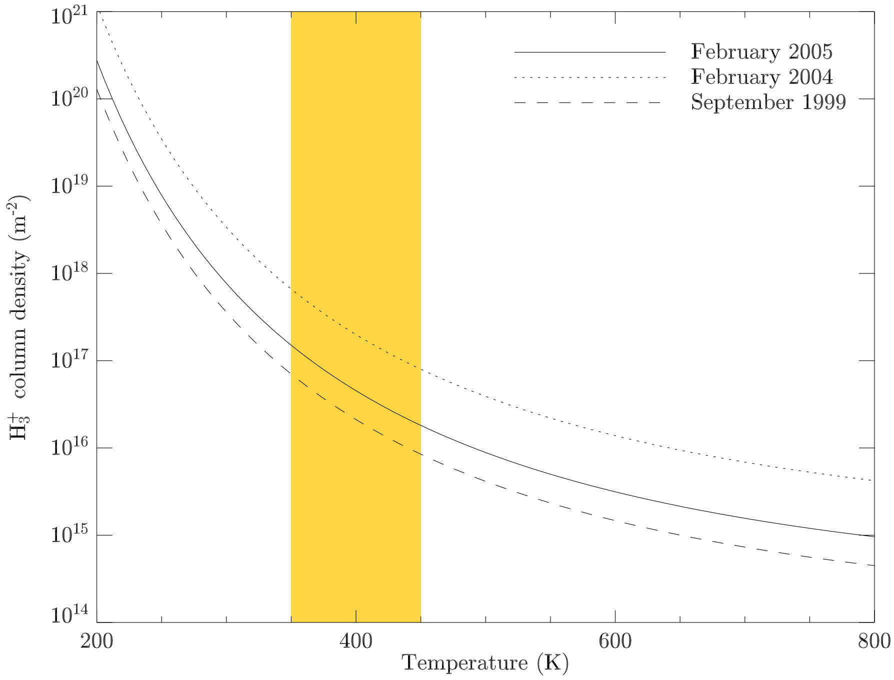

Figure 4.27: The range of line-of-sight corrected column densities for a given H_3^+ temperature assuming LTE conditions for all three sets of observations. The shaded region indicates the temperature range derived in this thesis.

Year	Pixelsize ($''$)	Intensity ($\mathrm{Wm^{-2}str^{-1}}$)
1992	1.1×2.2^a	1.5×10^{-7}
1999	0.595×0.625	5.3×10^{-8}
2004	0.41×0.85	5.0×10^{-7}
2005	0.61×0.61	1.1×10^{-7}

Table 4.3: The line-of-sight corrected intensity of the H_3^+ fundamental Q(3, 3^-) line for the available Saturn observations. [a]The spectrum of 1999 is corrected for the under-filling of the pixels.

on the average temperature is given by the familiar rule of propagation of errors:

$$\Delta T = \frac{1}{2}\sqrt{(\Delta T_{99})^2 + (\Delta T_{04})^2} \tag{4.4}$$

where ΔT_{99} is the error on the September 1999 temperature measurement and ΔT_{04} is the error on the February 2004 temperature determination. The error becomes:

$$\Delta T = \frac{1}{2}\sqrt{(70)^2 + (70)^2} = 50 \text{ K} \tag{4.5}$$

Therefore, the average ionospheric H_3^+ temperature of Saturn is found to be $T = 400 \pm 50$ K. This is the first reliable determination of the auroral ionospheric H_3^+ temperature on Saturn. It is similar to the Voyager 2 stellar occultation analysis of Sandel et al. [1982], although that was obtained at a much lower latitude (4°N).

The line-of-sight corrected column density derived in 1999 was $N_{99} = 1.9 \times 10^{16}$ $\mathrm{m^{-2}}$ and in 2004 it was found to be $N_{04} = 7.3 \times 10^{16}$ $\mathrm{m^{-2}}$. This gives an average column density of $N = 4.6 \times 10^{16}$ $\mathrm{m^{-2}}$. Note that the difference between the two column densities is only a factor of four, whereas the difference of intensity of the H_3^+ R(3, 3^-) line is a factor of 10 between the two years, because of this the slightly different temperatures derived for each year.

The average H_3^+ column density derived in this chapter for Saturn is equivalent to the column densities derived for Jupiter (e.g. Lam et al. [1997a]). This means that mechanisms which reduce the ion density, as discussed in Section 4.1, may no longer me required.

All the temperatures and column densities of H_3^+ derived for Saturn in this chapter are auroral averages. This is because the H_3^+ signal is too weak for the analysis of individual rows. There are large variations in the auroral average R(3, 3^-) intensity, with September 1999 being particularly bright – almost 10 times brighter than in 2004, see Table 4.3. The 1999 spectrum covered some 50% of one rotation of Saturn (1 day on Saturn = $10^h39'$), the 2004 spectrum covered about 20% of one rotation, whereas the 2005 data covered almost an entire rotation of the planet. Consequently, there could be local intensity variations where the 2004 spectrum sampled a very dense region of H_3^+. However, due to the viewing geometry of Saturn, no part of the aurora (i.e. co-latitude $< 15°$) is hidden as the planet rotates. This, in combination with the large data collection areas (Figure 4.5 and 4.12), suggests that it is not *local* intensity effects that give rise to the variations in intensity seen in Table 4.3.

For the 2004 datum to have a similar column density as in 1999, given the intensity of the H_3^+ R(3, 3^-) line, a temperature of some 550 K is required (Figure 4.27). However, the February 2004 spectrum, seen in Figure 4.18, is incompatible with a temperature of 600 K, suggesting that these are real intensity differences. As discussed in Section 4.2, large intensity variations have also been observed from the auroral region in the ultraviolet (e.g. Trauger et al. [1998b]).

How does the ionospheric temperature derived in this chapter fit into other existing observations? Geballe et al. [1993] could not attribute a temperature to their H_3^+ spectrum, but concluded that it could be compatible with the 800 K derived from the Voyager 2 occultation experiment analysed by Festou and Atreya [1982]. Their observed spectrum can be seen in Figure 4.28. They observed a maximum line flux in R(3, 3^-) of $\sim 3.3 \times 10^{-18}$ Wm^{-2} which gives a column density of $N = 5.8 \times 10^{16}$ m^{-2} for $T = 400$ K, which falls inbetween the values derived here for the years 1999 and 2004.

If a temperature of 400 K is assumed for both 1999 and 2004, then the column densities become $N_{99} = 2.1 \times 10^{16}$ m^{-2} and $N_{99} = 2.0 \times 10^{17}$ m^{-2}. They are different by a factor of 10 which is expected since there is an intensity difference in the R(3, 3^-) line of about 10.

On Jupiter and Uranus the use of medium resolution L′ spectra has been a cornerstone in the derivation of ionospheric H_3^+ temperature and densities. On Saturn, as was observed in 2005, such a spectrum does not show *any* of the H_3^+ Q region spectral lines and, consequently, no temperature or density can be derived. This is indicative of major differences in the upper atmosphere of these planets, e.g. differences in the composition and chemistry at the homopause.

The total H_3^+ emission (see Section 2.4.4) in 1999 is $E_{99} = 0.76$ μWm^{-2} and in 2004 is $E_{04} = 9.14$ μWm^{-2}. This large difference, coupled with the fourfold difference in the column density, suggests that when large amounts of energy are being injected through particle precipitation, creating large volumes of H_3^+, then the H_3^+ itself acts as a thermostat, keeping the temperature at a constant ~ 400 K.

In Chapter 4, the precipitation required to produce a column of H_3^+ was calculated using the Equation 3.44. Assuming that the the kronian upper atmosphere responds in the same fashion to particle precipitation, we can calculate what energy is required to produce the observed ion densities. The precipitation energy in 1999 is $P_{99} = 0.32$ mWm^{-2} and in 2004 is $P_{04} = 7.13$ mWm^{-2}. Hence there is a 22-fold difference in the energy injected by particle precipitation between the two years, and despite this very large difference, the thermosphere remains at a constant temperature. H_3^+ cannot emit enough energy and, thus, the thermostatic effect of H_3^+ is not observed on Saturn. This effect is known to be very important on Jupiter.

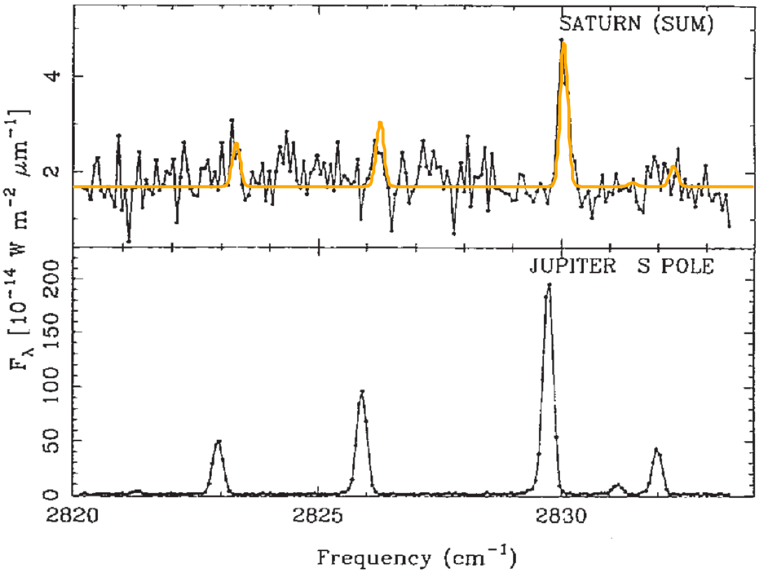

Figure 4.28: The spectra published by Geballe et al. [1993], of Saturn (top) and Jupiter (bottom). The Saturn spectrum has a theoretical H_3^+ spectrum of 400 K plotted over it.

Chapter 5

Uranus

5.1 Introduction

Before the arrival of Voyager 2 at Uranus in 1986, very little was known about this distant planet. Since both Jupiter and Saturn had a magnetic field and aurora, it was speculated that Uranus would also exhibit these phenomena. The first observational suggestion of an aurora was published by Clarke [1982], who studied Lyman-α emission using the International Ultraviolet Explorer (IUE). During their observations, the disc-average emission due to hydrogen Lyman-α varied by a factor of ~ 2, which, assuming that these variations were due to large variations in charged particle excitation, points toward the existence of an aurora. They suggested that the solar EUV emission at $\sim$ 20 AU could not disassociate enough H_2 to produce large quantities of H^+ nor could it produce the large variations in intensity. This view was supported by Caldwell et al. [1983] who observed an H_2 feature at 1600 Å.

Voyager 2 arrived at Uranus on the 24th of January 1986 and confirmed the existence of a magnetosphere (Ness et al. [1986]) and an aurora (Herbert and Sandel [1994]). The spacecraft presented scientists with the oddest magnetic field configuration seen in the solar system – schematically shown in Figure 5.1. The configuration was highly surprising since it was previously postulated that magnetic fields should line up more or less with the rotational pole of the planet, as is the case on Earth, Jupiter and Saturn. Since the rotational axis is almost aligned with the ecliptic and the magnetic pole is offset some 60° from that, the magnetic poles traverse from being aligned to the interplanetary field (IMF) to having opposite direction in a single uranian day. In addition, the centre of the magnetic field is offset some 0.3 R_U from the centre of the planet (Ness et al. [1986]). The configuration is likely to create a very dynamic and variable system. Tóth et al. [2004] constructed a three dimensional magnetohydrodynamic model (MHD) for the configuration at the time of the Voyager 2 encounter. It showed that a spinning magnetosphere results in a twisted magnetotail, as shown in Figure 5.2. The tail is also stretched, due to the plasma-flow within the magnetosphere.

There has been suggestions that both Uranus and Neptune, which has a similar configuration, are undergoing magnetic field reversal (Ye and Hill [1994]). However, the probability of observing this happening on two planets in the solar system at the same time is very small.

In understanding the emission from the auroral regions of Jupiter and Saturn, the processes that govern the particle population inside the magnetosphere have been shown to play a crucial part (e.g. Cowley and Bunce [2001] and Cowley et al. [2003a]). It is likely that such processes are important on Uranus too.

5.1.1 The ionosphere of Uranus

Before the arrival of Voyager 2 at Uranus, Clarke et al. [1986] performed a four year study of the H Lyman-α emission in the far ultraviolet, using the International Ultraviolet Explorer (IUE). They found that this emission varied independently of the solar H Lyman-α emission, suggesting that the main excitation mechanism is connected to the internal properties of the Uranus system, such as particle precipitation. They also compared the H Lyman-α emission to the solar wind velocity and density measurements of Voyager 2 and Pioneer 11, and found no evidence supporting a correlation. Consequently, these emissions from Uranus were believed to be powered by an active magnetosphere, such as is observed on Jupiter.

Once Voyager 2 arrived at Uranus, the interpretation of the observations of Clarke et al. [1986] changed. Uranus was found to have a hot thermosphere, with an exospheric temperature of $T = 800 \pm 100$ K (Herbert et al. [1987]), and an extensive atomic hydrogen corona extending beyond ~ 4 R_U, such that the H Lyman-α emission from the sunlit side of the planet is probably produced by dayglow. The dayglow

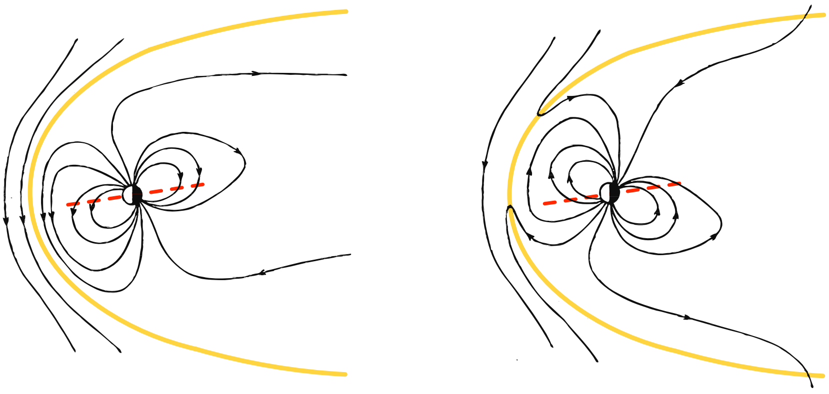

Noon

Midnight

Figure 5.1: The orientation of the magnetic field at noon and at midnight of Uranus at the Voyager 2 encounter in 1986, as seen in the plane perpendicular to the ecliptic. The solar wind direction is into the paper with the Sun to the left. The shaded line is the magnetopause and the dashed line is the axis of rotation. After an illustration by Ye and Hill [1994].

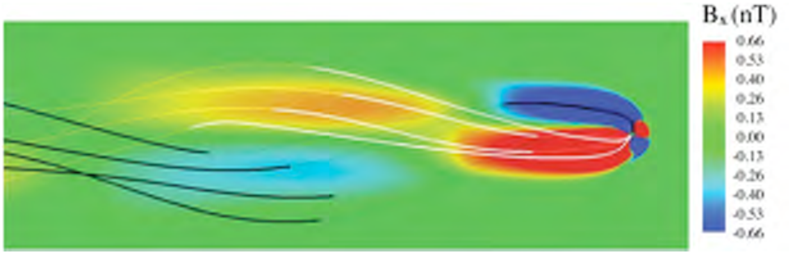

Figure 5.2: The MHD model by Tóth et al. [2004] showing that the magnetotail twists as the magnetosphere rotates daily at the time of the Voyager 2 encounter. The black lines are attached to the northern ULS pole and the white lines to the southern ULS pole.

reaction can be written as:

$$H^+ + e^- \rightleftharpoons H + h\nu \tag{5.1}$$

where $h\nu$ is the airglow emission, which is emission lines formed by recombination of ionised hydrogen in the very extended corona.

The aurora, as observed in the ultraviolet, is highly localised (Herbert and Sandel [1994]) and so the precipitation process might be incapable of causing any widespread ionisation. In such a case, the main mechanism for creating an ionosphere is likely to be the ionisation by solar EUV radiation. The ionising solar flux is only 0.3% of that received on Earth, compared to 3.7% for Jupiter and 1.1% for Saturn. The hot thermospheric temperature of Uranus poses a problem, as it does on all the giant planets. The exospheric temperature, based on the deposition of solar energy into the upper atmosphere, is $T = 150$ K (Strobel et al. [1991]), whereas the observed temperature is $T \approx 800$ K. Consequently, there must be additional heat sources.

The column electron density of the ionosphere of Uranus was measured by Voyager 2 to be in the region 2×10^{15} to 7×10^{15} m^{-2} (Lindal et al. [1987]). This is comparable with the observed column densities of H_3^+ between 1.5×10^{15} and 4.3×10^{15} m^{-2} of Trafton et al. [1999]. This suggests that H_3^+ is the main constituent of the ionosphere.

In this Chapter the ion will be used as a tool in trying to understand the energy balance of the upper atmosphere of Uranus. In addition, the source of the observed variability of the H_3^+ emission is investigated in detail.

5.1.2 H_3^+ emission from Uranus

H_3^+ was first detected from Uranus by Trafton et al. [1993], deriving an H_3^+ temperature of $T = 740 \pm 25$ K and a column density of $N = 6.5 \times 10^{15}$ m^{-2} from their spectrum. Lam et al. [1997b] observed Uranus using the ProtoCam imager on the NASA IRTF. Their images were very noisy, and they observed a variability of $\sim 20\%$ on short timescales. They suggested that this would be the level of any auroral emission sitting on top of a constant $\sim 80\%$ solar EUV produced H_3^+ emission. They could not, however, identify any auroral features in their images. The most comprehensive study of H_3^+ emission from Uranus was undertaken by Trafton et al. [1999] and they noted a lowering of the total H_3^+ emission, E(H_3^+), as the solar cycle approached its minimum. Encrenaz et al. [2000] observed the emission using the Infrared Space Observatory (ISO) which yielded a very low resolution spectrum ($R = 80$), which fitted to an H_3^+ LTE temperature of $T = 600 \pm 200$ K. The same group used SpeX on the NASA IRTF (Encrenaz et al. [2003]) and this data will be re-analysed to be incorporated in the long term study of H_3^+ emission performed within this chapter.

On Jupiter and Saturn we can observe H_3^+ emission produced by auroral processes. On these planets, this emission is much stronger than the H_3^+ emission produced by the photoionisation of H_2 by ultraviolet radiation from the Sun (e.g. Stallard et al. [1999]). Due to the peculiar configuration of Uranus and its small angular size on the sky, the observed H_3^+ emission has not been identified as being associated with the magnetic poles.

It has recently been shown using a simple 1D ionosphere model of Uranus (Chris Smith, personal communication) that the solar EUV is indeed capable of producing densities similar to the observed column densities of H_3^+, given the temperature profile derived from the Voyager 2 encounter (Herbert et al. [1987]). This indicates that whilst solar EUV is perhaps not the only source of ionisation, it is likely to be very important.

Opposing this view, Hallett et al. [2005] suggested that the main production mechanism of H_3^+ must be ionisation via particle precipitation. They constructed a chemical model of the uranian ionosphere/thermosphere system with two types of energy inputs: solar EUV and particle precipitation. Their model predicted that the energy injected by solar EUV was incapable of producing the observed H_3^+ and H_2 column densities (e.g. see Trafton et al. [1999]). Instead, the model required large amounts of particle precipitation to explain the observations. In the Hallett et al. [2005] model the particle precipitation needs to inject 400 times more energy than the solar EUV to reproduce the observed H_3^+ and H_2 densities of Trafton et al. [1999].

5.1.3 Sources of H_3^+ variability

Trafton et al. [1999] noted both large short-term and long-term variations in the observed H_3^+ emission. This chapter shall investigate the source of this variability, using the data published by Trafton et al. [1999] and Encrenaz et al. [2003] plus another three previously unpublished sets of data. In this section, the processes that might, or might not, be controlling the H_3^+ emission is discussed.

Solar UV flux

Equation 1.7 describes how H_2^+ is formed by the photoionisation of H_2 by the solar EUV radiation. The H_2^+ then very quickly reacts with neutral H_2 to form H_3^+. It follows that, if the flux of the ultraviolet radiation is large, lots of H_3^+ can feasible be formed. Conversely, in conditions of low ultraviolet solar flux, only small amounts of H_3^+ can be formed. If this was the main mechanism for H_3^+ on Uranus, then there would be a correlation between the solar UV flux and the observed total H_3^+ intensity emitted at all wavelengths, $E(H_3^+)$.

The electromagnetic radiation from the Sun varies in intensity over an 11 year cycle, known as the solar cycle. Radio wave energy is produced in the outer layers of

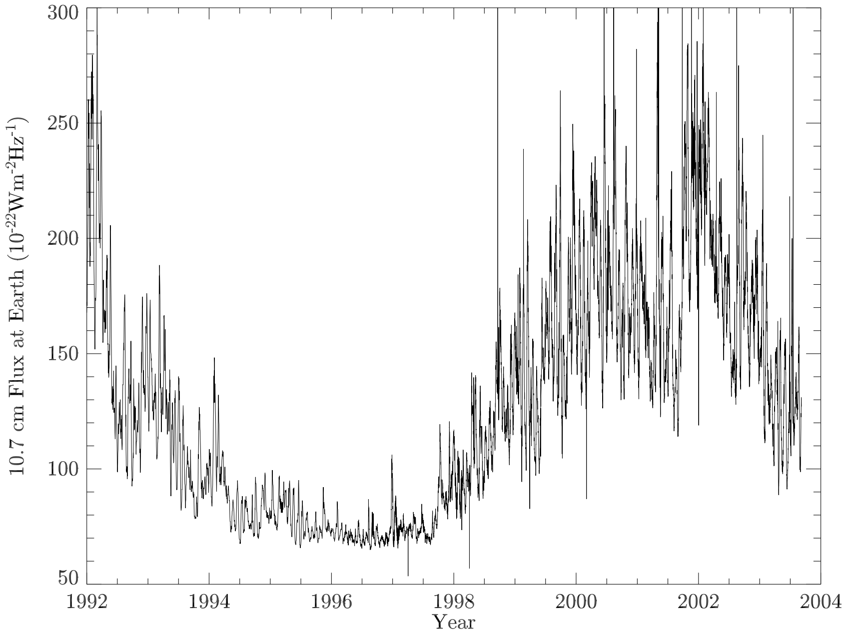

Figure 5.3: The solar 10.7 cm flux between 1992 and 2004. It is highly variable, but displays an overall large-scale 11 year cyclic variability.

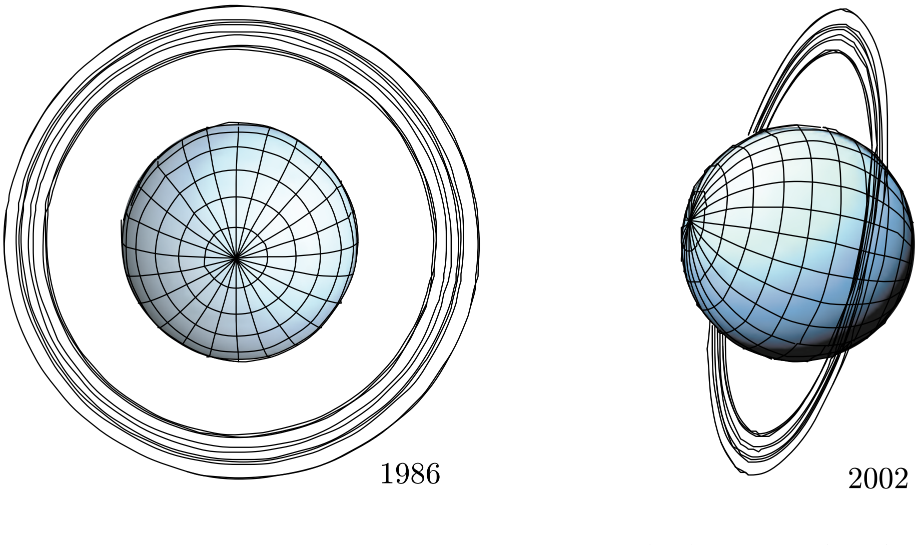

Figure 5.4: Uranus as seen from the Earth in 1986 (left) and 2002 (right). The planet has rotated such that the rotational north pole (using the ULS definition), which faced the observer in 1986, is facing eastward on the sky (left in picture) in 2002.

Decimal year	10.7 cm flux[a]
1977.38904110	80.3
1977.39178082	77.2
1977.39452055	75.4
1977.39726027	74.8
1977.40000000	75.9
1977.40273973	77.0
1977.40547945	79.5
1977.40821918	87.5
1977.41095890	89.5

Table 5.1: An example set of the 10.7 cm flux data obtained from NOAA as discussed in Section 5.1.3. This snippet is centered around the 26th of May 1977. [a]The 10.7 cm flux is given in units of $10^{-22}\mathrm{Wm}^{-2}\mathrm{Hz}^{-1}$.

the Sun and the emission varies, roughly, according to how many sunspots there are on the disc. Chatterjee and Das [1995] showed that there is a relationship between the solar UV emission and 10.7 cm flux. Their UV measurements are obtained from the the Solar Backscatter Ultraviolet experiment (SBUV) on the *Nimbus 7* satellite. The 10.7 measurements are taken daily from the Dominion Radio Astrophysical Observatory in Canada. The radio flux data can be downloaded from US National Geophysics Data Center (`http://www.ngdc.noaa.gov`), which is a data service operated by the US National Oceanic and Atmospheric Administration (NOAA). An example dataset extracted from this database can be seen in Table 5.1. Note that the variability within this small set is $\sim 20\%$, highlighting that the solar flux varies significantly over short timescales.

The light travel time between the Sun and Uranus is roughly 3 hours, and so, with the 10.7 flux being measured once a day at local noon, the flux values can be treated as being the same at Uranus, for any particular day.

Using the 10.7 cm flux as observed at the Earth as a measure of what the EUV flux was doing on Uranus assumes that the observed short-term variations in solar emission is the same in all directions radially out from the equatorial plane of the Sun. This is because the Earth very rarely lies in the Uranus-Sun line. The observed long-term 11-year cyclic variations in the solar EUV emission are, however, the same in all directions from the Sun. We know this as the Earth covers 11 complete journeys around the Sun in one single solar cycle.

Geometry and orientation of magnetosphere

Because of the large offset between the rotational axis and the magnetic axis, the dynamics of the uranian magnetosphere is difficult to model. As illustrated in Figure 5.1, the planetary and interplanetary field are aligned at noon, but some 8.5 hours later (half a rotation) the fields have the opposite orientation and so extensive reconnection would occur (Ye and Hill [1994]). How this affects the magnetosphere and the plasma environment within it, is as of yet unclear.

There could be magnetic configurations of Uranus that are more (or less) favorable for producing large fluxes of particle precipitation, giving rise to large column densities of H_3^+. It was postulated, at the time of the Voyager 2 encounter, that when the magnetic north pole was aligned with the solar wind flow direction, the magnetosphere would become a funnel for solar wind plasma, such that the precipitation flux would radically increase (Bergstralh et al. [1991]).

An example of how geometry with respect to the Sun affects the energetics of a planet, is the changing of seasons on the Earth as it moves around the Sun, with its rotational pole tilted at an angle of 23° from the normal to the ecliptic. It is unlikely, however, that the variations observed on Uranus are seasonal, since the orbital period is 84 years, and the H_3^+ data only covers ~10 years.

Aurora

On Jupiter and Saturn, H_3^+ is produced in large volumes by particle precipitation in the auroral regions. If there are large amounts of H_3^+ being produced by auroral processes on Uranus, they would produce significant short-term variability, due to the tilt of the rotational axis of the planet.

There has only been one spatially resolved observation of the uranian aurora, by Voyager 2 in the ultraviolet (Herbert and Sandel [1994]). It is not known the extent to which auroral processes produce H_3^+ on Uranus.

Solar wind pressure and velocity

Uranus lacks any significant internal plasma source, such as a volcanic moon (Belcher et al. [1991]), so any auroral particles are likely to be of solar wind origin. Baron et al. [1996] performed a study of H_3^+ variability on Jupiter while the Ulysses spacecraft, which was in the vicinity of the planet, measured the solar wind velocity and density, using the Solar Wind Plasma Wave Experiment (Stone et al. [1992]). They calculated the solar wind ram pressure using the formula:

$$P = \rho v^2 \tag{5.2}$$

where ρ is the solar wind density and v is the solar wind velocity (Vasyliūnas [2004]). Baron et al. [1996] found a close correlation between short-term variability of the H_3^+ emission and the solar wind pressure. Such variability, due to the changes to the properties of the solar wind, could also be important on Uranus, although Uranus presents a much smaller magnetosphere to the solar wind and, thus, the effect might be less significant. In addition the solar wind density is lower at Uranus than at Jupiter, due to the outward radial motion of the plasma from the Sun.

In general, we might expect the auroral activity on a gas giant to be a function of the gradient of the solar wind ram pressure, because the expansion and contraction of the flux tubes will increase the flux of charged particles streaming down them (Prangé et al. [2004]).

5.2 Coordinate system definitions

There are two commonly used longitude-latitude coordinate systems used for Uranus in the literature. The first is the Uranus Longitude System (ULS), defined in relation to the position of Voyager 2 in 1986, and the second is the definition of the International Astronomical Union (IAU), that defines longitude relative to a fixed point in time.

In the ULS system, the north rotational pole (i.e. the pole at a latitude of +90°) is defined as the visible pole in 1986 (see Figure 5.4 for the configuration of Uranus at the time of the Voyager 2 encounter). ULS longitude is defined such that the sub-Voyager 2 longitude at 18:00 UT on the 24th of January 1986 was 302° (Desch et al. [1991]). This definition is centred around the Uranus-Voyager 2 encounter as to minimise the uncertainty of the sub-spacecraft longitude introduced by the uncertainty in the measured rotational period of the planet (Desch et al. [1986]). This longitude definition does not tell us what the ULS sub-Earth longitude is for a given time – but using Uranus Viewer (`http://pds-rings.seti.org/tools/viewer2_ura.html`) we find that at there is a difference of 96.5° between the sub-solar longitude and the sub-Voyager 2 longitude at 18:00 24/01/1986 UT. This means that the sub-Earth longitude (which is approximately equal to the sub-solar longitude) is defined as 38.2° on the 24th of January 1986 18:00 UT. The ULS longitude evolves as per IAU convention: the longitude at the sub-observer point increases with time as seen from Earth (apart for on the Earth, Moon and the Sun, for historical reasons).

The International Astronomical Union (IAU) defines a geographic north pole as the pole lying in the same ecliptic hemisphere as the Earth's geographic north pole. In the case of Uranus, this means that the IAU North is defined as the *invisible* pole in 1986. The IAU longitude system III sub-Earth longitude of Uranus, ϕ, is defined as:

$$\phi = 203.81 - 501.1600928 \times d \tag{5.3}$$

where d is the interval in days from the standard epoch with the standard epoch being 2000 January 1.5 (noon), i.e. Julian date 2451545.0. The 501.1600928 factor is the number of degrees longitudes that Uranus rotates through in 1 Julian day.

The rotational period of Uranus, derived from Voyager 2 observations of its radio emissions is $P = 17.24 \pm 0.01$ hours (Desch et al. [1986]). This gives an uncertainty of ±2.6 hours being introduced on the period each year. This means that between 1986, when Voyager 2 encountered Uranus, and 1992, when the first set of H_3^+ observations analysed in this chapter were obtained, there is an uncertainty of ±16 hours $\approx \pm$ 1 rotation period. If it could be determined how the relationship between the IAU and ULS longitudes changes over time, the rotational period could be determined to a higher degree of accuracy.

5.3 Data and analysis

Numerous observers have analysed H_3^+ emission from Uranus over the past 15 years (e.g. Trafton et al. [1999] and Encrenaz et al. [2003]). In looking for simple scalable relations – e.g. variations due to any of the sources of variability discussed above – the integrated emission of H_3^+ over all wavelengths, $E(H_3^+)$, has been used as a correlation parameter (Trafton et al. [1999]).

A temporal analysis of the variation of H_3^+ emission from Uranus requires a consis-

Date	T (K)	$N(H_3^+)$ (m^{-2})	$E(H_3^+)^a$	Reference
1994 Jul 23	648 ± 75	4.2×10^{15}	14.1	Trafton et al. [1999]
2001 Sep 1-2	640 ± 40	4.0×10^{15}	18.2	Encrenaz et al. [2003]
This work	640	4.0×10^{15}	10.1^b	Equation 2.41

Table 5.2: Tables showing the discrepacy between the $E(H_3^+)$ calculation of Trafton et al. [1999] and Encrenaz et al. [2003]. [a]The units of $E(H_3^+)$ are $\mu Wm^{-2}str^{-1}$. [b]Note that $E(H_3^+) = 11.4$ $\mu Wm^{-2}str^{-1}$ when the values for T and $N(H_3^+)$ of Trafton et al. [1999] are used.

tent treatment of all the data, as errors can be introduced when comparing datasets from different telescopes and and different instruments, each having a different set of configurations. To highlight the importance of consistency in the analysis, it is noted that in the paper of Encrenaz et al. [2003], an observation made in 2001 produces a higher value of $E(H_3^+)$ than an observation made in July 1994 by Trafton et al. [1999] despite having lower temperature *and* lower column density – this is shown in Table 5.2. Note that the value of $E(H_3^+)$ obtained in this thesis is lower than in both of these papers. The reason for the high value of Encrenaz et al. [2003] is not clear but the higher value of Trafton et al. [1999] is a result of their fit to the total emission plot of Neale et al. [1996] being 'loose' at these low temperatures, and results in a too large a value for $E(H_3^+)$, see Figure 2.23. For higher temperatures, $\sim$ 1000 K, the Trafton et al. [1999] fit is good. See Section 2.4.4 for more details on the total emission parameter, $E(H_3^+)$.

To ensure consistency, all the available observations will be re-analysed using the new fitting routine described in Section 2.4, together with the new fit to the total H_3^+ emission curve of Neale et al. [1996], determined in Section 2.4.4. In addition, the raw data of Encrenaz et al. [2003], taken in September of 2000 and 2001, will be re-reduced.

5.3.1 Available observations

A very unique dataset exists at the Atmospheric Physics Laboratory (APL) at University College London. It comprises of the observations presented by Trafton et al. [1999], covering the years 1992 to 1995, plus three unpublished sets of observations, covering the years 1999, 2001 and 2002. These sets were reduced from observations by Larry Trafton (University of Texas), Tom Geballe (Gemini Observatory), Steve Miller and Thomas Stallard (both at University College London). In addition, data from

UT Date	Pixel size (″)	Resolution	Instrument & Telescope
1992 Apr 1	3.1 × 3.1	1300	CGS4 (UKIRT)
1992 Apr 2	3.1 × 3.1	1300	CGS4 (UKIRT)
1993 May 3	3.08 × 3.08	1200	CGS4 (UKIRT)
1993 May 4	3.08 × 3.08	1200	CGS4 (UKIRT)
1993 May 5	3.08 × 3.08	1200	CGS4 (UKIRT)
1994 Jul 20	1.54 × 4.62	1200	CGS4 (UKIRT)
1994 Jul 23	1.54 × 4.62	1200	CGS4 (UKIRT)
1995 Jun 11	1.23 × 1.35	900	CGS4 (UKIRT)
1995 Jun 12	1.23 × 1.35	900	CGS4 (UKIRT)
1995 Jun 13	1.23 × 1.35	900	CGS4 (UKIRT)
1995 Jun 14	1.23 × 1.35	900	CGS4 (UKIRT)
1999 Sep 14	0.595 × 0.695	5570	CGS4 (UKIRT)
1999 Sep 15	0.595 × 0.695	5570	CGS4 (UKIRT)
1999 Sep 16	0.595 × 0.695	5570	CGS4 (UKIRT)
1999 Sep 17	0.595 × 0.695	5570	CGS4 (UKIRT)
1999 Sep 18	0.595 × 0.695	5570	CGS4 (UKIRT)
2000 Sep 10[a]	0.15 × 0.8	2500	SpeX (IRTF)
2000 Sep 11[a]	0.15 × 0.8	2500	SpeX (IRTF)
2001 Jun 16	0.61 × 0.61	1200	CGS4 (UKIRT)
2001 Jun 18	0.61 × 0.61	1200	CGS4 (UKIRT)
2001 Jun 19	0.61 × 0.61	1200	CGS4 (UKIRT)
2001 Sep 2[a]	0.15 × 0.8	2500	SpeX (IRTF)
2002 Jul 18	0.5 × 0.15	2500	SpeX (IRTF)
2002 Jul 19	0.5 × 0.15	2500	SpeX (IRTF)
2002 Jul 20	0.5 × 0.15	2500	SpeX (IRTF)
2002 Jul 21	0.5 × 0.15	2500	SpeX (IRTF)
2002 Jul 22	0.5 × 0.15	2500	SpeX (IRTF)

Table 5.3: The data sources available for the temporal analysis of the H_3^+ emission from Uranus. [a]This data was originally published by Encrenaz et al. [2003] and is re-reduced and re-analysed here.

the years 2000 and 2001, originally published by Encrenaz et al. [2003], were kindly given to us in raw form by Thérèse Encrenaz at Laboratorie d'Etudes Spatiales et d'Instrumentation et Astrophysique (LESIA), Observatoire de Paris, Meudon, France. This data was obtained using SpeX on the NASA IRTF and was re-reduced and included in the temporal analysis of the H_3^+ emission from Uranus. This forms the most comprehensive collection of L′ infrared spectra of Uranus to date, spanning a decade, enabling the detailed analysis of both long-term and short-term variability.

The dates for which observations are available are listed in Table 5.3, including the pixel size, resolution, instrument and telescope used.

Most of the spectra were in units of either [$\mathrm{Wm^{-2}\mu m^{-1}str^{-1}}$] or [$\mathrm{Wm^{-2}\mu m^{-1}}$].

The latter set of units are 'instrumental' units, which means that the spectrum has the intensity as seen through the field-of-view of each pixel in the spectrograph. Theoretical intensities, which are what an observed spectrum is fitted to when extracting LTE temperature and densities, are given in units of flux per sterradian (str^{-1}), and so the conversion is calculated by:

$$\mathrm{I}[\mathrm{Wm}^{-2}\mu\mathrm{m}^{-1}\mathrm{str}^{-1}] = \mathrm{I}[\mathrm{Wm}^{-2}\mu\mathrm{m}^{-1}] \times \frac{4.2545 \times 10^{10}}{pixelarea} \tag{5.4}$$

where the 4.2545×10^{10} factor is the number of square arc-seconds that fits into one sterradian and *pixelarea*, given in units of square arc-seconds, is the width of the slit multiplied by the pixel-size along the direction of the slit. The *pixelarea* for each observation can be seen in Table 5.3.

Each spectrum analysed in this chapter has one of two slit-orientations: one is aligned with the rotational axis, along the central meridian longitude (CML), and the other is aligned parallel to the planet's equator.

5.3.2 The data of Encrenaz et al. [2003]

Encrenaz et al. [2003] used the SpeX spectrograph (Rayner et al. [2003]) on the NASA IRTF to observe Uranus on the 9th and 10th of September 2000 and on the 2nd of September 2001. Their data was supplied to us by Thérèse Encrenaz in raw form. The data was reduced as described in Chapter 2, although the SpeX data has the added complication of being curved on the array. This is best illustrated by looking at a flat-field, seen in Figure 5.5. The curvature was taken out by fitting a polynomial to the edge (extracted by detecting the upward intensity 'step') of each order and, then, performing a sub-pixel interpolated linear shift of the spectrum. The resulting straightened flat-field can be seen in Figure 5.6. All individual frames were subject to this straightening.

SpeX was used in a mode called LXD2.3, which gives a spectral resolution of R=2,500. The slit-width was 0.8″ with a pixel width of 0.15″ along the slit, compared with diameter of Uranus of 3.7″. The slit was aligned along the central meridian of the planet. For all observations the star HD 203387 (ι Cap) was used to produce the calibration spectrum. It has a magnitude at 3.5 μm of $m_{3.5} = 2.18$ (Glass [1974]) and a temperature of 4,860 K (Alonso et al. [1999]). As for all other spectra in this

Figure 5.5: A flat-field taken with SpeX using the LXD2.3 mode. Indicated is the approximate start and end wavelength of the different orders. After Rayner et al. [2003].

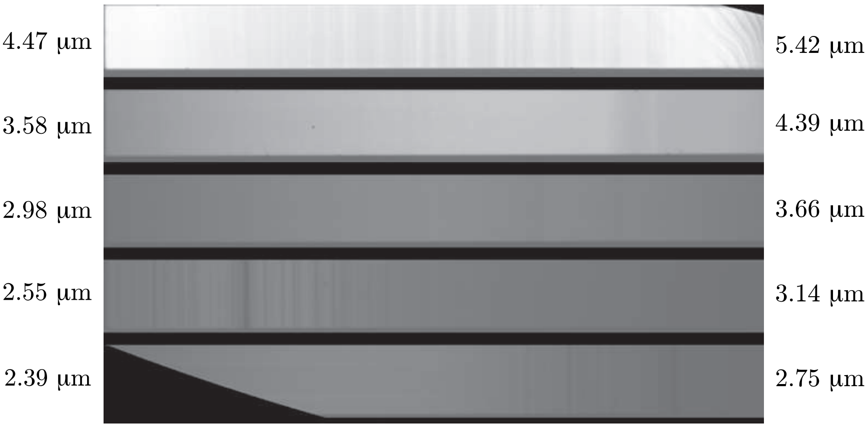

Figure 5.6: The flat-field in Figure 5.5 after being straightened.

analysis, the H_3^+ Q region was extracted, as discussed below.

5.3.3 Analysis of data

The H_3^+ Q spectral region is proven to be a very reliable region for extracting LTE temperatures and column densities (see e.g. Lam et al. [1997a] on Jupiter and Encrenaz et al. [2003] on Uranus). Here, we find some of the strongest observable H_3^+ spectral lines and the ratio evolution of the lines, as the temperature changes, is steep, so they allow a reliable fit to be made. For this reason, only the Q region was fitted on the available Uranus spectra. To do this, the region was extracted from within all available datasets, limiting the data between 3.94 μm and 4.05 μm. This region is highlighted on a theoretical H_3^+ spectrum covering the L and L′ atmospheric windows in Figure 5.7. This region is also free from any major telluric atmospheric absorption features.

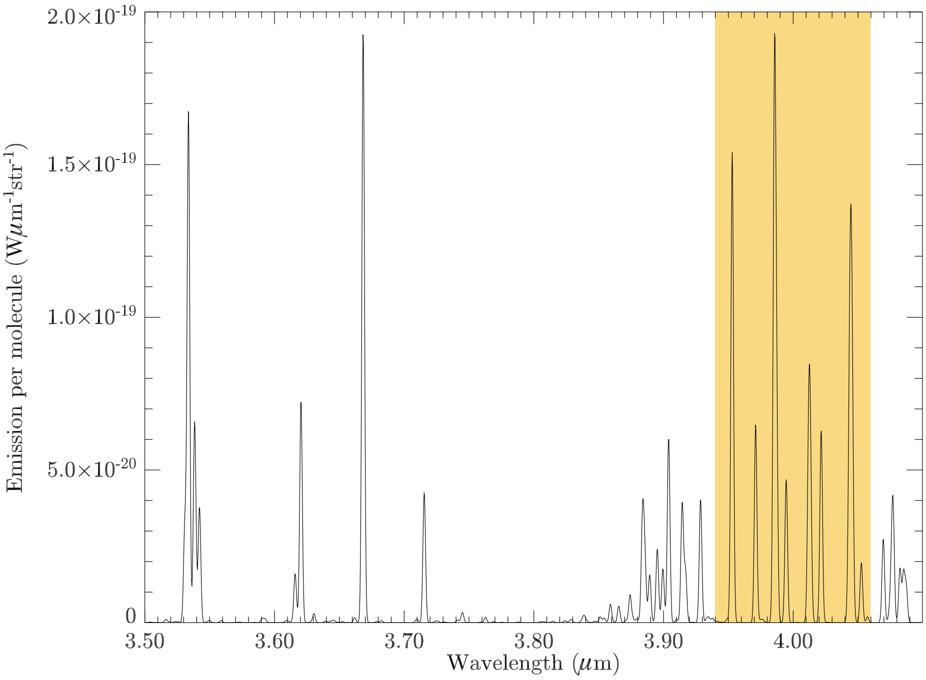

Figure 5.7: A theoretical H_3^+ spectrum with a temperature of $T = 800$ K assuming conditions of LTE. The shaded region indicates emission lines due to the H_3^+ Q branch – ‘the Q region’.

The integrated intensity of the H_3^+ fundamental $Q(1, 0^-)$ line ($\nu_2 \rightarrow 0$) at 3.953 μm for each and every available spectrum can be seen in Table 5.4. Note that there is only one observation in September 2001 (2001.7 in decimal year). The average intensity for a central meridian longitude (CML) aligned slit is 7.3×10^{-7} $\mathrm{Wm^{-2}str^{-1}}$ and the

UT Date	Year	Intensity (Wm^{-2}str^{-1})	Slit
1992 Apr 1	1992.2	8.5×10^{-7}	equ
1992 Apr 2	1992.3	8.0×10^{-7}	equ
1993 May 3	1993.3	7.8×10^{-7}	equ
1993 May 4	1993.3	6.9×10^{-7}	equ
1993 May 5	1993.3	7.5×10^{-7}	equ
1994 Jun 20	1994.5	8.4×10^{-7}	cml
1994 Jun 23	1994.5	9.6×10^{-7}	cml
1995 Jun 11	1995.4	4.4×10^{-7}	cml
1995 Jun 12	1995.4	5.2×10^{-7}	cml
1995 Jun 13	1995.4	5.0×10^{-7}	cml
1995 Jun 14	1995.5	7.2×10^{-7}	cml
1999 Sep 14	1999.7	9.2×10^{-7}	cml
1999 Sep 14	1999.7	9.8×10^{-7}	cml
1999 Sep 15	1999.7	10.4×10^{-7}	cml
1999 Sep 16	1999.7	12.7×10^{-7}	cml
1999 Sep 17	1999.7	12.2×10^{-7}	cml
1999 Sep 18	1999.7	11.7×10^{-7}	equ
1999 Sep 18	1999.7	14.4×10^{-7}	cml
2000 Sep 10	2000.7	2.4×10^{-7}	cml
2000 Sep 11	2000.7	3.6×10^{-7}	cml
2001 Jun 16	2001.5	5.9×10^{-7}	cml
2001 Jun 18	2001.5	8.5×10^{-7}	cml
2001 Jun 19	2001.5	7.2×10^{-7}	cml
2001 Sep 2	2001.7	6.8×10^{-7}	cml
2002 Jul 18	2002.5	3.7×10^{-7}	cml
2002 Jul 19	2002.5	4.2×10^{-7}	cml
2002 Jul 19	2002.5	5.4×10^{-7}	equ
2002 Jul 20	2002.5	4.2×10^{-7}	cml
2002 Jul 20	2002.5	5.7×10^{-7}	equ
2002 Jul 21	2002.6	4.5×10^{-7}	cml
2002 Jul 21	2002.6	5.6×10^{-7}	equ
2002 Jul 22	2002.6	4.8×10^{-7}	cml
2002 Jul 22	2002.6	6.0×10^{-7}	equ

Table 5.4: The intensity of the H_3^+ fundamental Q(1, 0^-) line in all the available data sets. 'equ' means a slit aligned with the equator and 'cml' refers to a slit aligned with the central meridian longitude.

Decimal year	Intensity ($\mathrm{Wm^{-2}str^{-1}}$)
1992.3	$8.3 \pm 0.3 \times 10^{-7}$
1993.3	$7.4 \pm 0.4 \times 10^{-7}$
1994.5	$9.0 \pm 0.9 \times 10^{-7}$
1995.4	$5.5 \pm 1.2 \times 10^{-7}$
1999.7	$11.5 \pm 1.8 \times 10^{-7}$
2000.7	$3.0 \pm 0.8 \times 10^{-7}$
2001.5	$7.2 \pm 1.3 \times 10^{-7}$
2001.7	$6.8 \pm 0.0 \times 10^{-7}$
2002.5	$4.9 \pm 0.8 \times 10^{-7}$

Table 5.5: The average intensity of the H_3^+ fundamental Q(1, 0^-) for each year covered by the data-set. The given error is the standard deviation of the intensity within each year. The date 2001.7 only has one spectra associated with it, so does not have a standard deviation.

average for an equator aligned slit is 6.8×10^{-7} $\mathrm{Wm^{-2}str^{-1}}$. In the whole dataset, 24 spectra are CML aligned and nine are aligned with the equator. The spectra with a CML aligned slit covers more of the solar cycle than the spectra with an equator aligned slit. Table 5.5 shows the average intensity of the Q(1, 0^-) line for each group of observations. The data from 1999 shows both the largest intensity and the largest variability of the Q(1, 0^-) line. The years 2000.7 and 2001.7 is the data supplied by T. Encrenaz. They noted that their co-added spectrum of September 2001(2001.7) was about twice as intense as the spectrum of September 2000 (2000.7). This is also noted in Table 5.5.

The Uranus spectra listed in Table 5.3 was fitted using the H_3^+ spectrum fitting routine described in 2.4. The initial input parameters are set at is $T = 600$ K and σ is 0.0015 μm. The routine was configured to fit the wavelength shift to second order (see Equation 2.55) and the σ to first order (see Equation 2.56). One spectrum from each group, fitted with a theoretical H_3^+ spectrum, can be seen in Figures 5.8 to Figure 5.15. The fitted parameters for all the available spectra can be seen in Table 5.6. Note that the wavelength shift, the line width and the background level for each spectrum is not listed here, although they were fitted. The Q region is an easy region to fit, and varying the starting values for the fitted parameters does not affect the result of the fit. This was confirmed by fitting a sample of spectra with different initial values, each time getting the same LTE H_3^+ temperature and ion density.

The average temperature for all the spectra with a CML aligned slit is $T = 630 \pm 50$ K and the average temperature for the equator aligned slit is $T = 660 \pm 70$ K. For all

UT Date	Temp. (K)	N(H_3^+) ($10^{15}m^{-2}$)	E(H_3^+) ($\mu Wm^{-2}str^{-1}$)	Slit
1992 Apr 1	762 ± 36	2.2 ± 0.4	14.1 ± 2.9	equ
1992 Apr 2	668 ± 21	3.5 ± 0.5	11.3 ± 1.8	equ
1993 May 3	736 ± 20	2.3 ± 0.3	12.6 ± 1.6	equ
1993 May 4	730 ± 15	2.1 ± 0.2	11.1 ± 1.0	equ
1993 May 5	651 ± 13	3.6 ± 0.4	10.2 ± 1.1	equ
1994 Jun 20	621 ± 11	5.1 ± 0.5	10.8 ± 1.1	cml
1994 Jun 23	620 ± 17	6.0 ± 0.9	12.6 ± 1.9	cml
1995 Jun 11	741 ± 37	1.2 ± 0.3	6.7 ± 1.5	cml
1995 Jun 12	638 ± 24	2.7 ± 0.6	6.8 ± 1.4	cml
1995 Jun 13	641 ± 29	2.6 ± 0.6	6.7 ± 1.6	cml
1995 Jun 14	679 ± 33	2.6 ± 0.6	9.2 ± 2.2	cml
1999 Sep 14	606 ± 8	6.1 ± 0.5	11.2 ± 0.8	cml
1999 Sep 14	616 ± 8	5.8 ± 0.4	11.8 ± 0.8	cml
1999 Sep 15	622 ± 8	6.0 ± 0.4	12.9 ± 0.9	cml
1999 Sep 16	609 ± 7	8.0 ± 0.6	15.1 ± 1.0	cml
1999 Sep 17	637 ± 9	6.1 ± 0.5	15.1 ± 1.2	cml
1999 Sep 18	595 ± 15	8.1 ± 1.2	13.3 ± 2.0	equ
1999 Sep 18	629 ± 11	8.0 ± 0.8	18.3 ± 1.8	cml
2000 Sep 10	557 ± 40	7.8 ± 3.3	8.4 ± 3.5	cml
2000 Sep 11	604 ± 36	5.9 ± 1.9	10.5 ± 3.4	cml
2001 Jun 16	684 ± 26	2.2 ± 0.4	8.0 ± 1.5	cml
2001 Jun 18	753 ± 34	2.2 ± 0.4	13.4 ± 2.7	cml
2001 Jun 19	617 ± 28	4.3 ± 1.1	8.7 ± 2.2	cml
2001 Sep 2	617 ± 32	3.8 ± 1.0	7.8 ± 2.1	cml
2002 Jul 18	638 ± 35	2.1 ± 0.6	5.3 ± 1.5	cml
2002 Jul 19	579 ± 29	3.8 ± 1.1	5.2 ± 1.6	cml
2002 Jul 19	563 ± 34	5.2 ± 1.9	6.0 ± 2.2	equ
2002 Jul 20	622 ± 30	2.7 ± 0.7	5.7 ± 1.5	cml
2002 Jul 20	626 ± 31	3.3 ± 0.9	7.3 ± 1.9	equ
2002 Jul 21	573 ± 23	4.2 ± 1.0	5.5 ± 1.3	cml
2002 Jul 21	606 ± 22	3.7 ± 0.8	6.9 ± 1.4	equ
2002 Jul 22	610 ± 20	3.1 ± 0.6	6.0 ± 1.1	cml
2002 Jul 22	574 ± 20	5.2 ± 1.1	6.8 ± 1.4	equ

Table 5.6: The fitted H_3^+ temperature, column density and total emission and their associated errors for the available Uranus observations.

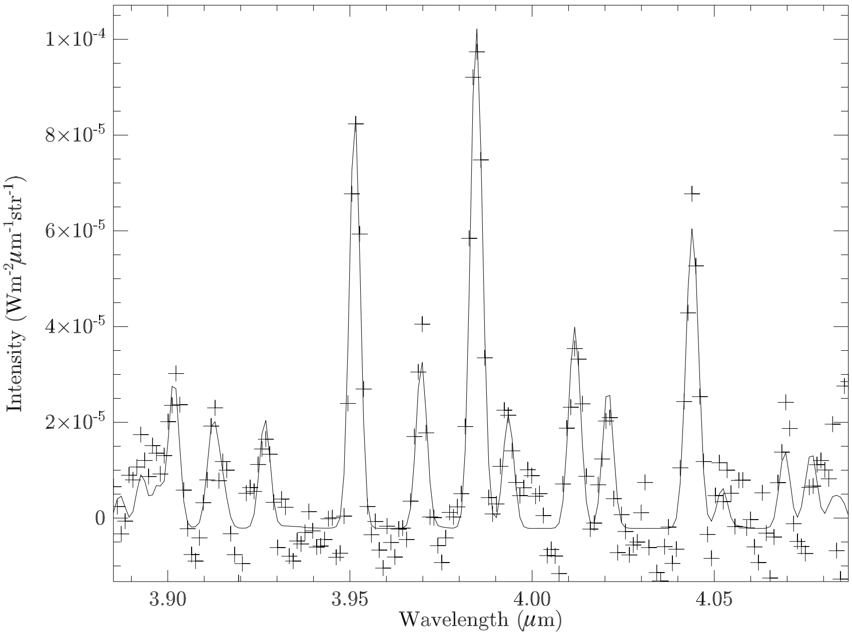

Figure 5.8: The Uranus H_3^+ spectrum taken on the 2nd April 1992. The solid line is the theoretical H_3^+ fit to the spectrum.

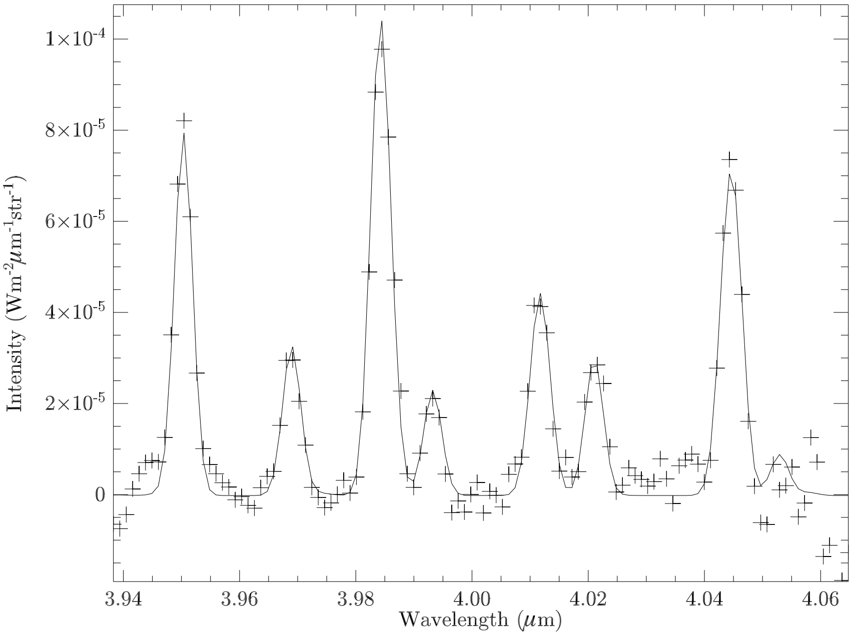

Figure 5.9: The Uranus H_3^+ spectrum taken on the 3rd May 1993. The solid line is the theoretical H_3^+ fit to the spectrum.

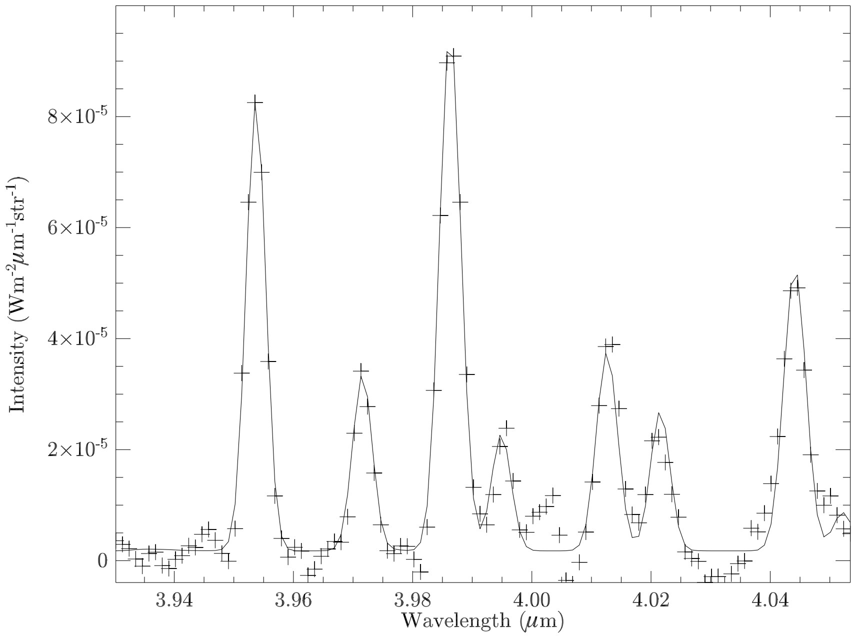

Figure 5.10: The Uranus H_3^+ spectrum taken on the 20th June 1994. The solid line is the theoretical H_3^+ fit to the spectrum.

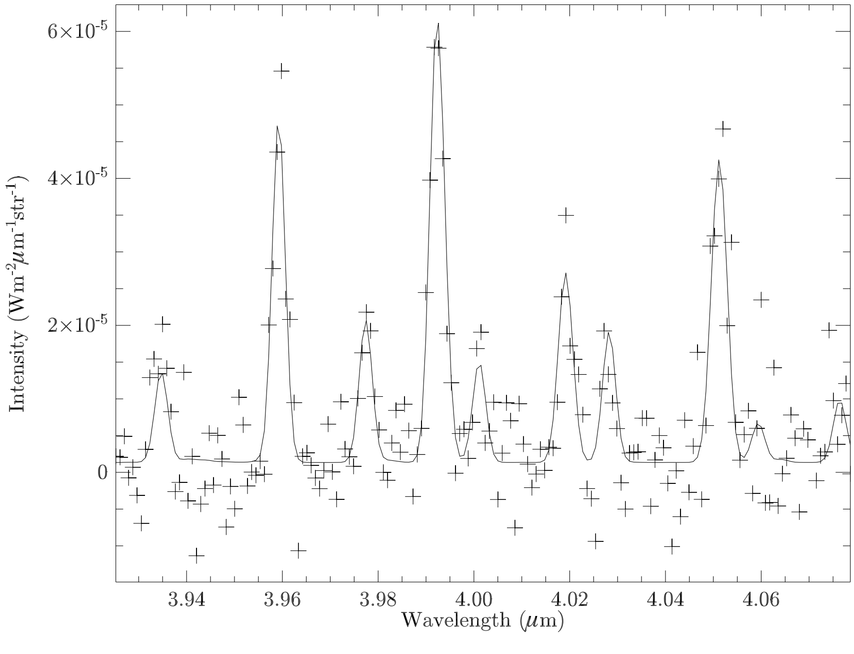

Figure 5.11: The Uranus H_3^+ spectrum taken on the 11th June 1995. The solid line is the theoretical H_3^+ fit to the spectrum.

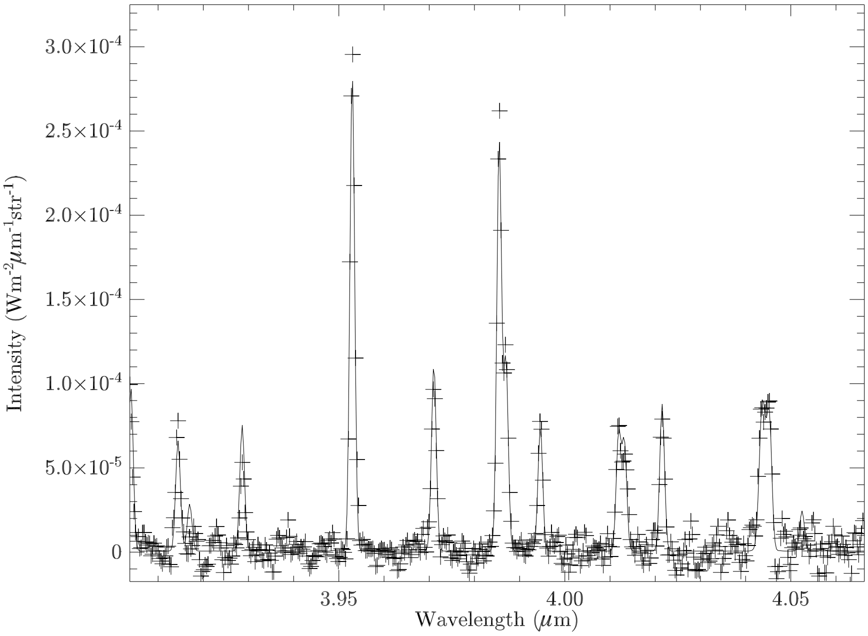

Figure 5.12: The Uranus H_3^+ spectrum taken on the 14th September 1999. The solid line is the theoretical H_3^+ fit to the spectrum.

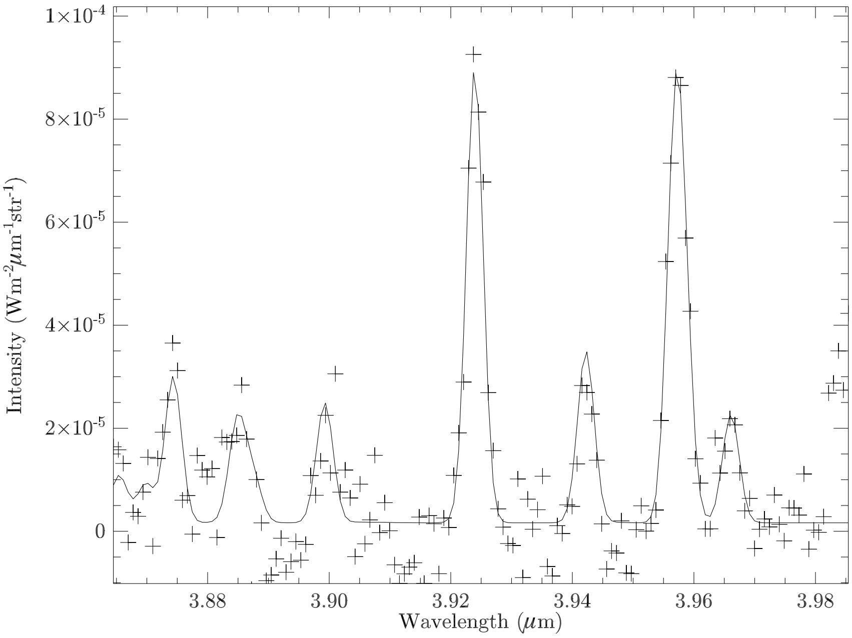

Figure 5.13: The Uranus H_3^+ spectrum taken on the 10th September 2000. The solid line is the theoretical H_3^+ fit to the spectrum.

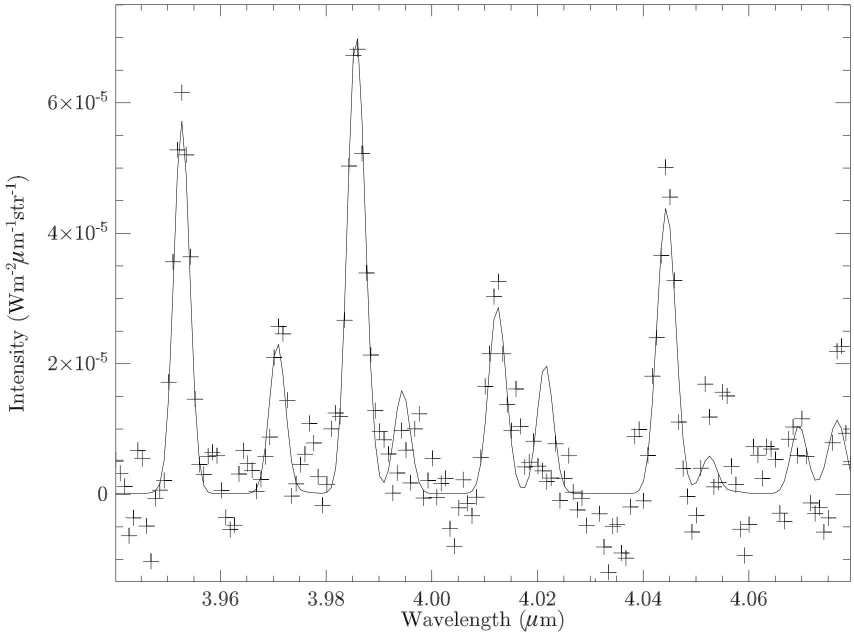

Figure 5.14: The Uranus H_3^+ spectrum taken on the 16th June 2001. The solid line is the theoretical H_3^+ fit to the spectrum.

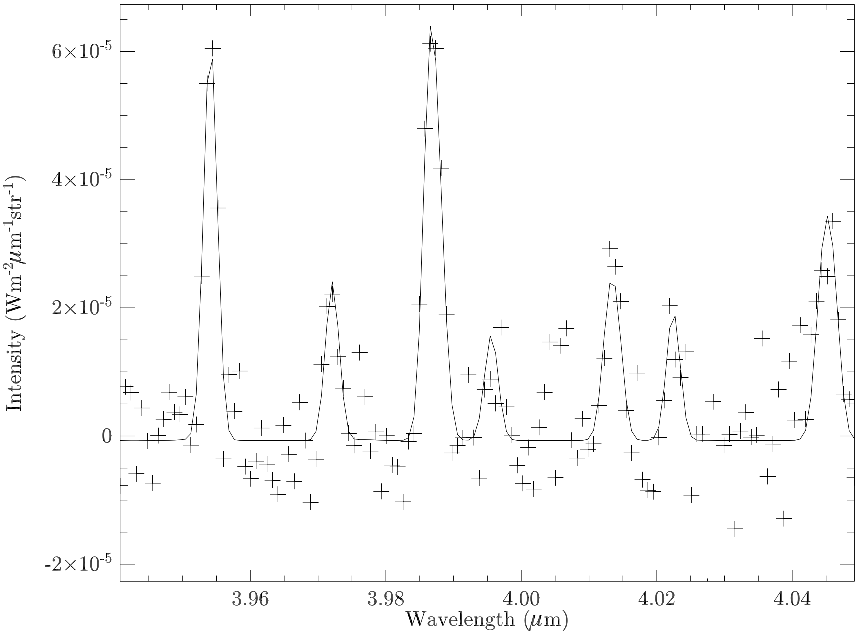

Figure 5.15: The Uranus H_3^+ spectrum taken on the 18th July 2002. The solid line is the theoretical H_3^+ fit to the spectrum.

Decimal year	E(H_3^+) (μWm^{-2}str^{-1})
1992.3	12.7 ± 2.0
1993.3	11.3 ± 1.2
1994.5	11.7 ± 1.2
1995.4	7.3 ± 1.2
1999.7	13.9 ± 2.4
2000.7	9.4 ± 1.5
2001.5	10.0 ± 2.9
2001.7	7.8 ± 2.4
2002.5	6.1 ± 0.7

Table 5.7: The average total H_3^+ emission for each year covered by the data-set. The given error is the standard deviation of the total emission within each year.

39 spectra the average is $T = 640 \pm 60$ K. The average CML aligned column density is $N = 4.6 \pm 2.1 \times 10^{15}$ m^{-2} and for the equator aligned slit it is $N = 3.5 \pm 1.2 \times 10^{15}$ m^{-2}. The average column density for all spectra is $N = 4.3 \pm 2.0 \times 10^{15}$ m^{-2}.

The total emission for each spectrum was calculated using the new, low temperature fit to the total H_3^+ emission curve of Neale et al. [1996], derived in Section 2.4.4. These values can be seen in Table 5.6 together with their associated errors. The average E(H_3^+) emission per set of spectra (i.e. for each group of observations) is shown in Table 5.7.

Discussion of temperatures and densities

The H_3^+ temperatures and densities seen in Table 5.6 are similar to values determined previously on Uranus (e.g. Trafton et al. [1999]). The maximum temperature, $T = 762 \pm 36$ K, was observed on the 1st of April 1992 and the lowest temperature, $T = 557 \pm 40$ K was observed on the 10th of September 2000.

The maximum column density was observed on the 19th of September 1999 of $N = 8.1 \pm 1.2 \times 10^{15}$ m^{-2} and the minimum was observed on the 11th of June 1995 with $N = 1.2 \pm 0.3 \times 10^{15}$ m^{-2}.

In Chapter 4, the H_3^+ on Saturn was determined as having a column density of the same order as observed on Jupiter, but with a much lower temperature. This means that Uranus, with a column density of a few $\times 10^{15}$ m^{-2} has the lowest H_3^+ column density of the three planets. On Jupiter, and perhaps, to a greater extent, on Saturn, the observed H_3^+ density is generated mainly via particle precipitation processes. The column density on Uranus does not vary outside an order of magnitude, which in combination with it being low, indicates that precipitation processes are less important on Uranus, and that solar EUV produced H_3^+ makes up a greater proportion of the observed emission. The processes that govern the long-term and short-term variability will be investigated in the following sections.

Whilst the column density is lower compared to Jupiter and Saturn, H_3^+ on Uranus is on average over 200 K hotter than Saturn, despite being almost twice as far away from the Sun. As of yet, the high thermospheric temperatures of the giant planets remains a mystery, and there must be significant energy sources available to the upper atmosphere.

5.4 Long-term variability of H_3^+ on Uranus

Trafton et al. [1999] carried out a comprehensive review of infrared spectra of Uranus taken between 1992 and 1995. During this time, the solar EUV activity, modulated by the solar cycle, as discussed in Section 5.1.3, was in decline, approaching a solar minimum in 1995. The work presented in this thesis extends this long-term variability study up to the year 2002. Figure 5.3 shows the 10.7 cm flux over the period that is covered by the available spectra. The data spans just under one solar cycle, and forms the most comprehensive self-consistent long-term study of H_3^+ variability on Uranus to date.

To investigate what the source of the observed long-term H_3^+ variability is, the average $E(H_3^+)$ per set of spectra will be plotted against parameters describing the intensity of solar EUV and the geometry of the system.

5.4.1 Variability due to solar UV flux

If the long-term variability is controlled by the variations in the solar EUV flux, as we move through the solar cycle, there should be some form of relationship between the 10.7 cm flux and the average $E(H_3^+)$ per set of observations. The $E(H_3^+)$ parameter, as listed in Table 5.6, can be seen plotted against the 10.7 cm flux, smoothed over half a year, in Figure 5.16. The 10.7 cm flux has been scaled by a factor of 10 onto the $E(H_3^+)$ plot. In the years 1992 to 1999 there is a general correspondence of the $E(H_3^+)$

Year	0 days	3 days	6 days	9 days	12 days	15 days
1992.3	173.7	182.8	182.4	180.7	177.4	174.8
1993.3	111.9	107.9	109.5	113.5	114.7	114.2
1994.5	74.0	76.5	79.7	81.1	81.5	80.0
1995.4	78.9	81.5	81.4	80.1	78.0	76.2
1999.7	155.7	153.4	139.3	134.6	134.7	142.8
2000.7	137.8	152.6	161.6	159.9	160.7	158.6
2001.5	207.2	203.4	189.4	185.8	181.8	173.3
2001.7	182.5	188.6	191.8	190.7	184.5	179.2
2002.5	187.6	183.8	173.5	164.8	159.5	156.5

Table 5.8: The 10.7 flux in units of $10^{-22}\mathrm{Wm}^{-2}\mathrm{Hz}^{-1}$ averaged over the duration of each set of observations and including the number of days *before* it as indicated.

to the fluctuations in the 10.7 cm flux. At years later than 1999, however, there is a very poor correlation with the smoothed 10.7 cm flux curve.

As seen in Figure 5.3, the 10.7 cm flux displays a lot of short-term variability and as a consequence, the half year smoothing might not be a good measure of how the E(H_3^+) varies in response to rapid changes in the solar EUV radiation. It is not known how rapidly uranian H_3^+ column densities and temperatures equilibrate when the EUV flux changes by a significant amount. Due to this uncertainty the average E(H_3^+) is compared to the average 10.7 cm flux between a number of days before the start of the observations to the end of the observation. This is to simulate a loading response to changes in the EUV flux of the formation of H_3^+. The average 10.7 cm flux, including zero, three, six, nine, twelve and fifteen days *before* the start of the observations can be seen in Table 5.8. The averages for zero, three, nine and fifteen days are plotted versus the average E(H_3^+) emission per dataset in Figure 5.17 to Figure 5.20.

None of the figures shows any clear relationship between the 10.7 cm flux and the average E(H_3^+), and there is generally a large spread of average E(H_3^+) at high values of 10.7 cm flux, ruling out any simple linear relationship. This indicates that the E(H_3^+) is not primarily controlled by the EUV flux. Figure 5.16 shows no general 11-year cyclic variability which would be expected if the E(H_3^+) was controlled solely by variations in solar EUV emissions with solar cycle.

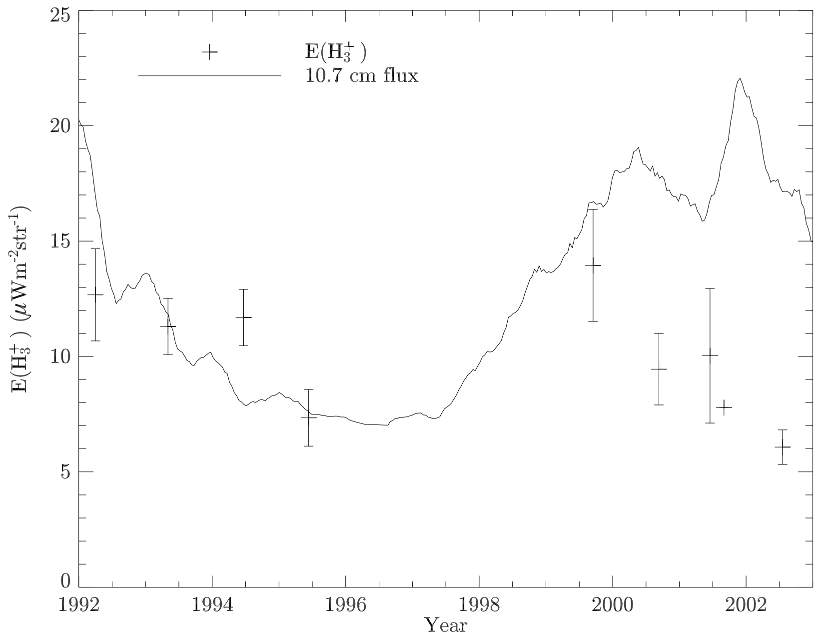

Figure 5.16: The average E(H_3^+) and the solar 10.7 flux smoothed over 180 days plotted against time.

5.4.2 Variability due to geometry

The complexity of the geometry of the uranian sytem is difficult to parameterise. One parameter that is readily available from the Uranus Viewer website, is the sub-solar latitude of the planet, for each set of observations. Whilst it only describes the alignment of the rotational pole to the Sun-planet direction, it does provide a starting point for analysing short-term variability. The sub-solar ULS latitude can be seen in Table 5.9 for each of the sets of observations. This data is plotted as a function of year in Figure 5.21. It shows a clear linear trend, with the sub-solar latitude decreasing linearly with increasing time. The average E(H_3^+) versus sub-solar latitude can be seen in Figure 5.22. There is a sharp decrease in E(H_3^+) emission as we approach smaller sub-solar latitudes. This very strong reduction appears to be correlated to the alignment of the north magnetic pole, which lies at a latitude of $\sim$ 15° North (Ness et al. [1986]), indicated as the dashed line in Figures 5.21 and 5.22. When the sub-solar latitude of Uranus is 15° N, the magnetic north pole points, once a day, in the direction of the Sun. This is a very similar configuration to that of Neptune at the time of the Voyager 2 encounter in August 1989 (Ness et al. [1989]). Cruikshank et al. [1995] reported that it was the configuration that produced

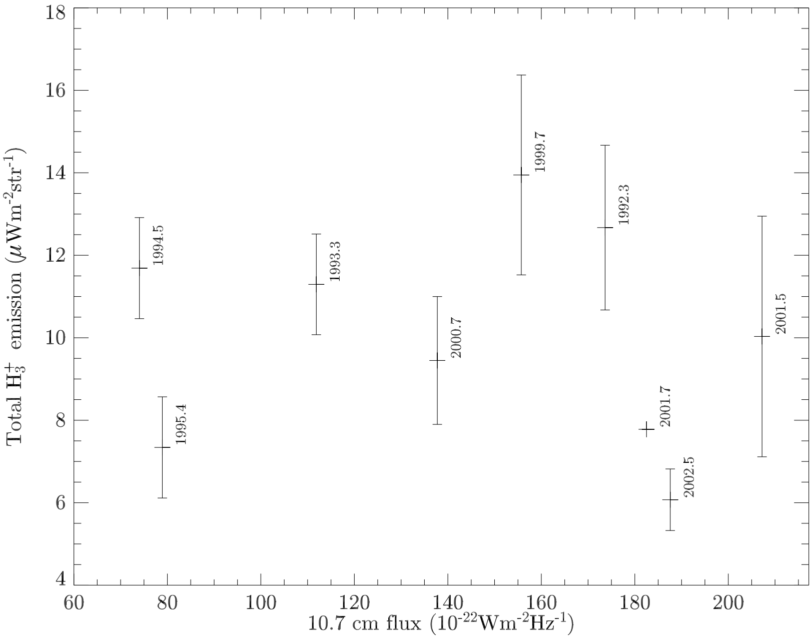

Figure 5.17: The average E(H_3^+) for each set of observations versus the 10.7 flux as observed on Earth for the duration of each set of observations. The error bars is the standard deviation of E(H_3^+) within each set of spectra.

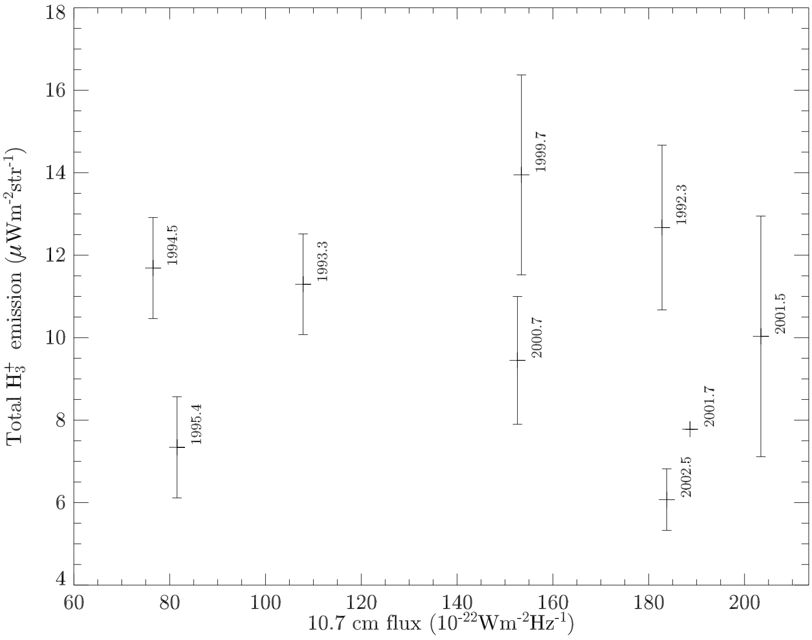

Figure 5.18: The average E(H_3^+) for each set of observations versus the average 10.7 flux as observed on Earth for the same period plus 3 days prior to each set of observations. The error bars is the standard deviation of E(H_3^+) within each set of spectra.

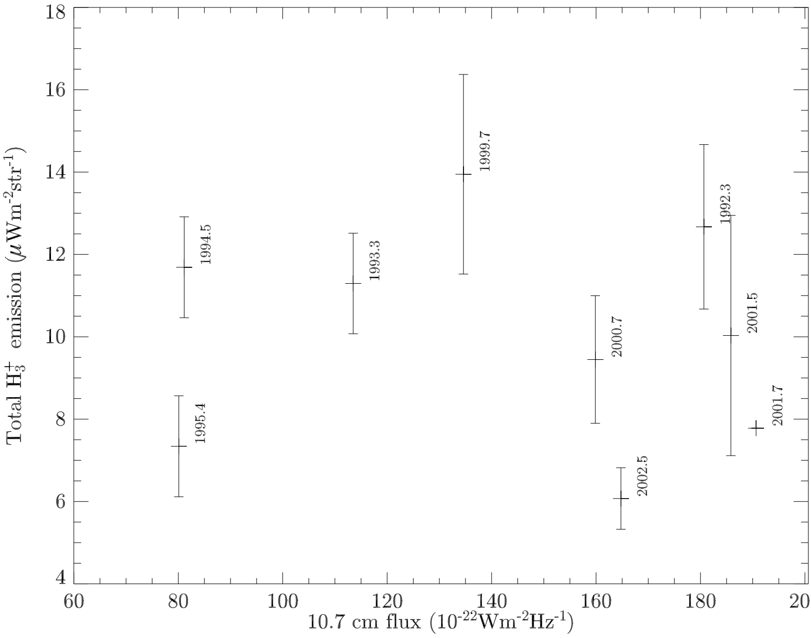

Figure 5.19: The average E(H_3^+) for each set of observations versus the average 10.7 flux as observed on Earth for the same period plus 9 days prior to each set of observations. The error bars is the standard deviation of E(H_3^+) within each set of spectra.

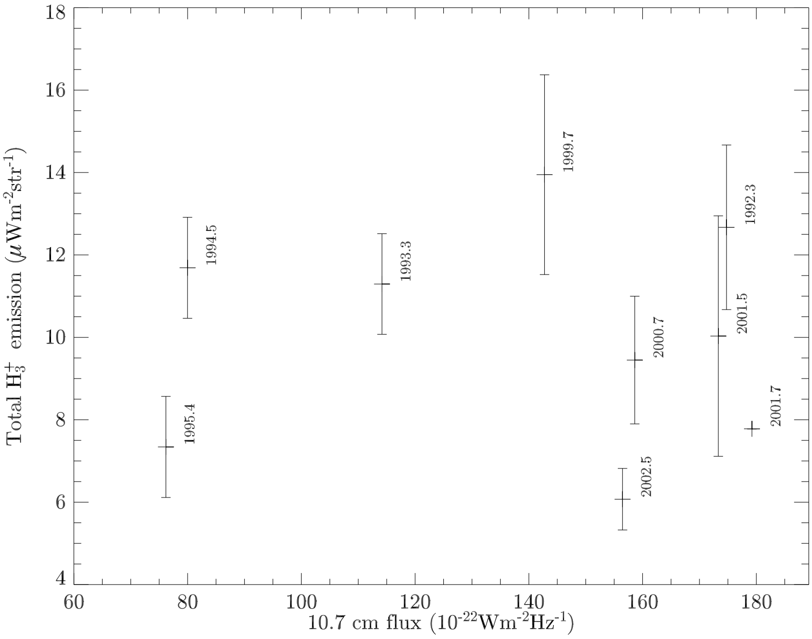

Figure 5.20: The average E(H_3^+) for each set of observations versus the average 10.7 flux as observed on Earth for the same period plus 15 days prior to each set of observations. The error bars is the standard deviation of E(H_3^+) within each set of spectra.

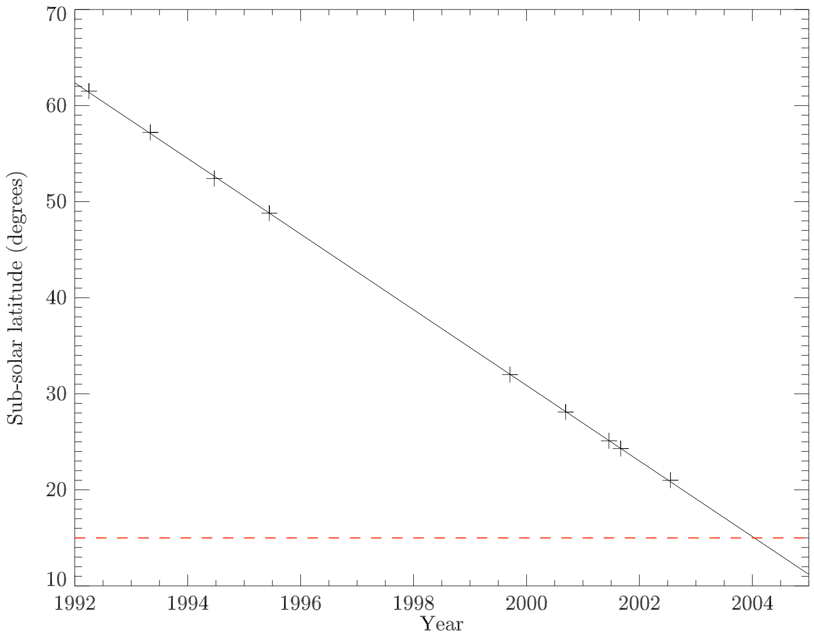

Figure 5.21: The sub-solar latitude of Uranus as a function of year. The crosses are the years of the available Uranus observations. The solid line is a linear fit to the crosses. The dashed line is the location of the magnetic pole at 15°N (Ness et al. [1986]).

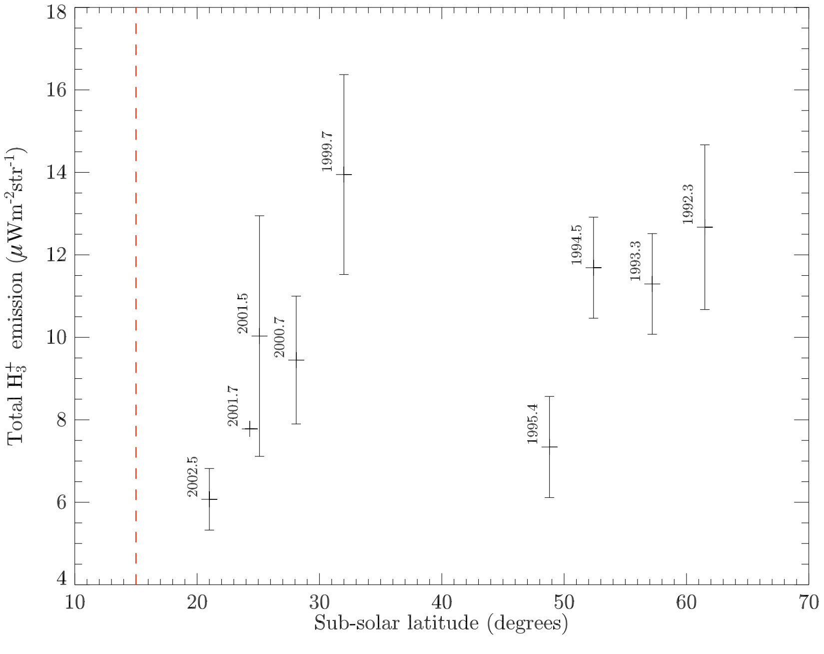

Figure 5.22: The average E(H_3^+) emission versus sub-solar latitude. The dashed line is the location of the north magnetic pole at 15°N (Ness et al. [1986]). The year of each datum is given to the right of each cross.

Year	Sub-solar ULS latitude (°)
1992.3	61.5
1993.3	57.2
1994.5	52.4
1995.4	48.8
1999.7	32.0
2000.7	28.1
2001.5	25.1
2001.7	24.3
2002.5	21.0

Table 5.9: The sub-solar ULS altitude for each set of observations.

a magnetosphere which was the least active in the solar system, with a very low plasma content. An inactive magnetosphere would imply that there are very few particles that could precipitate onto the atmosphere, reducing the quantities of auroral H_3^+. This could also be true for Uranus: the closer the alignment of the magnetic north pole to the sun direction, the less active a magnetosphere and the less emission generated by particle precipitation. The decline in $E(H_3^+)$ starts beyond the year 1999, at a sub-solar latitude at $\sim 30°$. This gives an angle between the sub-solar point and the magnetic pole of $30° - 15° = 15°$, suggesting that the cone subtending such an angle, is the limit of these effects.

The parker spiral angle at the orbit of Uranus at 19 AU is 88° which means that at around 2002, the magnetic field axis is approximately perpendicular to the flow of the solar wind. This configuration could impede the inflow of solar wind plasma into the magnetosphere. This configuration is in a sense a more ‘classic’ configuration, as observed at Earth, Jupiter and Saturn, where the dipole field is more or less perpendicular to the solar wind flow direction. This would suggest that when the magnetic axis of Uranus is more or less aligned with the soar wind flow direction large quantities of solar wind plasma can enter the magnetosphere, enabling the production of large quantities of H_3^+

5.4.3 Summary

Neither the solar EUV flux or the geometry can completely explain the observed long-term variations in the $E(H_3^+)$ emission. Prior to, and including, the year 1999, the emission can be explained, in broad terms, by the EUV variations seen in the the 11-

year solar cycle. After 1999, the sharp reduction in E(H_3^+) appears to be linked to the alignment of the north magnetic pole to the perpendicular direction of the solar wind flow direction. If the anti-alignment of the pole results in an inactive magnetosphere, resulting low densities of precipitation-produced H_3^+, then particle precipitation *and* EUV production mechanisms of H_3^+ are both important on Uranus.

The error bars on the E(H_3^+) in Figure 5.16 indicate the spread within each dataset as the size of one standard deviation of each set of data. On some of these points the spread is large, indicating that there is substantial short-term variability. This short-term variability shall be examined in the following sections.

5.5 Modelling the aurora

The previous section saw an attempt at explaining the long-term variability seen in the available H_3^+ spectra of Uranus. But what if there is only very little long-term variability such that the observed E(H_3^+) variations are simply an effect of geometry and timing of the observation as the aurora passes underneath the slit? To investigate if the short-term E(H_3^+) variability is related to auroral activity, a model of H_3^+ emission from Uranus is needed.

There has only been one spatially resolved observation of the aurora on Uranus. This observation was made in 1986 by Voyager 2 using the onboard Ultraviolet Spectrometer (UVS) and was analysed by Herbert and Sandel [1994]. An H_3^+ emission model was constructed, using these observations, assuming that the H_3^+ auroral emission has an identical morphology and intensity structure. The model also includes a solar EUV produced H_3^+ component.

5.5.1 Voyager 2 UV observations

Voyager 2 observed emission from H_2 in the ultraviolet, from almost the entire 'surface' of the planet. Herbert and Sandel [1994] analysed 32 hours of H_2 band airglow emission (found between $87.5 \leq \lambda \leq 111.5$ nm) using a singular value decomposition (SVD) approach to inversion. The analysis showed that the mapped intensity is larger than the error on the intensity over both magnetic poles, but only in part larger at the non-auroral regions. The auroral map they produced can be seen in Figure 5.23, showing auroral emission near both magnetic poles. The aurora associated with the northern magnetic pole emits more power and is larger than the aurora associated with the southern magnetic pole. This is in contrast to the fact that the northern pole has a weaker magnetic field strength than the south pole. The aurora is localised in structure and there are no auroral ovals as observed on Earth, Jupiter and Saturn.

The emission appears at lower L-shells than on both Jupiter and Saturn, which indicates that the energy of the precipitating particles is low, perhaps less than 10 keV (Herbert and Sandel [1994]). Obviously, the situation is made more complicated by the quadropole components of Uranus' magnetic field – Jupiter and Saturn have very small higher order magnetic moments. The effects that the field configuration of Uranus has on the magnetosphere/ionosphere interaction is not clear.

The units of the map in Figure 5.23 are [counts / 3.84 s] with the lowest intensity level being 6 counts / 3.84 s and the highest being 20 counts / 3.84 s. The background level below 6 counts / 3.84 s is a measure of the sensitivity of the observations, suggesting that the error of the intensity is of the order of 4 counts / 3.84 s. In other words, there are large errors on the observed H_2 intensity, such that the spatial resolution is much poorer than Figure 5.23 at first glance seem to display.

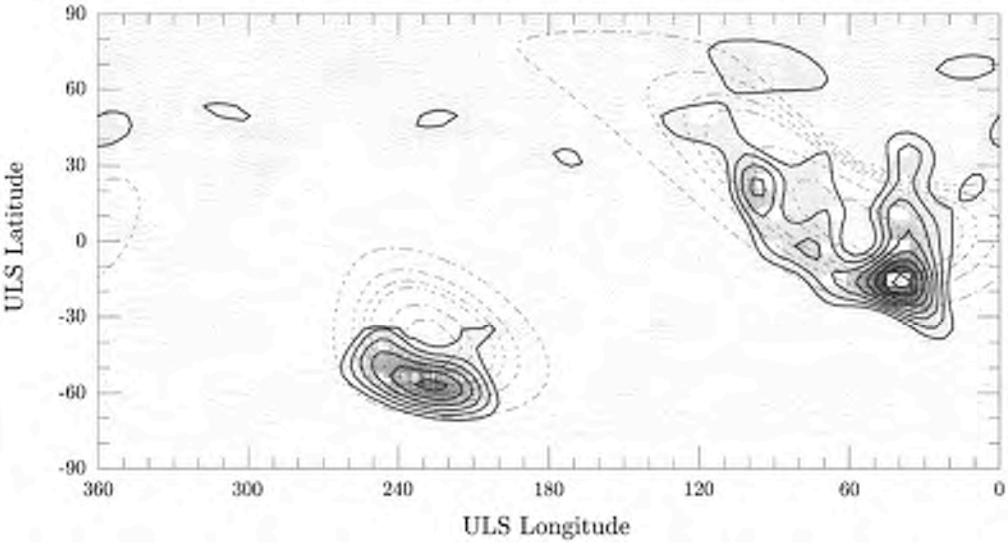

Figure 5.23: The uranian H_2 UV aurora as observed by Voyager 2 in 1986. The solid contours are the H_2 band emission intensity distribution and the dashed lines are the L-shells (from the outside L = 2, 3, 4, 5, 10, 20). Figure adapted from Herbert and Sandel [1994].

5.5.2 Assumptions

In what follows, we shall assume that the morphology of the auroral component of H_3^+ is the same as that of the auroral UV emission of Herbert and Sandel [1994]. There is support for this in the observations of other planets. We find that at high latitudes on Jupiter and Saturn (and, in these cases, high L-shells) the UV emission (e.g. Trauger et al. [1998b]) occurs at similar latitudes as the auroral infrared H_3^+ (e.g. Drossart et al. [1989]). However, there are significant differences in fine structure on both Saturn and Jupiter between the UV H_2 emission and the infrared H_3^+ emission. On Jupiter, the UV often shows sharp discrete structures (Grodent et al. [2003]) whereas Stallard et al. [2001] was able to identify regions within the auroral oval with significant continuous H_3^+ emission in regions identified as 'black' in the UV. This would seem to indicate that there are differences in production mechanisms. Similar differences are observed on Saturn (Grodent et al. [2005] in the UV and Stallard et al. [2004] in the infrared).

It is important to bear in mind that the observation of Herbert and Sandel [1994] is the *only* observation of the uranian aurora and as such it is a logical starting point when putting together an H_3^+ emission model. Parameters like the orientation of the rotational pole and the orientation of the magnetic field has changed a great deal since 1986 when Voyager 2 visited Uranus. However, while these parameters may well affect the aurora in unknown ways, for want of a better approximation, we assume that the H_3^+ aurora is not only morphologically identical to the UV aurora of Herbert and Sandel [1994], but also that the aurora has remained unchanged in structure and intensity since 1986. The validity of these assumption is as of yet impossible to ascertain, but we know that the H_3^+ aurora on Jupiter has retained a similar morphology since its detection in 1989, although with significant variations in intensity over shorter timescales (Grodent et al. [2003]).

5.5.3 Extracting the aurora

The auroral map published by Herbert and Sandel [1994] was scanned into an image editing program and for each intensity level an image was created, containing the outline shape of that particular level. All eight files can be seen in Figure 5.24. These images were imported into Macromedia Flash where were each level was converted into vector shapes. These were subsequently stacked to created the intensity map which was exported as a bitmap with a size of 360×180 pixels, representing a resolution of 360 degrees in longitude and 180 degrees in latitude. This file was then imported into IDL and scaled, with the lowest level being scaled to a value of 6 and the highest to 20, as per Herbert and Sandel [1994] (see Figure 5.23). The resulting digitised auroral map can be seen in in Figure 5.25. This map is near identical to the map published by Herbert and Sandel [1994].

5.5.4 The H_3^+ produced by solar EUV

Trafton et al. [1999] found that the H_3^+ intensity peak is for the the majority of their observations located at the sub-solar point on Uranus, indicating that the solar EUV mechanism is the dominant production mechanism, and estimated that auroral processes could only account for some $\sim 25\%$ of the H_3^+ emission. This is because at small angles from the sub-solar point the EUV radiation can penetrate deep into the atmosphere creating more H_3^+, since the H_2 density increases with decreasing altitude.

The amount of light received, per unit area, at the outer layer of the atmosphere is given by:

$$I = I_0 \cos(\theta) \tag{5.5}$$

where θ is the angle between the line connecting the centre of planet and the sub-solar point and the line connecting the centre of the planet and the latitude in question. I_0 is the flux per unit area at the sub-solar point. Assuming that the number of H_3^+ ions created is linearly proportional to the flux that the atmosphere receives, then Equation 5.5 will also describe the line-of-sight uncorrected $E(H_3^+)$, where I_0 becomes the sub-solar value of $E(H_3^+)$.

The line-of-sight correction for a spherical planet is given in Equation 2.12. The pathlength multiplier can be seen as the solid line in Figure 5.26. The diameter of Uranus is 51,118 km (Astronomical Almanac) and the H_3^+ layer is assumed to be small, some 500 km. Since the diameter is much larger than the layer emitting H_3^+, the line-of-sight correction factor remains fairly constant (see Section 2.3).

The modelled central meridian components of the solar EUV produced H_3^+ emission can be seen in Figure 5.26. Correcting for line-of-sight effects produces an almost flat emission profile across the planet. However, when this emission is smoothed, taking into account the seeing effects that prevailed on the night of observation, then the

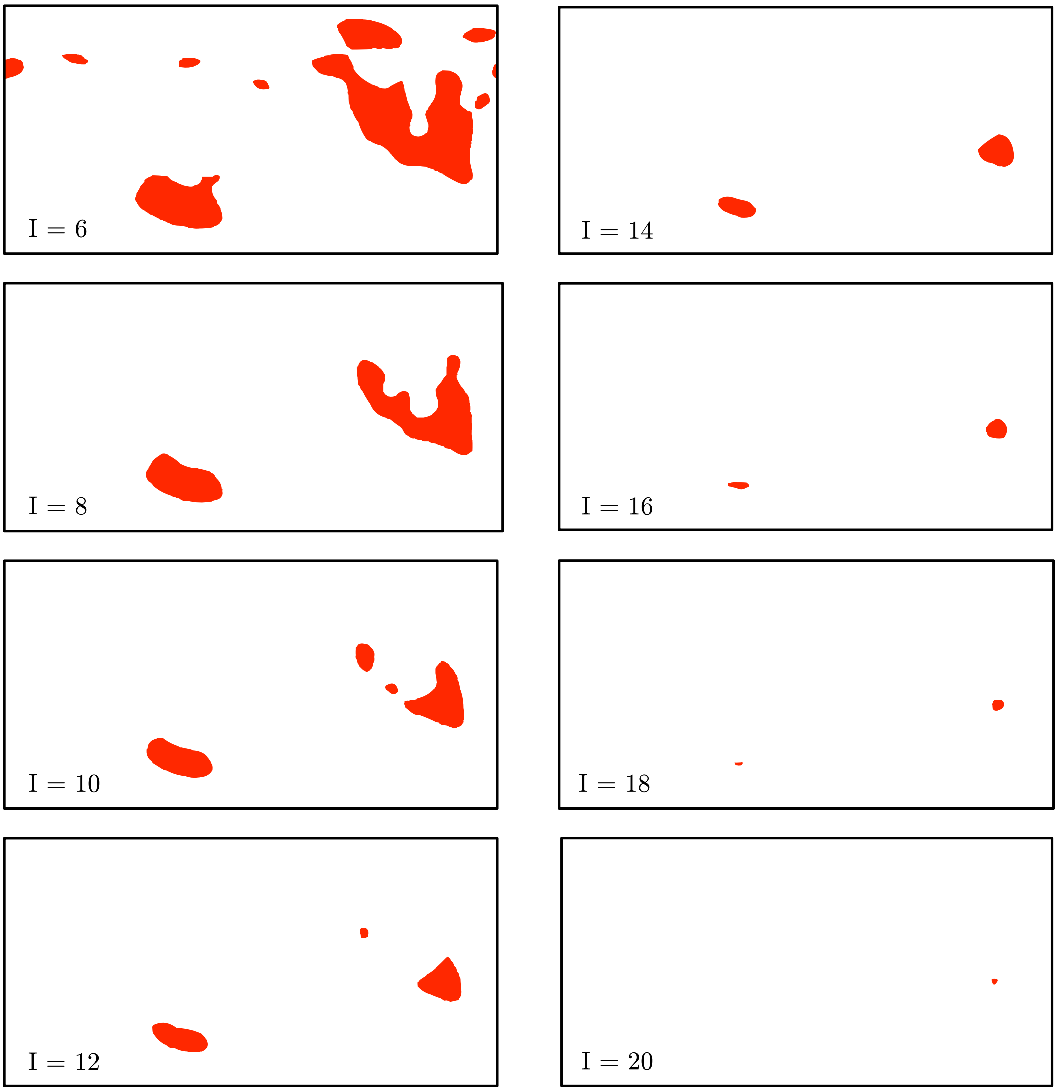

Figure 5.24: All the extracted levels in monochrome of the UV H_2 aurora observed on Uranus by Herbert and Sandel [1994]. The intensity, I, is in units of counts / 3.84 s.

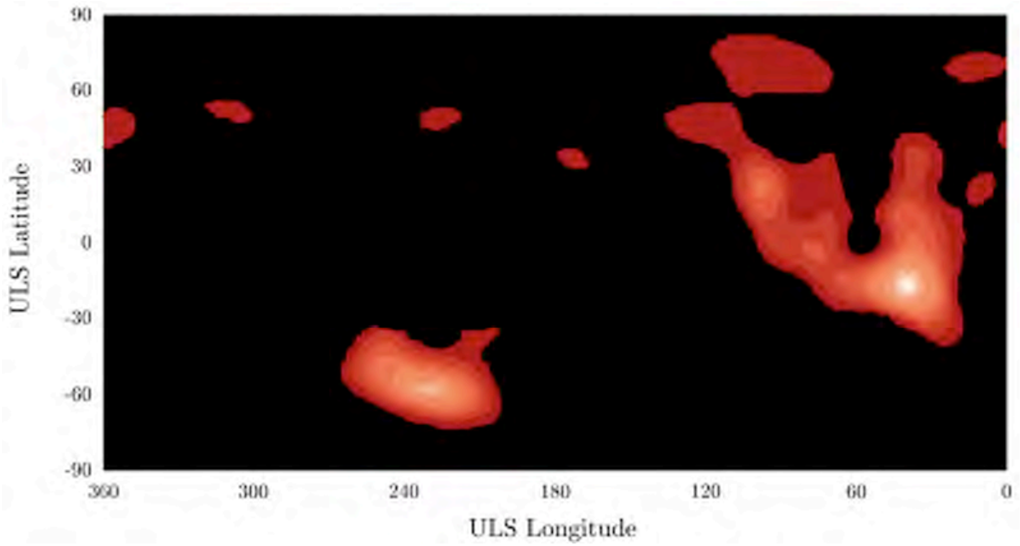

Figure 5.25: The intensity map extracted from the observations of Herbert and Sandel [1994]. The map has a resolution of 1° in both longitude and latitude. The lowest non-black level is I_{UV}=6 and the highest is I_{UV}=20 in units of counts / 3.84 seconds.

emission becomes peaked at the centre of the planet.

The observed H_3^+ intensity summed across the entire disc of Uranus can be seen in Figure 5.27. It is constructed from an image taken with NFSCam mounted on the NASA IRTF in July 1999 by Laurence Trafton (University of Texas) and Steve Miller (University College London). The image appears to contain little auroral emission and, as such, it can be used to set the base level of solar EUV emission (Laurence Trafton, personal communication). Figure 5.27 also shows the corresponding plot for the H_3^+ emission model. Comparing the model to the observations (crosses) gives good agreement. The residual data that fall outside the model is likely to be local effects, such as auroral emission.

5.6 Modeling NFSCam response of Uranus

An IDL procedure was written that models the response of a camera to the rotation of Uranus given the aurora as determined by Herbert and Sandel [1994]. See Appendix B.4 for more details of the procedure. The parameters needed for each model are:

- **Central meridian longitude (CML)** as defined by the IAU, at the mid-point in time of the observation (see Section 5.2).

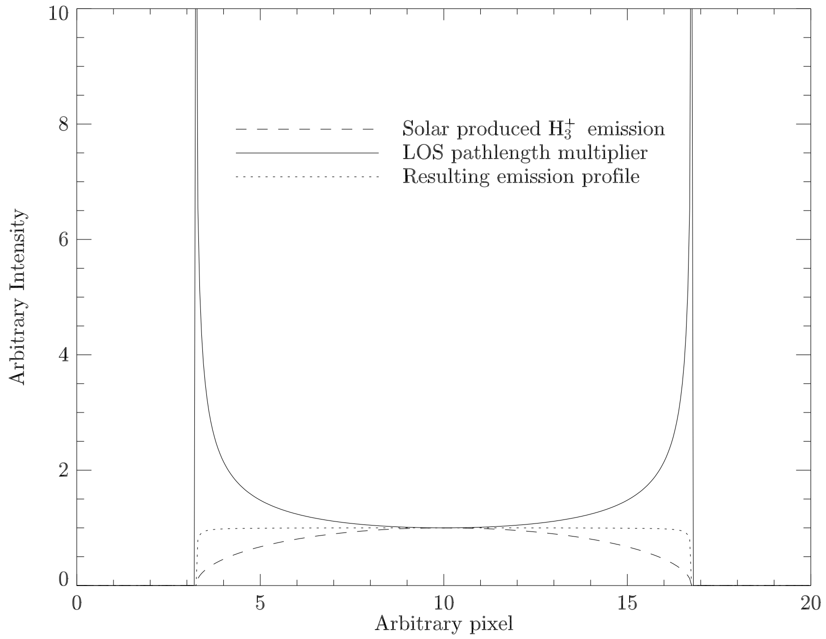

Figure 5.26: A central meridian cut through the model of the solar EUV emission. The solid line is the line-of-sight pathlength multiplier, the dashed line is the pre-line-of-sight solar produced H_3^+ and the dotted line is the product of these two lines.

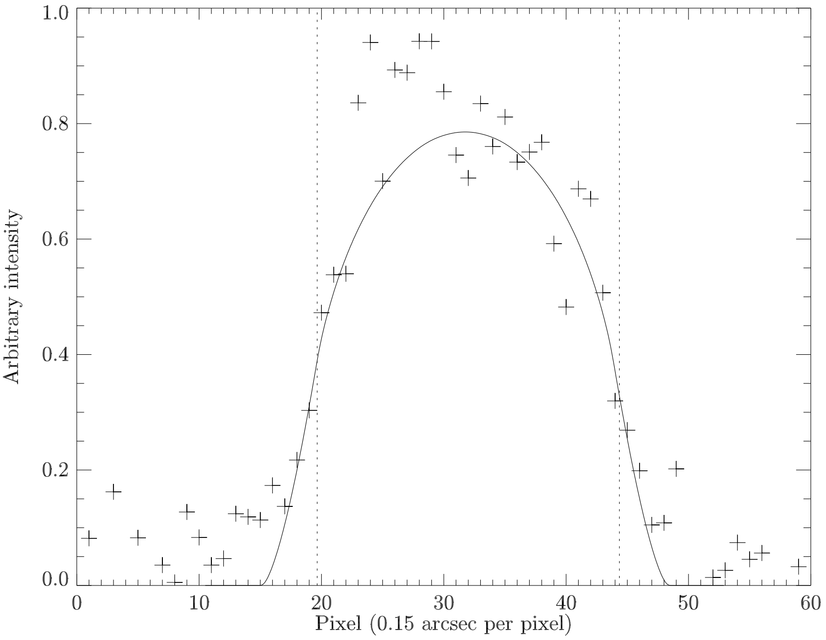

Figure 5.27: The average emission across the whole disc of an NFSCam image of Uranus (crosses) and the EUV H_3^+ emission model (solid).

- **The offset between the IAU from ULS central meridian longitude**. The period of Uranus is 17.24±0.01 hours (Desch et al. [1986]) and it is therefore not possible to accurately know the sub-observer ULS longitude some dozen years later. The offset describes the number of degrees between the IAU and the ULS central meridian longitude and is needed since the auroral map is given in ULS longitudes and the data is described by IAU longitudes.

- **The integration time**. From the integration time, the time spent exposing the image on Uranus, one can calculate through how many degrees Uranus rotated during the observation. The integration time is normally the number of quads multiplied by the integration time per quad (ignoring over-head times, which are generally small compared to the total integration time), where one quad is the A-B-B-A group of exposures, where A is the object exposure and B is the sky exposure (as outlined in Section 2.2).

- **The sub-observer latitude of Uranus at the time of observation**. This is the ULS sub observer latitude which can be found by entering the UT time and date of the observation on the Uranus Viewer website.

For each minute in each observation a projection is produced using the IDL procedures `map_set` and `map_patch`. These images are then averaged over the integration time, to produce the effect of the planet rotating. This is then repeated for all the observations using the sub observer IAU longitude for each individual set (e.g. see Table 5.10). All these images are then weighted-averaged with respect to the integration time of each observation to create the response to that particular longitude.

Figure 5.28 shows the components of the emission model for a single observation. The solar and auroral component are both subject to the line-of-sight effects, also known as limb-brightening, which is corrected for.

This H_3^+ emission model can mathematically be written as:

$$\texttt{model} = \sum_{j=0}^{obs} W_j \left(\sum_{i=0}^{mins} (\texttt{solar} + \texttt{auroral}_{ji}) \times \texttt{limb\_brightening} \right) \tag{5.6}$$

where `solar` is the H_3^+ component due to solar EUV (see Section 5.5.4), `auroral` is the H_3^+ component due to auroral processes as described by the Herbert and Sandel [1994]

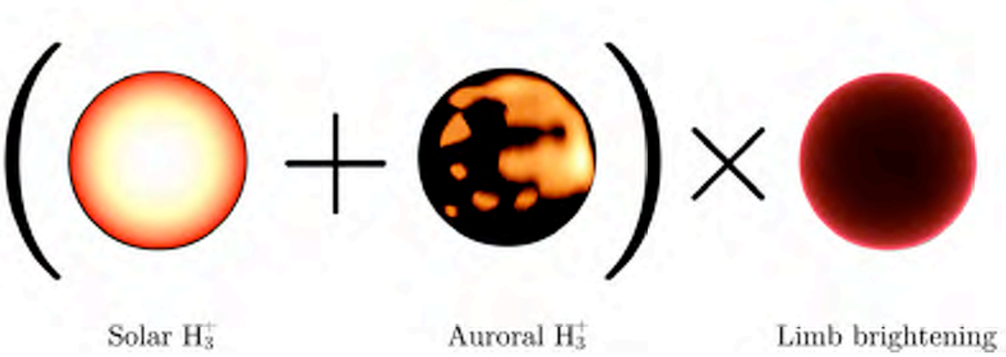

Figure 5.28: The components of the model of the NFSCam response to uranian H_3^+ emission.

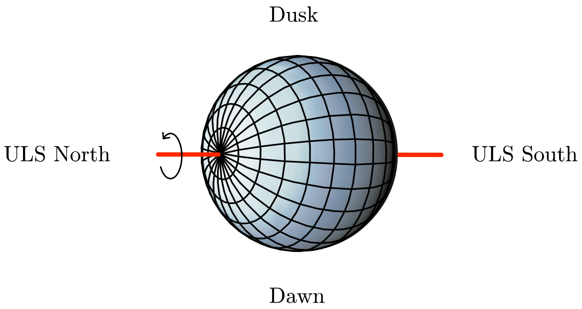

Figure 5.29: The orientation of the observations and models presented in this chapter.

map, for each observation j that constitutes the particular longitude and during a particular observation, the minute i of the observation. W_j is a weighting factor that takes into account the exposure time of each observation with respect to the total exposure time of the particular longitude (which is a sum of observations). `limb_brightening` is the line-of-sight correction shown in Figure 5.26. The product of this equation is then smoothed according to the seeing conditions at the time of a particular set of observations, typically $0.5''$ to $1.0''$. Seeing has the effect of blurring out features due to fluctuations in the Earth's atmosphere. If the observations experienced a seeing of $1''$ then the model is also smoothed by an equivalent $1''$. The IDL function `smooth` performs a boxcar smoothing, which is the moving average calculated for a box with the same size sides as the seeing limit.

An example set of emission models for every 15° ULS longitude can be seen in Figure 5.30 for a sub-observer latitude of 36° N, smoothed by $0.7''$, and each observation spanning one minute. The orientation of the models (and observations) is presented

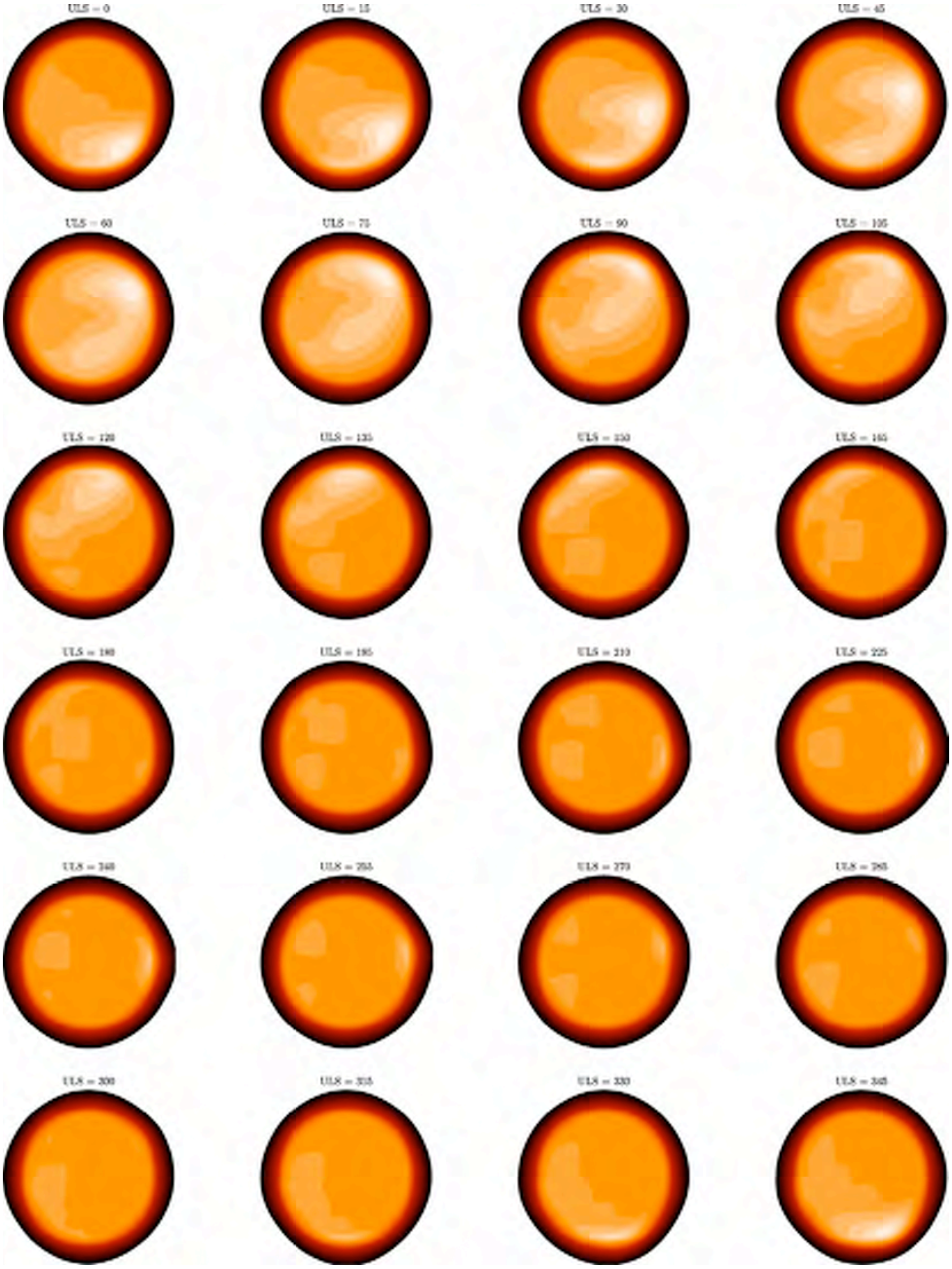

Figure 5.30: The Uranus H_3^+ emission model for every 15° ULS longitude. It is smoothed by $0.7''$ to simulate typical seeing conditions. The sub-observer latitude is 36° ULS North. Each observations spans 1 minute. ULS North is to the right and dusk is is at the top, as per Figure 5.29.

the same in all the figures: USL north is to the right and dusk is at the top of each image as shown in Figure 5.29. Since only the northern aurora is visible there are longitudes with strong emission covering about half a rotation (USL = 0° to ULS = 150° and USL = 315° to ULS = 345°). The remaining longitudes only show weak, patchy, aurora although the southern aurora can very faintly be seen to the right at ULS longitudes 225° to 255°. Consequently, the intensity of H_3^+ emission is a strong function of the sub-observer longitude at the time of observation, provided that the aurora is strong enough to stand out significantly from the solar EUV produced H_3^+.

5.6.1 Observations to model

Larry Trafton and Steve Miller used the NFSCam imager on the NASA IRTF when observing Uranus in July 1998 and July 1999. These observations will be compared to the H_3^+ emission model in an attempt in identifying auroral features in the images. The reduced images were supplied by Larry Trafton (University of Texas).

The first set of data was taken between the 26th and 29th of July 1998. During these observations the ULS sub-observer latitude was 36° ULS north and Uranus had a diameter on the sky of $3.74''$ or 24.9 pixels ($0.15''$ pixel^{-1}). The images were taken through the Connerney filter, centred around 3.541μm, and CVF filter, centred around 3.986 μm with a 2% full-width at half-maximum (FWHM). The transmission profiles of these two filters can be seen in Figure 5.31 and 5.32. Even though the latter filter contains much stronger H_3^+ emission, the signal-to-noise (SNR) is much better when using the Connerney filter. This is because that within the 2% FWHM of the CVF filter is dominant by non-emitting spectral regions, whereas the Connerney filter is much narrower, sampling more of the H_3^+ emission.

The 1998 data, grouped in IAU longitudes, can be seen in Figure 5.33 and the individual observations are listed in Table 5.10. The IAU longitudes are calculated as per Equation 5.3. The images show H_3^+ emission that is consistently stronger towards ULS South, showing large variability at lower latitudes. IAU = 179° has the weakest signal with a lot of noise, whereas the others show similar signal-to-noise ratio.

The second set of images were taken between the 9th and 12th of July 1999 with the same instrumet. Uranus had at the time of observation a ULS sub-observer latitude of 33° N. The diameter of Uranus on the sky was at the time $3.71''$ or 24.7 pixels. In

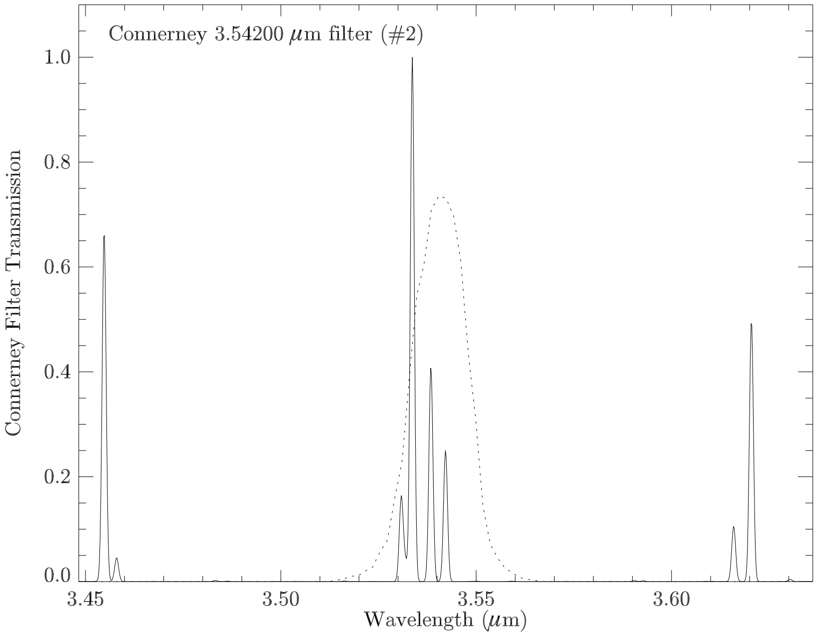

Figure 5.31: The transmission profile of the Connerney filter on NFSCam (dotted) and a normalised theoretical H_3^+ spectrum (solid) at a temperature of 600 K.

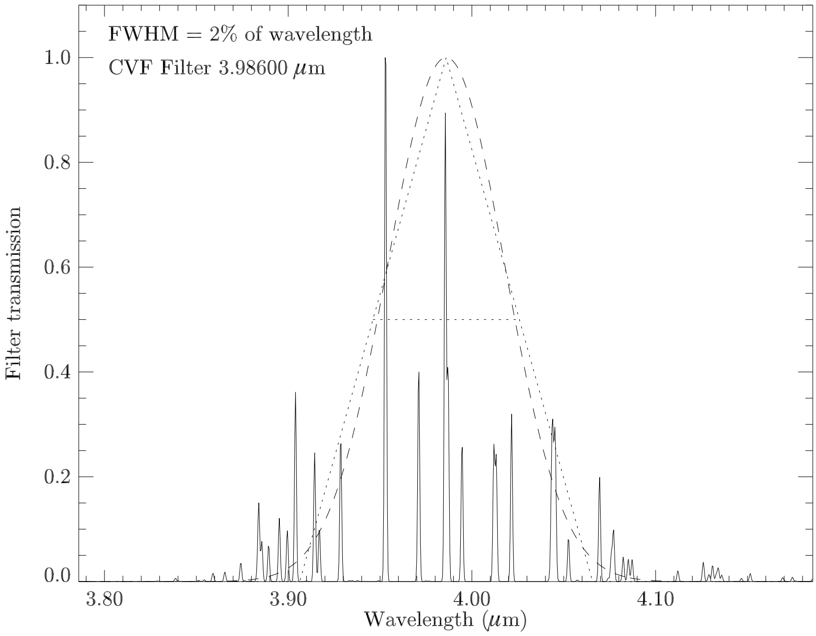

Figure 5.32: The transmission profile of the CVF filter centred around 3.986 μm filter described as a triangle (dotted), as a gaussian (dashed) and a normalised theoretical H_3^+ spectrum (solid) at a temperature of 600 K.

UT Date	UT Time^a	No. quads	Exp. (mins)	IAU (°)	Avg. IAU (°)
26 Jul 1998	07:57	2.5	22.7	018	26
26 Jul 1998	08:38	5	25.3	032	
26 Jul 1998	09:50	5	25.3	057	63
29 Jul 1998	06:51	5	25.2	058	
29 Jul 1998	07:20	5	25.2	069	
29 Jul 1998	09:06	5	25.5	105	105
27 Jul 1998	07:37	4	20.2	152	152
27 Jul 1998	08:14	2.5	21.5	165	179
27 Jul 1998	09:19	5	38	187	
28 Jul 1998	08:49	5	25.3	318	318

Table 5.10: Breakdown of the observations taken by L. Trafton and S. Miller using NFSCam on NASA Infrared Telescope Facility (IRTF) between 26th July 1998 and 29th July 1998. Note that the nod exposure time is not the same for all observations. ^{a}Mid-observation values.

addition to the filters used in 1998 two more filters were used: the Connerney filter centred around 3.42 μm and the CVF filter centred around 3.95 μm.

The data, grouped in IAU longitudes in a similar way to the 1998 data, can be seen in Figure 5.36 and the individual observations are listed in Table 5.11. These observations do not consistently show the intensity biased towards the ULS South, as the 1998 images do. Even though these images have a slightly lower signal to noise ratio than the 1998 images, they show significant variability between the six different longitudes. This could be indicative of auroral activity.

5.6.2 Modelling planetary phase-shift

Since the IAU longitude for each NFSCam observation is known, we can create a set of models, each having the same spacing in longitude, but having a different IAU to ULS offset. In other words, we can generate many sets of six models, keeping the spacing in longitude constant, but each time increasing the IAU to ULS longitude offset. For each year, 36 sets of models were created, increasing the IAU to ULS offset by 10° each time. From this collection of models, the one that bears the closest resemblance to the complete set of NFSCam images is selected, enabling us to determine the best fit offset between the IAU and ULS longitude.

The largest inconsistency when matching these model-sets to the observations is the presence of features in nearly all the NFSCam images. The southern auroral emission of Herbert and Sandel [1994] is mostly obscured due to the configuration of

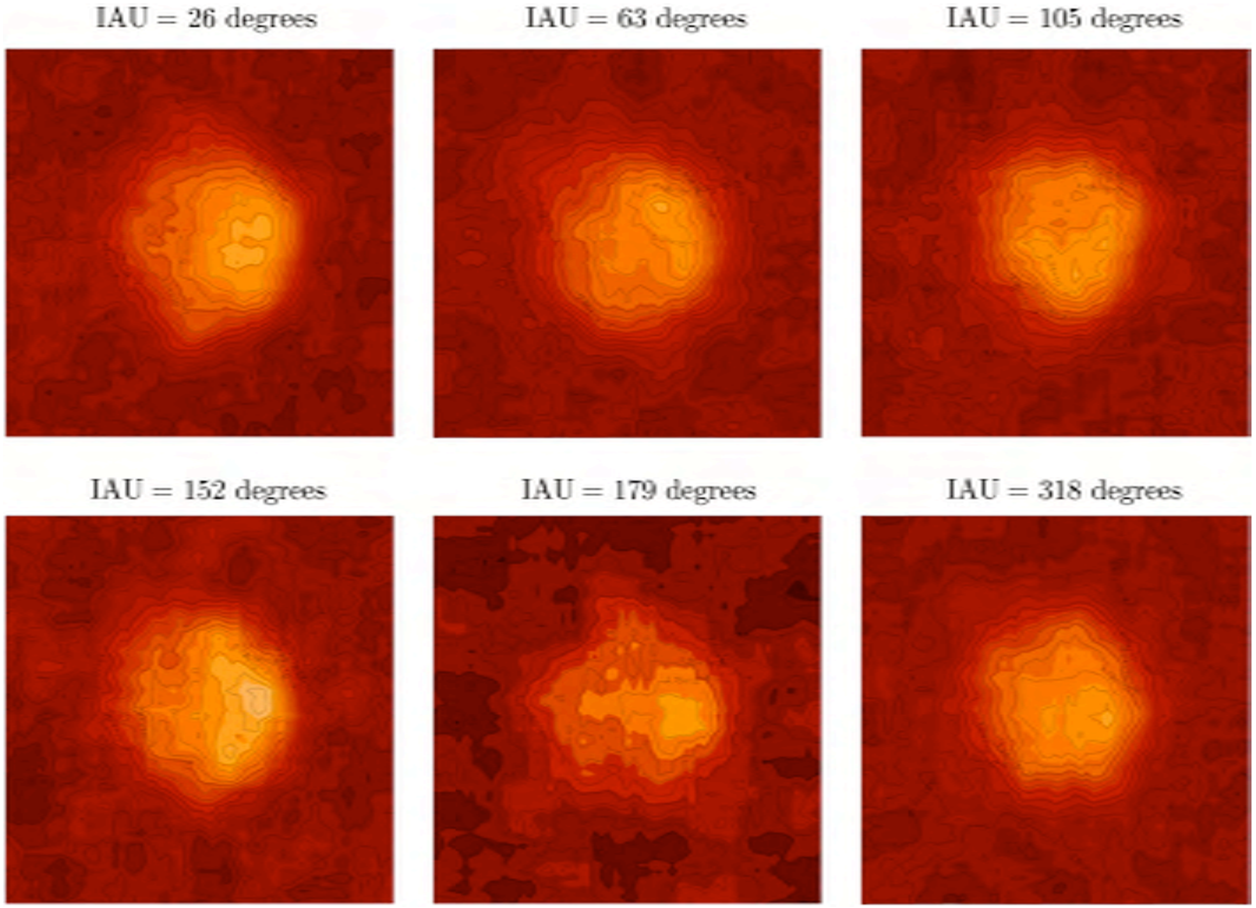
IAU = 26 degrees
IAU = 63 degrees
IAU = 105 degrees
IAU = 152 degrees
IAU = 179 degrees
IAU = 318 degrees

Figure 5.33: Intensity maps of Uranus taken with NFSCam on NASA IRTF in 1998. The dusk is at the top of each image and the ULS North is to the left as per Figure 5.29.

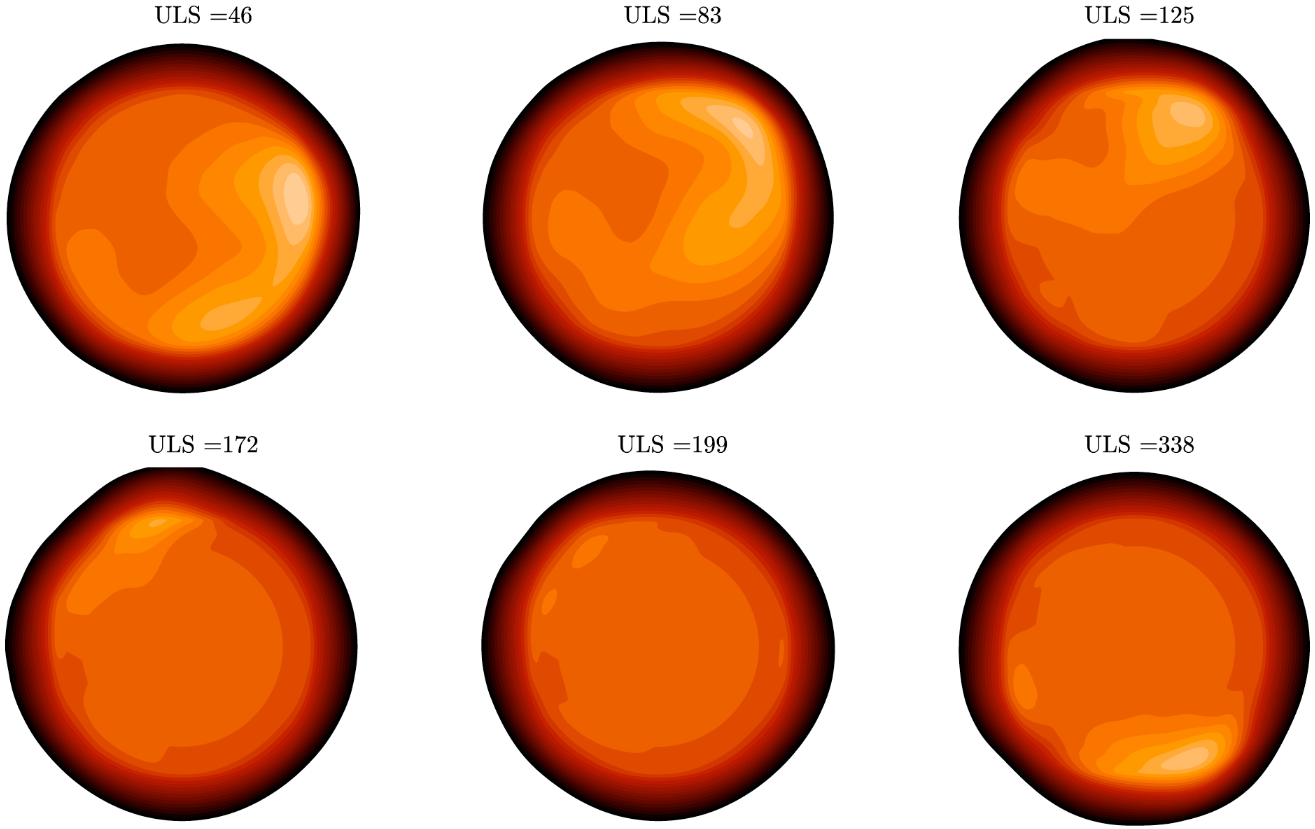

Figure 5.34: Model of the 1998 NFSCam images with an offset from ULS longitude of 20°. The dusk is at the top of each image and the ULS North is to the left as per Figure 5.29.

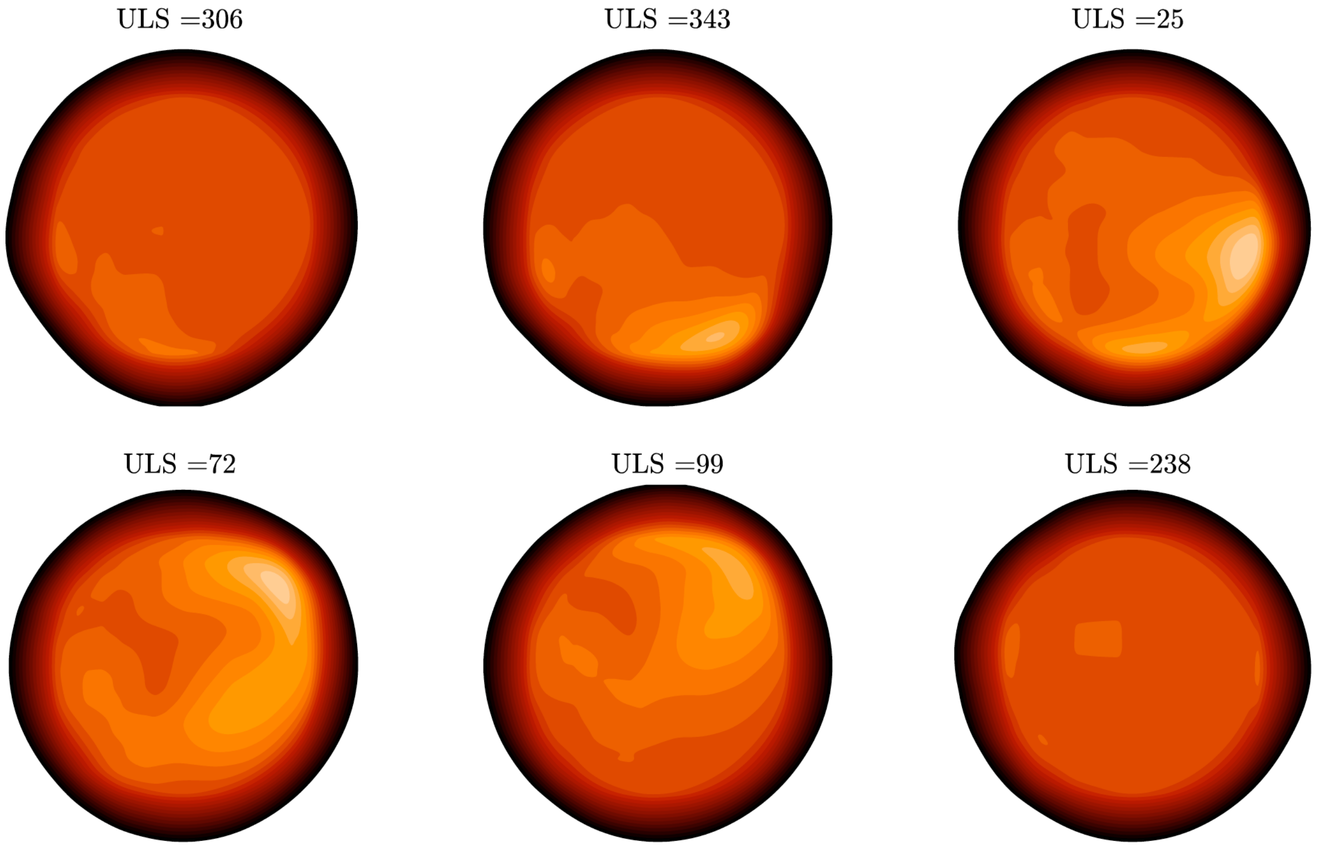

Figure 5.35: Model of the 1998 NFSCam images with an offset from ULS longitude of 280°. The dusk is at the top of each image and the ULS North is to the left as per Figure 5.29.

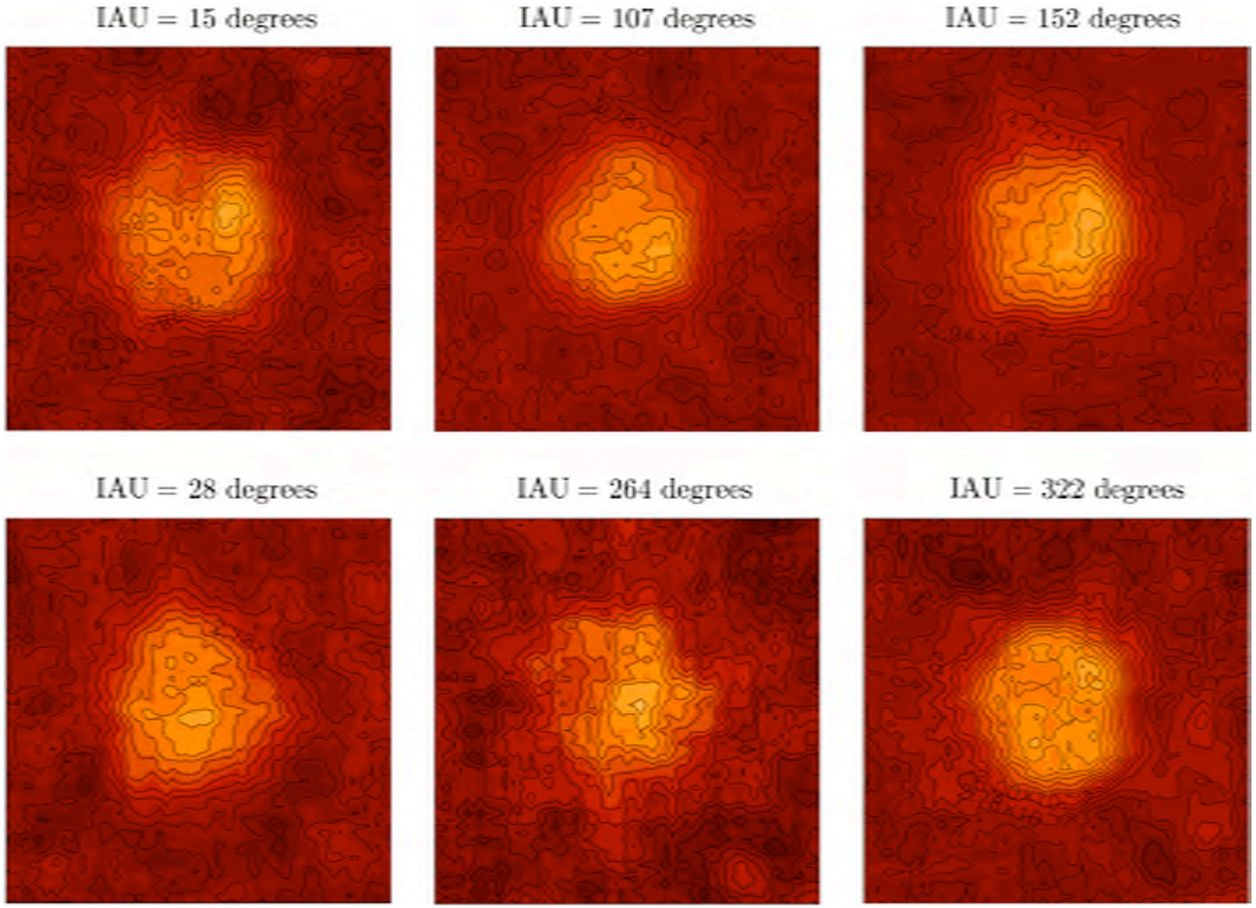

Figure 5.36: Intensity maps of Uranus taken with NFSCam on NASA IRTF in 1999. The dusk is at the top of each image and the ULS North is to the left as per Figure 5.29.

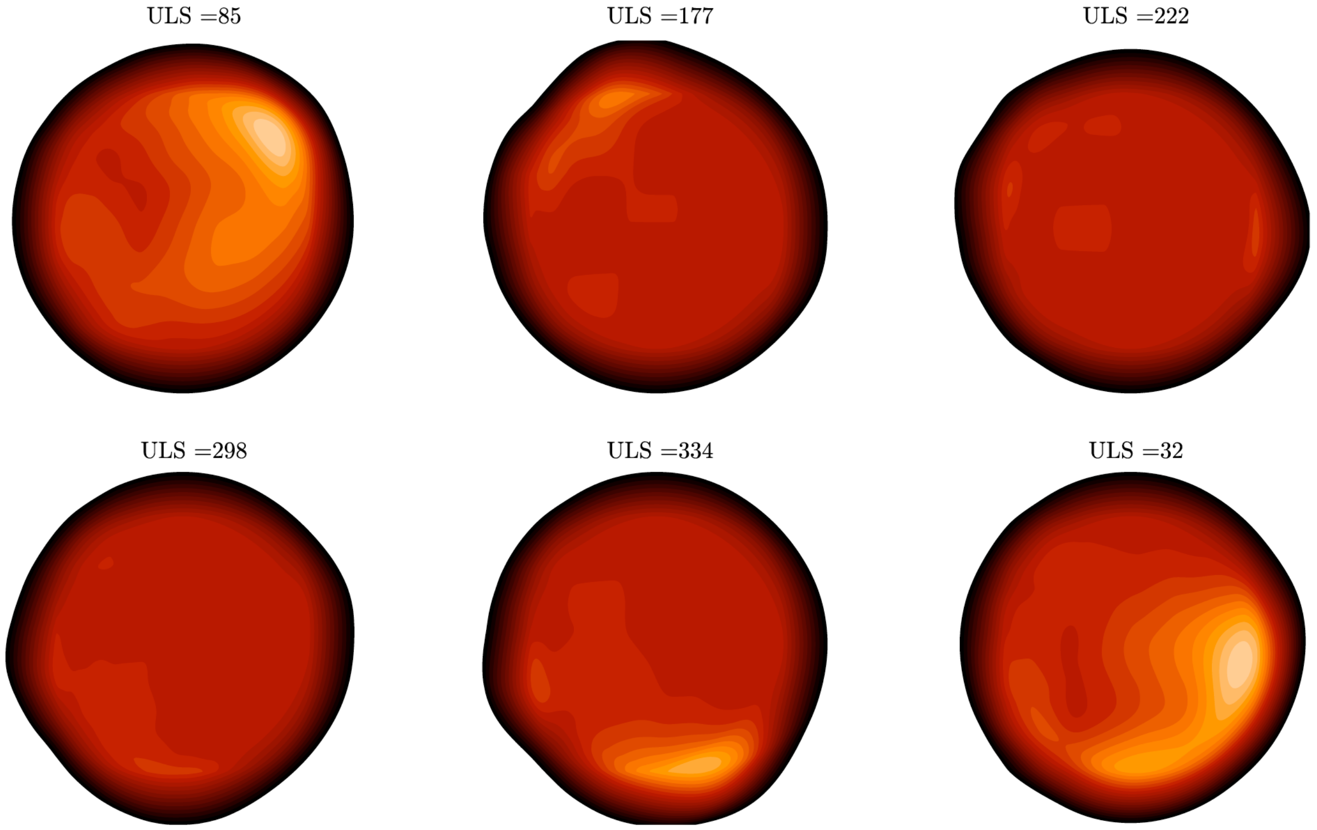

Figure 5.37: Model of the 1999 NFSCam images with an offset from ULS longitude of 70°. The dusk is at the top of each image and the ULS North is to the left as per Figure 5.29.

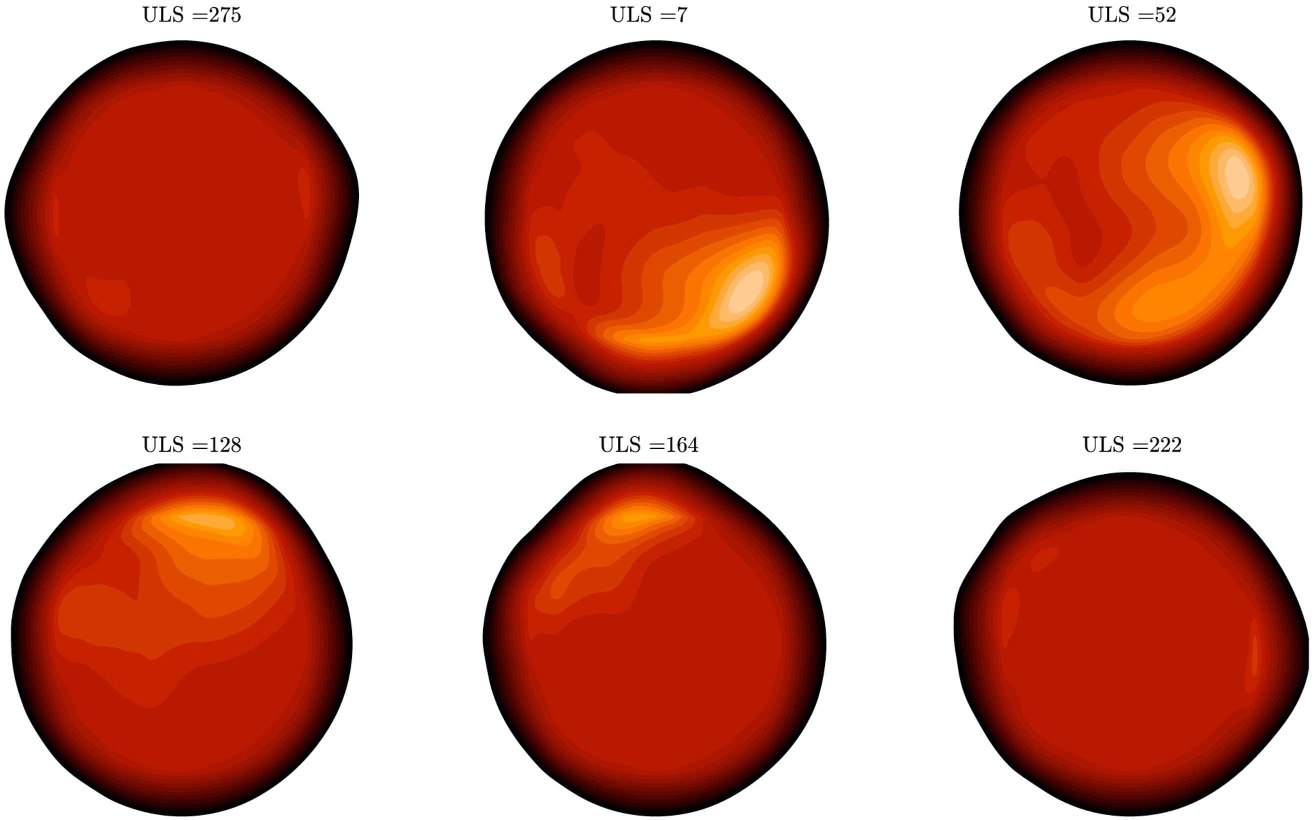

Figure 5.38: Model of the 1999 NFSCam images with an offset from ULS longitude of 260°. The dusk is at the top of each image and the ULS North is to the left as per Figure 5.29.

UT Date	File #	UT Time^{a}	Filter (μm)	IAU (°)	Avg. IAU (°)
9 Jul 1999	082	10:22	3.541	0	15
11 Jul 1999	348	14:14	3.986	3	
9 Jul 1999	130	11:44	3.541	29	
12 Jul 1999	148	12:00	3.986	98	107
12 Jul 1999	192	12:40	3.953	112	
10 Jul 1999	070	09:05	3.42	114	
12 Jul 1999	280	14:14	3.986	144	152
10 Jul 1999	118	10:33	3.986	145	
12 Jul 1999	324	14:54	3.953	158	
10 Jul 1999	142	11:16	3.953	160	
10 Jul 1999	238	13:37	3.42	209	228
10 Jul 1999	286	15:07	3.986	240	
11 Jul 1999	076	09:10	3.42	257	264
11 Jul 1999	100	09:49	3.42	271	
11 Jul 1999	216	11:54	3.986	314	322
11 Jul 1999	260	12:38	3.953	330	

Table 5.11: Breakdown of the observations taken by L. Trafton and S. Miller using NFSCam on NASA Infrared Telescope Facility (IRTF) between 9th July 1999 and 12th July 1999. The observations are grouped according to longitude. ^{a}Mid-observation value.

Uranus for both sets of observation. The northern aurora only occupies 0° to 120° degrees ULS longitude, and so it is difficult to account for all the distinct features in the majority of the images as both sets of images covers most longitudes. It is clear that one of the fundamental assumptions of Section 5.5.2 might not hold. For example, the H_3^+ intensity distribution might have a very different structure to the UV aurora.

In the following sections, references to ULS longitudes refers to models, since they are defined with respect to the Voyager 2 aurora of Herbert and Sandel [1994], and observations are referred to by the central meridian longitude (CML), as defined by the IAU at the time of observation (defined in Equation 5.3).

5.6.3 Results from the July 1998 data

The 1998 NFSCam images are best fitted with two offsets: 20° shown in Figure 5.34 and 280° shown in Figure 5.35.

The 20° offset in Figure 5.34 can fairly well model the appearance of IAU = 26°, 63° and 318° in Figure 5.33. The signal-to-noise ratio at IAU = 170° is low in comparison to the others, and is, in the model, an evenly illuminated disc. The emission appearing on the dusk side at ULS = 125° is not seen on the NFSCam image at IAU = 105°, nor can the model explain the emission at CML = 152°.

The NFSCam images that the 20° offset model is having trouble reproducing are fairly well modelled by the 280° offset model, seen in Figure 5.35. The longitudes that are modelled well are ULS = 195°, 152° and 179°, whereas the other 3 are poorly modelled.

5.6.4 Results from the July 1999 data

The 1999 observations can be seen in Figure 5.36. The best fit to these images is an IAU offset to ULS of 70°, shown in Figure 5.37, and an offset of 260°, shown in Figure 5.38.

The 70° offset model can reproduce the observed IAU = 15°, 264° and 322° (and perhaps ULS = 298°). The model produces emission on the dusk side at ULS = 177°, whereas the image show a prominent emission on the dawn side. The observed emission at ULS South at IAU = 152° is not reproduced either.

The 260° offset model can reproduce IAU = 107° and 152 well, whereas it cannot explain the emission in the other four sets of observed longitudes.

Again, the problem is that most images have features associated with them, whilst the H_3^+ emission model only has significant auroral emission covering some 180 degrees of longitude.

5.6.5 Summary

There are 350 days between the two available sets of NFSCam images. Since the period of Uranus is known to be 17.24 ± 0.01 the number of longitudes that the planet can shift over a year is:

$$0.01 \times \frac{24}{17.24} \times \frac{350}{17.24} \times 360 = 102^\circ \tag{5.7}$$

This would suggest that the offset of 20° in 1998 is not compatible with the offset of 260° in 1999 and similarly that the 280° offset in 1998 is not compatible with the offset of 70° in 1999. For the purpose of illustrating techniques we shall analyse the 20° offset in 1998 and 70° offset in 1999. Using the offsets between the IAU and ULS

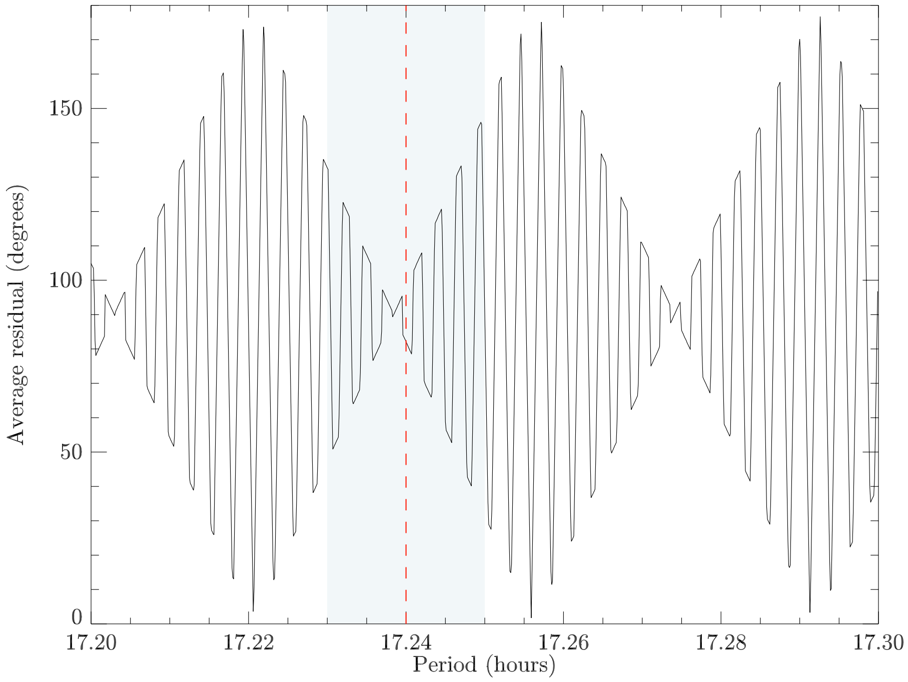

Figure 5.39: The possible periods of Uranus based on the ULS to IAU shift of 20° in 1998 and 70° in 1999. The dashed line is the determined period of 17.24 hours with the associated error of 0.01 hours shaded.

longitude, determined in this section, it is possible to calculate the rotational period that would best explain both the 1998 and 1999 longitude offset. Figure 5.39 shows the average residual, i.e. the difference between the calculated and the observed USL to IAU shift as a function of rotational period. It shows that there is a poor match with the period of Desch et al. [1986] (17.24 ± 0.01 hours). The analysis seem to imply a change of rotational period, although it is inconclusive if it has slowed down or speeded up.

The major caveat in this analysis is that the match between the observed sets of images and the models are not very convincing. It is important to recognise that the error in the Voyager 2 UV intensity measurements is most likely as bad, if not worse, than the H_3^+ images analysed here. Unfortunately, the spatial resolution of the UV data cannot be improved. However, the approach is readily adaptable to new sets of observations in which we might hope to obtain images with improved spatial resolution and signal-to-noise. There is good scope for further work on the analysis of infrared images of Uranus. NASA IRTF are soon installing NSFCam2; a 1-5 μm imaging device with a 2048×2048 Hawaii-2RG detector, and a spatial resolution of $0.04''$ pixel^{-1}. This camera is more sensitive than the old NFSCam thanks to the

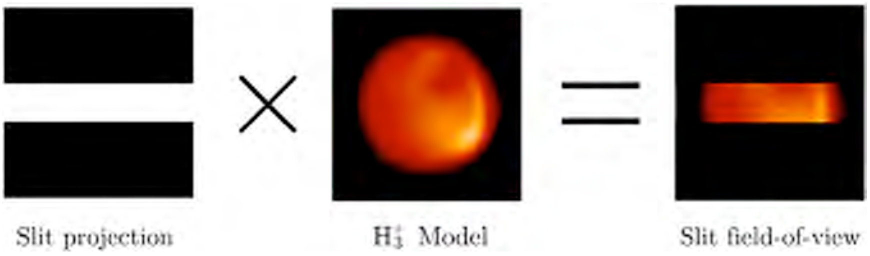

Figure 5.40: The components of the modelled field-of-view (FOV) of a slit aligned with the central meridian (CML). The dusk side is at the top and ULS North is to the left as per Figure 5.29.

new CCD chip. Taking similar images as in 1998 and 1999 could yield unprecedented spatial and temporal detail of the H_3^+ emission from Uranus.

5.7 Modelling spectrographic responses to Uranus

In this section, the $E(H_3^+)$ parameter listed in Table 5.6 will be compared to the modelled short-term intensity variations predicted by the H_3^+ emission model. The intensity variations are caused by the rotation of the planet moving the aurora in and out of the field-of-view of a spectrograph slit. Again, the assumptions of Section 5.5.2 apply.

Only sets of observations in Table 5.6 with three or more spectra will be used in this short-term analysis, as a dataset which only contains only one or two observations, does not provide a meaningful fit to the emission model. All the datasets in Table 5.6 will be looked at together, in the context of variability, in Section 5.8.

5.7.1 The model

The intensity of the H_3^+ emission as seen through the slit of a spectrograph is analysed using the model of the uranian H_3^+ emission, outlined in Section 5.5, but masked with the projection of a slit. This is illustrated in Figure 5.40 for a slit aligned with the central meridian longitude (CML). The slit projection is an array that acts as a switch where locations along the list are set to one, and all other areas are set to zero, so that when the slit is factored against the H_3^+ model, the slit intensity is produced. The width of the slit is different for most observations, with the widest being $3.08''$, which is almost equal to the diameter of Uranus ($\sim 3.7''$), thus having a significant effect on the amount of light that the detector receives.

For each set of observations an H_3^+ slit emission model was created for every fourth degree of sub-observer longitude. The modelled variations in H_3^+ intensity for the observations of 1999, with a slit-width of 0.6″, and a sub-observer latitude of 32°, can be seen in Figure 5.41. The profile for the CML aligned slit has two peaks, one at ∼45° and one at ∼250°. The first peak is a result of northern aurora passing under the slit and the second peak is produced when the partially obscured southern aurora passes under it. The slit aligned with the equator shows only one peak, which is extended, covering some half of a rotation (180°). This emission is produced by the longitudinally extended northern aurora.

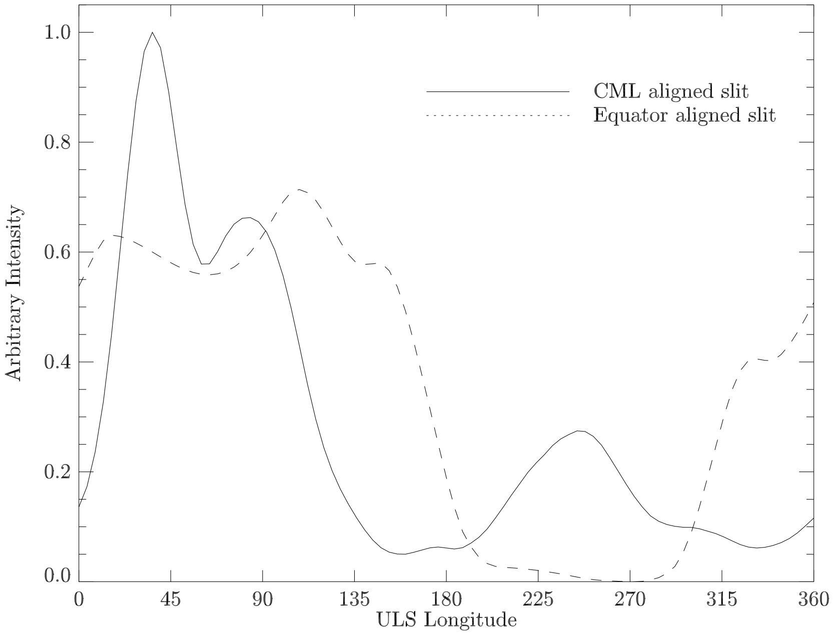

Figure 5.41: The modelled intensity of the 1999 observations, taken using a slit-width of 0.6″ and a sub-Earth latitude of 32°. Note that in the CML profile, there is always some part of the aurora in view on the slit.

5.7.2 Folding the data

The time of observation for each of the available spectra included in this shortterm analysis can be seen in Table 5.12, expressed in Universal Time (UT), UNIX time-stamp (which is seconds from 00:00 on the 1st January 1970), and Julian date, from noon on the 1st of January 2000. The UNIX time-stamp is found using the UT time and the PHP function `date` running locally on an Apache server. The Julian Date of each observation is found using the PHP function `unixtojd`. The IAU longitude is calculated using Equation 5.3, and the resulting value is folded by adding or subtracting 360° until the value is between 0° and 359°.

5.7.3 The model function

The model of the H_3^+ emission from Uranus includes the constant background emission due to solar EUV. For the purposes of determining the components of the H_3^+ emission, this background level is subtracted from the emission model. This means that the solar EUV produced H_3^+ can be treated as a free parameter. The intensity as a function of IAU longitude $I(\theta_{IAU})$ becomes:

$$I(\theta_{IAU}) = a \times I_0(\theta_{ULS} + s) + b \tag{5.8}$$

where θ_{IAU} is the IAU longitude, θ_{ULS} is the ULS longitude, I_0 is the normalised emission profile (e.g. see Figure 5.41), b is the level of the solar EUV produced H_3^+ emission on top of which the auroral emission lies, having an amplitude of a and s is the offset between IAU and ULS longitudes. When s is zero, then the IAU longitude is equal to the ULS longitude.

Using Equation 5.8, the shortterm variability of the H_3^+ can be investigated. This formulation assumes that b is constant over the timescale of each set of observations (a few days), which seems like a reasonable assumptions since the solar EUV changes over an 11-year cycle, albeit with some short-term variability. By fitting the model function to the observed values of $E(H_3^+)$, folded onto longitude, it is possible to extract the background solar H_3^+ level (b), the H_3^+ emission produced by auroral processes (a) and the offset between IAU and ULS longitude (s).

5.7.4 Fitting the model to the data

Fitting the parameters s, a and b is done most easily by eye. The background level of the H_3^+ emission, b, was initially estimated by the lowest value of $E(H_3^+)$ in the dataset, whereas the amplitude of the H_3^+ emission, a, was initially estimated by the largest minus the lowest value of $E(H_3^+)$. The shift parameter, s, was estimated by matching the peak in the H_3^+ emission model to the peak in the folded observations. The fine tuning of the fit was done by plotting and refining the values by visual means.

UT Date	UT Time	Timestamp (s)	$JD_{2000}(days)$	IAU Longitude (°)
1993 May 3	15:19	736438740	-2433.373	33.2
1993 May 4	14:09	736520940	-2432.414	272.6
1993 May 5	12:54	736602840	-2431.497	172.8
1995 Jun 11	11:55	802868100	-1664.534	281.8
1995 Jun 12	13:27	802960020	-1663.450	98.6
1995 Jun 13	13:15	803045700	-1662.449	317.1
1995 Jun 14	12:11	803128260	-1661.490	196.4
1999 Sep 14	05:52	937284720	-108.782	1.0
1999 Sep 14	09:22	937297320	-108.615	277.5
1999 Sep 15	08:52	937381920	-107.656	156.8
1999 Sep 16	06:39	937460340	-106.739	57.1
1999 Sep 17	06:45	937547100	-105.738	275.6
1999 Sep 18	06:04	937631040	-104.737	134.1
1999 Sep 18	07:41	937636890	-104.695	113.0
2001 Jun 16	14:32	992698320	532.594	48.7
2001 Jun 18	12:07	992862420	534.513	167.5
2001 Jun 19	14:36	992957760	535.597	344.2
2002 Jul 18	15:09	1027001340	929.638	146.6
2002 Jul 19	12:30	1027078200	930.513	67.7
2002 Jul 19	14:51	1027086660	930.597	26.0
2002 Jul 20	12:45	1027165500	931.514	286.2
2002 Jul 20	14:55	1027173300	931.597	244.5
2002 Jul 21	12:49	1027252140	932.515	144.7
2002 Jul 21	15:04	1027260240	932.640	82.1
2002 Jul 22	12:34	1027337640	933.515	3.2
2002 Jul 22	15:00	1027346400	933.640	300.6

Table 5.12: The mid-point of observation for the available sets of Uranus spectra. The timestamp is in seconds from 00:00 on the 1st of January 1970. JD_{2000} is the Julian Date measured from noon on the 1st of January 2000 as per the definition of IAU longitude.

It is possible to fit the folded E(H_3^+) arithmetically, but since the errors on the E(H_3^+) are generally fairly large, a visual approach to fitting is justified.

5.7.5 Analysis of data

As stated earlier, this analysis is only really meaningful for sets of observations in which there are more than two spectra. Therefore, only the years 1993, 1995, 1999, 2001 and 2002 will be considered.

The modelled H_3^+ emission was fitted to the observed values of E(H_3^+), given in Table 5.6, and is discussed in more detail below.

Analysis of the 1993 data

There were 3 CML aligned spectra available from May 1993. The sub-observer latitude was 57.2° and the slit-width was $3.08''$. This wide slit-width samples almost the entire disc of Uranus, which at the time of observation was $3.7''$.

The best fit to the data is seen in Figure 5.42, with the crosses being the observed values of E(H_3^+) and the shaded area being 1μWm^{-2} wide, centred around the best fit. The emission model is scaled as per Section 5.7.3 with $s = 52°$, $a = 3.6$ μWm^{-2} and $b = 10.0$ μWm^{-2}.

This emission model fits well to the observations. However, with the large errors on the E(H_3^+) values, it is also possible to fit a horizontal line through the data.

Analysis of the 1995 data

In June 1995 there were 4 CML aligned spectra, taken with a sub-observer latitude of 48.8° and a slit-width of $0.6''$. The best fit was achieved with $s = 216°$ with the emission model being scaled as $a = 3.0$ μWm^{-2} and $b = 6.4$ μWm^{-2}. This is seen in Figure 5.43. One could envisage how the model could be shifted to the right, towards smaller s, such that the model requires a higher value of a in order to fit the data, so there is probably an uncertainty in s of about 45°.

Again, whilst there is a good agreement between the data and the model, although the associated E(H_3^+) errors are as large.

Analysis of the 1999 data

In September 1999 only one spectrum had a slit aligned with the equator, whereas the remaining six were CML-aligned. The sub-observer latitude was 31.9° and the slit-width was $0.61''$. In Figure 5.44 the model can be seen fitted to the observations with a shift of $s = 324°$. The model is scaled with $a = 9.0$ μWm^{-2} and $b = 11.0$ μWm^{-2}.

The 1999 data is difficult to fit. This is due to the two points at around an IAU longitude of about 270° having different E(H_3^+) values, falling outside each other's error bars. The higher value could be sampling the second, smaller, intensity peak due to the south aurora, however, the model cannot account for different E(H_3^+) values at the same IAU longitude.

Analysis of the 2001 data

In June 2001, the sub-observer latitude was 25.1° and the slit-width was $0.61''$. The emission model can be seen in Figure 5.45, fitted with $s = 232°$, $a = 6.0$ μWm^{-2} and $b = 7.5$ μWm^{-2}.

The model can convincingly explain why one observation should yield a value for the E(H_3^+) almost twice as high as the other two data points, and the variation is larger than the size of the error bars.

Analysis of the 2002 data

The July 2002 dataset was taken with a sub-observer latitude of 20.9° and a slit-width of $0.5''$. The observations fitted with the model can be seen in Figure 5.46 for the CML aligned slit and in Figure 5.47 for the equator aligned slit. The best fit to the two slit alignments is $s = 232°$ with $a = 2.0$ μWm^{-2} and $b = 6.0$ μWm^{-2}. Obviously, one set of model parameters must be able to explain the emission observed through both slit orientations simultaneously.

Throughout the observations of 2002 we note both the lowest values and smallest variability in E(H_3^+). In addition, the CML aligned slit appears to be displaying a much weaker average value of E(H_3^+) than the equator aligned slit. This can not be explained by the emission model used here, but could be indicative of auroral features which are extended in longitude, but have limited extent latitudinally.

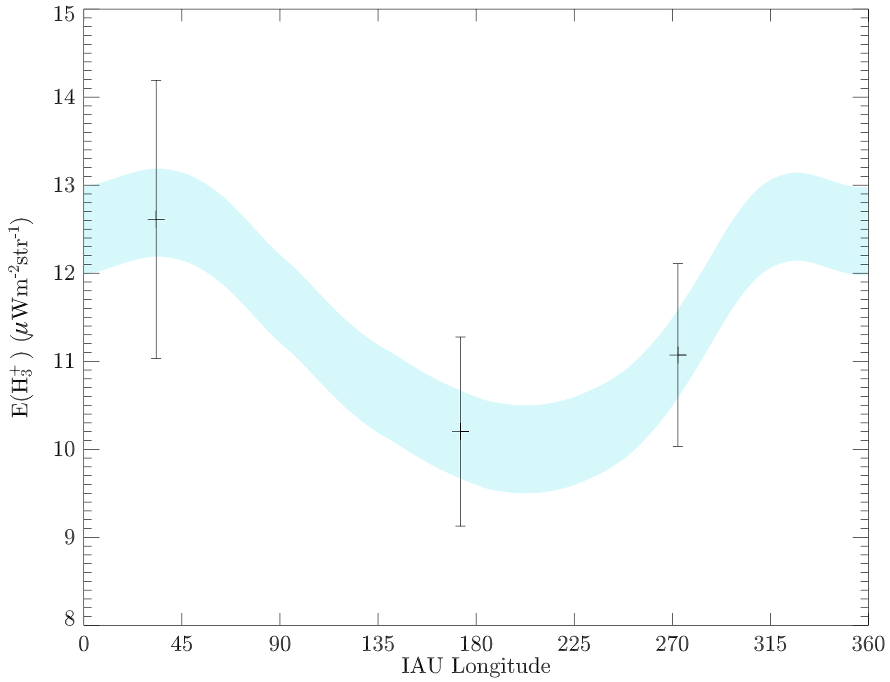

Figure 5.42: The modelled $E(H_3^+)$ response of the spectrograph as Uranus rotates under a equator-aligned slit fitted to the observations of May 1993.

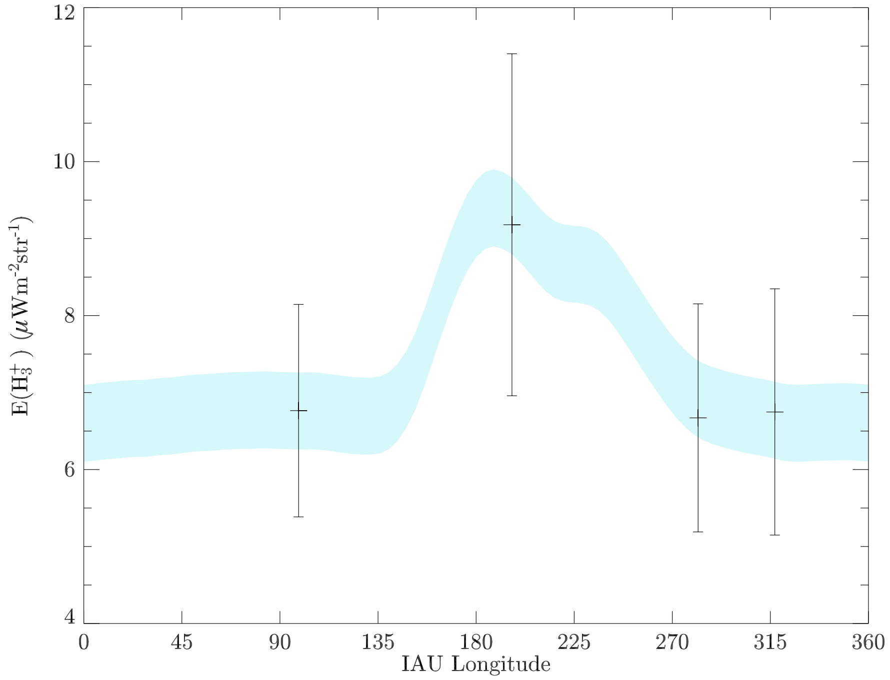

Figure 5.43: The modelled $E(H_3^+)$ response of the spectrograph as Uranus rotates under a CML-aligned slit fitted to the observations of June 1995.

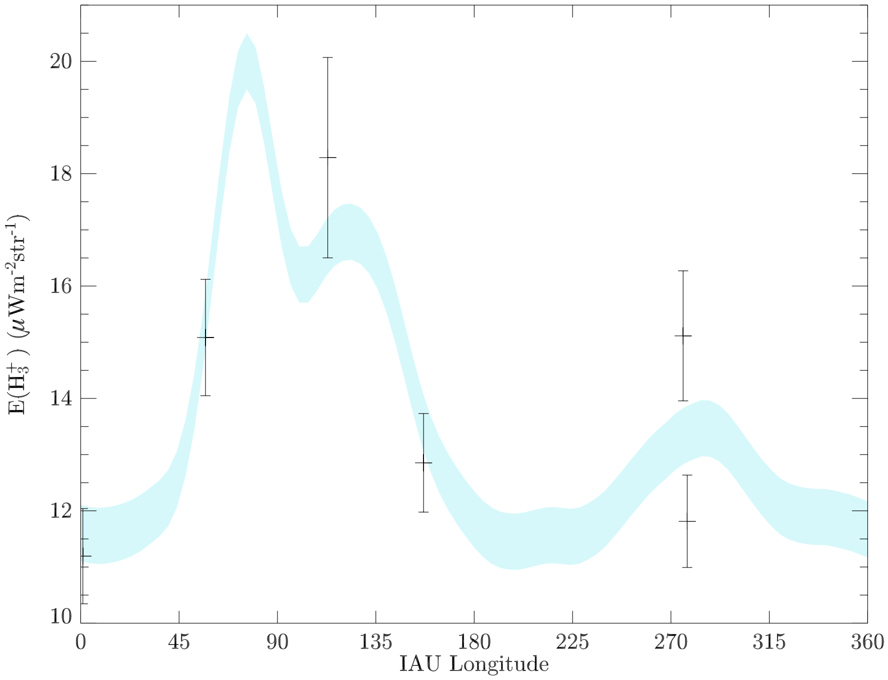

Figure 5.44: The scaled modelled E(H_3^+) response of the aurora as it passes under a CML-aligned slit in September 1999.

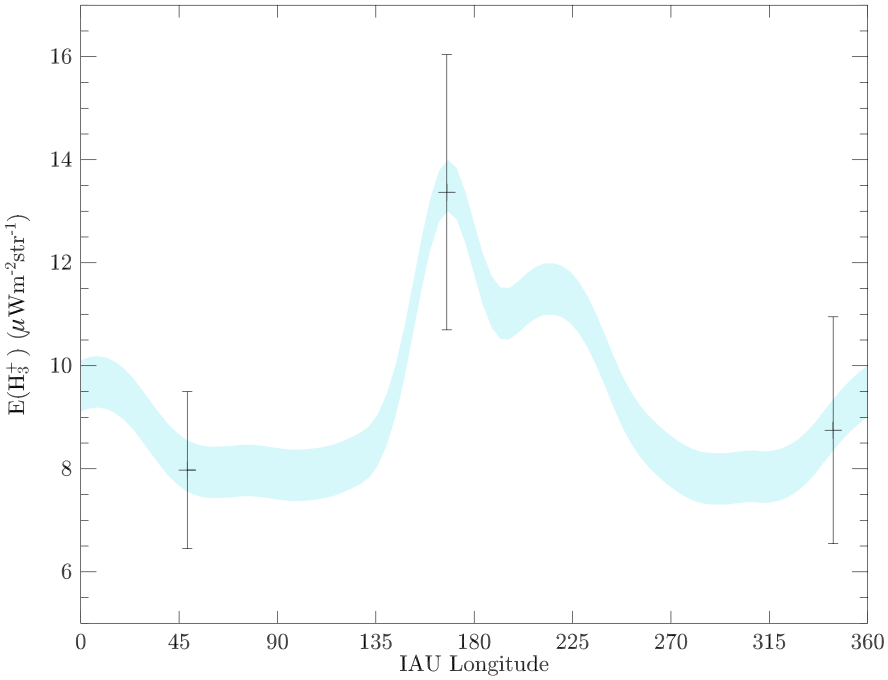

Figure 5.45: The modelled E(H_3^+) response of the spectrograph as Uranus rotates under a CML-aligned slit fitted to the observations of June 2001.

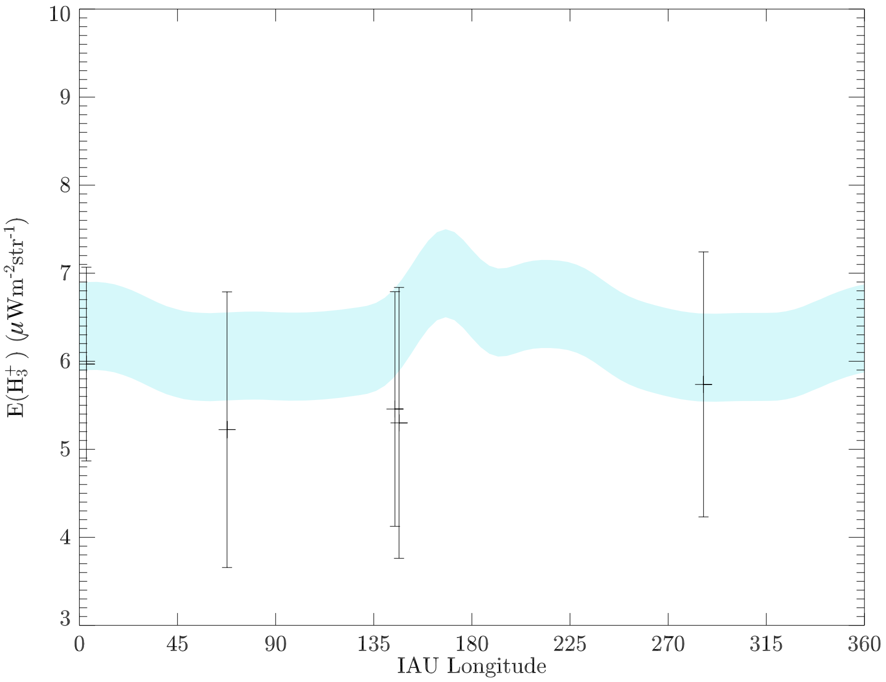

Figure 5.46: The modelled E(H_3^+) response of the spectrograph as Uranus rotates under a CML aligned slit fitted to the observations of July 2002.

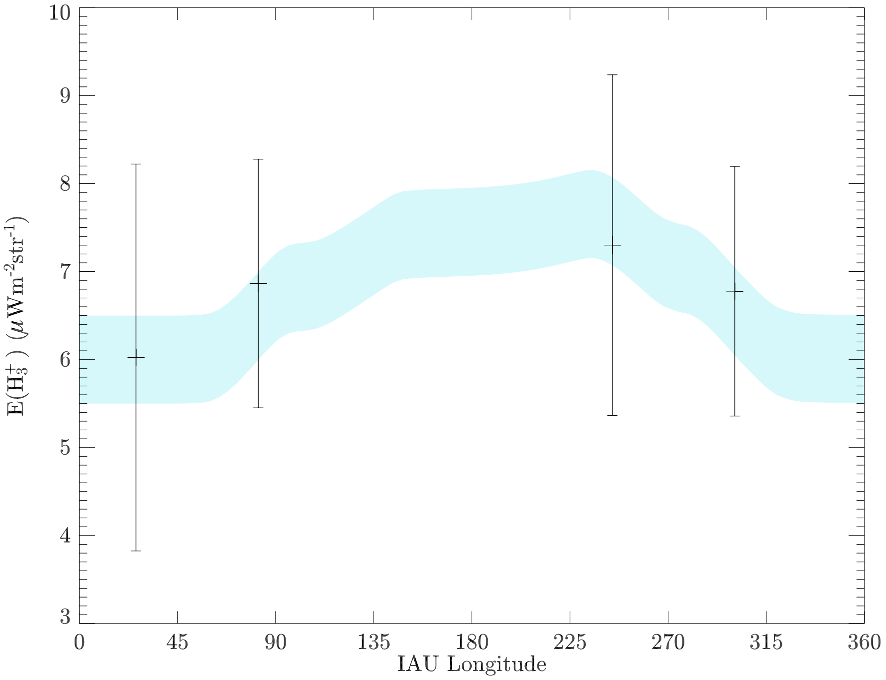

Figure 5.47: The modelled E(H_3^+) response of the spectrograph as Uranus rotates under a equator aligned slit fitted to the observations of July 2002.

Year	SOL (°)	Slit width ($''$)	s (°)	a	b	Auroral level
1993	57.2	3.08	52	3.6	10.0	26%
1995	48.8	1.25	216	3.0	6.4	32%
1999	31.9	0.61	324	9.0	11.0	45%
2001	25.1	0.61	232	6.0	7.5	44%
2002	20.9	0.50	232	2.0	6.0	25%

Table 5.13: The fitted parameters in the short term analysis of Uranus. a and b are values of E(H_3^+) in units of μWm^{-2}.

5.7.6 Finding the period

If the offset, s, between the ULS and IAU longitude for each set of observations is known, one can calculate the period that fits the value of s for all the years. This can mathematically be described as the sum of residuals, $R(P)$:

$$R(P) = \sum_{i}^{years} |S_i(P) - s_i| \tag{5.9}$$

where P is the period, S_i is the calculated longitude offset at year i and s_i is the observed offset, as before. This function can be seen plotted for a range of values of P in Figure 5.48, using the observed values of s listed in Table 5.13. The period that is within the errors of the period of 17.24 ± 0.01 hours determined by Desch et al. [1986] with the smallest residual offset is $P = 17.236 \pm 0.004$ hours. The error is based on the distance between the two adjacent minima.

5.7.7 Summary

In the short-term analysis performed here we observe a variation in E(H_3^+) in the available datasets between 25% and 45% of the maximum (see Table 5.13). There is also evidence that the E(H_3^+) has variability associated with the rotation of the planet. A prime candidate able to create an uneven intensity, but which is fixed in longitude, is emission produced by auroral processes. There is general agreement to the emission model, which is based on the observations by Voyager 2 analysed by Herbert and Sandel [1994]. This lends support for a tentative re-detection of the uranian aurora.

Similar to the short-term analysis of the NSFCam images, it is possible to calculate what period best explains the offset between ULS and IAU longitudes for all the observations. The period analysis for all the spectra can be seen in Figure 5.48 and fits best to 17.236 ± 0.004 hours, slightly slower than that derived by Desch et al. [1986].

5.8 Discussion

The long-term analysis in Section 5.4 sees a sharp reduction of the $E(H_3^+)$ emission as the magnetic pole moves to align itself to the perpendicular of the solar wind flow direction. At years prior to and including 1999, there appears to be a correlation between the solar cycle and the observed $E(H_3^+)$ emission.

In the short-term variability study of both images (Section 5.6) and spectra (Section 5.7) there is a tentative correlation between variations in $E(H_3^+)$ emission with longitude and the auroral features as observed by Herbert and Sandel [1994].

It seems that the solar EUV is the main mechanism for producing H_3^+ on Uranus, responsible for an average of $E(H_3^+) \approx 8\ \mu\text{Wm}^{-2}$. On top of this lies the H_3^+ component generated from auroral processes. This mechanism appears to be dependent on the geometry of the Uranus system, since it is severely reduced as the magnetic pole aligns itself perpendicular with the direction of the solar wind flow. The two components of H_3^+ production as derived from this analysis are shown in Figure 5.49. The figure shows the relative importance of the two H_3^+ production mechanisms for the period covered by this analysis. The triangles are the values of b obtained in the short-term variability study of the spectra, the crosses are $a + b$, i.e. the total value of $E(H_3^+)$ for that set of observations and the stars are the average values of $E(H_3^+)$ for sets of observations with only one or two spectra. The solar EUV produced H_3^+ is modulated approximately as the solar cycle, on top of which there is a highly variable auroral H_3^+ component, that is severely reduced as the magnetic pole moves to align itself with the perpendicular of the direction of the solar wind.

Uranus remains a very difficult planet to observe and understand. This can be attributed to two factors: its large distance from the Sun and its unconventional configuration. Nevertheless, observations of H_3^+ can provide a very useful tool in understanding the ionosphere-magnetosphere interaction, as shown here.

The work presented in this chapter is exploring a number of techniques used to investigate the origins of both short-term and long-term variability of H_3^+ on Uranus. Using telescopes and instruments capable of higher sensitivity and better time and

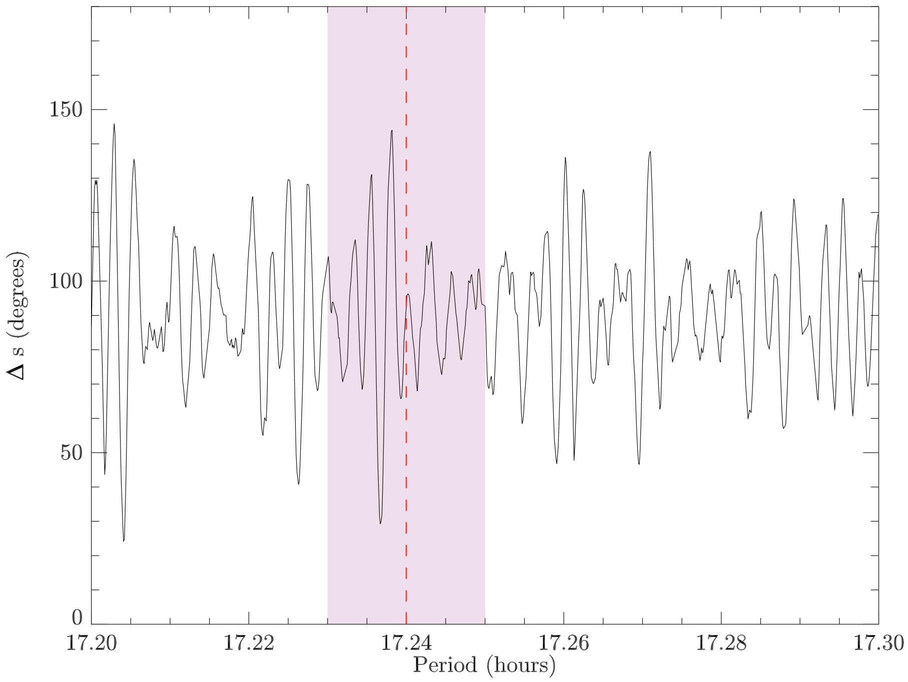

Figure 5.48: The residual between the calculated and observed offset of IAU to ULS longitude. The shaded area indicates the limits of the period of 17.24 ± 0.01 hours of Desch et al. [1986].

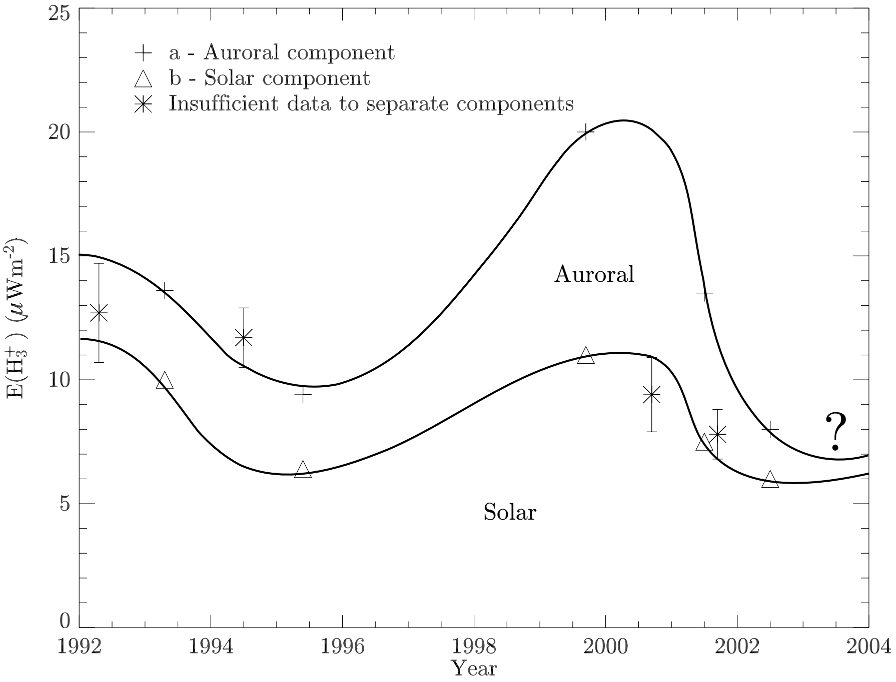

Figure 5.49: The components of the observed H_3^+ emission from Uranus.

spatial resolution, more reliable comparisons with the H_3^+ emission model can be achieved.

The magnetic North pole of Uranus, which lies at a latitude of 15°, aligned itself perpendicular to the solar wind flow direction in early 2004, but there are unfortunately no observations available from that time. It is, however, important that this long-term monitoring is continued so that the sources of variability may be better constrained and understood.

Chapter 6

Comparative aeronomy, discussion and conclusions

This thesis examines the properties of the H_3^+ emission observed from Jupiter, Saturn and Uranus. The results from the analyses of each planet is outlined below, followed by a section on comparative aeronomy, highlighting the differences and similarities between the giant planets upper atmospheres.

6.1 Jupiter

The H_3^+ emission observed from Jupiter is analysed in great detail, using two theoretical developments: the 1D atmospheric numerical model due to Grodent et al. [2001] of the discrete jovian aurora, and the principle of detailed balance formulation for H_3^+, contained in a volume of H_2 by Oka and Epp [2004]. Applying the detailed balance formulation to the atmospheric temperature and density profiles enables us to calculate the effect that departures from Local Thermodynamic Equilibrium (LTE) conditions have on the observed H_3^+ emission. All the vibrational levels are completely depopulated at altitudes above 2,500 km (above the 10^{-2} bar level), although they depopulate at different altitudes, and at different rates. By modelling the volume intensity of observable H_3^+ transitions, and comparing these to observations by Stallard et al. [2002] at 4μm and Raynaud et al. [2004] at 2μm, it is shown that the modelled reduction in H_3^+ intensity for the different vibrational levels due to non-LTE effects, is indeed observed.

Hotbands of H_3^+ are spectral lines that require high temperatures to emit any significant observable intensity since the wave-numbers of their upper energy levels are large. Modelling the volume intensity as a function of altitude for these lines shows that they are preferentially created higher up in the jovian upper atmosphere, compared to fundamental lines. Due to non-LTE effects the intensity of these high altitude H_3^+ lines is severely reduced, resulting in the hotbands being attenuated more than lines formed lower down. This means that a temperature derived from the ratio of a hotband line intensity to a fundamental line intensity is likely to be underestimating the true column-integrated temperature. The method of rationing lines to obtain the temperature and column density inherently assumes that the H_3^+ emission originates from a thin shell in conditions of LTE. It is clear that analysing the observed emission using an numerical model of the aurora, taking into account the effects due to the breakdown of LTE, gives a more complete picture.

Stallard et al. [2002] observed an auroral heating event where the temperature rose from $T = 940 \pm 15$ K to $T = 1065 \pm 15$ K, the column density rose from 1.55×10^{16} m^{-2} to 1.81×10^{16} m^{-2} and the ion velocity doubled from 0.55 kms^{-1} to 1.10 kms^{-1} over a period of three days. Both the densities and velocities are accurate to within 10%. This event is examined in great detail, in terms of energy inputs and outputs, and by using the above non-LTE treatment. It is assumed that the temperature profile of Grodent et al. [2001] can be scaled, as to approximate a first order response to the energy being injected into the atmosphere. The majority of the energy is shown to be Joule heating and ion-drag, and is able to inject more than the minimum heating required. The dominant heat sink is hydrocarbon cooling at the base of the upper atmosphere, at and around the homopause. Above that, H_3^+ emission to space is the dominant coolant.

After the auroral heating event, when the heating terms return to their normal values, the cooling terms are not strong enough to cool the atmosphere over short timescales. This indicates that mechanical means, in the form of thermally driven winds, could be removing excess energy from the auroral region.

This thesis also reports the first astronomical identification of the H_3^+ hotband R(2, 0^-) at 3.63 μm, in the spectrum taken of Jupiter, during the UKIRT observations of Saturn in September 1999.

6.2 Saturn

This thesis presents the first reliable H_3^+ temperature determination of Saturn. A total of three datasets, all taken with CGS4 on UKIRT, are analysed: September 1999, February 2004 and February 2005. The average temperature for the years 1999 and 2004 is $T = 400 \pm 50$ K with a column density of $N = 4.6 \pm 10^{16}$ m^{-2}. This is in accordance with the exospheric temperature of 400 K derived from the Voyager 2 occultation experiment analysed by Smith et al. [1983] at $\sim$ 30°N (i.e. non-auroral). It is much smaller, but not necessarily in disagreement with (Smith et al. [2005]), the 800 K derived from occultation measurements at 4°N by Festou and Atreya [1982].

The average temperature is calculated using two spectra: the September 1999 spectrum with $T = 380 \pm 70$ K and $N = 1.9 \times 10^{16}$ m^{-2} and the 2004 spectrum with $T = 420 \pm 70$ K and $N = 7.3 \times 10^{16}$ m^{-2}. The fact that there are large variations in column density (a factor of ~ 4) suggests large variations in the particle precipitation flux (~ 20). Despite this additional heating into the upper atmosphere, the temperature remains near constant, at around 400 K. The thermostatic role of H_3^+ as observed on Jupiter is not observed on Saturn.

It is of note that the H_3^+ densities on Saturn are of similar orders as derived for the auroral region on Jupiter. This suggests that there are similar levels of precipitation, which means that Saturn must also have significant plasma sources within its magnetosphere, as at Jupiter. This is in agreement with initial Cassini results, e.g. Young et al. [2005] Voyager 2 measured a lower plasma density in Saturn's magnetosphere (See Figure 1.16), but there might be significant differences in the energy distribution of the plasma, such that it is deposited at an altitude on Saturn where it might be able to produce large densities of H_3^+ with a smaller particle flux.

Another consequence of the large column densities derived here, is that it removes the need to reduce the ion density with mechanisms such as the influx of water or a high homopause at high latitudes on the planet. The low H_3^+ density of $\sim 1 \times 10^{15}$ m^{-2} cited by Geballe et al. [1993] is a result of their assumed temperature of 800 K – the E(H_3^+) parameter at 400 K is a factor of $\sim 10^2$ smaller than at 800 K.

The observing run in February 2005 attempted to extract H_3^+ temperatures from a low resolution spectrum ($R = 1520$) covering the regions 3.5 to 4.1μm. This spectral region, at such a spectral resolution, has proven to be very reliable for extracting LTE

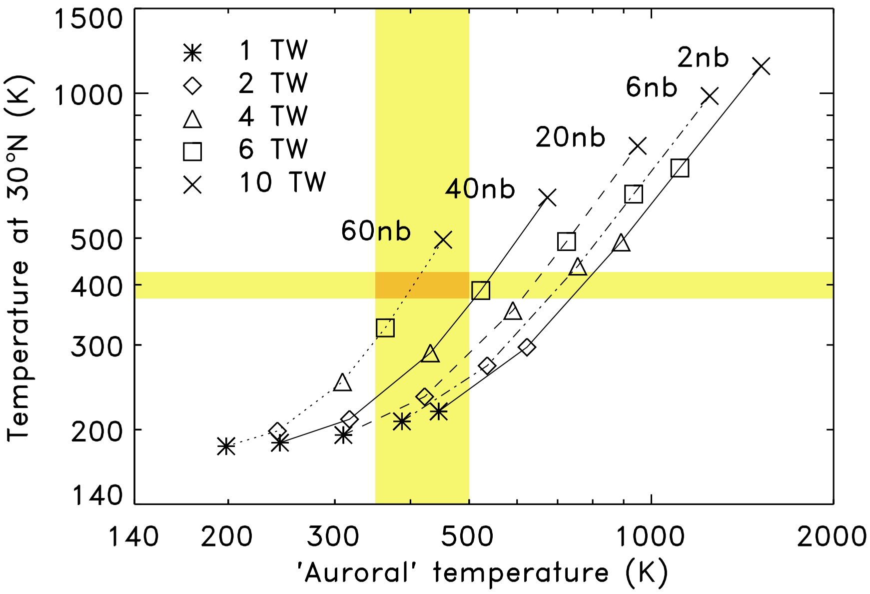

Figure 6.1: The required energy input to produce a given combination of aurora and ~30° N temperature of Saturn. After Smith et al. [2005].

temperatures and column densities on Jupiter and Saturn. However, on Saturn, this region is completely swamped by the reflected sunlight that hydrocarbons are unable to absorb. This suggests that Saturn has a different chemistry at, and around, the homopause compared to Jupiter and Uranus, in addition to very weak H_3^+ emission.

The 'low' auroral temperature of Saturn, derived in this thesis, has implications for models investigating the dynamics and energetics of the upper atmosphere. Smith et al. [2005] used this temperature, in combination with the 400 K at ~30°N of Smith et al. [1983], to calculate how much energy needs to be injected and at what altitude to produce both temperatures. This is shown in Figure 6.1. Five different sets of models were used, from 1 TW to 10 TW of total energy input, and the pressure at which the peak of the energy is deposited varied. The models show that large energies are required low down in the atmosphere (at high pressures), in order to produce the observed temperatures at auroral and equatorial latitudes.

6.3 Uranus

The H_3^+ emission from Uranus is incredibly difficult to interpret, due to the planet's peculiar configuration, and it is not known how the H_3^+ emission responds to changes in geometry or solar EUV flux. The unique set of medium resolution infrared H_3^+

spectra covering 10 years of observations, held at APL (UCL), was re-reduced and re-analysed to treat the entire collection of spectra in a consistent manner.

The long-term analysis of the variability of H_3^+ emission on Uranus indicates that the total E(H_3^+) is loosely connected to the variations in the solar EUV flux, as monitored by the 10.7 cm flux, between the period 1992 to 1999. However, as the magnetic pole moves to align itself with the perpendicular to the solar wind flow direction, beyond the year 1999, the level of the observed E(H_3^+) is severely reduced. The rapid reduction of E(H_3^+) between 1999 and 2002 appears to be related to the changing geometry of the Uranus system. Neptune had an orientation, when it was visited by Voyager 2 in 1989, similar to that of Uranus in 2002, and it was noted that the very inactive magnetosphere was likely to be linked to the once-a-day alignment of the magnetic pole with the direction of the solar wind flow (Schulz et al. [1995]). It appears that we may be observing a similar process on Uranus, although it it unclear exactly how this happens.

We use the only spatially-resolved observation of the uranian aurora available (Herbert and Sandel [1994]) to create an H_3^+ emission model that also includes a solar EUV produced component. This model is compared to both intensity variations in NFSCam images and E(H_3^+) variations in the collection of available spectra.

The NFSCam images of Uranus show that there is a great deal of variability across the disc of Uranus. This implies that there are local effects capable of creating such variations, with a prime candidate being localised particle precipitation. However, the emission model is unable to account for all the variability seen in the sets of NFSCam images.

The short-term H_3^+ variability study of the infrared spectra supports the tentative re-discovery of the aurora on Uranus, with auroral activity being responsible for 25% to 45% of the observed emission of H_3^+.

Whilst Uranus remains a difficult planet to observe, the work done in this thesis has enabled the disentanglement of the components of the H_3^+ auroral and solar production mechanisms, and it has become clear that Uranus is different from both Jupiter and Saturn. Uranus has significant non-auroral emissions, accounting for 55%-75% of the total H_3^+ emission. One significant difference between these planets is the rotational and magnetic configuration, with Uranus having a rotational axis almost aligned with the ecliptic and a magnetic field axis offset some 60° from that. It seems possible that the plasma environment, and hence the flux of precipitating particles, is governed by the orientation of the magnetic field to the solar wind flow direction and the IMF.

6.4 Comparative aeronomy

The three planets analysed in this thesis present three very different systems. Jupiter has very bright H_3^+ emission emanating from the auroral oval, with significant emission at lower latitudes. Saturn has a very faint auroral H_3^+ emission with no detectable on-body emission, whereas Uranus has very significant on-body EUV produced H_3^+ emission, together with a smaller auroral component.

6.4.1 Origin of the H_3^+ emission

Section 1.3.3 describes the two main creation mechanism of the H_2^+ required for the production of H_3^+. These are the production via the energy provided by solar EUV radiation and particle precipitation. The work done in this thesis shows that these two mechanisms have different importance in creating H_3^+ on the giant planets. On Jupiter and Saturn, auroral processes produce vast amounts of H_3^+, with the solar produced component being comparatively small (per unit area), whereas on Uranus the two components are almost equal.

Out of the large number of detected extrasolar planets, the vast majority orbit very close to their host star (< 0.1 AU, Yelle [2004]). During such conditions the solar EUV is likely to be a very important production mechanism, producing an H_3^+ rich upper atmosphere, which acts as a thermostat that prevents the 'boil-off' of the atmosphere (Williams [2004]).

6.4.2 Observed total H_3^+ emission

The total emission of H_3^+ at all wavelengths, $E(H_3^+)$, as a function of temperature, can be seen in Figure 6.2 with the observed H_3^+ temperature range of Jupiter, Saturn and Uranus. The $E(H_3^+)$ is about a factor of 100 larger at 1,000 K compared to at 400 K, which explains how Jupiter and Saturn, both with similar column densities, can have an H_3^+ intensity difference of about 100. Saturn is simply much colder. The fact

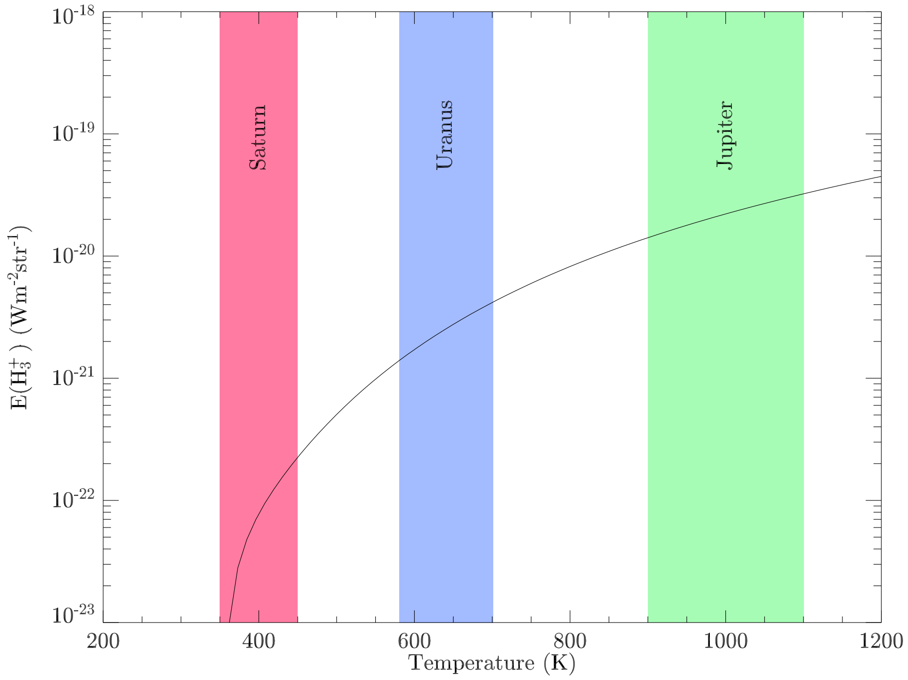

Figure 6.2: The E(H_3^+) as a function of temperature. Marked are the temperatures of the giant planets analysed in this thesis.

that the two planets have similar H_3^+ densities suggests that they have similar particle precipitation fluxes.

Figure 6.2 also highlights that E(H_3^+) is not simply a function of distance from the Sun. Instead, we find that there are internal mechanisms and conditions that affect the total emission of H_3^+, such as the low thermospheric temperature of Saturn.

Trafton et al. [1993] noted that the H_3^+ emission from Uranus is only a few percent of that of Jupiter. Even though there is only a factor of ∼10 difference in E(H_3^+) per molecule for the temperature observed on the respective planets, there is also a factor of ∼10 difference in observed column density, making a total factor of ∼100. This explains the observed difference between the observed E(H_3^+) of the different planets, seen in Table 6.1.

If the upper atmosphere of Saturn and Jupiter are similar in composition, having similar H_3^+ densities, then why is there no detectable H_3^+ on Saturn at non-auroral latitudes? Again, the answer is connected to the very low H_3^+ temperature. Saturn receives about a third of the solar EUV flux that Jupiter receives (based on distance from the Sun), suggesting that the low latitude H_3^+ density should be a factor of 3 smaller than the density at low latitudes on Jupiter. Since the low latitude H_3^+ density

Planet	Temperature (K)	Density (m^{-2})	E(H_3^+) ($Wm^{-2}str^{-1}$)
Jupiter	1100	few×10^{16}	few×10^{-3}
Saturn	400	few×10^{16}	few×10^{-6}
Uranus	650	few×10^{15}	few×10^{-5}

Table 6.1: The approximate temperature, density and E(H_3^+) for the three giant planets investigated in this thesis.

on Jupiter is only $\sim$ 3% of the auroral density (Lam et al. [1997a]), the low latitude H_3^+ density on Saturn is perhaps $\sim$ 1% of the auroral density, which is below the detection limit of currently available instruments.

Uranus receives only one-fourteenth of the solar EUV flux that Jupiter receives. In Chapter 5, it was shown that EUV production mechanisms are responsible for some 55-75% of the observed H_3^+ emission on Uranus. Why is solar EUV production a more dominant source than particle precipitation on this planet? The answer might be that hydrocarbons do not exist in large volumes in the lower parts of the upper atmoshere, removing the quenching effect they have on the H_3^+ density, such that all the solar EUV goes towards creating H_3^+. This effect can be produced by a low homopause, generating a clear and deep ionosphere (Trafton et al. [1999]).

6.4.3 Non-LTE effects

On Jupiter, non-LTE effects are shown to be important in the high temperature, low-density environment of its upper atmosphere at altitudes above 2,000 km above the 10^{-2} bar level. These effects could also, feasibly, be important on the other giant planets. Saturn's thermosphere, is both cold and dense and any effects are, as on Jupiter, likely to affect the high altitude emission of H_3^+. Uranus has an extended corona, and has an average column-integrated LTE H_3^+ temperature of $T = 640$ K (see Chapter 5). It is possible that non-LTE affects the planet in such a way that the amount of H_3^+ being produced by particle precipitation is severely reduced, whereas the solar produced component remains unaffected. This would require the EUV energy to be deposited deep in the atmosphere where the condition of LTE holds, and precipitation energy to be deposited high in the atmosphere, where conditions of LTE break down.

Observing spectral lines from different vibrational manifolds can reveal the extent to which non-LTE effects are significant for the observed emission on Saturn and Uranus, but since the H_3^+ emission from these planets is weak, there needs to be significant improvements to the sensitivity of the available instruments before this can be done.

6.4.4 Energy sources of the upper atmosphere

The ionosphere provides the means for transferring energy from the IMF and the magnetosphere into the upper atmosphere via Joule heating and ion-drag. The amount of energy that can be transferred depends in part on the the Pedersen conductivity, which is a function of ion density. This energy transfer could to some extent explain the high temperatures observed on all the giant planets.

The detailed analysis of energy sources during the auroral heating event observed by Stallard et al. [2002] showed that the dominant energy source available to the upper atmosphere of Jupiter is Joule heating and ion-drag. This energy source is likely to be important on other giant planets. Uranus, in particular, with its highly dynamic magnetosphere and hot upper atmosphere, requires significant energy inputs. Saturn is also hotter than expected, and there are significant current systems in the magnetosphere/ionosphere system (Cowley et al. [2004]), capable of transferring energy into the upper atmosphere. In addition, since Saturn has large column densities, it has a high Pedersen conductivity creating a system that is capable of injecting similar orders of magnitude of energy as Jupiter can.

A similar analysis, as performed for Jupiter, can be performed for Saturn and Uranus, once more cultivated and self-consistent models of their auroral atmospheres become available. These models need the input of observations, and consequently, observing H_3^+ will play a crucial part.

6.5 Future work

Observations of H_3^+ emission using Earth-based telescopes has played an important part in understanding the upper atmospheres of the giant planets. The greater the spectral and spatial resolution of new spectrographs and imagers, the more detail we are able to ascertain, and the more we can learn about these systems. Consequently, it is of vital importance to continue the long-term monitoring of the H_3^+ emission of all three planets. Hopefully, H_3^+ will also be detected on Neptune, and this planet can also soon be monitored in a similar fashion.

The simultaneous observation of emission lines from Jupiter from different vibrational levels will enable the determination of the full extent to which the H_3^+ emission is subject to non-LTE effects.

On Saturn, higher spatial resolution and sensitivity will enable the mapping of H_3^+ temperature and column density. Such mapping has on Jupiter revealed how energy is distributed across the planet in the upper atmosphere (Lam et al. [1997a]).

Uranus, whose H_3^+ emission is still very difficult to interpret, needs to be monitored, for short-term and for long-term analysis. Using imagers and spectrographs with higher spatial and spectral resolution will enable the auroral emission from the planet to be mapped properly. As the data set expands, better correlations between seasonal changes in the solar wind and how the emission varies as the angle between the solar wind and the magnetic changes can be investigated.

6.6 Conclusions

This thesis has shown that the study of H_3^+ emission provides one with a valuable insight to the energetics that govern the upper atmospheres of the giant planets. On Jupiter, non-LTE effects were shown to be important via theoretical considerations. These effects are confirmed using the observations of Stallard et al. [2002] and Raynaud et al. [2004]. Using the non-LTE formulation, the auroral heating event observed by Stallard et al. [2002] was analysed in great detail. It was shown that the majority of the energy required is generated by Joule heating and the major heat sinks are, emission to space of H_3^+ and hydrocarbons. The analysis also highlighted that the thin shell of H_3^+ in LTE assumption underestimates the derived column averaged temperature.

Saturn has an H_3^+ temperature of 400 ± 50 K, with large observed variations in column densities. The observed density is 1.9×10^{16} m^{-2} in 1999 and 7.3×10^{16} m^{-2} in 2004, which is comparable to those densities observed on Jupiter (e.g. Stallard et al. [2002]).

On Uranus, a large H_3^+ spectra dataset was re-analysed to ensure consistency. The average temperature for the entire dataset is $T = 640 \pm 60$ K and the average column density is $N = 4.3 \pm 2.1 \times 10^{15}$ m^{-2}. There is a very large solar EUV H_3^+ produced component, between 55%-75%, and an auroral component making up the rest. The auroral component displays significant variability, and it is drastically reduced as the magnetic north pole aligns itself with the perpendicular to the solar wind flow direction.

The work performed within thesis utilises a number of techniques, both observational and theoretical, to investigate the ionospheric properties of Jupiter, Saturn and Uranus. It is shown that the analyses of H_3^+ emission can reveal fundamental properties of the upper atmosphere of these planets. There is ample scope for more work, with improving models and instruments becoming available, in addition to a renewed international focus on space exploration. These are indeed exciting times for planetary science.

Appendix A

Derivatives of the spectral function

This Appendix describes the derivatives used in the spectra fitting routine outlined in Section 2.4. The intensity at a particular wavelength λ at temperature T can is described as a sum of gaussians:

$$I(\lambda, T) = k + \rho \sum_{i=0}^{n_{lines}} \frac{I_i(T)}{\sigma_i \sqrt{2\pi}} \exp\left(-\frac{(\lambda - (\lambda_i + s(\lambda)))^2}{2\sigma_i^2}\right) \tag{A.1}$$

where

$$I(T) = \frac{N \times g_{ns}(2J+1)100 \times hcw_{if} A_{if}}{4\pi Q(T)} \exp\left[-\frac{100 \times hcw_{upper}}{kT}\right] \tag{A.2}$$

The variables in these equations are defined in Table A.1. The wavenumbers given in Neale et al. [1996] are given in units of [cm^{-1}] so there is a factor of 100 in the equations in order to keep the equations in SI units.

A.1 Temperature derivative

The temperature derivative is given by:

$$\frac{\partial I}{\partial T} = \rho \sum_{i=0}^{n_{lines}} \frac{1}{\sigma_i \sqrt{2\pi}} \exp\left(-\frac{(\lambda - (\lambda_i + s(\lambda)))^2}{2\sigma_i^2}\right) \frac{\partial I_i(T)}{\partial} \tag{A.3}$$

such that

$$\frac{\partial I_i(T)}{\partial T} = I_i(T) \frac{100 \times hcw_{upper}}{kT^2} - I_i(T) \frac{1}{Q(T)} \frac{\partial Q(T)}{\partial T} \tag{A.4}$$

Parameter	Definition	Units
$I(\lambda, T)$	Intensity	$\mathrm{Wm^{-2}str^{-1}\mu m^{-1}}$
T	Temperature	Kelvin
ρ	Density	$\mathrm{m^{-2}}$
k	Background level	$\mathrm{Wm^{-2}str^{-1}\mu m^{-1}}$
λ	Wavelength	μm
$\sigma(\lambda)$	Line width	μm
$s(\lambda)$	Line shift	μm
g_{ns}	Spin weightening	–
J	Angular momentum quantum nbr	–
w_{if}	Emission frequency	$\mathrm{cm^{-1}}$
w_{upper}	Upper energy level	$\mathrm{cm^{-1}}$
A_{if}	Einstein A coefficient	–
h	Planck's constant	$\mathrm{m^{-2}kg\ s^{-1}}$
c	Speed of light	$\mathrm{m\ s^{-1}}$
k	Boltzmann's constant	$\mathrm{m^2kg\ s^{-2}K^{-1}}$

Table A.1: Definitions of parameters used in the expression for the spectral function derivatives.

where $\partial Q(T)/\partial T$ is given in Section A.2.

A.2 Partition function derivative

This parameter is described in Section 2.4.3. The derivative is given by:

$$\frac{\partial Z}{\partial T} = \log_{10}(Z) \times \frac{\partial}{\partial T}\left(\log_{10}(Z)\right) \tag{A.5}$$

where $\log_{10}(Z)$ is given in Equation 2.32 and

$$\frac{\partial}{\partial T}\left(\log_{10}(Z)\right) = \sum_{n=0}^{6} n a_n \left(\log_{10} T\right)^{n-1} \frac{1}{T} \tag{A.6}$$

The constants a_n are the same as given in section 2.4.3.

A.3 Density derivative

The density derivative is given by:

$$\frac{\partial I}{\partial \rho} = \sum_{i=0}^{n_{lines}} \frac{I_i(T)}{\sigma_i\sqrt{2\pi}} \exp\left(-\frac{(\lambda - (\lambda_i + s(\lambda)))^2}{2\sigma_i^2}\right) \tag{A.7}$$

A.4 Background level derivatives

The derivative of the constant background level k is given simply by:

$$\frac{\partial I}{\partial k} = 1 \tag{A.8}$$

A.5 Shift derivative

The shift $s(\lambda)$ parameterises the offset between the theoretical spectrum of Neale et al. [1996] and the observed spectrum. The derivative is given by:

$$\frac{\partial I}{\partial s} = \rho \sum_{i=0}^{n_{lines}} \frac{I_i(T)}{\sigma_i\sqrt{2\pi}} \exp\left(-\frac{(\lambda - (\lambda_i + s(\lambda)))^2}{2\sigma_i^2}\right) \frac{2(\lambda - (\lambda_i + s(\lambda)))}{2\sigma_i^2} \frac{\partial s(\lambda)}{\partial b_i} \tag{A.9}$$

where

$$\frac{\partial s}{\partial b_i} = \lambda^i \tag{A.10}$$

where s is defined in Equation 2.55.

A.6 Line width derivative

The line width, $\sigma(\lambda)$, describes the width of the line so that the full width at half maximum (FWHM) a particular wavelength is FWHM $= \sqrt(2\pi)\sigma(\lambda)$. The line width derivative is:

$$\frac{\partial I}{\partial \rho} = \rho \sum_{i=0}^{n_{lines}} \frac{I_i(T)}{\sigma_i\sqrt{2\pi}} \exp\left(-\frac{(\lambda - (\lambda_i + s(\lambda)))^2}{2\sigma_i^2}\right) \frac{(\lambda - (\lambda_i + s(\lambda)))^2}{2\sigma_i^2} \frac{(-1)}{\sigma^3} \frac{\partial \sigma(\lambda)}{\partial a_i} \tag{A.11}$$

where

$$\frac{\partial \sigma(\lambda)}{\partial a_i} = \lambda^i \tag{A.12}$$

Appendix B

IDL procedures

IDL stands for Interactive Data Language, and is a interpreted script language created for the handling and visualisation of data, astronomical or otherwise. It is very versatile, and the majority of the processing work of images and spectra was preformed using this language.

This Appendix will document the most important IDL routines developed for this thesis.

B.1 `wavegen.pro`

Inputs:

- Start of the wavelength scale in μm
- Start of the wavelength scale in μm
- Number of wavelength elements

Outputs:

- A wavelength array

Description: Generates a wavelength scale between the defined start and end wavelengths with a set number of array elements. It is a linear interpolation. This procedure is useful in conjunction with `h3p_model_spectra.pro`.

B.2 `h3p_model_spectra.pro`

Inputs:

- Temperature in K
- Wavelength array defining dispersion and coverage
- σ – the width of the spectral lines

Outputs:

- A theoretical H_3^+ spectrum in units of [Wμm^{-1}str^{-1}molecule^{-1}]

Description: This procedures writes the inputs to files and calls an external C++ program, through IDLs `spawn.pro` procedure. The C++ program calculates the theoretical emission per molecule and generates the line profile for all lines within the wavelength range provided.

B.3 `h3p_fit_auto.pro`

Required inputs:

- Array containing the intensity of a spectrum in units of [Wμm^{-1}str^{-1}]
- Array containing the wavelength scale of the above spectrum
- Initial guess for the temperature
- Array to store the fitted parameters

Optional inputs:

- Initial guess for σ
- Initial guess for the wavelength shift
- Initial guess for the background level
- The option of fixing σ, shift and backround level, so that these are not fitted – the supplied values are used instead.

- The option of setting the fitting of σ and the wavelength shift to any order desired.
- The option of suppressing all outputs to screen

Outputs:

- A theoretical H_3^+ spectrum that is a fit to the supplied spectrum

Description: This procedure calls the C++ fitting routine outlined in Section 2.4.

B.4 `uranus_generate_nfscam_observations.pro`

Inputs:

- Central Meridian Longitude (CML) of observation.
- Offset of model from ULS Longitude.
- Number of quads in observation
- Integration per quad
- Sub-observer latitude of Uranus at the time of observation.

Outputs:

- A 2-D model image of the H_3^+ emission

Description: This function creates a model given the observational parameters of the H_3^+ emission from Uranus assuming only production by solar EUV radiation and auroral emissions. This is described in more detail in Section 5.6.

Bibliography

N. Achilleos, S. Miller, R. Prangé, G. Millward, and M. K. Dougherty. A dynamical model of Jupiter's auroral electrojet. *New Journal of Physics*, 3:3–+, 2001.

N. Achilleos, S. Miller, J. Tennyson, A. D. Aylward, I. Mueller-Wodarg, and D. Rees. JIM: A time-dependent, three-dimensional model of Jupiter's thermosphere and ionosphere. *Journal of Geophysical Research*, 103:20089–20112, 1998a.

N. Achilleos, S. Miller, J. Tennyson, and UCL Jupiter Group Team. Models of Jupiter's Auroral Electrojet. *Bulletin of the American Astronomical Society*, 30:1083–+, 1998b.

A. Alonso, S. Arribas, and C. Martínez-Roger. The effective temperature scale of giant stars (F0-K5). II. Empirical calibration of T_{eff} versus colours and [Fe/H]. *Astronomy and Astrophysics Supplement*, 140:261–277, 1999.

S. K. Atreya. *Atmospheres and Ionospheres of the Outer Planets and their Satellites.* Springer-Verlag, 1986.

S. K. Atreya, T. M. Donahue, A. F. Nagy, J. H. Waite, and J. C. McConnell. *Saturn*, chapter Theory, measurements, and models of the upper atmosphere and ionosphere of Saturn, pages 239–277. University of Arizona Press, 1984.

R. L. Baron, T. Owen, J. E. P. Connerney, T. Satoh, and J. Harrington. NOTE: Solar Wind Control of Jupiter's H_3^+ Auroras. *Icarus*, 120:437–442, 1996.

J. W. Belcher, R. L. McNutt, J. D. Richardson, R. S. Selesnick, E. C. Sittler, and F. Bagenal. *The plasma environment of Uranus*, pages 780–830. Uranus, 1991.

E. A. Bergin, E. Lellouch, M. Harwit, M. A. Gurwell, G. J. Melnick, M. L. N. Ashby, G. Chin, N. R. Erickson, P. F. Goldsmith, J. E. Howe, S. C. Kleiner, D. G. Koch,

D. A. Neufeld, B. M. Patten, R. Plume, R. Schieder, R. L. Snell, J. R. Stauffer, V. Tolls, Z. Wang, G. Winnewisser, and Y. F. Zhang. Submillimeter Wave Astronomy Satellite Observations of Jupiter and Saturn:Detection of 557 GHZ Water Emission from the Upper Atmosphere. *The Astrophysical Journal*, 539:L147–L150, 2000.

Jay T. Bergstralh, Ellis D. Miner, Mildred Shapley Matthews, and 84 collaborating authors. *Uranus*. The University of Arizona Press, 1991.

P. R. Bevington and D. K. Robinson. *Data reduction and error analysis for the physical sciences*. McGraw-Hill, 2003.

D. E. Blackwell, S. K. Leggett, A. D. Petford, C. M. Mountain, and M. J. Selby. Absolute calibration of the infrared flux from VEGA at 1.24, 2.20, 3.76 and 4.6 microns by comparison with a standard furnace. *Monthly Notices of the Royal Astronomical Society*, 205:897–905, 1983.

S. W. Bougher, J. H. Waite, T. Majeed, and G. R. Gladstone. Jupiter Thermospheric General Circulation Model (JTGCM): Global structure and dynamics driven by auroral and Joule heating. *Journal of Geophysical Research (Planets)*, 110:4008–+, 2005.

H. S. Bridge, J. W. Belcher, R. J. Butler, A. J. Lazarus, A. M. Mavretic, J. D. Sullivan, G. L. Siscoe, and V. M. Vasyliunas. The plasma experiment on the 1977 Voyager mission. *Space Science Reviews*, 21:259–287, 1977.

A. L. Broadfoot, S. K. Atreya, J. L. Bertaux, J. E. Blamont, A. J. Dessler, and S. Linick. Ultraviolet spectrometer observations of Neptune and Triton. *Science*, 246:1459–1466, 1989.

A. L. Broadfoot, M. J. Belton, P. Z. Takacs, B. R. Sandel, D. E. Shemansky, J. B. Holberg, J. M. Ajello, H. W. Moos, S. K. Atreya, T. M. Donahue, J. L. Bertaux, J. E. Blamont, D. F. Strobel, J. C. McConnell, R. Goody, A. Dalgarno, and M. B. McElroy. Extreme ultraviolet observations from Voyager 1 encounter with Jupiter. *Science*, 204:979–982, 1979.

A. L. Broadfoot, F. Herbert, J. B. Holberg, D. M. Hunten, S. Kumar, B. R. Sandel, D. E. Shemansky, A. J. Dessler, S. Linick, and R. Springer. Ultraviolet spectrometer observations of Uranus. *Science*, 233:74–79, 1986.

R. P. Butler, S. S. Vogt, G. W. Marcy, D. A. Fischer, J. T. Wright, G. W. Henry, G. Laughlin, and J. J. Lissauer. A Neptune-Mass Planet Orbiting the Nearby M Dwarf GJ 436. *The Astrophysical Journal*, 617:580–588, 2004.

J. Caldwell, R. Wagener, T. Owen, M. Combes, and T. Encrenaz. Tentative confirmation of an aurora on Uranus. *Nature*, 303:310–312, 1983.

G. D. Carney and R. N. Porter. Ab initio prediction of the rotation-vibration spectrum of H_3^+ and D_3^+. *Physical Review Letters*, 45:537–541, 1980.

T. N. Chatterjee and T. K. Das. Relation between solar UV flux and 10.7-cm radio emission. *Monthly Notices of the Royal Astronomical Society*, 274:858–860, 1995.

J. Clarke, J. Caldwell, T. Skinner, and R. Yelle. The Aurora and Airglow of Jupiter. In *NASA Special Publication Series, NASA-SP-494, 211-220*, pages 211–220, 1989.

J. Clarke, S. Durrance, W. Moos, J. Murthy, S. Atreya, A. Barnes, J. Mihalov, J. Belcher, M. Festou, and C. Imhoff. Continued observations of the H Lyman α emission from Uranus. *Journal of Geophysical Research*, 91:8771–8781, 1986.

J. T. Clarke. Detection of auroral hydrogen Lyman-alpha emission from Uranus. *Astrophysical Journal Letters*, 263:L105–L109, 1982.

J. T. Clarke, J.-C. Gérard, D. Grodent, S. Wannawichian, J. Gustin, J. Connerney, F. Crary, M. Dougherty, W. Kurth, S. W. H. Cowley, E. J. Bunce, T. Hill, and J. Kim. Morphological differences between Saturn's ultraviolet aurorae and those of Earth and Jupiter. *Nature*, 433:717–719, 2005.

J. E. P. Connerney, M. H. Acuña, N. F. Ness, and T. Satoh. New models of Jupiter's magnetic field constrained by the Io flux tube footprint. *Journal of Geophysical Research*, 103:11929–11940, 1998.

J. E. P. Connerney and J. H. Waite. New model of Saturn's ionosphere with an influx of water from the rings. *Nature*, 312:136–138, 1984.

S. W. H. Cowley. A Beginner's Guide to the Earth's Magnetosphere. *Earth in Space Volume 8*, 26, March 1996.

S. W. H. Cowley and E. J. Bunce. Origin of the main auroral oval in Jupiter's coupled magnetosphere-ionosphere system. *Planetary Space Science*, 49:1067–1088, 2001.

S. W. H. Cowley, E. J. Bunce, and J. D. Nichols. Origins of Jupiter's main oval auroral emissions. *Journal of Geophysical Research (Space Physics)*, 108:3–1, 2003a.

S. W. H. Cowley, E. J. Bunce, and J. M. O'Rourke. A simple quantitative model of plasma flows and currents in Saturn's polar ionosphere. *Journal of Geophysical Research (Space Physics)*, pages 5212–+, 2004.

S. W. H. Cowley, E. J. Bunce, T. S. Stallard, and S. Miller. Jupiter's polar ionospheric flows: Theoretical interpretation. *Geophysical Research Letters*, 30:24–1, 2003b.

F. J. Crary, J. T. Clarke, M. K. Dougherty, P. G. Hanlon, K. C. Hansen, J. T. Steinberg, B. L. Barraclough, A. J. Coates, J.-C. Gérard, D. Grodent, W. S. Kurth, D. G. Mitchell, A. M. Rymer, and D. T. Young. Solar wind dynamic pressure and electric field as the main factors controlling Saturn's aurorae. *Nature*, 433:720–722, 2005.

D. P. Cruikshank, M. S. Matthews, and A. M. Schumann. *Neptune and Triton.* University of Arizona Press, 1995.

M. C. Cushing, W. D. Vacca, and J. T. Rayner. Spextool: A Spectral Extraction Package for SpeX, a 0.8-5.5 Micron Cross-Dispersed Spectrograph. *Publications of the Astronomical Society of the Pacific*, 116:362–376, 2004.

M. D. Desch, J. E. P. Connerney, and M. L. Kaiser. The rotation period of Uranus. *Nature*, 322:42–+, 1986.

M. D. Desch, M. L. Kaiser, P. Zarka, A. Lecacheux, Y. Leblanc, M. Aubier, and A. Ortega-Molina. *Uranus*, chapter Uranus as a radio source, pages 894–925. University of Arizona Press, 1991.

B. M. Dinelli, S. Miller, and J. T. Tennyson. Bands of H_3^+ up to $4\nu_2$: Rovibrational transitions from first principles calculations. *Journal of Molecular Spectroscopy*, 153:718–725, 1992.

P. Drossart, B. Bezard, S. K. Atreya, J. Bishop, J. H. Waite, and D. Boice. Thermal profiles in the auroral regions of Jupiter. *Journal of Geophysical Research*, 98: 18803–+, 1993.

P. Drossart, J.-P. Maillard, J. Caldwell, S. J. Kim, J. K. G. Watson, W. A. Majewski, J. Tennyson, S. Miller, S. K. Atreya, J. T. Clarke, J. H. Waite, and R. Wagener. Detection of H_3^+ on Jupiter. *Nature*, 340:539–541, 1989.

J. W. Dungey. Interplanetary Magnetic Field and the Auroral Zones. *Physical Review Letters*, 6(2):47–48, January 1961.

T. Encrenaz, P. Drossart, G. Orton, H. Feuchtgruber, E. Lellouch, and S. K. Atreya. The rotational temperature and column density of H_3^+ in Uranus. *Planetary and Space Science*, 51:1013–1016, 2003.

T. Encrenaz, B. Schulz, P. Drossart, E. Lellouch, H. Feuchtgruber, and S. K. Atreya. The ISO spectra of Uranus and Neptune between 2.5 and 4.2 mum: constraints on albedos and H_3^+. *Astronomy & Astrophysics*, 358:L83–L87, 2000.

A. Eviatar and D. D. Barbosa. Jovian magnetospheric neutral wind and auroral precipitation flux. *Journal of Geophysical Research*, 89:7393–7398, 1984.

M. C. Festou and S. K. Atreya. Voyager ultraviolet stellar occultation measurements of the composition and thermal profiles of the Saturnian upper atmosphere. *Geophysical Research Letters*, 9:1147–1150, 1982.

H. Feuchtgruber and T. Encrenaz. The infrared spectrum of Neptune at 3.5-4.1 microns: Search for H_3^+ and evidence for recent meteorological variations. *Astronomy and Astrophysics*, 403:L7–L10, 2003.

D. Flower. *Molecular collisions in the interstellar medium.* Cambridge University Press, 1990.

P. H. M. Galopeau and A. Lecacheux. Variations of Saturn's radio rotation period measured at kilometer wavelengths. *Journal of Geophysical Research*, 105:13089–13102, 2000.

T. R. Geballe, M.-F. Jagod, and T. Oka. Detection of H_3^+ infrared emission lines in Saturn. *The Astrophysical Journal*, 408:L109–L112, 1993.

J. Geiss and A. Buergi. Diffusion and thermal diffusion in partially ionized gases in the atmospheres of the sun and planets. *Astronomy & Astrophysics*, 159:1–2, 1986.

G. R. Gladstone, R. V. Yelle, and T. Majeed. *Solar System Upper Atmospheres: Photochemistry, Energetics, and Dynamics*, pages 23–+. Atmospheres in the Solar System: Comparative Aeronomy, 2002.

I. S. Glass. JHKL Photometry of 145 Southern Stars [errata: 1974MNSSA..33...71G]. *Monthly Notes of the Astronomical Society of South Africa*, 33:53–+, 1974.

M. Goto, B. J. McCall, T. R. Geballe, T. Usuda, N. Kobayashi, H. Terada, and T. Oka. Absorption Line Survey of H_3^+ toward the Galactic Center Sources I. GCS 3-2 and GC IRS3. *Publications of the Astronomical Society of Japan*, 54:951–961, 2002.

T. P. Greene, A. T. Tokunaga, and J. S. Carr. High Resolution Spectroscopy with CSHELL at the IRTF. In *ASSL Vol. 190: Astronomy with Arrays, The Next Generation*, pages 511–+, 1994.

D. Grodent, J. T. Clarke, J. Kim, J. H. Waite, and S. W. H. Cowley. Jupiter's main auroral oval observed with HST-STIS. *Journal of Geophysical Research (Space Physics)*, 108:2–1, 2003.

D. Grodent, J.-C. Gérard, S. W. H. Cowley, E. J. Bunce, and J. T. Clarke. Variable morphology of Saturn's southern ultraviolet aurora. *Journal of Geophysical Research (Space Physics)*, 110:7215–+, July 2005.

D. Grodent, J. H. J. Waite, and J. Gerard. A self-consistent model of the Jovian auroral thermal structure. *Journal of Geophysical Research*, 106:12933–12952, July 2001.

J. T. Hallett, D. E. Shemansky, and X. Liu. Fine-structure physical chemistry modeling of Uranus H_2 X quadrupole emission. *Geophysical Research Letters*, 32:2204–+, 2005.

F. Herbert and B. R. Sandel. The Uranian aurora and its relationship to the magnetosphere. *Journal of Geophysical Research*, 99:4143–4160, 1994.

F. Herbert, B. R. Sandel, R. V. Yelle, J. B. Holberg, A. L. Broadfoot, D. E. Shemansky, S. K. Atreya, and P. N. Romani. The upper atmosphere of Uranus – EUV occultations observed by Voyager 2. *Journal of Geophysical Research*, 92:15093–15109, 1987.

M. P. Hickey, R. L. Walterscheid, and G. Schubert. Gravity Wave Heating and Cooling in Jupiter's Thermosphere. *Icarus*, 148:266–281, 2000.

T. W. Hill. Inertial limit on corotation. *Journal of Geophysical Research*, 84:6554–6558, 1979.

T. W. Hill. Corotation lag in Jupiter's magnetosphere – Comparison of observation and theory. *Science*, 207:301–+, January 1980.

D. P. Hinson, F. M. Flasar, A. J. Kliore, P. J. Schinder, J. D. Twicken, and R. G. Herrera. Jupiter's ionosphere: Results from the first Galileo radio occultation experiment. *Geophysical Research Letters*, 24:2107–+, 1997.

D. P. Hinson, J. D. Twicken, and E. T. Karayel. Jupiter's ionosphere: New results from Voyager 2 radio occultation measurements. *Journal of Geophysical Research*, 103:9505–9520, 1998.

W. B. Hubbard, V. Haemmerle, C. C. Porco, G. H. Rieke, and M. J. Rieke. The occultation of SAO 78505 by Jupiter. *Icarus*, 113:103–109, 1995.

D. M. Hunten. Atmospheres and ionospheres. In *IAU Colloq. 30: Jupiter: Studies of the Interior, Atmosphere, Magnetosphere and Satellites*, pages 22–31, 1976.

D. L. Judge, F.-M. Wu, and R. W. Carlson. Ultraviolet photometer observations of the Saturnian system. *Science*, 207:431–434, 1980.

M. L. Kaiser, M. D. Desch, and J. E. P. Connerney. Saturn's ionosphere - Inferred electron densities. *Journal of Geophysical Research*, 89:2371–2376, 1984.

L. Kao, T. Oka, S. Miller, and J. Tennyson. A table of astronomically important rovibrational transitions for the H_3^+ molecular ion. *Astrophysical Journal Supplement Series*, 77:317–329, October 1991.

Y.H. Kim, J. L. Caldwell, and H. S. Porter. Densities and vibrational distribution of H_3^+ in the Jovian auroral ionosphere. *Journal of Geophysical Research*, 97:6093–6101, 1992.

M. G. Kivelson and C. T. Russell. *Introduction to space physics*. Cambridge University Press, 1995.

A. J. Kliore, G. F. Lindal, I. R. Patel, D. N. Sweetnam, H. B. Hotz, and T. McDonough. Vertical structure of the ionosphere and upper neutral atmosphere of Saturn from the Pioneer radio occultation. *Science*, 207:446–449, 1980.

H. A. Lam, N. Achilleos, S. Miller, J. Tennyson, L. M. Trafton, T. R. Geballe, and G. E. Ballester. A Baseline Spectroscopic Study of the Infrared Auroras of Jupiter. *Icarus*, 127:379–393, 1997a.

H. A. Lam, S. Miller, R. D. Joseph, T. R. Geballe, L. M. Trafton, J. Tennyson, and G. E. Ballester. Variation in the H_3^+ Emission of Uranus. *Astrophysical Journal Letters*, 474:L73+, 1997b.

S. K. Leggett, T. G. Hawarden, M. J. Currie, A. J. Adamson, T. C. Carroll, T. H. Kerr, O. P. Kuhn, M. S. Seigar, W. P. Varricatt, and T. Wold. L' and M' standard stars for the Mauna Kea Observatories Near-Infrared system. *Monthly Notices of the Royal Astronomical Society*, 345:144–152, 2003.

M. T. Leu, M. A. Biondi, and R. Johnsen. Measurements of Recombination of Electrons with H_3^+ and H_5^+ Ions. *Physical Review A*, 8:413–419, 1973.

G. F. Lindal, J. R. Lyons, D. N. Sweetnam, V. R. Eshleman, and D. P. Hinson. The atmosphere of Uranus – Results of radio occultation measurements with Voyager 2. *Journal of Geophysical Research*, 92:14987–15001, 1987.

D. R. Linder, A. J. Coates, R. D. Woodliffe, C. Alsop, A. D. Johnstone, M. Grande, A. Preece, B. Narheim, and D. T. Young. The Cassini CAPS Electron Spectrometer. In *Measurement Techniques in Space Plasmas – Particles*, pages 257–+, 1998.

W. Livingston and L. Wallace. *An atlas of the solar spectrum in the infrared from 1850 to 9000* cm^{-1} *(1.1 to 5.4* μm*)*. NSO Technical Report, Tucson: National Solar Observatory, National Optical Astronomy Observatory, 1991.

G. W. Lockwood and D. T. Thompson. Photometric Variability of Neptune, 1972-2000. *Icarus*, 156:37–51, 2002.

D. Lummerzheim, M. Brittnacher, D. Evans, G. A. Germany, G. K. Parks, M. H. Rees, and J. F. Spann. High time resolution study of the hemispheric power carried by energetic electrons into the ionosphere during the May 19/20, 1996 auroral activity. *Geophysical Research Letters*, 24:987–990, 1997.

J. Maillard, P. Drossart, J. K. G. Watson, S. J. Kim, and J. Caldwell. H_3^+ fundamental band in Jupiter's auroral zones at high resolution from 2400 to 2900 inverse centimeters. *The Astrophysical Journal Letters*, 363:L37–L41, 1990.

T. Majeed and J. C. McConnell. Impact of the "Electroglow" Ionization Source on the Upper Ionospheres of the Outer Planets. *Bulletin of the American Astronomical Society*, 18:777–+, 1986.

K. I. Matcheva and D. F. Strobel. Heating of Jupiter's Thermosphere by Dissipation of Gravity Waves Due to Molecular Viscosity and Heat Conduction. *Icarus*, 140: 328–340, 1999.

B. J. McCall. Laboratory spectroscopy of H_3^+. *Royal Society of London Philosophical Transactions Series A*, 358:2385–2401, 2000.

B. J. McCall. *Spectroscopy of H_3^+ in Laboratory and Astrophysical Plasmas.* PhD thesis, University of Chicago, June 2001.

M. A. McGrath, P. D. Feldman, G. E. Ballester, and H. W. Moos. IUE observations of the Jovian dayglow emission. *Geophysical Research Letters*, 16:583–586, 1989.

M. Mendillo, A. Nagy, and J. H. Waite. *Atmospheres in the solar system: comparative aeronomy.* American Geophysical Union, 2002.

S. Miller, N. Achilleos, G. E. Ballester, T. R. Geballe, R. D. Joseph, R. Prangé, D. Rego, T. Stallard, J. Tennyson, L. M. Trafton, and J. H. Waite. The role of H_3^+ in planetary atmospheres. In *Astronomy, physics and chemistry of H_3^+*, pages 2485–+, 2000.

S. Miller, N. Achilleos, G. E. Ballester, H. A. Lam, J. Tennyson, T. R. Geballe, and L. M. Trafton. Mid-to-Low Latitude H_3^+ Emission from Jupiter. *Icarus*, 130:57–67, 1997.

S. Miller, A. Aylward, and G. Millward. Giant Planet Ionospheres and Thermospheres: The Importance of Ion-Neutral Coupling. *Space Science Reviews*, 116:319–343, January 2005.

S. Miller, H. A. Lam, and J. Tennyson. What astronomy has learned from H_3^+. *Canadian Journal of Physics*, 72:760–771, 1994.

S. Miller and J. Tennyson. Calculated rotational and rovibrational transitions in the spectrum of H_3^+. *Astrophysical Journal*, 335:486–490, 1988.

S. Miller, J. Tennyson, and R. D. Joseph. Infrared emissions of H_3^+ in the atmosphere of Jupiter in the 2.1 and 4.0 micron region. *Astrophysical Journal Letters*, 360: L55–L58, 1990.

G. Millward, S. Miller, T. Stallard, A. D. Aylward, and N. Achilleos. On the Dynamics of the Jovian Ionosphere and Thermosphere III. The Modelling of Auroral Conductivity. *Icarus*, 160:95–107, 2002.

A. Morioka, S. Yaegashi, H. Nozawa, H. Misawa, Y. S. Miyoshi, F. Tsuchiya, and S. Okano. H_3^+ emissions in the Jovian sub-auroral region and auroral activity. *Geophysical Research Letters*, 31:16806–+, 2004.

J. I. Moses and S. F. Bass. The effects of external material on the chemistry and structure of Saturn's ionosphere. *Journal of Geophysical Research*, pages 7013–7052, 2000.

L. Neale, S. Miller, and J. Tennyson. Spectroscopic Properties of the H_3^+ Molecule: A New Calculated Line List. *The Astrophysical Journal*, 464:516–+, 1996.

L. Neale and Jonathan Tennyson. A High-Temperature Partition Function for H_3^+. *Astrophysical Journal Letters*, 454:L169, December 1995.

N. F. Ness, M. H. Acuna, K. W. Behannon, L. F. Burlaga, J. E. P. Connerney, and R. P. Lepping. Magnetic fields at Uranus. *Science*, 233:85–89, 1986.

N. F. Ness, M. H. Acuna, L. F. Burlaga, J. E. P. Connerney, and R. P. Lepping. Magnetic fields at Neptune. *Science*, 246:1473–1478, 1989.

T. Oka. Collision-induced transitions between rotational levels. *Advances in Atomic and Molecular Physics*, 9:127 – 205, 1973.

T. Oka. Observation of the infrared spectrum of H_3^+. *Physical Review Letters*, 45: 531–534, 1980.

T. Oka and E. Epp. The Nonthermal Rotational Distribution of H_3^+. *The Astrophysical Journal*, 613:349–354, 2004.

F.-S. Pan and T. Oka. Calculated forbidden rotational spectra of H_3^+. *The Astrophysical Journal*, 305:518–525, 1986.

R. Prangé, L. Pallier, K. C. Hansen, R. Howard, A. Vourlidas, R. Courtin, and C. Parkinson. An interplanetary shock traced by planetary auroral storms from the Sun to Saturn. *Nature*, 432:78–81, November 2004.

E. Raynaud, E. Lellouch, J.-P. Maillard, G. R. Gladstone, J. H. Waite, B. Bézard, P. Drossart, and T. Fouchet. Spectro-imaging observations of Jupiter's 2-μm auroral emission. I. H_3^+ distribution and temperature. *Icarus*, 171:133–152, 2004.

J. T. Rayner, D. W. Toomey, P. M. Onaka, A. J. Denault, W. E. Stahlberger, W. D. Vacca, M. C. Cushing, and S. Wang. SpeX: A Medium-Resolution 0.8-5.5 Micron Spectrograph and Imager for the NASA Infrared Telescope Facility. *Publications of the Astronomical Society of the Pacific*, 115:362–382, 2003.

D. Rego, S. Miller, N. Achilleos, R. Prangé, and R. D. Joseph. Latitudinal Profiles of the Jovian IR Emissions of H_3^+ at 4 μm with the NASA Infrared Telescope Facility: Energy Inputs and Thermal Balance. *Icarus*, 147:366–385, 2000.

J.D. Richardson, J. W. Belcher, A. Szabo, and R. L. McNutt Jr. *Neptune and Triton*, chapter The plasma enviroment of Neptune, pages 279–340. University of Arizona Press, 1995.

B. R. Sandel and A. L. Broadfoot. Morphology of Saturn's aurora. *Nature*, 292: 679–682, 1981.

B. R. Sandel, D. E. Shemansky, A. L. Broadfoot, J. B. Holberg, G. R. Smith, J. C. McConnell, D. F. Strobel, S. K. Atreya, T. M. Donahue, H. W. Moos, D. M. Hunten, R. B. Pomphrey, and S. Linick. Extreme ultraviolet observations from the Voyager 2 encounter with Saturn. *Science*, 215:548–553, 1982.

T. Satoh, J. E. P. Connerney, and R. L. Baron. Emission Source Model of Jupiter's H_3^+ Aurorae: A Generalized Inverse Analysis of Images. *Icarus*, 122:1–23, 1996.

M. Schulz, M. C. McNab, R. P. Lepping, and G. H. Voigt. *Neptune and Triton*, chapter Magnetospheric configuration of Neptune, pages 233–278. University of Arizona Press, 1995.

R. W. Schunk and A. F. Nagy. Ionospheres. *Cambridge University Press, Cambridge*, 2000.

A. Seiff, D. B. Kirk, T. C. D. Knight, L. A. Young, F. S. Milos, E. Venkatapathy, J. D. Mihalov, R. C. Blanchard, R. E. Young, and G. Schubert. Thermal structure of Jupiter's upper atmosphere derived from the Galileo probe. *Science*, 276:102–104, 1997.

C. G. A. Smith, A. D. Aylward, S. Miller, and I. C. F. Müller-Wodarg. Polar heating in Saturn's thermosphere. *Ann. Geophys.*, pages 2465–2477, 2005.

G. R. Smith, D. E. Shemansky, J. B. Holberg, A. L. Broadfoot, B. R. Sandel, and J. C. McConnell. Saturn's upper atmosphere from the Voyager 2 EUV solar and stellar occultations. *Journal of Geophysical Research*, 88:8667–8678, 1983.

D. J. Southwood and M. G. Kivelson. A new perspective concerning the influence of the solar wind on the Jovian magnetosphere. *Journal of Geophysical Research*, 106: 6123–6130, 2001.

T. Stallard. *Dynamical Studies of the Jovian Ionosphere*. PhD thesis, University College London, April 2000.

T. Stallard, S. Miller, G. E. Ballester, D. Rego, R. D. Joseph, and L. M. Trafton. The H_3^+ Latitudinal Profile of Saturn. *The Astrophysical Journal*, 521:L149–L152, 1999.

T. Stallard, S. Miller, G. Millward, and R. D. Joseph. On the Dynamics of the Jovian Ionosphere and Thermosphere. I. The Measurement of Ion Winds. *Icarus*, 154: 475–491, 2001.

T. Stallard, S. Miller, G. Millward, and R. D. Joseph. On the Dynamics of the Jovian Ionosphere and Thermosphere. II. The Measurement of H_3^+ Vibrational Temperature, Column Density, and Total Emission. *Icarus*, 156:498–514, 2002.

T. S. Stallard, S. Miller, L. M. Trafton, T. R. Geballe, and R. D. Joseph. Ion winds in Saturn's southern auroral/polar region. *Icarus*, 167:204–211, 2004.

R. G. Stone, J. L. Bougeret, J. Caldwell, P. Canu, Y. de Conchy, N. Cornilleau-Wehrlin, M. D. Desch, J. Fainberg, K. Goetz, and M. L. Goldstein. The Unified Radio and Plasma wave investigation. *Astronomy and Astrophysics Supplement Series*, 92:291–316, 1992.

D. F. Strobel and G. R. Smith. On the Temperature of the Jovian Thermosphere. *Journal of Atmospheric Sciences*, 30:718–725, May 1973.

D. F. Strobel, R. V. Yelle, D. E. Shemansky, and S. K. Atreya. *Uranus*, chapter The upper atmosphere of Uranus, pages 65–109. University of Arizona Press, 1991.

L.P. Theard and W.T. Jr. Huntress. Ion-molecule reactions and vibrational deactivation of H_2^+ ions in mixtures of hydrogen and helium. *The Journal of Chemical Physics*, 60(7):2840–2848, 1974. URL `http://link.aip.org/link/?JCP/60/2840/1`.

J. J. Thomson. Further Experiments on Positive Rays. *Phil. Mag.*, 24:209–253, 1912.

G. Tóth, D. Kovács, K. C. Hansen, and T. I. Gombosi. Three-dimensional MHD simulations of the magnetosphere of Uranus. *Journal of Geophysical Research (Space Physics)*, 109:11210–+, 2004.

L. M. Trafton, T. R. Geballe, S. Miller, and T. Stallard. On the Mapping Efficiency of Integral Field vs Longslit Spectrographs: Comparison of the UIST/IFU and CGS4 at UKIRT using Uranus in the K-L Bands. *UKIRT Newsletter*, 16, Spring 2005.

L. M. Trafton, T. R. Geballe, S. Miller, J. Tennyson, and G. E. Ballester. Detection of H_3^+ from Uranus. *The Astrophysical Journal*, 405:761–766, 1993.

L. M. Trafton, S. Miller, T. R. Geballe, J. Tennyson, and G. E. Ballester. H_2 Quadrupole and H_3^+ Emission from Uranus: The Uranian Thermosphere, Ionosphere, and Aurora. *The Astrophysical Journal*, 524:1059–1083, 1999.

J. Trauger, J. T. Clarke, G. E. Ballester, K. Stapelfeldt, R. Evans, and WFPC2 Science Team. An Observation of Saturn's Aurora with HST/STIS. *Bulletin of the American Astronomical Society*, 30:1096–+, 1998a.

J. T. Trauger, R. E. Griffiths, J. J. Hester, J. G. Hoessel, J. A. Holtzman, J. E. Krist, J. R. Mould, R. Sahai, P. A. Scowen, K. R. Stapelfeldt, and A. M. Watson. Saturn's hydrogen aurora: Wide field and planetary camera 2 imaging from the Hubble Space Telescope. *Journal of Geophysical Research*, 103:20237–20244, 1998b.

G. L. Tyler, V. R. Eshleman, D. P. Hinson, E. A. Marouf, R. A. Simpson, D. N. Sweetnam, J. D. Anderson, J. K. Campbell, G. S. Levy, and G. F. Lindal. Voyager 2 radio science observations of the Uranian system Atmosphere, rings, and satellites. *Science*, 233:79–84, 1986.

V. M. Vasyliūnas. Comparative magnetospheres: lessons for Earth. *Advances in Space Research*, 33:2113–2120, 2004.

J. H. Waite and T. E. Cravens. Current review of the Jupiter, Saturn, and Uranus ionospheres. *Advances in Space Research*, 7:119–134, 1987.

J. H. Waite, T. E. Cravens, J. Kozyra, A. F. Nagy, S. K. Atreya, and R. H. Chen. Electron precipitation and related aeronomy of the Jovian thermosphere and ionosphere. *Journal of Geophysical Research*, 88:6143–6163, 1983.

J. H. Waite, W. S. Lewis, G. R. Gladstone, T. E. Cravens, A. N. Maurellis, P. Drossart, J. E. P. Connerney, S. Miller, and H. A. Lam. Outer planet ionospheres – A review of recent research and a look toward the future. *Advances in Space Research*, 20: 243–+, 1997.

S. Warren. Scientific goals of the UKIRT Infrared Deep Sky Survey. In *Survey and Other Telescope Technologies and Discoveries*, pages 313–320, 2002.

J. K. G. Watson. Forbidden rotational spectra of polyatomic molecules. *J. Mol. Spectrosc.*, 40:536–544, 1971.

A. D. C. Williams. *JIM-e – The Explanet Ionospheric Model.* PhD thesis, University College London, 2004.

G. Ye and T. W. Hill. Solar-wind convection in the Uranian magnetosphere. *Journal of Geophysical Research*, 99:17225–+, 1994.

R. V. Yelle. Aeronomy of extra-solar giant planets at small orbital distances. *Icarus*, 170:167–179, July 2004.

R. V. Yelle and S. Miller. *Jupiter's thermosphere and ionosphere*, pages 185–218. Cambridge University Press, 2004.

L. A. Young, R. V. Yelle, R. Young, A. Seiff, and D. B. Kirk. Gravity Waves in Jupiter's Thermosphere. *Science*, 267:108–+, 1997.

L. A. Young, R. V. Yelle, R. Young, A. Seiff, and D. B. Kirk. Gravity waves in Jupiter's stratosphere, as measured by the Galileo ASI experiment. *Icarus*, 173: 185–199, 2005.